WARWICK
THE UNIVERSITY OF WARWICK

A Thesis Submitted for the Degree of PhD at the University of Warwick

Permanent WRAP URL:

http://wrap.warwick.ac.uk/165893

Copyright and reuse:
This thesis is made available online and is protected by original copyright.
Please scroll down to view the document itself.
Please refer to the repository record for this item for information to help you to cite it.
Our policy information is available from the repository home page.

For more information, please contact the WRAP Team at: wrap@warwick.ac.uk

warwick.ac.uk/lib-publications

University of Warwick

Doctoral Thesis

Interdisciplinary biomedical research

Biophysical mechanisms of antimicrobial resistance in swarming *B. subtilis*

Author: Iago Grobas

1st Supervisor: Dr. Munehiro Asally

2nd Supervisor: Dr. Marco Polin

October 4, 2021

Contents

List of Figures

List of Tables

Declaration statement

This thesis is submitted to the University of Warwick in support of my application for the degree of Doctor of Philosophy. It has been composed by myself and has not been submitted in any previous application for any degree.

The work presented (including data generated and data analysis) was carried out by the author except in the cases outlined below:
The sequencing results obtained by MicrobesNG and BGIsequencing companies were checked using Sanger Sequencing by the following students: Mar Moreno, Nikitha Sam, Joshua Selvaratnam and Roseanne Dean-Milward. Mar Moreno also contributed to the fitness characterization of the microcolonies at the swarming front.

Parts of this thesis have been published by the author:
1. Grobas, I., Bazzoli, D. G. and Asally, M. Biofilm and swarming emergent behaviours controlled through the aid of biophysical understanding and tools. *Biochem. Soc. Trans.* 48, 2903–2913 (2020).
2. Grobas, I., Polin, M. and Asally, M. Swarming bacteria undergo localized dynamic phase transition to form stress-induced biofilms. *elife* 10, e62632 (2021).

Acknowledgements

The only thing you need to remember is that you are going to forget

This is definitely a sentence which has left a mark on me during this PhD, said to me by my first supervisor Munehiro Asally. To him, I thank not only this sentence but all the uncountable lessons that he taught me during these years. I feel so lucky that someone so talented and wise has dedicated so much time to me. Definitely one of the persons I learnt from the most and that I hope to keep learning from over the coming years. I would like to thank also my second supervisor Marco Polin who I consider one of the most brilliant and thorough scientists I ever met. Marco has believed in me and encouraged me to challenge myself as a student and in my academic career. I can say that thanks to him I have gone farther than I thought I could because he thought I could.

This adventure would have been very different without some people that every now and then took me out of work to live some crazy experiences. Thanks Randa Elsayed for being literally next to mevevery day of this PhD, for listening to my complaints and for all the times we laughed together throughout these years. Thanks Magda Karlikowska for taking me to party every week, for being a supportive friend and for keeping the drama going. Thanks Marco Delise for introducing me to the lab, photographing me at my best and organizing amazing trips together. Thanks Manjari Ghanshyam for being one of the most inspiring people I have ever come across, I hope one day I can buy a book written by you. I would like to thank in general the Asally's and Polin's labs and all their members who helped and supported me during this PhD. Thanks also to Maria Solsona and Ramon Garcia for the amazing time we spent together and the scientific exchange.

I would like to thank also the members of the MRC IBR DTP, a great community of people that taught me science, the sense of community in the scientific world and that forced me to have very needed breaks. Within this community I want to highlight the scientific advise that I received from Darius Köster and Meera Unnikrishnan which I believed was essential during my PhD.

I want to thank one of the biggest discoveries of my time in the UK which are the student societies. They were an incredible sink of stress and so much fun. Without them I would not have enjoyed this experience nearly as much.

Finally, I want to thank my partner Iago Diez. I am convinced that thanks to him I could do this PhD. He is immensely clever and I cannot count the times he has helped me with the most challenging parts of my project. I admire him in all aspects of life and I hope one day I can become the amazing scientist and person that he is.

Abstract

Swarms and biofilms are the two major modes of bacterial collectives and confer cells with emergent properties that lack as individuals, such as an increase in antibiotic tolerance. Swarming is a rapid type of surface colonization, and therefore its ability to withstand high antibiotic concentrations could lead to the subsequent establishment of highly resilient biofilms or genetically resistant bacteria in regions that could not otherwise have been colonized. However, whether the development of biofilms or resistant microcolonies by swarms is possible is unknown. Using swarming *Bacillus subtilis*, we reveal that a biophysical mechanism, reminiscent of motility-induced phase separation (MIPS), underpins a swarming-to-biofilm transition through a localized dynamic phase transition. This transition, triggered by an external stressor, is underpinned by a localized multilayer formation. Inspired by the thermodynamic properties of active matter, we demonstrated that such multilayer formation forms through a nucleation and growth process near an antibiotic gradient, and through spinodal decomposition in absence of stress. The nucleation and growth of multiple layers near the antibiotic, triggers waves of bacteria that move towards the antibiotic source, suggesting a novel mechanism of bacterial transport. When swarming to biofilm transition was prohibited by the environmental conditions, the swarm uses an alternative strategy to cope with the antibiotic gradient by developing resistant microcolonies. Quantification of this resistance displayed that the higher resistance to kanamycin is acquired together with resistance to other antibiotics targeting the same process. Inspired by the medical motivation of this project, we suggested solutions to both the emergence of the biofilm and the development of resistant bacteria by using the insight that we gained throughout the study. In particular, we proved that the biofilm formation can be reduced when splitting the total dose of antibiotics in two different time steps: the first triggers the multilayer formation and the second targets this key region in the swarm. Alternatively, when the swarm develops resistant colonies, we observed that these become more vulnerable to other drugs, so a tratement using certain sequence of antibiotics could be highly effective to kill multidrug resistant bacteria. These could lead to new strategies to tackle antimicrobial resistance.

Abbreviations

MSD: mean square displacement

s.e.m.: standard error of the mean

EPS: extracellular polymeric substances

MIC: minimum inhibitory concentration

CSF: competence and sporulation factor

ABC: ATP-binding cassette

ccdf: complementary cumulative distribution function

ar: aspect ratio

SNPs: single nucleotide polymorphysms

InDels: Insertion and deletion sequences

Kan: Kanamycin

LB: Lysogeny-broth

CFU: Colony forming units

KB: Kirby-Bauer

WT: wild type

DI: deionised

PIV: particle image velocimetry

ROI: Region of interest

str: streptomycin

apra: apramycin

spt: spectinomycin

cm: chloramphenicol

amp: ampicillin

GFAT:Glutamine: fructose-6-phosphate aminotransferase

RMSE: root mean square error

Chapter 1

Introduction

1.1 Antibiotic resistance

The use of antibiotics is essential in most of the complex medical interventions such as organ transplantation, management of patients with cancer and surgery [2]. In the scenario of an infection, the antibiotic is transported along the different organs and diffuses through the tissues eventually killing the infecting bacteria [3]. However, these microorganisms adapt to a wide range of threats in their environment and can develop strategies to improve their survivability in presence of external changes. Unfortunately, scientific development of new drugs occurs slower (only 5 antibiotics introduced clinically in the last 20 years [4]) than this adaptation which seriously compromises many clinical procedures and highly decreases the successful outcomes of critically ill patients [5]. Therefore, new ways to tackle antibiotic resistance and more insight into the already known resistance mechanisms are needed.

One common case is that bacteria develop resistance due to stress under exposure to sub-lethal concentration of antibiotics [6]. This naturally occurs in the human body when treating an infection with antibiotics since the antimicrobials create gradients of concentration in the tissues that not always kill the bacteria [7, 8, 3, 9]. In this scenario, random mutations appear in subgroups of the population during the replication process. Potentially, some of these mutations can alter the way bacteria machinery interacts with the drug, protecting the cell against the antibiotic. As a result, populations which are resistant to the drug will survive and overcome the susceptible ones. In many cases, changes in this internal machinery leading to resistance come with a metabolic cost [5]. As a consequence, the susceptible subgroup will grow faster in antibiotic free conditions. Therefore, the presence of antibiotic works as a selective pressure to choose certain mutations, since under treatment, just the resistant mutants survive. Those mutations may result in many

and diverse mechanisms to deal with the antimicrobials.

One of the main strategies by which bacteria become resistant is the production of enzymes which block the interaction of the antibiotic with its target [5]. Curiously, most of the antimicrobials affected by these enzymes target bacterial ribosome [10]. Ribosomes are the cell machinery which guarantees accurate conversion of the genetic information into proteins [11].

1.1.1 Protein synthesis

These machines have two subunits (the big 50S subunit and the small 30S) which are made by ribosomal RNA (rRNA) and proteins. The process by which ribosomes synthesize proteins is called translation. In translation, ribosomes work as platforms which facilitate the binding of complementary tRNA anticodon sequences to messenger RNA (mRNA) codons. Here, mRNA functions as a template which binds to the 30S subunit and determines the specific aminoacid sequence. The tRNAs carry the specific aminoacids which bind the mRNA as it passes through. Translation takes place in three different stages: initiation, elongation and termination [12].

During initiation, the two main subunits of the ribosome assemble around the target mRNA. This new platform has three different sites where tRNA substrates can move through: exit (E), peptidyl (P) and aminoacyl (A). The A site is the point of entry for the aminoacyl-tRNA (aa-tRNA) or charged tRNA, except for the very first aa-tRNA, which enters at the P site [13]. This first aa-tRNA gives place to the next step of protein syntheis: elongation.

The elongation of the polypeptide starts when the elongation factor Tu (EF-Tu) adds a new aa-tRNA to the A-site of the ribosome. This tRNA anticodon pairs the mRNA codon by peptide-bound formation in the P- and A-sites. When P- and A-sites are occupied by aa-tRNA, an aminoacid is transferred from P to A thanks to the enzymatic activity of aminoacyltransferases. Now, the aa-tRNA loses its aminoacyl group giving place to deacylated or uncharged tRNA and the aa-tRNA in the A site adds one aminoacid to the chain [14].

Following peptide bond formation, the acceptor ends of deacylated (in P site) and peptidyl tRNAs (in A site) translocate spontaneously into the 50S subunit's E and P sites, respectively. The anticodon ends of deacylated and peptidyl tRNAs maintain their interactions with the 30S subunit's P and A sites, respectively, resulting in hybrid P/E and A/P binding states [15].

The process continues with translocation by which aa-tRNA is moved from the A- to

P-site and uncharged tRNA from the P- to E-site at the 30S subunit. This translocation is catalysed by the elongation factor G which facilitates tRNA transfer through the different binding sites of the ribosome [10]. After translocation, the E-site is occupied by the peptidyl tRNA coming from the A-site [13]. The cycle continues until a stop codon binds the ribosome, releasing the peptide chain that is being formed (Figure 1.1a).

1.1.2 Ribosome-targeting antibiotics

The fact that protein synthesis is a fundamental process for any living organism, makes the ribosome a very convenient target for antimicrobials since they would affect a fundamental process in the cell, probably leading to cell death [16, 17]. Thus, most antimicrobials target the 30S subunit of the ribosome. This subunit is formed by the 16S ribosomal rRNA and 19 different proteins. The 16S rRNA guides the start codon of the mRNA into the right position. Conventionally, 16S rRNA is labelled with "H#" to indicate the helix number. Proteins are labelled "S#" to indicate the different peptides involved in rRNA stabilization [18].

The binding sites for the drugs are usually found along the path of the mRNA and tRNAs. Depending on their chemical structure, antibiotics might bind to different parts and hence, they will affect different processes within protein synthesis. Some antibiotics as kasugamycin and streptomycin (str) affect the initiation by preventing a stable bound state between the tRNA and the start codon of the mRNA. The other ribosome-binding antibiotics alter the elongation process in two different ways: by blocking the delivery of tRNA to the A-site or the subsequent translocation of the mRNA-tRNA complex. The main group of antibiotics responsible for this disruption is called aminoglycosides [10].

Aminoglycosides are a group of antibiotics which contain, as a portion of the molecule, an amino-modified glycoside (sugar) joined to a dibasic cyclitol. In most of them, this cyclitol is 2-deoxystreptamine (2-DOS), such as in neomycin (neo), kanamycin (kan), gentamycin (gent), etc; and a different chemical group for the aminoglycosides streptomycin (str) and apramicin (apr) [19]. Neo, kan and gent increase the probability of accepting a non-cognate tRNA during the translation process [20]. This causes misreading during translation and premature termination of protein synthesis giving rise to misfolded proteins which end up in the cell membrane [21]. The last process produces high polar molecules which increase the permeability of the cell membrane and promotes the uptake of more aminoglycosides by the cell.

One of the most used aminoglycosides to study bacterial adaptation in research is kanamycin. Kanamycin prevents the formation of the initiation complex with messenger

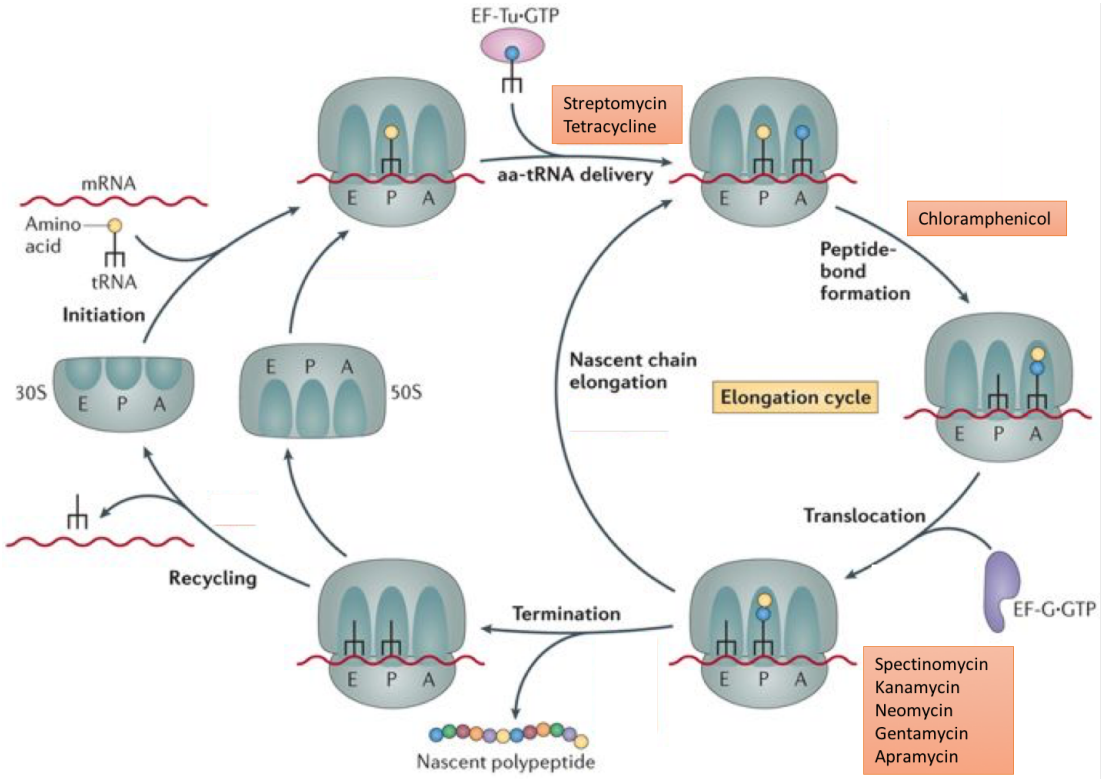

(a)

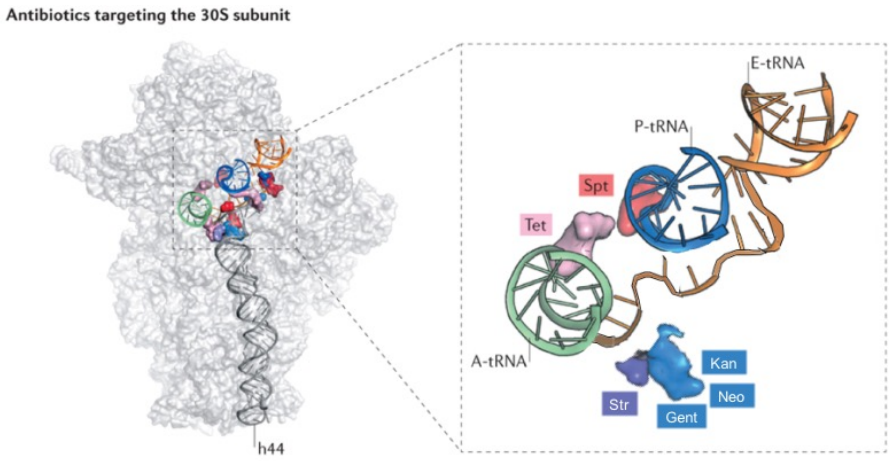

(b)

Figure 1.1: **Ribosome structure and its aminoglycosides target sites during bacterial protein synthesis**. (a) During the initiation the 30S and 50S subunits of the ribosome bind, together with the initiator tRNA and the mRNA in the P-site. The elongation of the polypeptide involves the assembly of tRNA to the A-site by EF-Tu, which is inhibited by streptomycin (Stp) and tetracyclines (Tet). Subsequent translocation of the tRNAs is catalysed by EF-G and inhibited by the aminoglycosides gentamicin (gent), neomycin (Neo) and kanamycin (Kan) and spectinomycin (Spt). (b) Ribosome-targeting antibiotics which target the 30S subunit of the ribosome bind into different places. Binding into different sites disrupts the mechanism of protein synthesis in different ways. Reproduced from [10].

RNA by binding irreversibly to the bacterial 30S ribosomal protein S12 and to the h44 of 16S rRNA (Figure 1.1b) [22, 23, 24]. The ribosomal protein S12 is located at the interface

of the 30S and 50S subunits. This protein interacts with the 16S rRNA which selects the tRNA which binds the A site [25]. Cryo-EM studies suggest that S12 contacts the EF-Tu bound tRNA in the A site during codon recognition [26]. Since kan binds to the S12 protein which presumably contacts the EF-Tu bound tRNA in the A-site, it will alter the bound between mRNA to tRNA.

Gentamicin and Neomycin act in a very similar way. Nevertheless, neomycin contain sugars at the C4 and C5 positions whereas kanamycin and gentamicin have a substituent at the C6 and a hydroxil group at the C5. All these three antibiotics target both, the 30S ribosomal protein S12 and the 16S rRNA. Apramycin and tetracycline have in common that they bind the 16S rRNA and, unlike kanamycin, they do not target the ribosomal protein S12. Str reduces the rate at which cognate tRNA is selected. It binds a subunit which connects h1, h18, h27 and h44 and it interacts with the protein S12 (Figure 1.1b). Finally, spectinomycin targets the ribosomal protein S12 too but not the 16 rRNA. Spectinomycin blocks the translocation of tRNAs from the A-site to the P-site by inhibiting the binding of elongation factor G to the ribosome [27]. Even though it inhibits protein synthesis, it does not cause misreading. In contrast to the aminoglycosides, it acts bacteriostatically meaning that it does not kill the cell but it stops cell growth [28].

1.1.3 Mechanisms of resistance at molecular level

The majority of the ribosome-targeting drugs, such as aminoglycosides, chloramphenicols and tetracyclines, target the elongation cycle [5]. To inhibit protein synthesis they need to reach their targets inside the cell. Therefore, the antibiotic must penetrate at least the cytoplasmic membrane to reach the ribosome. One of the strategies used by bacteria to defend themselves is to decrease the concentration of antibiotic which is inside the cell. This can be done in two different ways: by reducing the uptake of the antimicrobial or actively pumping out antibiotic through efflux pumps.

There are many classes of efflux pumps and they differ in terms of energy source, structural conformation and the specificity of substrates they can extrude. Depending on the sort of pump, they will extrude a wide range of drugs or they will select specific ones [29]. The main families of efflux pumps are: the major facilitator superfamily (MFS), the small multidrug resistance family (SMR), the resistance-modulation-cell- division family (RND), the ATP-binding cassette family (ABC), and the multidrug and toxic compound extrusion family (MATE) [30].

Other mechanism of resistance is decreasing the affinity between drug-target. This can be done in two different ways. First, with chemical changes in the binding site which

reduces the affinity for the drug. This specific mechanism of resistance is very common in ribosome-targeting antibiotics and it usually comes with a fitness cost, meaning that bacterial growth rate will decrease with respect to the wild type [10, 31]. Second, by creating chemical changes in the drug producing aminoglycosides modifying enzymes (AMEs) [20, 32]. Depending on how they modify the aminoglycoside, they can be classified in three groups [33]: aminoglycoside phosphotransferases (APHs), nucleotidyltransferases (ANTs), and acetyltransferases (AACs).

1.1.4 Cell growth

Many of these mutations might affect bacterial growth [10]. In bacterial growth, 4 different distinct phases can be identified: lag phase, exponential phase, stationary phase and dead phase [34].

During the lag phase, bacteria start to adapt to the new media. In this period, they synthesise enzymes and other molecules but they are not able to divide. Between the no-growth condition and the exponential phase there is a continuous transition and therefore the lag time has no unique duration.

After adaptation, bacteria start replicating exponentially by binary fission. Here, bacterial culture mimics a first-order chemical reaction, and hence, the increase in number of cells is proportional to the number of bacteria already present [35]. According to this model of growth, the natural logarithm of the number of cells will lead to a straight line:

$$ln(N(t)) = ln(N_0) + m(t - t_0) \tag{1.1}$$

where N(t) is the number of cells in the culture for a given time, N_0 is the initial number of cells before the lag phase finishes and m is the net growth rate of the organism. This slope measures the number of divisions per cell per unit of time.

Theoretically, this relationship would be linear until bacteria finish the available nutrients or oxygen sources. These sources are consumed progressively in a sequential pattern, specifically the sugars [36]. This is called diauxie and it divides the exponential phase in two different subphases. During the first one, bacteria metabolise the sugar on which they grow faster. Once the sugar concentration is very low, cells undergo a small lag period called diauxic shift when they produce the enzymes to metabolize the second sugar.

When the environment becomes very crowded, bacteria find difficult to uptake nutrients or they are affected by inhibitory compounds segregated by their neighbours. This is called stationary phase and, here, the growth rate and the death rate become very similar.

Finally, the last phase named the death phase, the death rate overcomes the replication death and the total turbidity of the sample decreases.

1.2 Swarming bacteria

So far, we have overviewed some of the mechanisms of bacterial resistance at a single cell level, specifically to aminoglycosides antibiotics. Nevertheless, in nature, bacteria live mostly in communities of millions of microorganisms that coordinate their behaviour. These communities display a higher resistance to the antibiotics but the employed mechanisms are attributed to the emergent properties of the collective rather than to the molecular mechanisms at single cell level. Thus, these collectives do not need to develop genetically resistant bacteria to stand high concentrations of antibiotics or other stresses. In the next sections, we will describe the two major forms of bacterial collectives, swarms and biofilms, and we will focus on the former to explain the biophysical mechanisms underlying the emergent properties of bacterial swarms and their implications in antimicrobial resistance.

1.2.1 Bacterial collectives

Swarms and biofilms cause 80% of infections, present a higher resistance to antibiotics, compromise food safety and quality and have advantageous properties for industrial processes [37, 38, 39, 40]. Swarming can be induced by soft (elastic modulus 20-100 kPa [41]) moist surfaces and recently, it was observed in mice intestinal tissues [42]. In laboratory experiments, swarming can be promoted by inoculating cells on a semi-solid agar plate, with agar concentration between 0.3% and 1.0% (w/v) [43]. When agar concentration is lower (<0.3%), cells swim, instead of swarm, through the porous agar [43]. When first inoculated, the swarm undergoes a lag period whose duration is quite stochastic and correlated to the incubation temperature, the species and the concentration of the inoculum [44, 43]. During the lag phase, the inoculated cells undergo phenotypic changes such as hyperflagellation, elongation and segregation of sufactants such as surfactin in *B. subtilis* [45] and serrawettin in *Serratia marcescens* [46]. These surfactants reduce the surface tension allowing the swarm to expand, once a critical cell density is reached. Within the swarm the cells do not move as individuals. Instead, small groups of cells gather to move collectively forming rafts [43], groups of about 20 cells which recruit bacteria from the environment. These rafts are highly dynamic and they continuously exchange cells with the surrounding environment [43]. Although these rafts are highly motile, they do not

participate in the overall expansion of the swarm [47]. Instead, bacteria within the swarm are continuously releasing surfactant to spread and reach further locations [48].

Biofilms are, like swarms, a collective state where planktonic cells attach to a surface to then replicate and produce extracellular polymeric substances (EPS) that are essential to form their characteristic matrix. This extracellular matrix contains a mix of water, ions, DNA and proteins released by biofilm bacteria [49]. The matrix can act as diffusion barrier that reduce the antibiotic levels inside biofilms [50], making them up to 1000 times more resistant to antibiotics than planktonic cells [51, 52]. Unlike swarms, biofilms are initiated in either hard-solid (colony biofilm) or liquid media (pellicles) and their formation is favoured by stress-inducing chemicals [53, 54, 55].

1.2.2 The dynamic properties of swarming bacteria

Swarming bacteria are characterised by a coordinated way of surface locomotion. Thus, despite many similarities, swarming is not just a collective movement of swimming cells at high densities. Swarming is a natural state, i.e. cells "decide" to become swarmers by undergoing phenotypical changes which give them an advantage with respect to the planktonic state [56]. The trigger for such decision remains elusive although it is likely to be related to the cell membrane or the flagella [57]. The proteins that modulate swarming motility act upstream of the master regulator transcription factors. Environmental signals, presumably the surface stiffness, act on the master regulators, activating flagellar gene expression, and regulating the production of flagellar basal bodies [57]. In fact, although the collective dynamics of swarms and swimmers at the same cell density are very similar, it has been demonstrated that they show distinct patterns in confinement [42].

The hydrodynamic properties of swarmers make them the fastest mode of bacterial locomotion, reaching speeds up to 70 μm/s [44]. The distribution of velocities in a swarm is gaussian, meaning that the cells do not have a preferred direction of expansion. Even in presence of chemoattractans or chemical cues, swarmers do not bias their trajectories, unlike swimmers [58, 59]. The hydrodynamic properties of the swarms are also affected by the cell shape. Swarmers have a larger aspect ratio with respect to swimmers and, their swirling motion characteristic of elongated particles confers supperdiffusivity, used by bacterial collectives to actively mix up nutrients and oxygen [60, 61]. Super-diffusivity on a surface happens when the mean square displacement (MSD) follows a power law with exponent greater than 1. In *B. subtilis* and *S. marcescens* swarms, this exponent is 1.6 [62], which decreases for high cell densities. In *B. subtilis* swarms, aspect ratios from 1 to 9 permit normal swarming dynamics, characterized by a unimodal distribution

of surface densities and a Gaussian distribution of the velocities (kurtosis close to 3). When the aspect ratio is >10, the swarm segregates in two subpopulations with high and low surface densities. The velocity distribution gives very large kurtosis, indicating heavy tailed distributions, unlike for smaller aspect ratios. Cell shape not only affects the distribution but also the magnitude of the velocities which reaches a maximum value of 50 μm/s for aspect ratios around 5 [63], which matches nearly the WT's shape. For lower or higher values of aspect ratios the speed decreases by nearly 5-fold, indicating that there is a preferred aspect ratio to reach the maximum speed (for aspect ratios of 3.8 or 8).

Seeing how these changes in the physical parameters affect the swarm suggests that there is a set of values that can enhance or detriment swarming motility. Indeed, certain combinations of cell shapes and cell densities can enhance or even prohibit swarming [63]. At surface coverages lower than 0.15, cells are practically immotile. This bottom threshold is slightly reduced for large aspect ratios, suggesting that high aspect ratio favours swarming at low surface densities. Increasing surface densities up to a threshold of 0.8 enhances swarming motility but, for higher values, cells stop moving efficiently and form a jam phase [56, 63]. This threshold again depends on the aspect ratio since larger aspect ratios permits swarming at surface coverage slightly greater than 0.8.

Aspect ratio, cell speed and density are not uniform throughout the swarm. The centre of the colony is typically formed by immotile or poorly motile cells [45, 44], which is sometimes referred to as the biofilm state [56, 44]. However, whether these immotile cells express biofilm-related genes is something that has not been studied so far. The region of highest motility is just behind the advancing front (cell speed ~ 70 μm/s), which also corresponds to a region of high cell density (0.07 cells/μm^2) [44], in agreement with the theory of collective motion which predicts that high cell density in active particle systems leads also to higher velocities [56]. In addition, the denser the swarm, the larger is the variation in local instantaneous density since dynamic clusters split and merge which eventually leads to giant number fluctuations [64].

Swarming bacteria can take advantage of this variability in cell speed to promote bacterial segregation within the swarm [65]. Thus, single-cell tracking revealed that in *E. coli* swarms exposed to a kanamycin gradient, cells with larger cell speeds within the swarm were more biased to go towards the outer region of the swarming colony. In this case, the difference in speed arises from a transient increase in resistance in subpopulations of bacteria within the swarm (heteroresistance) [66]. These bacteria will not be affected by the kan and hence their speed will be higher than the surrounding bacteria. This implies that the more tolerant cells are segregated to the leading edge. Due to this mechanism,

the swarm could invade regions of antibiotic concentration 3.5 times higher than the MIC. The relationship between how bias the tolerant cells were to go outwards and their cell speed, increased linearly, indicating that higher speeds enhance this phenomenon.

Another example of emergent properties in swarms is that they can work as a carriers of particles or even other bacteria [67]. This property can suppose and advantage for the swarm itself since it has been reported that swarming *Paenibacillus vortex* carries cells that confer advantage against antibiotics. Indeed, swarming *P. vortex* can invade regions of high ampicillin concentration by carrying antibiotic resistant non motile *E. coli* which synthesizes enzymes that degrade ampicillin. In absence of ampicillin *E. coli* was not needed, i. e. the relative amount of *E. coli* dropped to 0.06 as supposed to 1.3 when the antibiotic was present [67].

The elongated shape of swarming bacteria plays also a protecting role for the swarm against macrophages by preventing engulfment. Overnight cultures of swarming *Serratia liquefaciens* with the phages led to an only 4-fold increase in phage number whereas it resulted in a 20-fold increase when the phages were co-cultured with swimmers. This difference was due to the different cell length between swimmers and swarmers. After 5 h of co-culture with the swarmers, the number of cells shorter than 10 μm were completely cleared but the number of cells longer than 20 μm increased dramatically.

To sum up, we have seen that the physical interactions within the swarm have important implications in the ability of the colonies to tolerate stress. This pinpoints the importance of understanding the physics of these systems to tackle and predict how they can adapt to antibiotic treatments. This also indicates that there could be yet new physical mechanisms that could confer swarms with higher tolerance to stress. One emerging field with the ability to predict new phenomena in swarming bacteria is active matter and it will be the subject of study in the coming section.

1.2.3 Swarming bacteria as an active matter system

The field of active matter studies systems out of thermodynamic equilibrium in which the individual units consume energy from the environment to convert it into motion or, equivalently, kinetic energy. Its aim is to shed light onto the fundamental principles leading to the emergence of large-scale patterns and behaviours not present in the thermodynamic equilibrium [68]. As overviewed in the previous section, the characteristic phenomena emerging from active matter can have physical and biomedical implications and those implications are not exclusive of bacteria, but also in tissue cells and artificial systems [69, 70].

Research on the biophysics of collective motion started with the seminal work of Vicsek on active particles [71]. In this initial model, the active particles are represented as an ordered phase where each particle is associated to a velocity vector of fixed magnitude, which is aligned to the mean of its neighbors' velocities, within an angular tolerance. Each moving particle generates fluid flow, which moves and reorients other swimmers far away. These flows create constant stresses that stir the fluid and affect the other particles, resulting in large wavelength fluctuations, a hallmark of active systems [72].

The main difference in the density fluctuations of passive and active matter systems can be understood by a quantitative description. For systems at equilibrium, the fluctuations in cell density should decrease proportionally to the square root of the number of particles [56]. By definition, the density ρ is the mean number of particles N in a given area A (ρ=N/A). According to the central limit theorem, which only works at equilibrium, ΔN$\sim \sqrt{N}$, being ΔN the standard deviation of the number of cells. From here, we can establish the following relationship for the fluctuations in cell density at equilibrium:

$$\frac{\Delta\rho}{\rho} = \frac{\Delta N}{N} \sim \frac{1}{\sqrt{N}} \tag{1.2}$$

which goes to zero with increasing number of cells. In contrast, the theory for active systems says that the central limit theorem is not valid, since these systems are inherently out of equilibrium. For this case the standard deviation of cells $\Delta N \sim N$ [56], so making a similar calculation we can conclude that $\Delta\rho/\rho \sim 1$, i. e. the density fluctuations do not decrease with increasing density. This phenomenon is known as giant fluctuations, and makes clear that the density within an active matter system is highly irregular. This has been reported experimentally in both non-living systems of active matter [73, 74], and swarming *B. subtilis* [64] although with a lower exponent, $\Delta N \sim N^{0.75}$. This confirms that swarming bacteria behaves according to the theory of collective motion.

The theory of collective motion makes a second important prediction that, in principle, can be applied to bacterial swarms. This theory suggests a well-defined phase transition from a disordered phase to a coherent flock where active particles aggregate into clusters even in the absence of cohesive forces [72]. This aggregation is based on feedback between the decrease in particles' speed at high concentration, caused by physical interactions, and the spontaneous accumulation of active particles in the places where their speed is lower [75]. When the particles' speed is sufficiently high and their concentration is in the appropriate range (surface coverages of 0.3-0.8 or 0.6-0.7 for round or rod-shaped particles, respectively [76, 1]), inherent density fluctuations are amplified by the particles'

slowing down, and the system effectively phase separates into high-density/low-motility clusters surrounded by a low-density high-motility phase [77]. This implies that high cell density and motility in bacterial swarms could result in an emergent phenomenon of phase separation from a dilute phase of fast movers into a dense phase of slow movers, resembling liquid-gas phase separation. This phase separation is known as motility-induced phase separation (MIPS) and it is impossible for passive colloidal particles in absence of attractive forces (Figure 1.2a). While the experimental validation of this theory is yet to be seen in bacterial swarms, a numerical model of active rods suggests that this is due to the high aspect ratio of swarming cells since increasing aspect ratios restrict the region where phase separation is possible [1]. To map the phase diagram of MIPS, normally the surface coverage or cell density of the system is plotted against the speed or the Peclet number (Pe), which is a ratio between how much the particles move due to active motion and how much due to diffusion (Figure 1.2a). This shows a region of the space diagram where MIPS is possible and whose shape depends on the specific system.

The shape of the MIPS region can be predicted and characterized by means of numerical simulations. However, the theory has a number of assumptions and limitations that differ from experimental systems such as swarming *B. subtilis* . The closest numerical simulations to a system of swarming bacteria have been carried out by [1] for a system of 2D disks. We justify that the 2D system of rods represents better swarming bacteria than 3D spherocylinders because swarming bacteria are confined in a thin layer of liquid on a surface, so it is considered as a quasi-2D system. In these numerical simulations, the model calculates the rotational Peclet number (Pe_r) for individual particles whereas this is not possible for swarming bacteria since in swarms the cells travel in rafts of cells. This might affect the values of Pe_r for which MIPS is possible in the experimental system vs in the model. Another crucial difference between the model and the theory is the aspect ratio of the particles. In the model, MIPS disappears for particles with aspect ratios larger than 2 but swarming *B. subtilis* has a typical aspect ratio of 7 [44]. These and other differences have been summed up in Table 7.1.

This phase separation has been characterized in experimental studies mainly through the next magnitudes:

Temporal correlation: Represents how similar two vectors are when separated in time in both magnitude and direction. Applied to velocities, it is defined as:

$$I_v(\Delta t) = \frac{< \mathbf{v}(x,y,t) \cdot \mathbf{v}(x,y,t+\Delta t) >}{< \mathbf{v}(x,y,t) \cdot \mathbf{v}(x,y,t) >} \tag{1.3}$$

where **v** is the velocity field, x and y the positions of the active particles in the 2D plane and t the time. Triangle-like brackets denote averaging over all positions. The autocorrelation function represented against the lag time Δt provides useful information about the time scale of the system. Thus, within the characteristic autocorrelation time τ the dynamics of the system are supposed to remain invariant. Taking logarithms in the autocorrelation function, we obtain a straight line whose slope gives the autocorrelation time.

Spatial correlation: represents how similar certain velocity vector at certain position is with respect to those that surround it. For each spatial direction, the expression is:

$$\begin{aligned} C_{v_x}(\Delta x, y) &= \frac{< v_x(x,y,t)v_x(x+\Delta x,y,t) >}{< v_x(x,y,t)v_x(x,y,t) >}, \\ C_{v_y}(x, \Delta y) &= \frac{< v_y(x,y,t)v_y(x,y+\Delta y,t) >}{< v_y(x,y,t)v_y(x,y,t) >} \end{aligned} \tag{1.4}$$

For systems that have radial symmetry, it is convenient to calculate instead the radial correlation defined as:

$$C_r = \frac{\sqrt{C_{v_x}^2 + C_{v_y}^2}}{max(\sqrt{C_{v_x}^2 + C_{v_y}^2})} \tag{1.5}$$

In the case of bacterial swarms it has been suggested that the temporal autocorrelation does not represent the physical system accurately when big differences in velocities exist. This is because the autocorrelation function is biased towards elements with high speed [47]. Thus, contribution by particles with low velocity is small and the function cannot detect the different behaviours between the fast particles and the slow ones. This difference becomes more important when bacteria are affected by antibiotics since their velocity decrease and can segregate into subpopulations of motile and non motile cells. To overcome this, the velocity vectors presented in Equation 1.4 will be normalized such that they become unitary vectors. Hence, these magnitudes will represent the normalized vector field or directions of the velocities. This directional or angular correlation function is defined as:

$$\hat{I}_v(\Delta t) =< \hat{v}(x,y,t) \cdot \hat{v}(x,y,t+\Delta t) > \tag{1.6}$$

where $\hat{v}(x,y,t) = \frac{\mathbf{v}(x,y,t)}{|\mathbf{v}(x,y,t)|}$.

The theory of active-matter predicts heavy-tailed auto-correlation velocity functions at the single-particle level [78], which has only been confirmed recently [62]. This implies that the autcorrelation functions decay as a power law $I_v(\Delta t) \sim t^{-\alpha}$ instead of an exponential. For 2D active particles on a substrate is estimated that $\alpha = 1$, although this is difficult to check experimentally given the challenge of tracking single cells in a swarm.

Another important magnitude that we briefly talked about in the previous section is the

kurtosis or more generally the fourth moment of the velocity probability distribution.The moments are quantitative magnitudes used to characterize a probability density function. The nth-order moment of a continuous function f(x) about a value c is:

$$\mu_n = \int (x - c)^n f(x) dx \tag{1.7}$$

The first moment represents the mean, the second central moment is the variance, the third and the fourth normalized central moments are the skewness and the kurtosis, respectively. The skewness is the measure of asymmetry of the probability distribution. A totally symmetric distribution would have a skewness of 0. The kurtosis represents the measure of tailedness or similarly the presence of outliers of the distribution. For a Gaussian distribution, this magnitude acquires a value of 3. Larger kurtosis display a larger peak around the mean whose tails drop faster than a distribution with lower kurtosis [79].

The magnitude of the speed and kurtosis have demonstrated to be affected by by sub-lethal concentrations of antibiotics, specifically by the aminoglycoside kanamycin. Kanamycin reduces the motility of the cells in *B. subtilis* swarms and results in changed collective dynamics. In particular, the velocity distributions become heavy-tailed (kurtosis up to 14) and the characteristic decay of the correlation function of the normalized velocity field turns into a double exponential decay [47]. It was found that this anomalous dynamics is caused by immotile rafts that appear when the swarm is treated with a homogeneous concentration of kanamycin.

1.2.4 Phase separation: nucleation and growth and spinodal decomposition

As we mentioned in the previous section, bacterial swarms are predicted to undergo MIPS and phase separate. In classical thermodynamics, phase separation is a transient process by which an initially well-mixed equilibrium state suffers a change in its thermodynamic conditions (temperature, pressure, chemical potential, etc.) and results into a demixed equilibrium state. The thermodynamic variables tilt the global balance between contributions that promote molecular mixing, such as entropy (entropy always increases upon mixing since the system becomes more disordered), and those that promote demixing, such as attractive interactions. The most stable phase is the one with the lowest Gibbs free energy (G), so any variable affecting G can also affect the phase.

The phase transitions between two states of the matter can be characterized by the phase diagrams that plot the evolution of the system in function of two thermodynamic

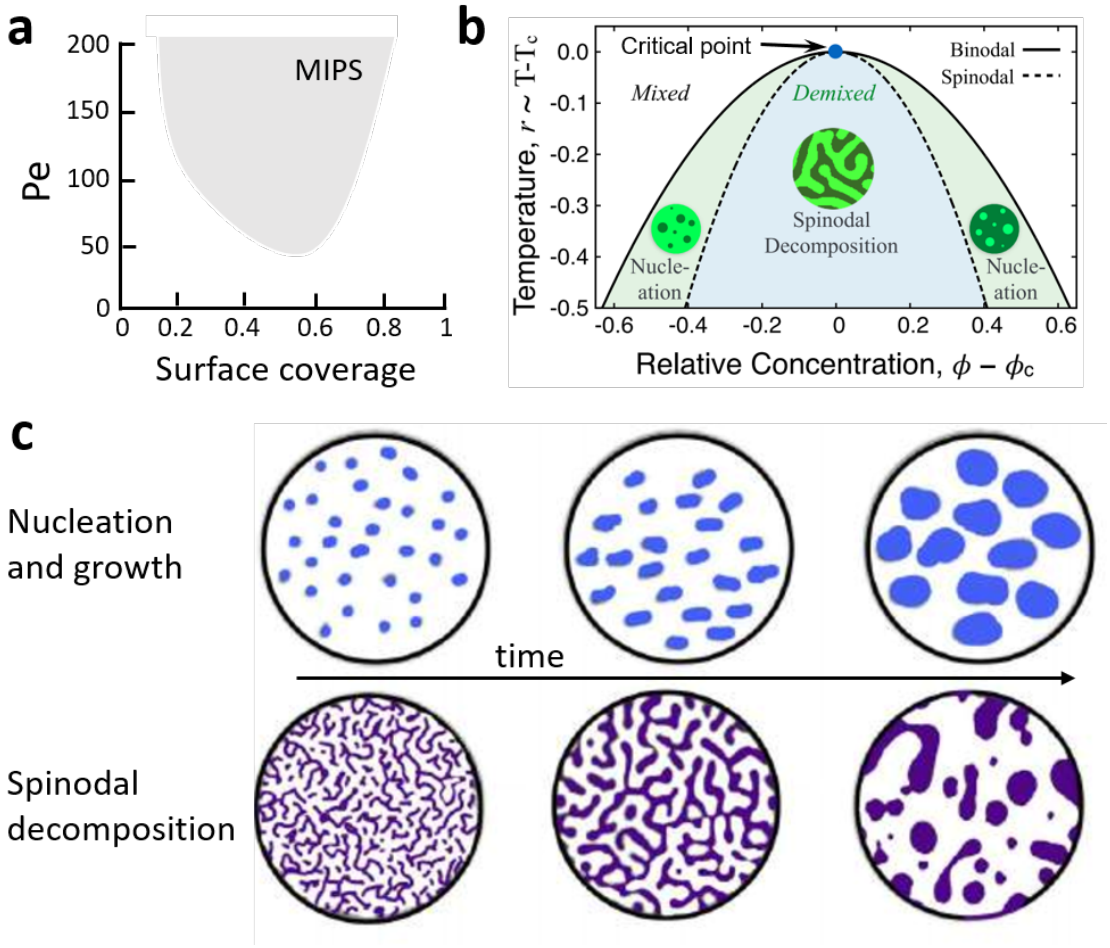

Figure 1.2: **Phase separation in active matter systems**. a) Phase diagram of a system of spherical active brownian spherical particles where the shaded region indicates where the system undergoes MIPS. Inspired from [75]. b) Phase diagram of phase separation indicating the possible phase transitions through either binodal or spinodal decomposition in a binary mixture in function of temperature and the relative concentration with respect to the critical point (ϕ_c). Adapted from [80]. c) Difference between a binodal phase transition, where new domains nucleated and then grow in size, and spinodal decomposition where large instabilities give place to a mixture of two phases in absence of an energy barrier. Adapted from [81]

variables such as pressure and temperature. In phase diagrams, the different phases are separated by the coexistance lines which determine the phase transition from a mixed state to a demixed state. For example, in the case of water, the phase diagram has three states: solid, liquid and gas; and the coexistance lines separate each of these. In the case of the solid-liquid transition, the coexistance line exists for any given value of pressure and temperature. This is because the solids have a certain symmetry that the liquids lack so no matter how much the temperature or the pressure increase, the solid will always have to lose this symmetry to become a liquid, i. e. there is always a phase transition. This does not happen for the coexistance line between liquid and gas. An increase in pressure has little effect in the liquid state since liquids are difficult to compress. On the contrary, the gas phase is very compressible and a pressure rise leads to fewer possible positions for its

molecules, i. e. its entropy decreases too. As the molecules are closer together,it is easier to make bonds which decrease the overall energy. Therefore, for high enough pressures the energy difference between the liquid and gas phase disappears up to a point where both phases are indistinguishable. This point is called the critical point (Figure 1.2b).

Commonly, a phase transition happens through the formation of nuclei that grow in size until they merge and form the new phase. Again, we can use water near the freezing temperature as an example of this nucleation. The liquid water, upon slow decreases in temperature, will form small blocks of ice (the nuclei). This is usually what happens with phase transitions once crossed the coexistance line, also known as the binodal line. This phase transition is not only applicable to different states of matter but also to mixtures of solvents or alloys. In this case the binodal curve defines the region of composition and temperature across which the miscibility of the components changes: in one side of the line the components would be miscible and in the other each component would be separated, such as the blocks of ice on the water (Figure 1.2b). The reason for the mixed state to become demixed is that it minimizes G, the magnitude that determines the stability of the solution. This will happen only on one side of the binodal line where single-phase mixtures are unstable or metastable so the system tends to separate its components.

There is a way to bypass this nucleation processes and still undergo a phase transition, which can only happen when the system phase transits through the critical point. Here, the mixed phases become globally unstable as the critical point is approached and large-scale fluctuations emerge. Unlike nucleation, this process does not have an energy barrier to overcome so such fluctuations lead to highly dynamic and unstable phase separated domains that eventually become stable below the critical point, establishing a characteristic morphology that may coarsen with time. This phenomenon is coined spinodal decomposition (Figure 1.2c). Spinodal decomposition happens for example upon an abrupt decrease in temperature (quench) of a liquid phase. As we said before, for this liquid phase to become solid, the molecules need to occupy specific locations that confer certain symmetry. Nevertheless, if the temperature drops fast enough, the molecules will not have time to reorganize themselves to form the symmetries, resulting in a mixed state between liquid and solid.

Inside the binodal curve, the system is metastable and, inside the spinodal curve, the system is unstable. Therefore, the spinodal separates an unstable region from a metastable region. Both curves meet at the critical point and this is the only point where the system can undergo a purely spinodal phase transition (Figure 1.2b). A phase transition following any other trajectory in the phase diagram would be either purely binodal or a combination

of both. The spinodal curve is not a sharp boundary in real systems as a result of fluctuations. In alloys, this decomposition happens uniformly throughout the material unlike the binodal decomposition that occurs just at specific nucleation sites.

So far, we have talked about systems that are at equilibrium, where the internal energy of the system remains constant. Bacteria are quite the opposite, they are injecting energy to the system by transforming nutrients into motion (kinetic energy). This new source of energy shifts the binodal and spinodal lines in the phase diagram. Referring back to the example of water, if water was like bacteria and the molecules were active particles, we could observe water becoming ice spontaneously in a hot summer day. Thus, this shift in the phase diagram can introduce long-lived nonequilibrium steady-states that display phase-separated morphologies.

A clear example of phase separation in living systems is fruiting body formation in *Myxococcus xanthus* [82]. Here, the phase separation is characterized in terms of cell density and a dimensionless Peclet number calculated as the ratio between the cell speed and the reversal rate of the bacteria. Fruiting body happens through a physical mechanism, meaning that cells do not have a sensory mechanism to change their motility in response to specific chemical or mechanical stimuli. Rather, the collective mechanics naturally induces phase separation of the entire population. This phenomenon can be described within the framework of the MIPS theory. During fruiting body formation, the authors demonstrate that *M. xanthus* can phase separate through both nucleation and growth and spinodal decomposition, for low or high inoculation cell densities respectively.

The phase separation kinetics depends mainly on two factors: the nucleation, growth and coarsening rates and the rate-controlling physical transport mechanism that can vary across different systems. One of the main analytical tools to categorize and comprehend phase separation kinetics is dynamic scaling. Dynamic scaling assumes that the time evolution of the phase separation is always given by the same principle and therefore controlled by a single emergent length scale L within a given interval. This implies that the emergent domains display self-similarity in time, i. e. features of the domain morphology increase in size with time, but without altering their properties. In other words, considering the morphology in a region of size L at time t1, would be equivalent to the morphology within a region of size $L(t2/t1)^n$ for a later time t2, where n is the dynamic scaling exponent [80]. This method allows the characterization of a wide variety of systems just by scaling L with time. For example, it is normally found that the average domain size

$< s >$ increases as a power law of the time:

$$< s >= (Kt)^n \tag{1.8}$$

Where K is a prefactor that, together with n, depends on the mechanism underlying the phase transition. A list of prefactors and exponents associated to different mechanisms can be found in the table 1 of [80]. This scaling approach has been used to characterize experimental systems such as Janus particles and bacteria [83, 84], where n is estimated as in Equation 1.8. Another example is fruiting body formation of *M. xanthus* where for high densities, the transition is abrupt with a well-defined length scale of the phase-separated domains that increases with time as a power law as the domains grow self-similarly [82].

In practice, this scaling law is calculated across distinct processes during phase separation. The first characteristic stage is the growth of the nuclei, which dominates during early stages following nucleation. Notice that for early times, the exponent n will be understimated since the nucleation and growth processes overlap. Here, the scaling law in Equation 1.8 applies to individual nucleated domains until the nucleation rates become negligible. Then, Equation 1.8 will describe mainly the population average $< s >$, since it will consider old big nuclei that have grown already and the recently small nucleated ones. Finally, the growth of the nuclei leads to coarsening, the final stage of the phase separation.

An interesting a approach to characterize the process of phase separation and more specifically the characteristic shape features of the nucleated domains is by parametrizing the boundaries with Fourier series [85, 86, 87]. Fourier series provide a way of representing functions as a sum the periodic functions *sin* and *cos*. The series can be used to parametrize a closed contour by describing the x and y coordinates of such contour as:

$$\begin{aligned} x(t) &= a_0 + \sum_{n=1}^{\infty} a_n cos\frac{2n\pi t}{T} + b_n sin\frac{2n\pi t}{T}, \\ y(t) &= c_0 + \sum_{n=1}^{\infty} c_n cos\frac{2n\pi t}{T} + d_n sin\frac{2n\pi t}{T} \end{aligned} \tag{1.9}$$

where

$$\begin{aligned} a_0 &= \frac{1}{T}\int_0^T x(t)dt \\ a_n &= \frac{2}{T}\int_0^T x(t)cos\frac{2n\pi t}{T}dt \\ b_n &= \frac{2}{T}\int_0^T x(t)sin\frac{2n\pi t}{T}dt \end{aligned} \tag{1.10}$$

and equivalently for c_0, c_n and d_n just swapping in the previous equation x by y. In this description, the boundary is divided in small segments. Each of these segments take a time T to traverse. The individual segments in the contour are defined as described in Fig. 1a in [85], and t is the time required to traverse those segments.

The important characteristic of this definition is that it decomposes complex shapes in very fundamental modes that then can be quantitatively compared. This description have been successful at describing differences in cranial shapes [88], shape changes of human fetus over time [89] and extracting geometric signatures of different phases in alloys [90]. Thus, Fourier series can offer a useful description when identifying common features in the nuclei shapes during phase separation.

1.2.5 Models of MIPS

While the physics of phase transitions at equilibrium is very well studied, active dynamics need further description beyond traditional themodynamics and this gave rise to new models that study the physics out of thermal equilibrium [78, 91, 92]. Two of the most widely used are the run-and-tumble particles (RTP) and the active Brownian particles (ABP). RTP is more used for swimming bacteria performing run and tumble motion. The model represents bacteria as single particles travelling in a straight line at constant speed v_0 for intervals interrupted by a random tumble event, which reorients the bacteria to swim in a different direction [93]. These reorientations happen at a rate α. For example, for *E. coli* v_0 can go from 1 to 50 μm/s and the tumbling rate is around 0.1 s^{-1} [94]. This model is not only applicable in bacteria but also for other active particles such as mammalian cells. The main difference in the model would be in these two parameters since in mammalian cells v_0=15 μm/h and α=0.2 min^{-1}, so they also reorient slower [95]. The case of ABPs is slightly different but it usually leads to similar results as RTP unless the particles are under confinement [96]. In ABP, the cells have a persistent motion of fixed speed whose trajectory is randomized by noise. Spherical ABPs with repulsive-only potentials is one of the simplest models to study the many-body physics of active matter [92]. With this model, the system can undergo MIPS through spinodal decomposition by tuning the persistence length and the density of the particles. Thus, MIPS occurs when the time for a particle to re-orient after a collision becomes long relative to the typical mean free time between those collisions [77].

Such agent-based standard models are complemented by continuum field theory. Continuum models describe the evolution of continuous variables such as velocity and the density [92]. The simplest model of spinodal decomposition is given by the Cahn-Hilliard

continuum model of a binary alloy [96]. According to this model, the binary alloy spontaneously separate and form domains of each component which grow in time according to a power law [97]: L(t)$\sim$ $t^{1/3}$, where L(t) is the typical domain size and t is the time. The concentration of each domain is described by the nonlinear diffusion equation:

$$\frac{\partial c}{\partial t} = D\nabla^2\mu \tag{1.11}$$

where D is a diffusion coefficient and μ the chemical potential. The chemical potential mainly depends on the length of transition between the domains, which is the main parameter to change in numerical simulations.

To fully characterize the dynamics of bacterial suspensions continuum models incorporate a variety of effects such as steric interactions, alignment and meso-scale turbulence [98]. In continuum theory, steric interactions (through volume exclusion) and alignment (through elongated shapes) are the key components for MIPS to emerge. Aditionally, experiments using suspensions of Bacillus subtilis [99, 100], Escherichia coli [101, 102] and Serratia marcescens [103] demonstrate that these systems also present meso-scale turbulence. In the models, meso-scale turbulence emerges when combining alignment and hydrodynamic interactions (through self-propulsion in the surrounding medium).

1.3 Objectives

The implications of the novel dynamic properties coming from the active matter theory in bacteria are still not well understood. This is partially because of the lack of controlled experiments that can characterize the predicted phenomena in living systems such as phase transitions. It was only recently that MIPS was linked to fruiting body formation in *Myxococcus xanthus* or glassy dynamics of multilayer formation in growing colonies of *Pseudomonas aeruginosa* [104, 105].

In this work, we aim to unravel novel biophysical mechanisms that bacterial swarms use to overcome antibiotic gradients. We will use swarming *B. subtilis* to understand how swarms can react to sub-lethal concentrations of antibiotics and to other stresses such as physical confinement. As aminoglycosides can induce biofilm formation in planktonic cells, we will study whether this is also possible in swarms, a question that remains unexplored since swarms and biofilms are believed to be antagonistic [106, 107].

Secondly, we will map and sketch a phase diagram where swarming bacteria can potentially undergo MIPS by measuring the Pe and the surface coverage of the system at different stages. As kanamycin changes the dynamic properties of the swarm, we will use

the antibiotic to see how different dynamics can give place to different phase transitions. Such transitions will be quantified following the dynamic scaling method overviewed above during the three main regimes in a phase separation: nucleation, growth and coarsening.

Finally, we will study whether swarms can develop resistance at single cell level in antibiotic gradients, as it happens for the swimming counterparts. We will quantify the resistance for several antibiotics and suggest sequential administration strategies using different antibiotics to try to mitigate the emergence of such resistance. We believe these questions will unravel novel pathways that swarms can use to tolerate antibiotics and it will shed light onto new properties predicted by the active matter theory that bacterial collectives could use to become more resilient.

Chapter 2

Swarming *B. subtilis* undergo a localized phase separation to form stress-induced biofilms

2.1 Introduction

The ability to respond and adapt to environmental cues and stresses is crucial for the survival of species [108, 109]. In addition to general stress-response pathways at individual cell level, which activate target genes in response to a variety of stresses, multi-cellular systems can tolerate stresses through self-organization, i. e. the emergence of order in space and time resulting from local interactions between individual cells [110, 111, 112]. An example of this organization are biofilms, which have been considered as a type of stress response due to their elevated tolerance against various stresses, including antibiotics, extreme pH and temperature [113, 114, 115]. The biofilms' resilience is associated with physicochemical properties of their EPS [37], metabolic coordination [116], slow cell growth [50], and in the case of air-exposed biofilms, diffusion barrier by archetypical wrinkled morphology [117]. Biofilm formation can be induced, from planktonic cells, by a wide range of biochemical and mechanical stressors, such as aminoglycoside antibiotics [53], redox-active compounds [54], nutrient depletion [55] and mechanical stress [118].

Swarms, another example of collective coordination, can also tolerate antibiotic treatments that are lethal to individual cells -although in a less extent than biofilms- through motility-induced mixing and reduced small-molecule uptake [119, 120, 121]. Therefore, the swarm's ability to withstand high antibiotic concentrations could therefore lead to the subsequent development of highly resilient biofilms in regions that could not have

been reached otherwise. Nonetheless, this possibility has been widely neglected since it is believed that these two forms of collective behaviour are antagonistic. The reason for this comes from the studies in the first step of biofilm formation, the irreversible attachment to the surface. The internal machinery of the cell plays an essential role in the attachment and plays an antagonistic role in swarming motility and biofilm formation. For example, in *P. aeruginosa*, the proteins SadC, SadB, and BifA are required for the switch from reversible to irreversible attachment by regulating several surface-associated behaviors, including swarming, EPS production, and modulation of flagellar reversal rates [106]. Merritt et al. [107] demonstrated that deletion of sadC results in a hyperswarming strain deficient in polysaccharide production necessary for the EPS. Similarly, SadB was found to inversely regulate biofilm formation and swarming motility via its ability to both modulate flagellar reversals in a viscosity-dependent fashion and influence the production of exopolysaccharides. In contrast, inactivation of BifA was shown to promote hyper-biofilm formation and severe swarming defects [122]. Therefore, whether the transition from swarming collectives into more resilient biofilms when exposed to stressors is possible and how the transition can be initiated, is unknown.

Understanding biophysical mechanisms regulating the emergence of tolerance through bacterial collective behavior is important to understand whether these emergent properties can trigger unexpected behaviors in bacteria. For example, collectively moving clusters of planktonic *E. coli* cells can colonize regions of high antibiotic concentration only when the cluster is above a threshold size [123], highlighting the potential biological advantages of structures that can emerge spontaneously in a group, as a consequence of the physics of cell motility. Theoretical models of collective motion have repeatedly predicted that, at a sufficient concentration, a collection of motile particles can spontaneously form high-density clusters of particles [75, 124]. This transition, known as Motility Induced Phase Separation (MIPS), suggests that persistent heterogeneity in cell density -the MIPS clusters- can develop spontaneously when both cell speed and density are appropriate (Figure 2.1, gray U-shape region) [125]. Therefore, such phase separation should be observed in swarming bacteria and the absence of this observation has been a subject of discussion in recent studies [56]. Given that cell-density heterogeneity can induce biofilm formation mediated by localized cell death [126, 127], we wondered whether the heterogeneity caused by putative MIPS-like clusters could in turn underpin the transition from bacterial swarms into biofilms (Figure 2.1). As MIPS-like clustering is an emergent phenomenon arising from physical interactions between individual agents, it may endow swarms with a collective response to a wide spectrum of stressors that cause changes in cell motility and/or density.

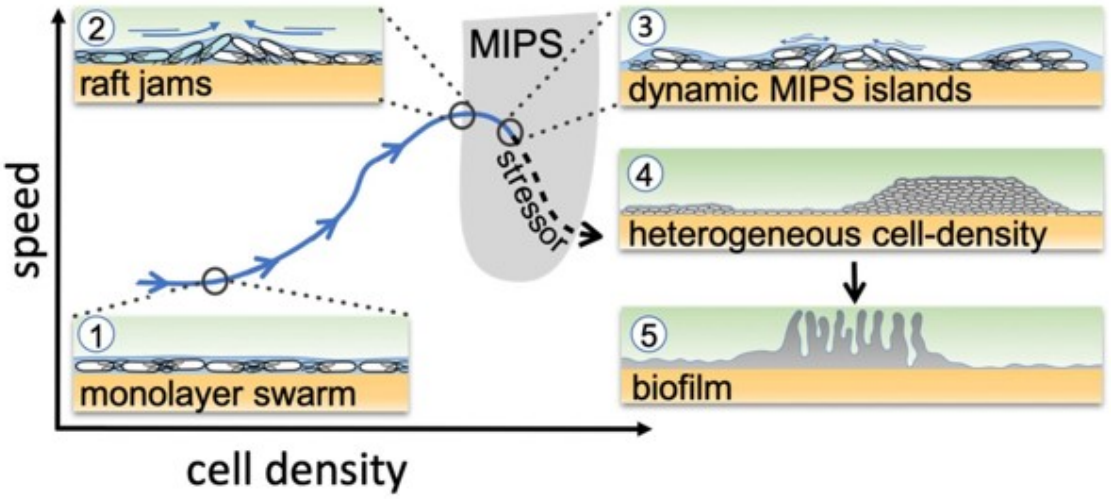

Figure 2.1: **Schematic of the transition from swarming to biofilm formation through MIPS.** *B. subtilis* cells swarm in a monolayer (stage 1). As cell density increases, cells form fast-moving rafts which can collide and form transient jams. Cells at the boundary between the colliding rafts are pushed upwards and protrude from the surrounding monolayer (stage 2). Further increase in cell density can promote the formation of dynamic MIPS-like islands where cells accumulate within the swarm while still being dynamic (stage 3). Eventually, this uneven distribution of cell density gives rise to macroscopic spatial heterogeneity in cell density (stage 4), which can lead to the formation of biofilms (stage 5).

Here we show that *B. subtilis* swarms can indeed transit into biofilms through a MIPS-like process, induced by physical or chemical stresses applied at the swarming front. The stresses promote a localized phase separation where the expanding swarm monolayer generates multilayer clusters of cells. Based on the insights gained from our investigation, we then showed that targeting the multi-layered region by administering a given amount of antibiotic in two separate doses is effective in suppressing the formation of biofilms from swarming cells.

2.2 Results

2.2.1 Swarming expansion in a kanamycin gradient

To examine if a stressor triggers biofilm formation from a swarming colony, we performed swarming assays using *B. subtilis* with a spatial gradient of the aminoglycoside kanamycin. Concretely, a diffusive disk containing 30 μg of kanamycin was placed on the side of a swarming plate (0.5% agar) and allowed to rest for 24 hours to establish an antibiotic gradient (Figure 2.2a and b). An inoculum of *B. subtilis* culture was then placed at the centre of the dish, 4 cm away from the kanamycin source, and the plate was imaged while being kept at 30°C (Figure 2.2a). The amount of kanamycin in the agar was estimated up to 2 cm away from the kan disk for 3 timepoints: when the bacteria were inoculated

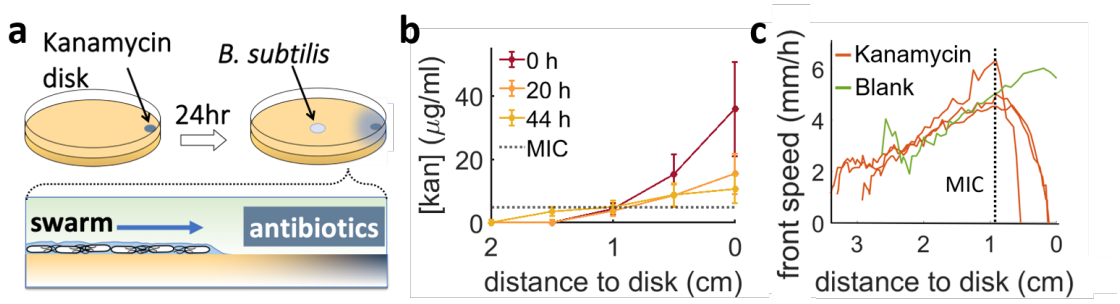

Figure 2.2: **Characterization of the kanamycin gradient and its effect in the expanding swarm** a) Schematics of swarming bacteria expanding concentrically from the centre of a 9 cm Petri dish. Kanamycin disk was placed for 24 hours to form a spatial gradient. b) Evolution of the kanamycin profile along the plate measured from the kanamycin disk. The initial profile was made by placing a kanamycin diffusive disk for 24 h on the swarming agar plate. At this point bacteria were inoculated in the centre of the plate (t = 0 h). The kanamycin concentration was measured again 20 and 44 h later to check the evolution of the gradient with time. The MIC for *B. subtilis* (5 μg ml^{-1}) has been indicated with a dotted line. Data indicate the mean and s.e.m. of three independent replicates. c) Speed of the swarming front when approaching the diffusive disk. In presence of antibiotic the front speed rapidly decays to then halt completely before it reaches the disk. When a blank disk is placed instead, the swarm invades the whole plate and the decay in speed is not observed (green curve). The position in the plate corresponding to the MIC (dotted line) was calculated by looking at the position of the MIC in b).

(0 h), 20 and 44 h later (Figure 2.2b). To see how this concentration profile would affect the swarm, we estimated the MIC of planktonic *B. subtilis* by making 5 cultures with kan concentrations from 1 to 5 μg ml^{-1} . After an overnight culture, there was no visible growth for the culture at 5 μg ml^{-1} so we define this concentration as the minimum inhibitory concentration (MIC). According to the estimation of the kan profile, the MIC happens at a distance of 0.9 cm from the kan disk. As this MIC is for planktonic cells, we expect the swarming front to reach farther than this point due to its increased tolerance to antibiotics.

After inoculation, the swarm underwent a 2 hours lag period that then led to a rapidly expanding swarming front, whose speed increased the bigger the colony became (Figure 2.2c). When the expansion began, the front speed was 1.8 mm/h to then peak 1 cm away from the disk at a speed of 5 mm/h, where became progressively slower towards the source of kanamycin until it completely stopped 0.3 cm away from the disk (Figure 2.2c and Video 1). According to our measurements, at this distance the concentration of kan was expected to be around 30 μg ml^{-1} , confirming that swarming bacteria are more resistant to the antibiotic than in the planktonic state. In absence of kanamycin, the front just kept expanding until it invaded the whole agar plate (green curve in Figure 2.2c).

2.2.2 Swarming *B. subtilis* transitions into a biofilm in presence of a spatial kanamycin gradient

After incubating the plate at 30°C for 36 h more, the colony developed prominent wrinkles, the morphological feature of *B. subtilis* pellicles and colony biofilms [128, 129], across a 3 mm band 1.3 cm away from the kanamycin disk (Figure 2.3a), where the antibiotic concentration is approximately the calculated MIC (Figure 2.2b).

To further verify the association of these wrinkles to biofilms, we repeated the assay using Δeps, a mutant known to be uncapable of forming biofilms [130], but capable of swarming (Video 2), and confirmed no wrinkles with this mutant (Figure 2.2b). The emergence of wrinkles across a 3 mm-band away from kanamycin suggests that the swarm-to-biofilm transition corresponds to exposure to a certain concentration range of kanamycin. We checked this by increasing the concentration of antibiotics in the disk and we observed that, indeed, the wrinkles appeared further away from the disk (Figure 7.1), while a disk without antibiotic did not usually promote wrinkle formation (Figure 2.3c). There were times, when wrinkles could form in absence of kanamycin, but only at the borders of the petri dish both in the experiments with a kanamycin disk and in experiments without kanamycin (Figure 7.2). We suspect that this may be due to the agar meniscus at the petri boundary. This meniscus is both a complicating factor for swarm visualisation and causes potentially different local conditions in nutrient availability, as the local thickness of the agar is different from the rest of the petri dish. Thus, the presence of wrinkles at this meniscus was not consistent and it was often that the wrinkles did not appear here (Figure 7.2). We will discuss further this point in following sections of this chapter.

To quantify the degree of biofilm formation, we measured the characteristic wavelength and roughness of the wrinkles. In this thesis, the term biofilm is interpreted as wrinkly biofilm, and the wrinkles' wavelength is used to quantify biofilm formation since it has been reported to correlate with biofilm stiffness and extracellular matrix [126]. More specifically, the wavelength is smaller in colonies of matrix mutants and greater in hyper biofilm-forming mutants. The roughness of the biofilm, defining roughness as the variation in the intensity profile of the biofilms, was also correlated to the biofilm's stiffness [131], so we used this magnitude as a further quantification of wrinkle formation. The wrinkles appearing near the kanamycin disk had a wavelength of $\lambda = 560$ μm and roughness r = 10, indicating a much stiffer biofilm than the case without kanamycin, which was characterized by a shorter wavelength and surface roughness ($\lambda = 91$ μm , r = 5.5; Figure 2.4a and b). At the same time, wrinkle formation was also quantified at the back of the kanamycin plates (defined as the region of the plate opposite to the kanamycin disk). We hypothesized

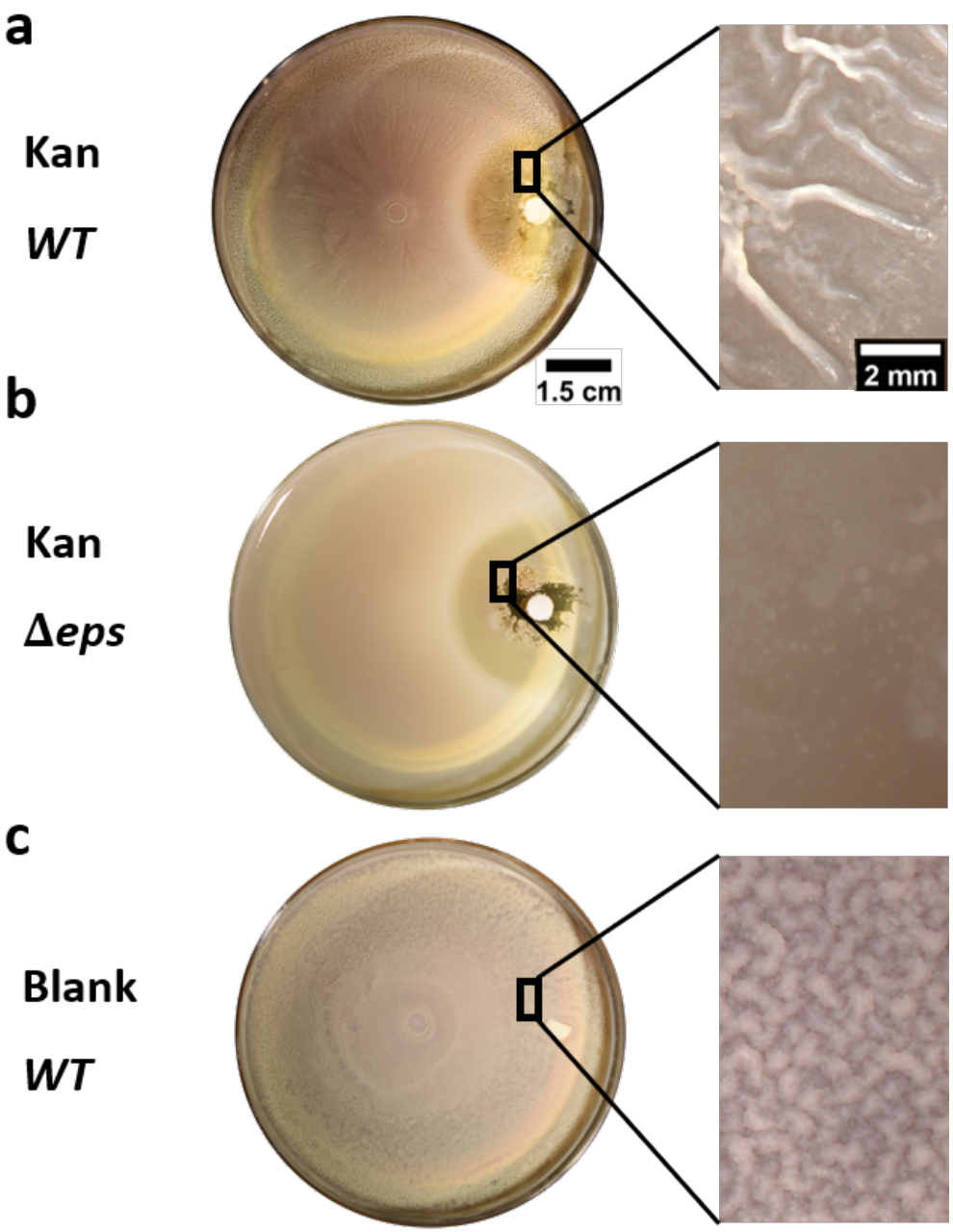

Figure 2.3: **Swarming cells transit into a biofilm in presence of a kanamycin gradient.** Swarming *B. subtilis* plates after 40 h incubation at 30°C . Wrinkles are formed at the region 2 cm away from disk with a) wildtype (WT), but not with b) Δeps deletion strain. d) WT swarming plate with a diffusive disk without antibiotics. Zoomed images show the colony surface.

that farther away from the disk, bacteria would not sense the stress coming from the kan so the system would behave as in stress-free conditions. Effectively, the wavelengths and roughness measured at the back of the plate were comparable to the blank case. We observed some outliers in both blank and back cases where wrinkles could appear at the boundaries of the petri dish as commented before (Figure 7.2), resulting in larger wavelength and roughness values.

Furthermore, we measured the expression of *tasA*, which encodes an essential ma-

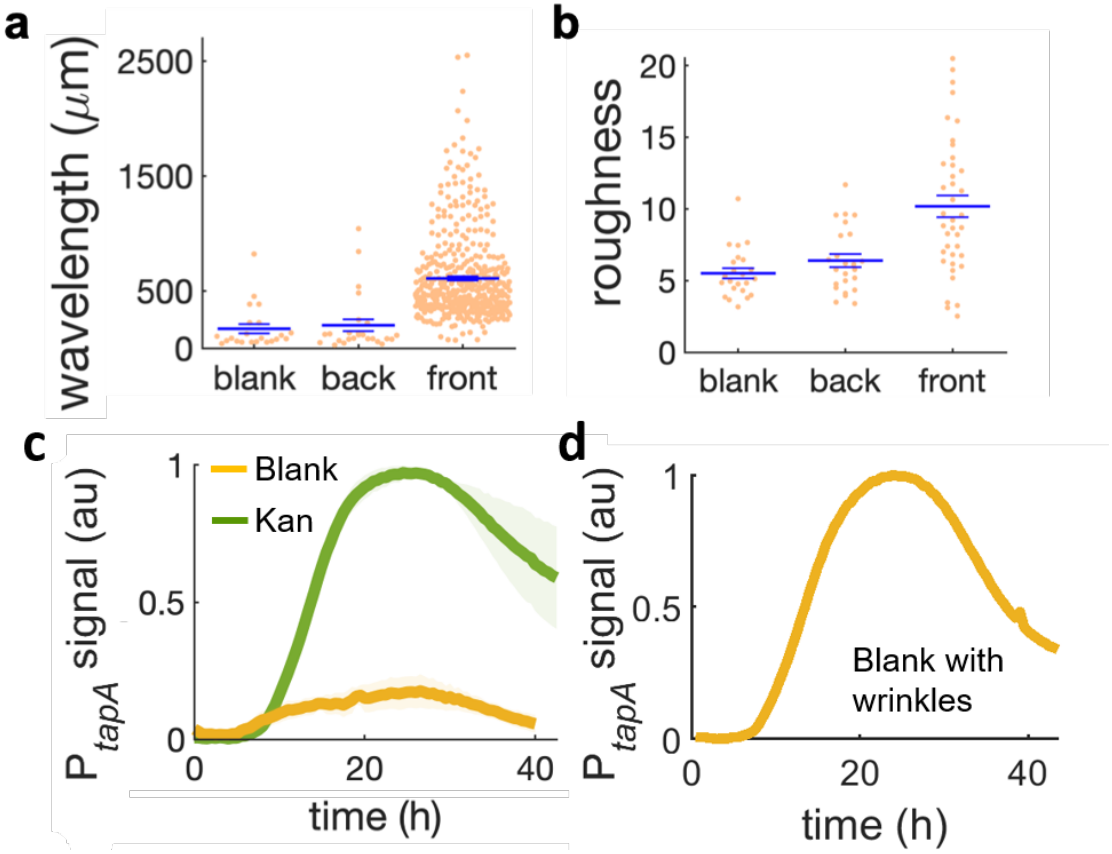

Figure 2.4: **Quantification of wrinkle formation in the kan and blank cases.** a) Scatter plot of the wavelength of the wrinkles near the kanamycin disk (front), in the bulk of the plate (back) and in absence of kanamycin (blank). b) Scatter plot of the roughness of the wrinkles in the same regions than for the wavelength. The large horizontal line shows the mean of the distributions and the small bars the s.e.m. c) Mean fluorescence intensity of P_{tapA}-*yfp* for the front of the plate in presence (green) and absence of kanamycin (yellow). The mean was taken from three independent experiments. The shady areas represent the s.e.m. d) Same as c) for a plate in absence of kan where wrinkles appear. Data comes from a single replicate.

trix component for *B. subtilis* biofilm formation [132], using a strain carrying P_{tapA}-*yfp*, a fluorescence reporter for the expression of the *tapA-sipW-tasA* operon [133]. The result showed a greater fluorescence signal when swarming cells are exposed to kanamycin (Figure 2.4c), suggesting that the exposure to kanamycin results in higher abundance in extracellular matrix and induces biofilm formation in a swarming colony on a soft-agar plate. Again, there were cases when wrinkles were promoted at the boundary of the petri dish even without kan. For these cases, the fluorescent signal was comparable to the kan case (Figure 2.4d).

2.2.3 Wrinkles are promoted by kanamycin just in swarming motility

To address whether swarming motility is necessary for this transition in presence of kanamycin, we have repeated the kan gradient assay in a swimming 0.25% agar plate. Bacteria inoculated at the centre expanded as in the swarming case and 3 days later

formed a pellicle biofilm over the plate. As expected, the pellicle biofilm formed wrinkles everywhere but, unlike the swarming case, the wrinkles were more inhibited near the kan disk (Figure 2.5a).

To further look at the effect of motility in this transition, we spotted colonies on hard agar at different distances from the kanamycin disk. We note that when a colony is spotted on hard agar, it does not expand more than 1 cm (Figure 2.5b). We spotted 4 μl of culture at 4 different positions (4 μl at each): the closest, 2 cm away from the kanamycin disk, shows a strong inhibition of wrinkle formation. The two on the sides, 2 cm away from the previous one, showed partial inhibition of wrinkles in the sides closest to the kanamycin disk. These should be compared to the normal growth that can be observed in the farthest colony. Therefore, spotting individual colonies on hard agar plates (1.5%) typically used for biofilm colony assays, showed that kanamycin inhibited biofilm formation (Figure 2.5b). When cells were instead uniformly spread across the hard agar plate, the system developed only faint wrinkles around the antibiotic exclusion zone (Figure 2.5c). We note that these wrinkles might well be appearing due to the presence of motile bacteria within the culture that we spread on the plate, although at present we have not tested this. We repeated this assay with a diffusive disk without kan and we observed that the surface just developed certain roughness but no wrinkles were observed (Figure 2.5). The fact that a kanamycin gradient promotes wrinkle formation significantly more in swarms than in a non-motile culture or in other types of motility, pointed to a fundamental role played by swarming motility and suggested the need to investigate the swarming dynamics in detail.

2.2.4 The emergence of the biofilm is templated by a transition from mono- to multi-layers localized at the swarming front

To study the potential link between swarming dynamics and biofilm formation, we characterized the swarming dynamics at the single-cell level, with and without a kanamycin gradient. We combined time-lapse imaging at both microscopic (10×; 30 fps) and macroscopic (2×; 0.006 fps) scales to capture both swarming, which is microscopic and fast (70 μm^2 cell rafts; speed 60 μm/s), and biofilm formation, which occurs at a macroscopic scale over days. For the microscopic imaging, we focused on the cells at ∼1 cm from the kanamycin disk, where wrinkles eventually appear and kanamycin level is around MIC (Figure 2.2b). The cells displayed typical swarming dynamics during the expansion of the colony front (Figure 2.6a). As time progressed, we observed the local surface coverage of the monolayer swarm to progressively increase from 20% to >60%, at which point the swarming rafts started displaying jamming events lasting 1-2 s, leading to a drop in

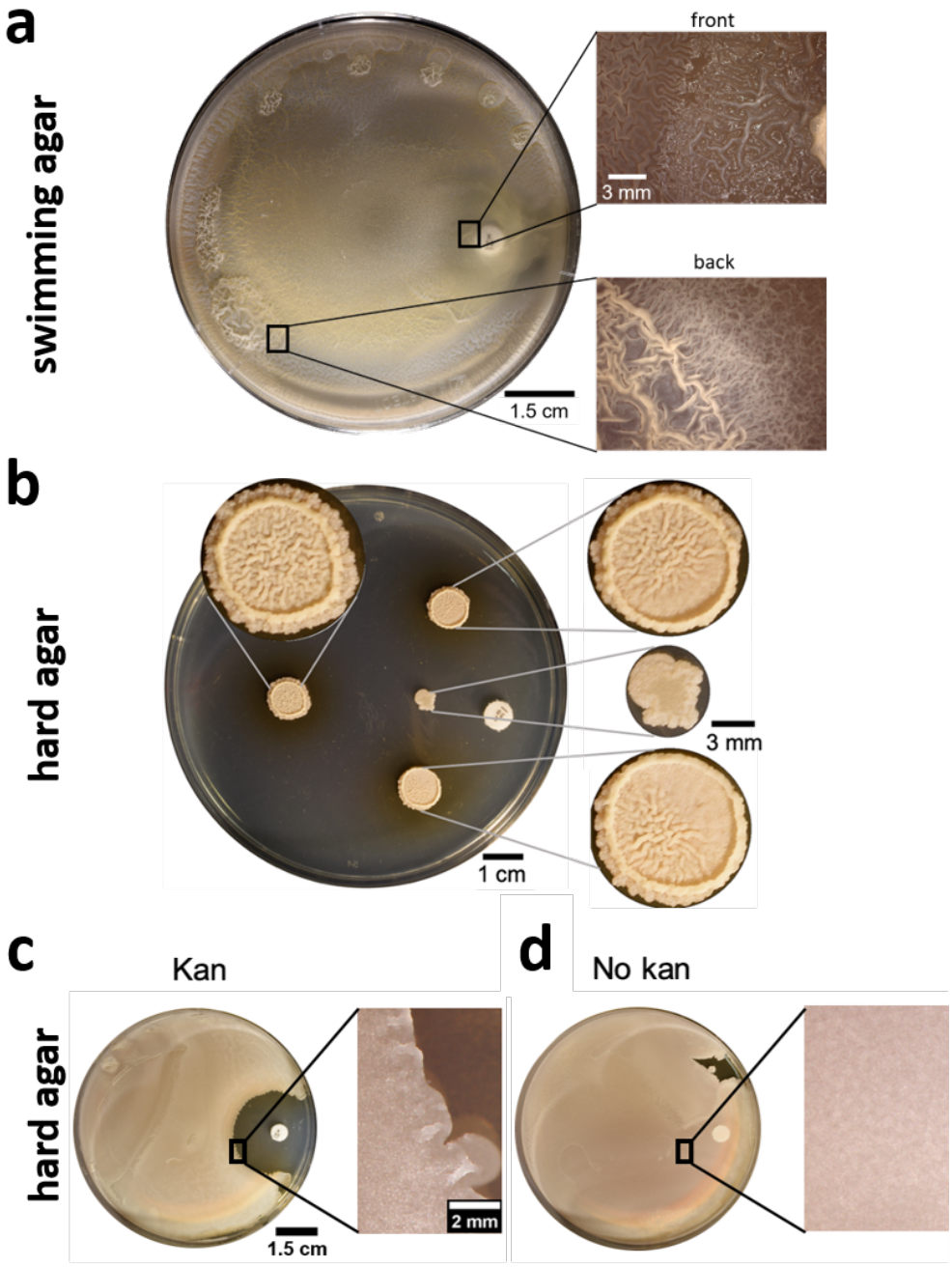

Figure 2.5: **Comparison of wrinkle formation between swimming agar and hard agar in presence of a gradient of kanamycin.** a) Swimming 0.25% agar plate 3 days after inoculation showing a pellicle biofilm in the whole plate with weaker wrinkle formation near the kan. b) 4 μl of *B. subtilis* were spotted in 4 different points on a hard agar plate. The colony spotted 2 cm away from kanamycin was inhibited and a wrinkly biofilm did not grow. Other two colonies on both sides were spotted so just part of the colony would be affected by the kanamycin. The colony at the back in absence of antibiotic is a commonly wrinkly biofilm in LBGM. c) Wrinkle formation in hard agar when the 800 μl of bacteria are spread over the plate. Weak wrinkles appeared at the edges of the clearance zone made by kanamycin for the hard agar case in comparison to the swarming agar case. d) Same as c) but with a blank disk where there is no wrinkle formation.

cell speed to rafts protruding temporarily from the swarming monolayer (typical size of jammed group 500 μm^2, see Video 3). Interestingly, in this area we did not observe a significant fraction of immotile cells, as previously reported for swarming in presence of a

uniform concentration of kanamycin [47].

The jamming of aligned rafts has been predicted numerically for elongated self-propelled particles on a plane [134, 135] although in that case the planar confinement prohibited bacteria buckling up out of the plane. With the further increase in local cell density, the temporary jams led to permanent isolated multi-layered regions, which we call 'islands', typically 27,000 μm^2 in size and with constantly fluctuating boundaries (Figure 2.6b inset, Video 4). Within the islands, cells were still dynamic and meandered across the layers although at a reduced speed (Figure 7.3, Video 5). Cell movement within the islands highlights the fact that these are formed by motile cells, rather than groups of immotile bacteria which spontaneously separate from the monolayer. These motile cells were constantly exchanged between the multilayer and the surrounding monolayer. Following a continuous increase in cell density with time, islands grew in size and merged with each other, eventually forming a much larger multi-layered region (Figure 2.6c, Video 6).

The formation of islands was also observed by macroscopic time-lapse imaging. In absence of kanamycin, islands emerged with a typical size of 2000 μm ^{2} from the centre of the colony and from the boundary of the petri dish but nearly simultaneously throughout the plate (Figure 2.6c). In contrast, the process of islands formation and growth was markedly different in presence of kanamycin (Figure 2.6d). After the swarming front expansion was stopped due to inhibition by the antibiotic, well-defined islands emerged within a 5 mm-wide band just inside of the arrested swarming front, and then grew with a strongly anisotropic pattern oriented transversally to the front of the swarm (Video 6). This phenomenology will be subject of study in the Chapter 3 of this thesis. The resulting macroscopic cell-density heterogeneity was followed by the subsequent formation of biofilm wrinkles, 1 cm away from the disk (Figure 2.3a).

As buckling inducing wrinkles in biofilms has been correlated in previous studies with cell-death [126], we decided to use the Sytox Green, a cell-impermeant dye that bind to nucleic acids within cells. Thus, sytox can only bind to the cells genetic material upon membrane lysis, indicating cell death. To test whether cell death plays a role, we recorded a timelapse from island formation to wrinkle formation (Video sytox. What we observed is that the sytox signal is not coming particularly from the places where the wrinkles are formed. Moreover, in [126], cell death occurs prior to wrinkle formation since this is what promotes the cell buckling, necessary to shape the wrinkles. However, in our timelapse, the sytox signal happens in the same timescale as wrinkle formation, making difficult to discern whether the signal is increasing due to an increase in cell death or due to the resulting change in spatial conformation of the cells when they form wrinkles. Therefore,

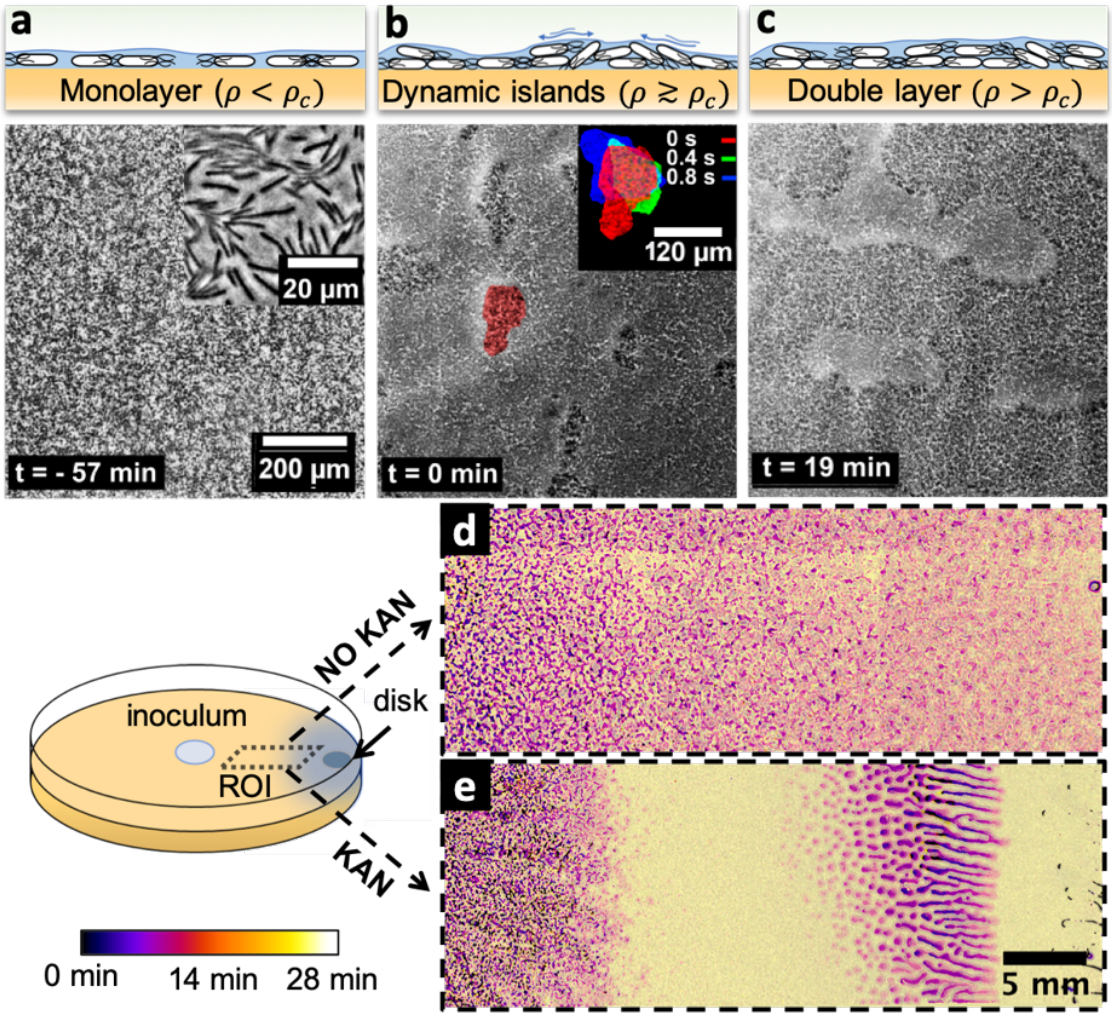

Figure 2.6: **Swarming bacteria form patterned multi-layer regions in presence of kanamycin.** a, b, c) Microscopy images of swarming bacteria and side-view illustrations at different levels of cell density (ρ). a) When cell density is below a threshold ρ_c, cells swarm in a monolayer. The image was taken 57 minutes prior to islands formation. The inset shows a zoomed image of the swarming rafts. b) Increase in cell density leads to formation of second layers, that appear as darker regions in the swarm. These islands are highly dynamic, and cells are motile. The shape of the islands changes dynamically within one second (insert). See also Video 4. c) Over time, the islands increase their size and merge together to double-layered regions, coexisting with mono-layered regions. Double layered regions are seen darker than mono layered regions. d, e) Images of swarming colony without and with kanamycin. Diagram illustrates the regions of interest (ROI) used for panels. The dynamics of island formation are color coded using the lookup table. The origin of times is the appearance of the islands. The earliest islands correspond to the darkest colors whereas the new features correspond to the lightest ones. See also Video 6. d) In the absence of kanamycin, multilayer regions are much grainer, with no clear patterns of propagation. e) In the presence of kanamycin, multi-layered regions have a defined pattern, starting from the regions closer to kanamycin to form an elongated shape. These regions appear approximately 0.7 mm away from kanamycin.

it is not clear the role played by cell death during wrinkle formation in swarming *B. subtilis* .

Bacterial communities can regulate fluctuations in cell density through the secretion of diffusive molecules [136]. We wondered whether this system, named quorum sensing, could

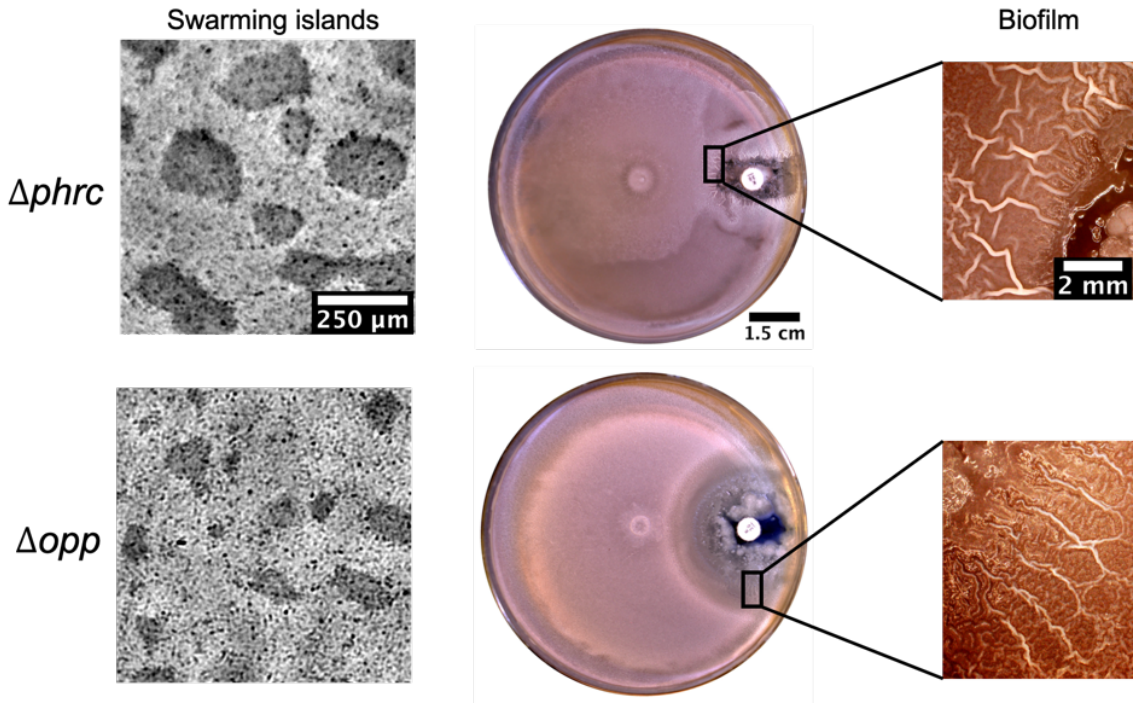

Figure 2.7: **Islands and posterior wrinkle formation in presence of a kanamycin gradient by the quorum sensing knock out strains Δ*phrc* and Δ*opp*.** For both mutants the islands and the wrinkles were formed as in the WT. The smaller clearance zone around kanamycin in the Δ*phrc* case is because this strain is genetically resistant to neomycin.

influence the formation of the islands since islands themselves are local inhomogeneities in cell density. We therefore repeated the experiments with Δ*phrC* and Δ*opp* mutant strains. *phrC* encodes the competence and sporulation factor (CSF), a quorum-sensing pentapeptide part of the signalling system in *B. subtilis* . The Δ*opp* strain lacks the transporter ATP-binding cassette (ABC) which allows CSF inside the cell. Despite being deficient in the *Phr* quorum-sensing system, both strains are still capable of swarming. In both cases, we observed the wild-type phenomenology of wrinkled biofilms and the emergence of islands (Figure 2.7). The results indicated that this quorum-sensing system is not responsible for the multi-layer transition, suggesting that exposure to kanamycin can promote cell-density heterogeneity by multi-layer islands formation in a quorum-sensing independent manner.

2.2.5 Transition from monolayer to multilayer resembles motility induced phase separation

To address the mechanism of multi-layer formation, we wondered if the active matter model of MIPS for rod-like particles [77] could act as a useful paradigm for understanding the emergence of multi-layer regions. We therefore plotted our experimental results onto the typical phase space considered when studying MIPS transitions, where an active 2-

dimensional system is characterized by its surface coverage, ϕ, and its rotational Péclet number, $Pe_r = u/LD_r$. The latter is defined in terms of the average speed u, characteristic size L, and rotational diffusivity D_r of the active particles. MIPS clusters are expected within a U-shaped region characterized by a sufficiently large Pe_r and a range of surface coverages that, for rod-shape particles like *B. subtilis* , is higher than 0.5, typical of circular particles, due to antagonistic effects of cell-to-cell alignment (Figure 2.8a, grey U-shape region shows the prediction for aspect ratio 2 from [1]). We then quantified the cell density (surface coverage, ϕ) and the rotational Péclet number from the different stages of the swarming process. Figure 2.8a shows these two quantities for cells in the monolayer (blue dots) and for bacterial jams (red dots). While bacteria in the monolayer were scattered outside the MIPS region (Figure 2.8a blue dots), bacterial jams -the first stage in the development of stable multilayer islands- clustered around the region expected for MIPS in two-dimensional self-propelled disks (Figure 2.8a, red dots; MIPS region from [1]. Jamming events were also characterized by a sudden drop in cells' speed (Figure 2.8b and Video 3, consistent with the basic premise of MIPS. This is only a temporary slow down due to cell-cell interactions and after the bacteria dispersed the rafts recovered normal motility. Altogether, these results show that the mechanism leading to the development of multilayered islands is compatible with the MIPS process in active matter.

2.2.6 Local accumulation of swarming cells induces multilayer transition and biofilm formation

The MIPS paradigm makes the experimentally testable prediction that multilayer formation could be induced by altering the local density of motile cells, thereby forcing the system to enter the MIPS region in phase space (Figure 2.8a, shaded region). We tested this by creating an experimental set up that allow us to control cell speed and density. Near-UV light can decrease cell speed in gram-negative bacteria like *E. coli* and *S. marcescens* [137, 138], as well as, as we report here, in *B. subtilis* (Figure 2.8c). The white region in the graph corresponds to an initial period when bacteria were not being irradiated. The cell speed and surface coverage were measured in a ROI 4 times smaller than the area being irradiated with UV. This prevented cells outside of the irradiated area from entering the field of view during the experiment. Once we activated the UV light in an area >200-fold greater than the field of view, there was an initial drop in cell speed that then continued for 3 min until the cells in the ROI became immotile. During this time, the surface coverage increased only marginally (ϕ=0.45 to ϕ=0.47 in 3 min; Figure 2.8c). The UV illumination caused an initial sudden drop in average speed from 65

to 50 μm/s (Figure 2.8c), followed by a nonlinear progressive slow down over the course of 3 min. The slope of this decrease in cell speed highly depends on the initial cell speed of the timelapse (Figure 7.4a). For regions with low initial speed, cells go from 10 to 0 μm/s in 3 min, in contrast to what happens when the initial cell speed is high, where cells go from 60 to 0 μm/s in the same time interval. Regardless of the initial speed, the cell density increase is always the same. Within the phase space picture (Figure 2.8d), this corresponds to a trajectory that essentially just moves towards progressively lower values of Pe_r. This should not lead to either jams or island formation, which in fact were never observed (Figure 2.8d). Therefore, we can confirm that UV illumination by itself does not induce multilayer formation.

We next illuminated a region of size similar to the field of view. Locally slowing down motility by light can lead to a local increase in cell concentration through the accumulation of cells from non-irradiated regions (Figure 2.8e). Thus, this UV light set up acts as a spider web, bacteria outside from the irradiated region enter in the ROI to then get trapped. As a consequence, the cell density increased significantly ($\phi \approx 0.42$ to $\phi \approx 0.7$ in 2 min; Figure 2.8e). For the first 2 min, the average drop in cell speed was likely compensated by the density increase. It is well known, that cell density can enhance swarming motility through cooperative raft formation [56, 44]. Eventually, however, the increase in cell density resulted first in the formation of jams and finally of multi-layered islands (Figure 2.8e, Video 7). For situations when ϕ >0.45, the cell speed would drop during the irradiation period (Figure 7.4b, last panel) since high ϕ reduces the freedom of the cells to abandon the irradiated region which results in a continuous exposure of the same cells, leading to a complete slow down. However, even in these cases jams could be observed due to the increase in cell density produced by this set up. Figure 2.8f shows the trajectories followed by the irradiated swarms in phase space. Jamming of swarming cells, the first step in island formation, occurs only for cell densities within a range that compares with predictions by MIPS for self-propelled rod-like particles (Figure 2.8f shaded region and [1]). These results provide a direct support to the hypothesis that a biophysical MIPS-like process underpins the transition from swarming monolayers to multilayers in *B. subtilis* .

We further examined if local cell-density increase by itself is sufficient to induce a localized phase transition from monolayer to multilayer. To this end, we used a physical barrier to impede the advance of the swarm and locally increase cell density (see subsection 6.2.7 for details). Again, consistently with the MIPS picture, the arrest of the swarm front led to an increase in cell density and the subsequent formation of multi-layer islands near the

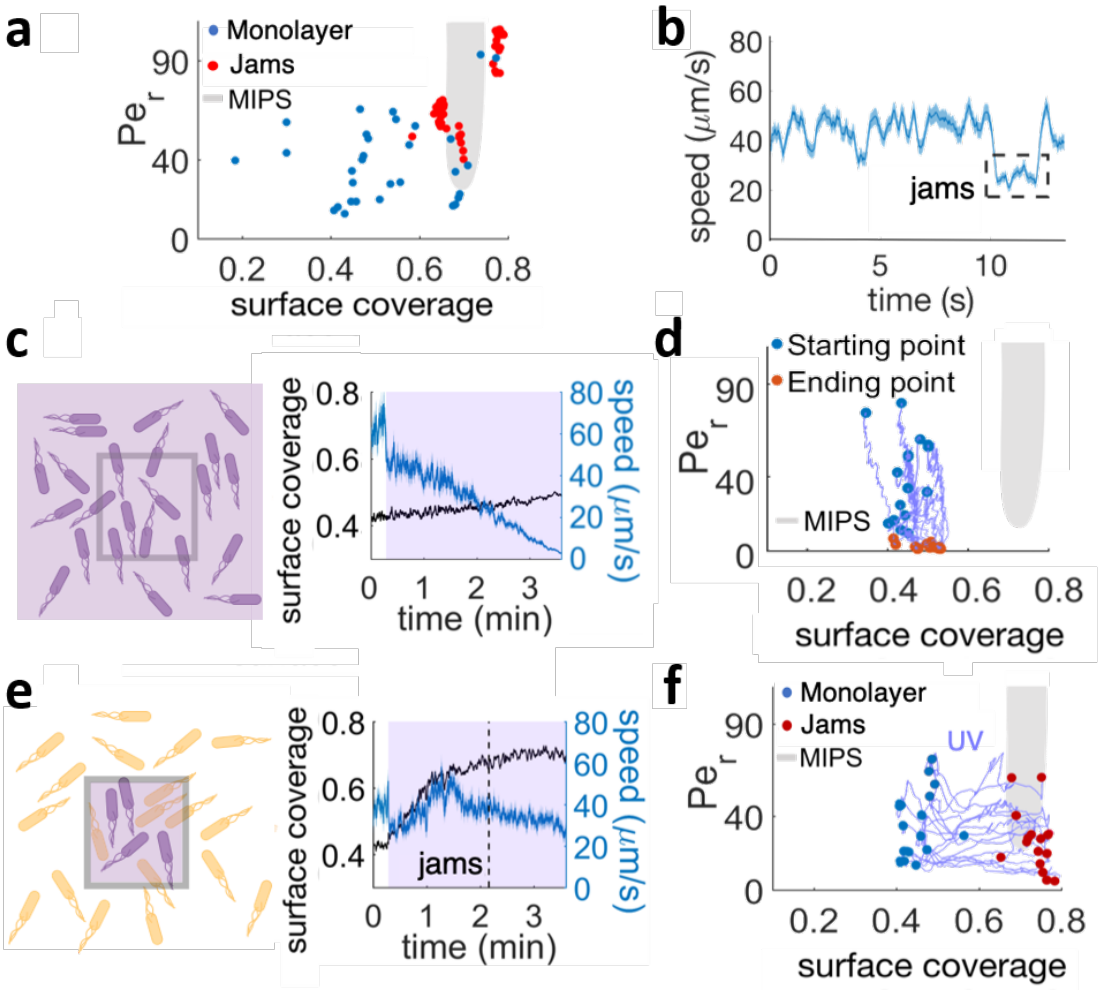

Figure 2.8: **Certain combinations of cell density and cell speed lead to jamming and multi-layer formation.** a) Phase diagram of surface coverage and the rotational Péclet number (Pe_r). Pe_r is proportional to the cell speed (see subsection 6.3.3). The greyed region indicates motility-induced phase separation (MIPS). Each data point represents an average of a 4 s single-cell time-lapse microscopy data. The time-lapse data in which jamming events are observed are shown in red (see Video 3). Jams cluster around the MIPS area. b) The speed of motile cells drops by half during jamming (highlighted by dashed rectangle). Increase in jamming events lead to formation of islands (see Figure 2.6 and Video 4). c) When a region approximately four times larger than the field of view is irradiated with UV, the surface coverage stays constant and the cell speed drops over time. Graph shows the dynamics of surface coverage (black) and cell speed (blue). Magenta is the period with UV light illumination (1.2 mW/mm^2). d) Trajectories in the phase diagram for bacteria continuously irradiated with this set up. The trajectories just decrease their cell velocity and hence they never approach the MIPS region. e, left) Illustrative diagram showing the accumulation of cells by UV irradiation when a region as large as the ROI is irradiated. e, right) UV irradiation elevates surface coverage. Vertical dashed line shows a jamming event. f) Time evolution trajectories of surface coverage and rotational Péclet number with UV illumination experiment. Blue dots are before UV illumination and red dots are when jams appear. Increasing surface coverage by UV induces formation of jams near the MIPS region (gray).

barrier (Video 8, Figure 3.1b). After 36 hours of further incubation, wrinkles developed near the physical barrier in the region where the islands had started to appear initially (Figure 2.9a). Different geometries and types of barriers were tried in this experiment: agarose wall, plastic wall, barriers forming a triangular shape, etc. and all of them led to

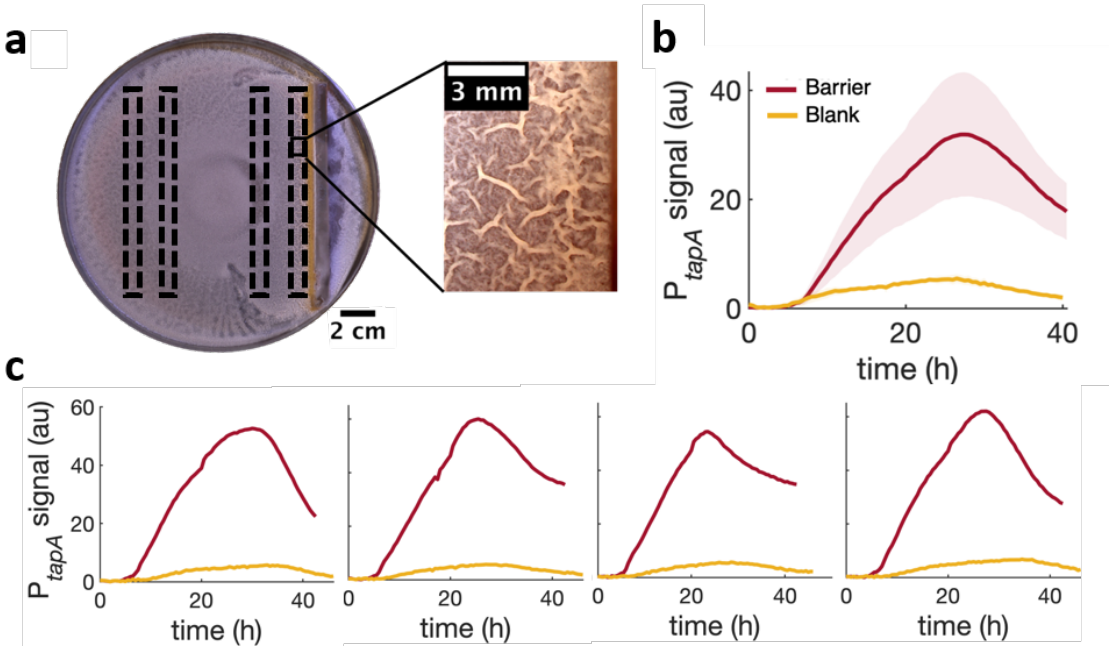

Figure 2.9: **Locally increasing cell density is sufficient in inducing wrinkle formation.** a) A physical barrier placed on agar triggers wrinkle formation. Wrinkles are formed at the region close to the barrier. The plate was incubated for 40 hours as in Figure 2.3. b) Mean fluorescence intensity of P_{tapA}-*yfp* measured just by the barrier for 4 different experiments and for 2 different experiments in the blank case. The shade indicates the s.e.m. c) P_{tapA}-*yfp* expression for 4 different regions across a swarming plate with a physical barrier in it. The fluorescent profiles are very similar across the plate, indicating that the *tapA-sipW-tasA* operon is upregulated equally in the whole plate and not just next to the stressor (the physical barrier in this case). The graphs corresponds to the dashed ROIs in a) in the same order from left to right.

wrinkle formation near the barrier. As it happened in the kanamycin case, the development of wrinkles at the barrier is accompanied by an increase in the fluorescent intensity of the P_{tapA}-*yfp* reporter (Figure 2.9b). This intensity was measured in a rectangular ROI just by the barrier so lacked knowledge about the spatial distribution of the fluorescent signal throughout the plate. To further clarify this point, we took time lapses measuring the fluorescence in four different regions across the plate for the barrier case (Figure 2.9c). It is interesting to note that the fluorescent profile was similar for the four regions measured. We believe that this might be connected to communication across the petri dish, possibly through volatile compounds, i. e. small molecules which can spread through the air and communicate the bacteria from different regions [139].

Altogether, these results show that *B. subtilis* swarms can undergo a single-to-multilayer transition driven principally by a physical mechanism compatible with MIPS. When this transition is localized, regardless of it being caused by antibiotics or physical confinements, the resultant macroscopic cell-density heterogeneity could determine the emergence of wrinkled biofilms.

2.2.7 There is an additional hidden variable behind the swarming to biofilm transition

Since the wrinkle formation is simply triggered by a local accumulation of cells happening next to a barrier, we can understand better why the wrinkles were promoted near the boundary of the petri dish (Figure 7.2). However, this transition was not always observed near the petri boundary and even in presence of kanamycin there were periods lasting months when wrinkle formation was either very weak or did not happen (commonly during Winter). This source of irreproducibility was a long subject of study during this project. We checked changes in the geometry of the plates, trying to promote the wrinkle formation in square plates rather than circular, or even bigger petri dishes of 15 cm diameter. We also tested different incubation temperatures and humidities by adding silica beads inside the plates or wet paper. Additionally, we made changes in the media composition. We made plates with different agar concentrations from 0.5% to 0.8% and plates with homogeneous concentrations of kanamycin but none of these helped. The only component that seemed to affect significantly the transition was the glycerol content. There were periods when increasing the glycerol from 1% to 2% or even 3% helped the transition to happen but it also increased the background noise, meaning that the roughness in the bulk of the plate also increased so it was difficult to characterize the wrinkles particularly promoted by the barrier or the kanamycin gradient.

Inspired by the inconsistency of the wrinkles in the boundaries of the petri dish, we thought that the symmetry of the physical barrier that stops the front may influence the transition. To test this, we repeated the swarming assay in absence of any stress but enclosing the swarm with a 3 cm petri dish Figure 2.10. After a 3 days incubation at 30°C , we observed that the wrinkles were formed in the outer boundary of the inner petri dish. We point out that these wrinkles are highly reproducible and that they develop even in those periods when wrinkles could not form in presence of a kanamycin gradient. As the enclosed part grows in a significantly different environment than the common swarming assay, we decided to repeat this experiment with a hollow concentric petri that allows better air circulation in the interior of the swarm. In this case, wrinkles formed but in the inner -rather than in the outer- boundaries of the concentric petri dish (Figure 7.5). Under this condition we also observed an anomalous high condensation in that region which could have increased the surface wetness and promote pellicle formation.

Another difference in Figure 2.10a is that the swarm that grew inside the petri was practically transparent in comparison to the swarm in the rest of the dish. The border between the transparent and the opaque region matches where the wrinkles are formed.

We realized that this also can arbitrarily happen in plates with a gradient of kan and, when it happens, we observed a strong wrinkle formation at the front (Figure 2.10b). These two regions can happen also in absence of any stress (Figure 7.6) but in this case wrinkles are not necessarily promoted at the edge between these two regions albeit there is also an increase in surface roughness.

In conclusion, there might be a hidden factor that affects the transition from swarming to biofilm. This led to a lack of reproducibility in the transition that could be solved by enclosing the swarm with a smaller concentric petri dish. This assay promoted the transition even when the wrinkle formation in the kan gradient was very weak.

2.2.8 Sequential administration of antibiotics reduces the emergence of biofilms from swarms

While more complex signalling pathways regulating biofilm matrix production are likely involved in the passage from localized multi-layers to wrinkles, our results suggest that simply altering the expansion dynamics of a swarm can promote biofilm formation. This implies that exposing bacterial swarms to stressors, such as kanamycin, a physical barrier or UV light, may increase their resilience by promoting the formation of biofilms that are much more challenging to eradicate. This is difficult to prevent by simply increasing the amount of antibiotics. In fact, when we used a 7-fold greater dose of kanamycin in the diffusion disk (200 μg), wrinkles still appeared on the plate (Figure 2.10b), although at a greater distance from the disk (Figure 7.1). However, our findings suggest that the localized multi-layer band is key during biofilm development since the wrinkly biofilm is not observed in absence of it. This indicates that this loclalized multi-layer could be a good target for antibiotic treatment aimed at suppressing the emergence of biofilms. Such multilayer band happens at a concentration of antibiotic that bacteria can tolerate since the cells are still motile (Figure 7.3, Video 5). We thereby wondered if a two-step sequential antibiotic administration could prevent biofilm development, where the first administration induces multilayer formation and the second targets the multilayer area before completing biofilm formation. To test this hypothesis, we decided to administer a total amount of 200 μg of kanamycin in two steps, an initial one when placing the disk on the plate, and the second inoculating again in the disk as the swarming front halted. The administration of these two doses follows four different protocols: 200+0 μg , 150+50 μg , 100+100 μg and 50+150 μg . In this way, we had 4 different scenarios: all in one dose, an initial dose higher than the second one, two equal doses and an initial dose smaller than the second one. This protocol aims to induce the multilayer formation necessary to trigger

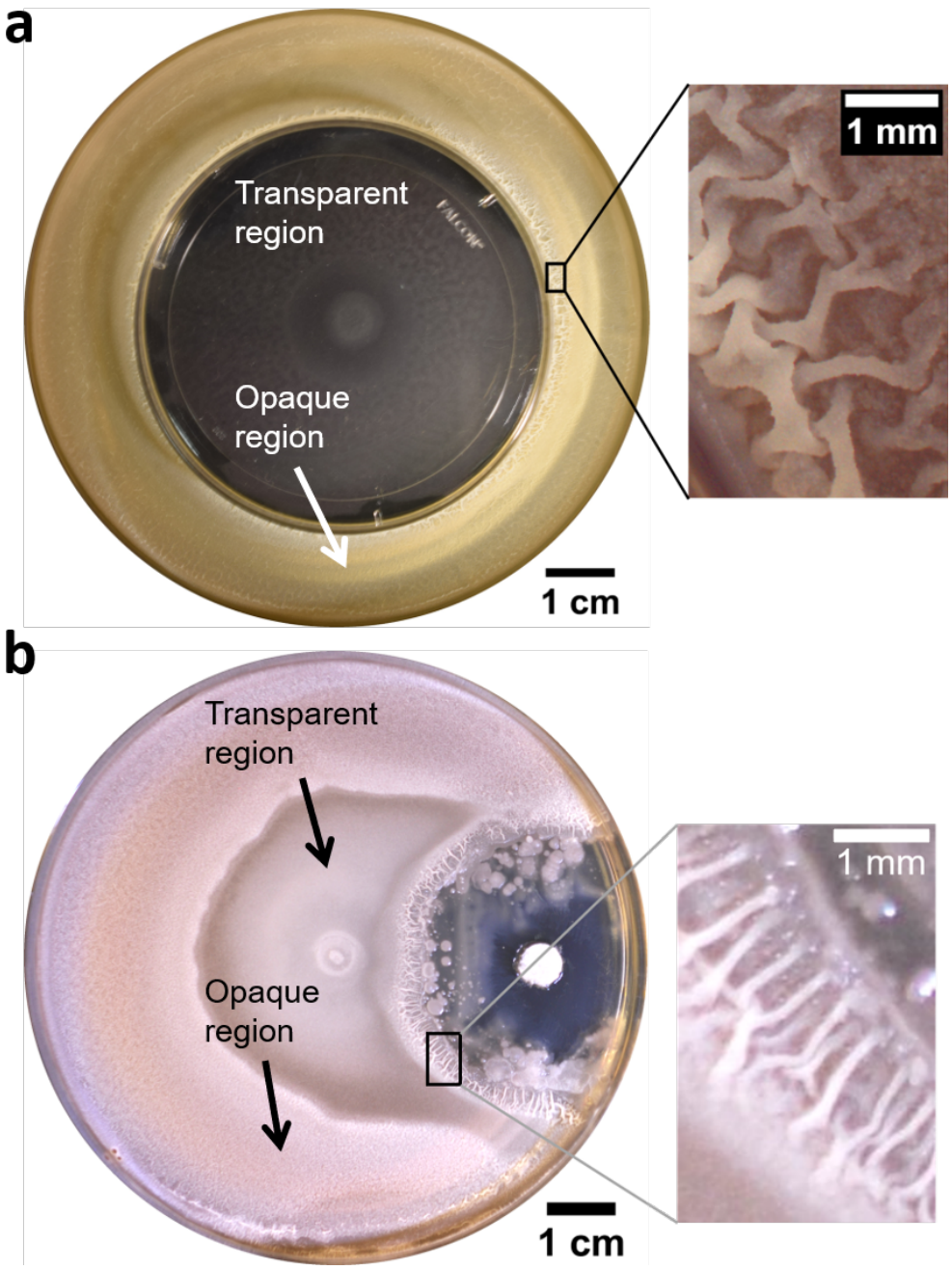

Figure 2.10: **The contrast between a clear region and a transparent region promotes wrinkle formation.** a) Swarm enclosed by a smaller petri dish promotes wrinkle formation at the outer boundary of the inner petri dish. b) Contrast between a transparent region in a kanamycin plate with a 200 μg and a opaque region. Wrinkles form as usual near the kan.

the biofilm but then increasing locally -but not globally- the concentration of antibiotic in the multilayer region which we believe is essential for wrinkle formation.

For each of these cases, we tried to measure the local antibiotic concentration at the distance from the kanamycin disk where the wrinkles were formed. To this end, we used a variation of the Kirby-Bauer assay as we did in Figure 2.2b to measure the antibiotic concentration profile at 5 different positions along the line connecting the centre of the

petri dish and the disk (Figure 7.7). We performed the measurements at 0 h -corresponding to the inoculation time-, 20 h and 44 h. Each time point measurement was repeated 3 times for each of the administration protocols. Different plates were used at different time points for a total of 36 plates. We stress that the experiments were performed on inoculated swarming plates, not on blank plates with just the kanamycin disk. This is because the spread of the antibiotic could in principle be influenced by surface effects (e.g. flows driven by biosurfactants) that would be different between a plate with a swarming colony and one without. The curves were then used to estimate the antibiotic concentration in the area where the wrinkles formed (Figure 2.11a), which is dependent on the antibiotic dosage protocol. As we expected, the highest increase in kan concentration corresponds to when we initially put the lowest dose of antibiotic (50 μg) and then we added the maximum, up to 200 μg . The local concentration for the other treatments at the time when the wrinkles are formed is always lower than in this case.

The emergence of wrinkles was greatly suppressed when kanamycin was administered sequentially, despite keeping constant the total amount of antibiotic added to the disk (Figure 2.11b and c, Figure 7.8). The effect was most evident when the second dose was greater than the first since it registered the highest local increase of antibiotic at the wrinkles site (Figure 2.11a). For this case, both the wavelength and the roughness of the wrinkles were 2 and 1.6 times lower than for when the treatment is not split in two doses.

The question that we wanted to pose is whether, without increasing the use of antibiotics, there are antibiotic-administration strategies that are better at preventing -or at least reducing- the emergence of the wrinkly biofilm we observe. According to our experiments, splitting the same total amount of antibiotic added to the disk into a low initial dose followed by a higher one, brings a noticeable reduction in the wrinkle wavelengths compared to using all of the antibiotic in a single initial dose. These results thus propose a promising strategy for treating bacterial collectives with aminoglycosides while minimizing the emergence of biofilms.

2.3 Discussion

This work reveals a biophysical mechanism underpinning the emergence of biofilms from swarms through a localized phase transition governed by the motility and the cell density. We demonstrated that the transition from monolayer to multilayer can be induced by different stresses, from antibiotics to UV and physical confinement. Based on our findings, we showed that a sequential monotherapy can be effective in treating swarming bacteria

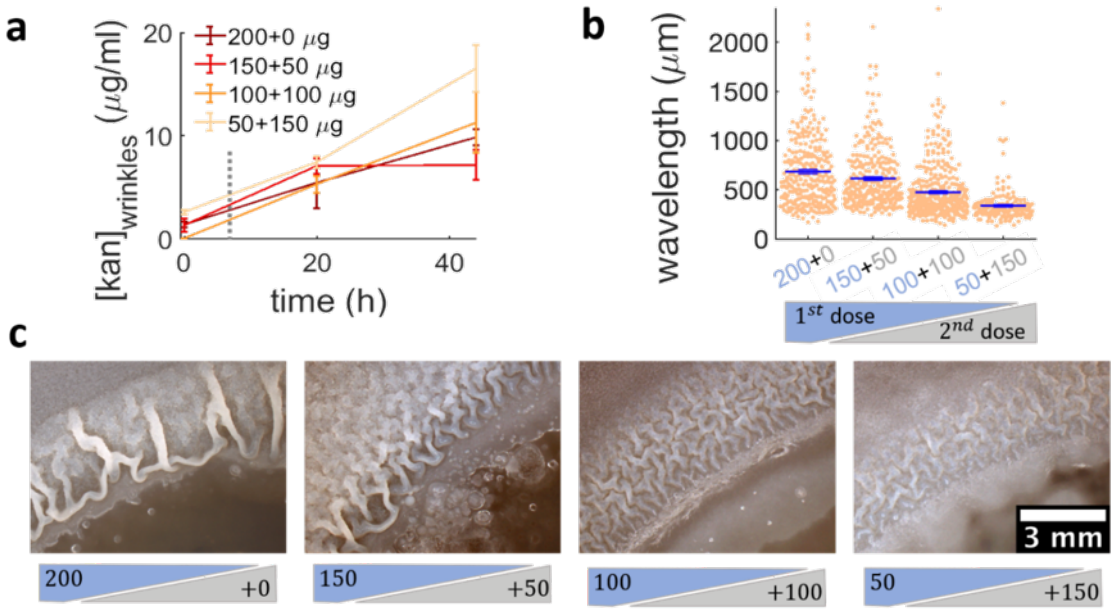

Figure 2.11: **Administering the same amount of kanamycin in two sequential doses reduces wrinkle formation.** a), b), c) Kanamycin was sequentially administered in two different doses to a disk while keeping the total to be 200 μg . The first administration was added as in other experiments, while the second was added to the disk as a 4 μl drop when the islands were about to appear. a) Concentration profile of kanamycin over time for the four concentrations of the sequential administration of antibiotic assay. The measurements were made using the modified Kirby-Bauer assay (see subsection 6.1.2) at the distance from the kanamycin disk where the wrinkles are formed for the 4 different initial concentrations: 1.32 cm for 50 μg , 1.59 cm for 100 μg , 1.74 cm for 150 μg and 1.85 cm for 200 μg . The time when the second dose of antibiotic is added is indicated with a dotted gray line around 7 h after inoculation. b) The wavelengths of wrinkles with respect to the doses of first (blue font) and second (gray font) administrations (μg). c) Microscopy images of wrinkles induced by kanamycin. The first dose is in the blue shade and the second dose in the gray shade.

in order to prevent biofilm formation. Further optimization of this approach in terms of timing and concentrations would be an important point in biomedical research.

As the underpinning mechanism of the transition is an emergent phenomenon driven by physical interactions between swarming cells, we believe similar transitions should also happen in other rod-shape bacterial swarms of clinically relevant species, such as *Pseudomonas aeruginosa* and *Salmonella enterica*. Such investigations would be an important step forward to see if sequential antibiotic administrations could be effective in suppressing, and eventually altogether preventing, stress-induced biofilm formation in pathogenic bacteria.

This study makes also more evident the distinction between swarms and biofilms. In the literature it is sometimes considered that swarms and biofilms are two different states of the same bacterial collective. Thus, the centre of the swarming colony would be called a biofilm. However, we highlight that experimental studies have not been carried out to prove that the centre of the swarm is actually expressing biofilm-related genes. Using the

P_{tapA}-*yfp* we observed no differences between different regions in the swarm, including the centre, suggesting that extracellular matrix is not particularly produced there. In the same way, using our Δeps knock out, we did not observe apparent differences between the centres of the swarm for the WT and Δeps. Future detailed studies are encouraged to elucidate the exact differences and similarities in a centre of a swarm with respect to biofilms.

We also addressed a fundamental question about the mechanism by which cell collectives adapt their behavior in response to various physical and chemical stresses. In the present case, a local cell-density increase caused by the halting of the swarming front, may be part of a general collective stress response mechanism, which triggers a switch in the collective behavior from swarming to biofilm. The stress response mechanism that we observe at the collective level could allow the swarming colony to develop biofilms in response to various stressors, regardless of the stressors' exact molecular mode of action. In this regard, we investigated the role of cell death during island formation in presence of kanamycin but we did not observe a higher signal coming from the islands induced by kanamycin and the other areas in the swarm, suggesting cell death does not participate in island formation. We expect that further research will determine whether this form of environmental sensing and adaptation of cell collectives via cell-density increase is common to other biological systems. The connection we discovered could represent a primitive example of a collective mechanochemical feedback loop, underpinned by emergent phenomena (MIPS) in collections of motile agents either alive or synthetic. To this end, the gained biophysical insights may not only offer new biomedical treatment strategies against the rise of biofilm-associated antimicrobial resistance but may also contribute to our understanding of development and cell-fate determination.

Another important question lies in the interplay between biophysical and molecular mechanisms regulating stress-induced biofilm development. Characterizing the gene expression profiles in the high-cell-density clusters resulting from multilayered islands, while simultaneously monitoring the mechanical interactions, would be an important step forward towards understanding collective stress responses. This has been done in epithelial cells demonstrating that they can regulate replication upon extrusion [69].

Chapter 3

B. subtilis undergoes two modes of phase transition to form multiple layers

3.1 Introduction

Collective motion is intrinsic to living systems, from bird flocks to swarming bacteria and despite the differences in length scales and the properties of the individuals they share similar patterns of spatiotemporal coherence [140, 141]. Investigating these patterns experimentally or theoretically (e.g. through numerical simulations) reveals characteristic features like large fluctuations in population density and cluster dynamics [140, 56, 134]. For example, studies in collective behaviour of swarming *B. subtilis* monolayers have found that bacteria move collectively in aligning clusters undergoing large fluctuations in cell density over a period of a few seconds [64]. The particular properties of this collective motion depend strongly on the physical properties of the swarm such as cell density, cell velocity and the aspect ratio of the cells [63, 142]. According to the theory of collective motion, at high concentration, a collection of motile particles can spontaneously form clusters of high-density and low-motility, surrounded by a low-density high-motility phase [75, 124]. This process, known as Motility Induced Phase Separation (MIPS), is based on a feedback between the decrease in particles' speed at high concentration, caused by physical interactions, and the spontaneous accumulation of active particles in the places where their speed is lower [77]. The theory of MIPS, then, suggests that persistent heterogeneity in cell density -the MIPS clusters- can develop spontaneously when both cell speed and cell concentration are sufficiently high. In swarming bacteria, densities can easily approach

the maximum allowed by steric repulsion (0.75 volume fraction [63]) and it is therefore natural to wonder whether the system undergoes a transition similar to MIPS. Such transition would generally depend on cell shape, speed or density. Recently, Jeckel et al [44] categorized the different parts of an expanding swarming colony of *B. subtilis* in function of some of the above mentioned parameters relevant for MIPS, identifying regions with different dynamical properties. However, such phase transitions have not been experimentally observed in bacterial swarms, likely due to the difficulty of controlling cell speed, density and shape in these living systems. Only recently such phase transition has been reported for first time in bacterial systems that move 100-1000 times slower than swarms such as gliding *Myxococcus xanthus* and in expanding colonies of *Pseudomonas aeruginosa* [143, 105]. Here, we report that swarming *B. subtilis* can develop very localized multilayers called islands to then merge and form a new layer of bacteria. This multilayer formation in *B. subtilis* resembles the different phases predicted by the theory of MIPS in active particles systems: a fluid-like swarming monolayer that coexists with a denser bilayer of cells.

Previous studies speculated -but did not show- that multilayer formation may play a key role in the higher resistance that bacterial swarms have over the swimming counterparts [121, 144]. Here, we report that, when forming multiple layers, swarming *B. subtilis* can move towards regions of high antibiotic concentration where -instead- cells in a simple monolayer are immotile.

3.2 Results

3.2.1 *B. subtilis* develops a multilayer through a mechanism that resembles a phase transition in binary fluids

To characterize whether and how swarming *B. subtilis* can develop multiple layers within the swarming state, we inoculated 4μl of *B. subtilis* culture at the centre of a 9 cm diameter petri dish (Figure 2.2, subsection 6.1.2). After 2 hours of lag period, the cells formed a rapidly expanding swarming front (4 mm/h) that after nearly 5 hours at 37°C covered the whole plate (Video 1). This was followed by the development of dark spots (typically of size 0.001 mm^2) that in brightfield images typically indicate regions of localized high cell density. As we said in the previous chapter, at a closer inspection, we recognized these as multi-layer regions of the swarm, which we will henceforth refer to as 'islands' (Figure 3.1a). Islands are initially unstable and intermittently appear and disappear well separated from each other. However, after 10min persistent larger islands appear and

quickly form a percolating network (Figure 3.1a) reminiscent of the phenomenology of spinodal decomposition in binary fluids [145]. The network progressively grows giving rise to a complete second layer. The formation of islands is first observed at the centre of the swarm and, unexpectedly, at the very boundary of the petri dish. It then spreads from these locations until both sides converge in an intermediate point within the dish, finally forming a complete second layer (Video 9).

As we observed that the boundaries of the petri dish could trigger the local accumulation of the cells and promote the second layer, we decided to repeat the experiment with a physical barrier inserted in the agar to arrest the swarming front (Figure 3.1b). Indeed, once the barrier stops the progression of the swarm, we observe that islands start forming close to it. This happens much earlier than the spontaneous emergence of islands observed within the swarm without a physical barrier. Altogether, these observations suggest that the simple act of blocking the advance of the swarming monolayer is enough to induce a localized thickening of the swarming front. The formation of multiple layers has been proposed to increase a swarm's tolerance to antibiotics [121]. Given the fact that antibiotics can severely reduce motility, we wondered whether -similarly to the barrier case- they could also influence the local thickening of the swarm and therefore its antibiotic tolerance. We decided to test this by conducting a swarming assay with a spatial gradient of the aminoglycoside kanamycin (Figure 2.2a). Specifically, a disk containing 30 μg of kanamycin was placed on the side of a swarming plate (0.5% agar) and allowed to rest for 24 hours to establish a space-dependent antibiotic concentration profile. An inoculum of *B. subtilis* culture was then placed at the centre of the dish as in the previous cases, 4 cm away from the kanamycin source. As before, the swarm expanded towards the boundary of the petri dish. However, the side of the swarm moving towards the kanamycin was clearly affected by the antibiotic, as it started slowing down after 0.7 cm and then completely stopped approximately 0.3 cm away from the kanamycin disk (Figure 2.2c). As the swarming front expansion stopped, well-defined, distinct islands first emerged within a 5 mm-wide band just inside of the arrested swarming front, grew with a strongly anisotropic pattern oriented transversely to the front of the swarm until finally merged to form a localized second layer right behind the front (Video 10). This phenomenology is clearly different from what is observed in the unperturbed case. It is reminiscent of a binodal liquid-liquid phase separation in a temperature gradient [146] which here might reflect a kanamycin-induced speed gradient (Video 10), and in copolymers where the liquid-liquid phase separation is driven by surfactants [147]

The clear differences that we observe in the transition from mono to multilayers in

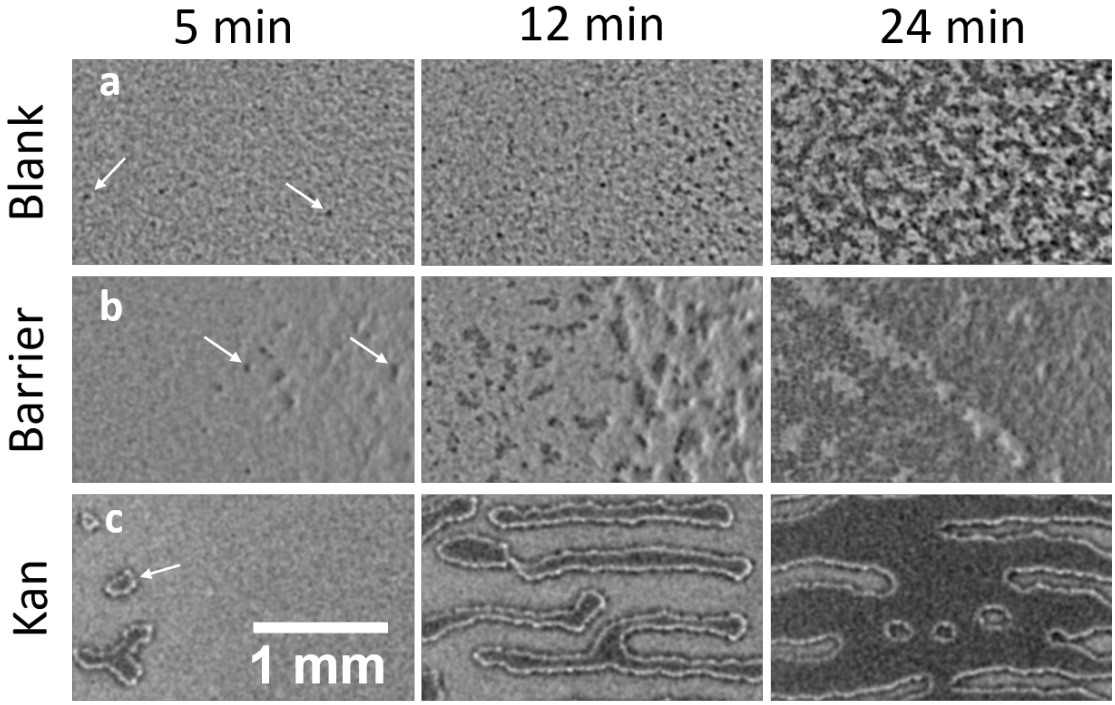

Figure 3.1: **Island formation in swarming *B. subtilis* in a confluent plate in absence of stress, in presence of a physical barrier and in a gradient of kanamycin.** a,b and c represent a timelapse of islands formation 5 min, 12 min and 24 min after the first island was observed in each condition. a) Formation of islands in absence of stress. The islands appear as small dark spots in the brightfield image that eventually merge and form large dark areas. b) Island formation in presence of a physical barrier where the wall was placed just at the right of the shown field of view. c) Island formation in presence of a gradient of kanamycin. The islands appear as well defined regions that grow in size transversely to the kanamycin disk, placed on the right of the shown field of view. The arrows point at examples of the islands in each of the cases.

absence and presence of an externally imposed stress could point to a generic mechanism that bacterial swarms harness to react to environmental stresses like antibiotics. It is therefore worth to better characterize quantitatively the differences and similarities between these two transitions. To this end, we will follow in the steps of earlier studies of phase separation in active particles [84, 83, 104].

3.2.2 Nucleation of islands in absence of stress resembles a spinodal decomposition whereas it resembles nucleation and growth for the kanamycin case

The defining characteristic of spinodal decomposition is that the phase separation happens at once across the whole system, since there is no energy barrier that prevents the growth of fluctuations (the system is intrinsically unstable) [148]. In contrast, during nucleation and growth, the nucleated clusters have to overcome an energy barrier [148]. This is usually associated with the existence of a characteristic nucleation size as well as a slower

phase separation dynamics [80]. To see if something similar is taking place in our system, we started by characterizing the nucleation of islands over time (Figure 3.2) in the three cases of no antibiotic disk (blank); physical barrier (barrier); antibiotic disk (kan), taking the origin of times as the first observed island in the field of view. It is also important to keep in mind that the time window for the formation of a confluent second layer, 50 min, is comparable to the doubling time of swarming *B. subtilis* (43 min) [44]. Cell replication is therefore expected to play a major role in the phenomenon.

To characterize the emergence of islands in the blank case, we focused on a 5.3x5.3 mm^2 region of interest coming from plates with a blank disk, a barrier, and a kanamycin disk. In the last two cases, the regions were selected such that they were at least 4 cm from the stressor (either the barrier or the kanamycin disk). This allowed us to confirm that islands are produced in the same way as in the blank case. Furthermore, in all cases, the region of interest was chosen approximately 2 cm away from the edge of the Petri dish to minimize the influence of the boundary, which acts as a barrier. The emergence of islands is first observed when the swarm has nearly covered the whole dish, at which point the monolayer is already quite crowded (surface coverage of monolayer >0.6). Nucleation follows a clear two-stage dynamics. In the first stage the nucleation rate increases exponentially, with a rate of 0.195(0.013) min^{-1}. In this regime, small islands of typical size 0.002 mm^2 continuously appear and disappear (Figure 3.2a and inset). As the nucleation rate increases, islands of progressively larger size start to appear, and quickly merge into a multilayer network intercalating the monolayer swarm. At this point, which corresponds to the maximum in islands nucleation rate, approximately 50% of the field of view is occupied by the multilayer (orange dashed line in Figure 3.2a). The system enters the second stage, characterized by an exponential decrease in the nucleation rate, with a rate of -0.1408(0.0095) min^{-1}. The proportion of surface covered by the multilayer continues to grow but at a progressively slower rate (Figure 3.2a). This rate can be modelled as a logistic growth of the form:

$$N(t) = \frac{C}{1 + e^{-k(t-t_0)}} \tag{3.1}$$

Where N is the number of islands in the second layer at certain time t, k is the rate of appearance of those islands, C and t_0 are constants that do not necessarily have a physical meaning in this case. From here, we can obtain the growth rate of the second layer k=0.2591(0.0054) min^{-1}. Comparing this growth rate with replication rate of swarming *B. subtilis* cells (0.06 min^{-1}), we can see how the second layer grows faster than it would

do as if it was covered just due to cell replication. This indicates that there is a mechanism beyond cell replication that promotes the second layer formation.

In the case of the barrier, to avoid the contribution of islands from other regions of the swarm, we selected a rectangular region of size 7x14.5 mm^2 just by the barrier. Due to the local confinement, the increase in cell number is expected to be higher than in the blank case, since now the source of the new islands will not come only from cell replication but also from the local accumulation of cells due to the physical barrier. As we can see in Figure 3.2b, the nucleation rate follows a temporal evolution that is very similar to the blank case, albeit with a slightly worse agreement of the initial rate increase to an exponential dynamics (R^2 =0.96 for barrier vs. 0.99 for blank) and a faster decrease past the peak (-0.178(0.011)min^{-1}). A clearer difference can be found instead in the size distribution of nucleated islands (histograms in Figure 3.2a, b) which show a smaller spread of sizes, in particular at the lower end. These and other differences will be discussed further in Sections 3.2.3 and 3.2.4. The growth rate of the second layer is k=0.310(0.025) min^{-1}, higher than for the blank case, confirming that cell accumulation from other regions of the swarm contributes to the formation of the second layer.

In the kanamycin case, we considered a region 8.8x15 mm^2 oriented such that islands grow nearly parallel to the long side of the region of interest. The region considered was 0.7 cm from the antibiotic disk, in a position which is unaffected by islands coming from the centre of the swarm. Figure 3.2c reveals three main differences, at this level, between the kanamycin case and the previous two. Firstly, the increase and decrease of the nucleation rate are largely linear, rather than exponential. This means that island nucleation is faster than in the barrier and blank cases at the beginning, but significantly slower later on. This brings us to the second main difference, which is that the peak nucleation rate is significantly smaller than in the previous cases (0.08 mm^{-2} vs 0.2 mm^{-2} respectively for blank and barrier). A lower nucleation rate suggests the need for a larger stochastic fluctuation to generate a new island. Indeed, this is reflected in the third main difference: the size distribution of nucleated islands has a well defined peak at an area of 0.025 mm^2, more than an order of magnitude larger than the average size of the islands nucleated in the blank and barrier cases (histogram in Figure 3.2c). The lower nucleation rate and the larger size of newly nucleated islands determine the fact that, differently from the previous cases, the multi-layered region increases at an approximately steady rate. This expansion is mainly the consequence of the growth of well-defined islands, rather than the coarsening of a percolating cluster as in the previous cases. Interestingly, islands in the kanamycin case grow with a marked anisotropy (see Figure 3.1a) along the spatial

gradient of antibiotic. Although we do not currently know the origin of this phenomenon, we speculate that it could be related to a gradient in cell motility caused by exposure to kanamycin. The coverage of the second layer 0.1056(0.0037) min^{-1} is also slower than for the previous two cases, agreeing with what we observed for the nucleation rate.

Altogether, the emergence and expansion of multilayer regions of the swarm follow a distinct dynamics in the kanamycin case compared to the other two. In the blank and barrier cases, an extremely rapid increase in nucleation of small islands leads to the formation of intercalating networks of mono- and multi-layers. Instead, in the kanamycin case, the multilayer coverage is the result of slow nucleation and growth of large, well-defined, coherent islands. The slower growth rate is characteristic of nucleation and growth, where just a few instabilities overcame the energy barrier and can grow. Overall, we argue that these two contrasting phenomenologies are strongly reminiscent of the difference between spinodal and binodal decomposition in liquid-liquid phase separation. Indeed, the possibility of both binodal-like and spinodal-like phase-separation has been recently predicted for an active matter model related to the biological system that we are studying here [98].

3.2.3 Fourier analysis identifies a characteristic wavelength which does not evolve as an increasing power law

The differences in the nucleation and expansion of a multilayer swarm between the blank and barrier case on one side and the kanamycin case on the other, and their similarities with spinodal and binodal decompositions respectively, made us wonder whether these two distinct cases would be compatible with properties intrinsic to the structure of phase transitions. For example, a hallmark of spinodal decomposition is a well-defined length scale of the phase-separated domains that increases with time as a power law as the domains grow self-similarly [149, 150]. This characterization has proven useful for *Myxococcus xanthus* fruiting body formation [104]. This species can form fruiting bodies through a spinodal decomposition for high inoculation densities and through nucleation and growth for lower inoculation densities, following in both cases a power law increase in their characteristic wavelengths. Thus, we wondered whether, in a similar way, we could identify a well-defined initial wavelength in our phase transition and study the dynamic of its coarsening in time, possibly revealing further differences between the spinodal-like and binodal-like cases.

With this in mind, we decided to start by measuring the y component (k_x=0) of the structure factor of the swarm images, during the island formation process. The structure factor, or power spectrum, is the modulus squared of the Fourier transform of the image intensity. In our case, we chose the k_x=0 component because in presence of kanamycin

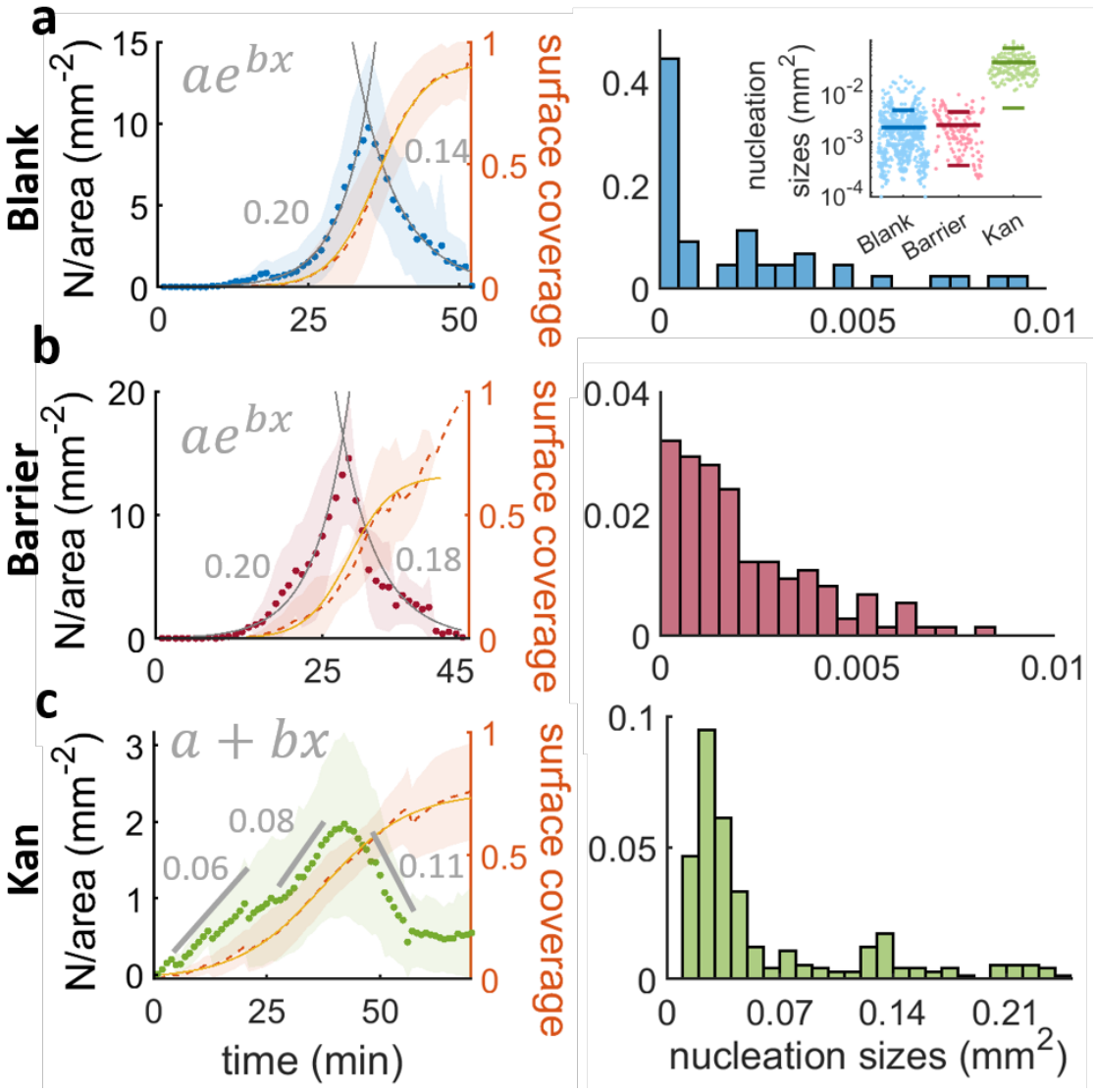

Figure 3.2: **Nucleation and nucleation size distributions for the islands in absence of stress, with a physical barrier and with a kanamycin gradient.** a,b and c describe the nucleation over time for the three conditions studied. The fits drawn as gray lines in a) and b) are fits to exponential functions and the numbers in gray are the exponent b of the exponential fit. For c) the nucleation was fitted to three straight lines (two increasing and one decreasing) and their slopes are: 0.0605(0.0064), 0.00841(0.0057) and -0.1127(0.0099) mm^{-2}. The histograms show the distribution of sizes of the nucleated islands. The bin width for the blank and barrier cases are 0.0005 mm^2 and for the kanamycin is 0.01 mm^2. The inset in a) represents the distribution of the sizes, the mean and the standard deviation for the 3 cases studied.

the islands form patterns that are oriented towards the antibiotic, for us the x-direction of the images, and hence we expect to see a different characteristic wavelength along this direction than the other. For consistency, we will give the same component for the barrier and blank cases. To calculate the peak of the structure factor, we fitted it to a sum of two Gaussians, extracting the characteristic wavelength as the inverse of the wavenumber at the peak of the gaussian fit (Figure 3.3a, b and c).

In the blank case, the structure factor gives a very weak peak for times earlier than

15 min (Figure 3.3a), probably due to the absence of any stable nucleated islands, which we saw in Figure 3.2a, that appear for times around 14 min. From 15 to 30 min there is a periodic pattern given by the formation of well separated islands (Figure 3.1c) that then decays for later times probably due to the merging of the islands. The classical theory of coarsening predicts that the microstructure of a two-phase system will evolve to be self-similar, or time independent when scaled by a time-dependent length [151]. To check whether this is the case here, we rescaled the structure factor and the wavenumber by their value at the peak. We found that the decomposition in the blank case evolves in a self-similar manner only for a restricted period of time from 20 min to 40 min. This is similar to what happens in *M. xanthus* fruiting body formation [104]. In the barrier case, the structure factor appears to be strongly self-similar already for times around 10 min, similar to what we observed for the nucleation process (Figure 3.2b). This feature is kept throughout the coarsening until the confluent second layer is formed (Figure 3.2b inset). For kanamycin, the islands form a very well defined pattern indicated by the fact that the structure factor is tight around a clear peak (Figure 3.3c). The rescaling shows a good degree of self-similarity in the process (Figure 3.3c inset), which can be concluded from the narrower gaussians in the fit and for the shorter average gaussian width (σ_y) with respect to the barrier and blank cases (Figure 3.3c and d). The average width of the structure factor tends to go down with time indicating that the islands form a consistent pattern for later nucleation times. As mentioned before, this order fades away when the islands merge, making the peaks to flatten and σ_y to slowly rise for the last 10 min of the timelapse in the blank and barrier cases.

From the gaussian fits we extract the characteristic wavelengths (λ_y) for the three processes, corresponding to the wavenumber at the peak of the structure factors. For a true spinodal decomposition, these are predicted to increase with time as a power law [149, 150]. This, however, is not borne out of our measurements. In both the blank and the barrier cases, the characteristic wavelength appears to decrease, at least initially, with a weak power law (-0.551(0.045) for the blank; -0.53(0.13) for the barrier case; -0.652(0.048) for kan. See Figure 3.3e and f). This initial reduction of the characteristic length scale has been predicted by the 'domain insertion model' as a consequence of the non-conservation in the number of units within the system [152]. During a phase transition with increasing number of particles, if the nucleation of newer domains is faster than the phase separation process, the new domains created in the inter-cluster regions lead to smaller inter-domain distances [152]. Indeed, as discussed in Sec. 3.2.2, the rate of nucleation of new islands increases initially in all three cases (Figure 3.2), and we see now that the increase in newly

nucleated islands shortens the characteristic wavelength of the system. However, a change in trend can be observed in the latter part of the timelapse especially for the kan case, which is characterized by a lower nucleation rate for new islands. The wavelengths start to fluctuate or even increase, indicating that nucleation stops and islands start merging with each other until they cover the field of view. As expected, this change in trend is clearest in the kanamycin case (Figure 3.3g). Again, the characteristic wavelength decays in the first part of the nucleation (exponent -0.652(0.048); Figure 3.3g), but the trend then inverts and the wavelength starts growing (exponent 0.320(0.034)). This change suggests that at the beginning, when the surface coverage is sufficiently low, it is the nucleation of new islands that determines the characteristic wavelength. At later times, however, the growth of previously nucleated islands becomes the dominant feature in the evolution of the characteristic wavelength. We note that, despite the differences in the characteristic wavelength dynamics for the blank, barrier and kanamycin cases, the average wavelength of the system is nearly the same (Figure 3.3h). However, the distribution of average wavelengths is significantly narrower in the kanamycin case compared to the blank one, with the barrier distribution intermediate between the two (Figure 3.3h).

The results coming from the Fourier analysis suggest that the phase transition dynamics follows the 'domain insertion model' for the blank and the barrier cases. In the kanamycin case, there is a turning point that indicates the end of the period dominated by nucleation and the start of the period dominated by a prolonged growth of the islands. To better determine the differences in the properties of the islands during the phase separation, we will now characterize the evolution of the swarm during the nucleation process and how the islands change in size and shape over time.

3.2.4 The phase transition resembles cluster formation characteristic of motility-induced phase separation

As we observed in Figure 3.1, the islands sizes and shapes are very different in the barrier and blank cases compared to the kanamycin. Despite these differences, since swarming bacteria is a system of active particles, we wondered whether the growth of the islands in time could still follow a power law, which is prescribed for domain growth in a phase-separating gas-liquid system and suggested by the Cahn-Hilliard models [75, 148].

We therefore measured the evolution of the islands' size distribution over time for the three cases (Figure 3.4a). The initial average size for kanamycin (0.0247(0.0034) mm^2) is clearly different to either the blank (0.0031(0.0060) mm^2) or barrier case (0.0020 mm^2). To quantitatively describe the changes in size, we fitted the size evolution to a sum of a

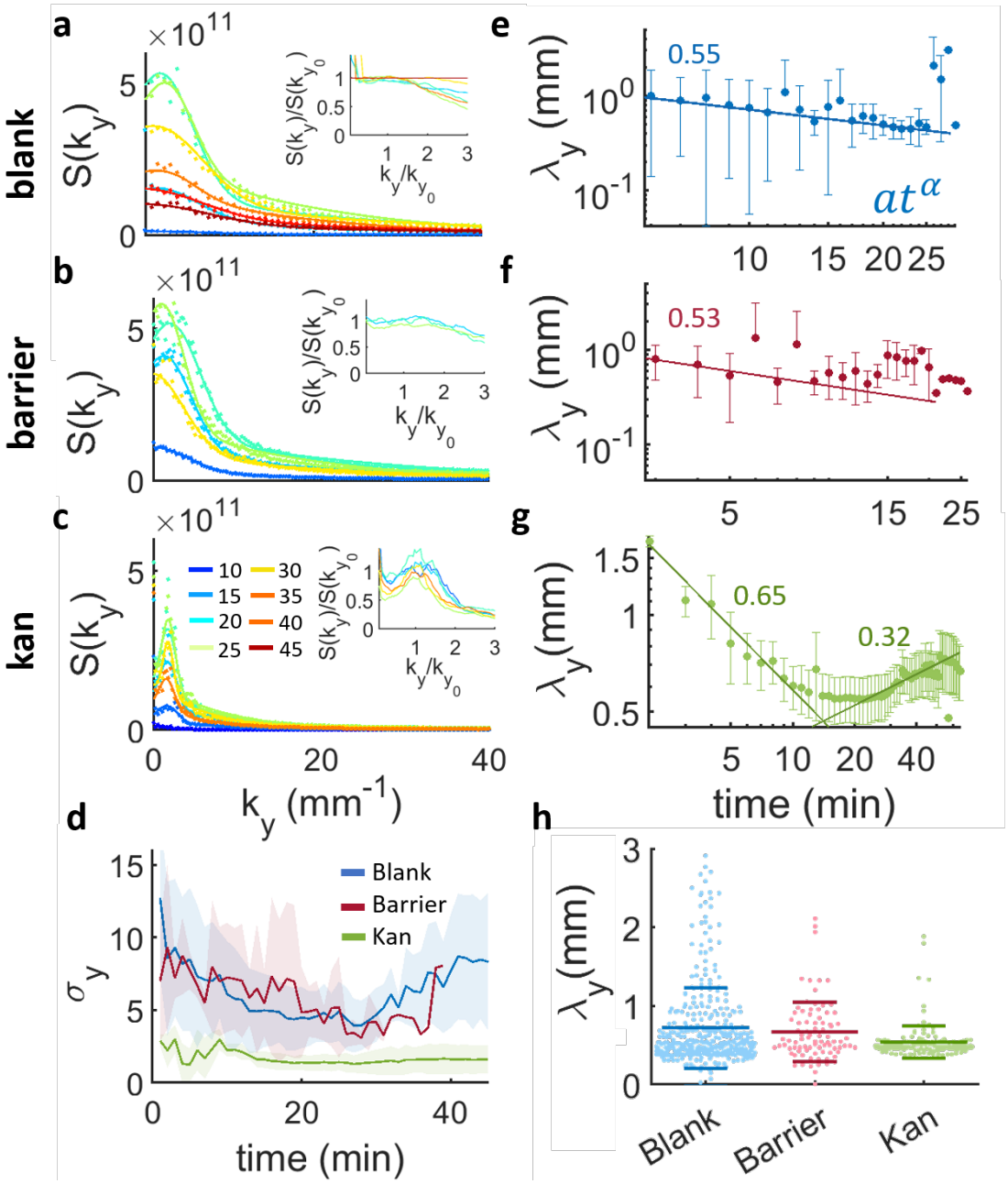

Figure 3.3: **Structure factors and evolution of the characteristic wavelengths during island formation for the blank, barrier and kanamycin.** a),b) and c) show the y component of the structure factors during island formation. The lines are fits to a sum of two gaussians from one of which the characteristic wavenumber of the peak is obtained. The colorcode represents the time in minutes, indicated in the legend of panel c). The insets represent the structure factors rescaled by their peak plotted against the wavenumber rescaled by the wavenumber at the peak. For clarity, we just plotted a single experiment. d) Mean width of the gaussian (σ) and standard deviation (shaded region) for the structure factors in the blank, barrier and kanamycin cases. e), f) and g) display the characteristic wavelengths λ_y calculated as the inverse of the peak's wavenumbers over time. The points represent the mean of 20 and 5 samples for blank, barrier and kan respectively, and the bars the standard deviation of the mean. The continuous lines are fits to power laws whose exponents are written on the figure. h) Distribution of all the calculated wavelengths obtained from the gaussian fits. The long horizontal lines indicate the mean of the distribution and the short lines their standard deviation

power law and an exponential of the form:

$$< s >= At^d + Ce^{rt} \tag{3.2}$$

In the kanamycin case, the initial increase of the average island size is indeed well described by a simple power law $< s > \propto t^d$, with a power d=0.664(0.024) which is surprisingly close to the value of 0.67 reported for the equivalent phase for the Janus particles in [83]. This stage represents the growth of individual islands, and it appears to follow a dynamic similar to what has been reported for clustering of active colloidal particles. In case of Janus particles, the next phase is characterized by a slowing down of the coarsening when most particles have aggregated (regime II in fig. 2a in [83]). In our case, this slow down does not happen. On the contrary, we observe a rapid acceleration, with $< s >$ increasing exponentially in time (rate r=0.249(0.018) min^{-1}). We attribute this to the continuous increase in the number of bacteria which is ultimately leading to the complete coverage of the field of view by the multilayer. New bacteria must come from a combination of replication and flow from other regions of the swarm. In the blank case, we do not observe a significant increase in the average island size until 5 min after the first island appears. As we have seen, during this period new islands continuously appear and disappear, with no significant coarsening. Indeed, the blank case could not be fitted to Equation 3.2 but just to an exponential. As time progresses, islands' nucleation increases exponentially, the average separation between islands decreases rapidly until they start to merge, resulting in a sudden increase in the average islands size (rate r=0.348(0.015) min^{-1}). Finally, in the barrier case, the average island size also displays a two-stages evolution. The latter is an exponential increase with r=0.390(0.014)min^{-1} similar to the blank case and 1.5 times higher than for the kanamycin case. The initial stage, instead, appears to be intermediate between the clear coarsening dynamics of the kanamycin case and the nucleation-dominated constant $< s >$ of the blank case. The power law fit returns an exponent d=0.205(0.094) which is only about a third than in the kanamycin case. Including a constant term in the fit returns a significantly higher exponent, 0.5, but with a large potential error (0.5). Unfortunately, lack of a specific model of the single-to-multilayer transition means that it is currently unclear what one should be expecting at all for the evolution of the average island size in any of these three cases.

The average evolution in cluster sizes suggests that the formation of the islands could follow a phase separation dictated by MIPS but with some quantifiable differences due to the increase in cell number over time, either caused by cell replication (in the three

studied cases) or by the arrest of the swarming front (in the barrier and kanamycin cases). The drawback of studying the instantaneous average island magnitude is that we are considering old long islands that have already grown, together with the small ones that just nucleated. This potentially confounds islands' nucleation with growth. To overcome the limits of studying the spatial average of the islands sizes, we have calculated the size distribution of the individual islands, ρ(s,t), and from that, the complementary cumulative distribution function (ccdf) as:

$$C_\rho(s,t) = \int_s^\infty \rho(u,t)\, du \tag{3.3}$$

This is plotted in Figure 3.4b for successive times, indicated by the color scheme, from dark blue, when the islands first appear, up to red 50 min later. We can immediately see that the kanamycin case lacks islands of sizes smaller than 0.01 mm^2, dominant even for late times in the other two cases. The small-size end of the distribution (indicated with a gray line in Figure 3.4b) is expected to follow a power law phase, as predicted by the Callan-Hilliard model [75, 148], and has been reported for Monte Carlo models of self-propelled hard disks [153], experimental studies of active Janus colloids [83], gliding *M. xanthus* [84] and swarming *B. subtilis* monolayer clusters [64]. If this is the case for small sizes we will have:

$$\rho(s,t) = s^{-a} => C_\rho \propto s^{-a+1} \equiv s^\alpha \tag{3.4}$$

Fitting the first ∼5 points in Figure 3.4b, we can obtain α and therefore a whose typical values in cluster formation through MIPS are $a \in$ [1.7,2] [84, 153, 154, 155]. We note that this value of a is obtained for cluster formation of systems where the amount of particles is assumed to be constant and in a 2D layer. As the distribution of the calculated exponent α is quite broad (Figure 7.9), we calculated the average minimum value and the average maximum values across all the samples and their standard deviation (see subsection 6.4.3 and Table 7.2). For simplicity, here we report only the mean value of the time averages calculated for each experiment. For the blank case, the mean α across all the experiments is -0.264(0.083) which would give a=1.264, matching the one reported for MIPS in Janus particles (1.25) [83]. The barrier and kanamycin give a=1.076 and 1.0389 respectively, with values even lower than in the blank case and more similar to the 0.95(0.05), reported for cluster formation in gliding bacteria [156, 134]. In the ccdfs, we can see that for times larger than 10 min, or equally, for high cell densities, there is a tail on the far end of the size range, due to large islands that appear as a consequence of the increase in cell number.

A similar tail in the distribution ρ (Figure 7.10a) has been reported also in gliding *M. xanthus* and interpreted there as the emergence of collective motion, since the tail was absent for immotile bacteria [84].

Below a critical density, according to the theory developed for systems of self-propelled particles with nematic alignment, the probability distribution function of island sizes is actually predicted to follow [156, 134]:

$$\rho(s,t) = Cs^a e^{s/s_0} \tag{3.5}$$

We fitted these distributions to Equation 3.5 from the maximum value of the distributions to their end (Table 7.3). However, we found the distributions lack the power law phase, since normally the exponents obtained from the fits are extremely low (Figure 7.10b), suggesting that only an exponential decay would be enough to fit the distributions. A possible reason to see a power law for small s in the ccdf but not in $\rho(s,t)$ might be that the specific shape of ρ depends on the binning (see subsection 6.4.3) and that the distribution is more noisy than the ccdf. In Equation 3.5, the parameter s_0 represents an intrinsic size scale for the islands, which marks the transition from the power law to the exponential behaviour. This parameter was reported to increase with cell density or, equivalently here, with time, for monolayered clusters [64]. To determine whether this is the case during island formation, we calculated the evolution of s_0 over time (Figure 7.10c). For the blank case, this seems to be the case although it is not possible to determine the general trend for the other two cases due to the high dispersion in the mean value along time. We highlight that the time average of s_0=0.145(0.069) mm^2 for kanamycin is higher than for the blank and barrier: s_0=0.037(0.020) and s_0=0.0215(0.0021) mm^2, respectively (Figure 7.10c), as we would expect given the higher average sizes for island formation in the kanamycin case.

Beyond the nucleation and coarsening, merging of different islands is the final main aspect of their dynamics. In order to characterize islands' merging, we looked at the cluster size distributions, defined as:

$$c_s(t) = n_s(t)/N(t); \tag{3.6}$$

where n_s(t) is the number of islands with size s and N is the total number of islands in the field of view at a given time. This definition differs from the traditional definition of cluster size distribution, where n_s is commonly normalized by the total number of particles, which is a fixed parameter in the system and therefore follows $c_s \propto t^{-2}$ (equation 5.13 in [157]).

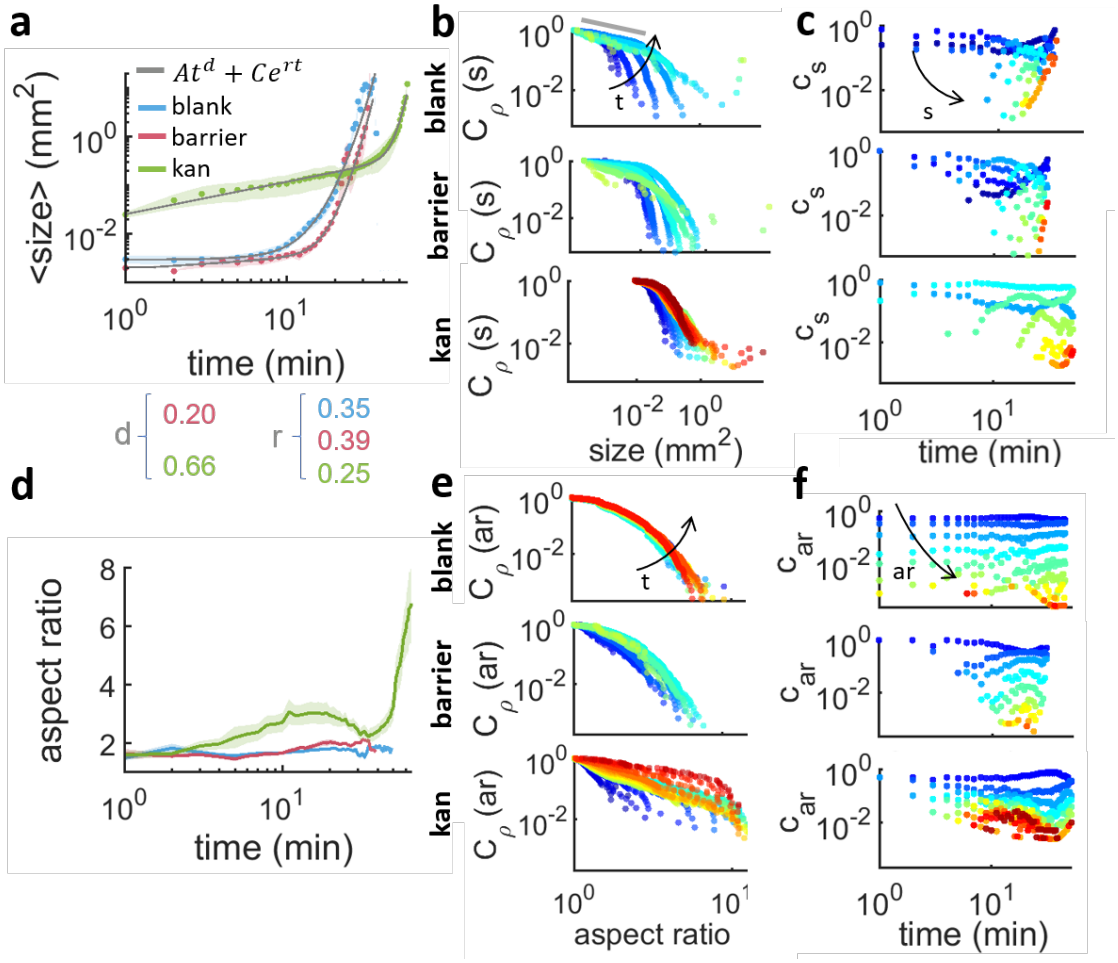

Figure 3.4: **Characterization of the size and shape of island formation at the swarming front in absence of stress, in presence of physical barrier and in presence of kanamycin.** a) Average size of the islands tracked along time within an area of: 5.31x5.31 mm^2 for blank (in blue), 7x14.47 mm^2 for barrier (in red) and 8.8x14.97 mm^2 for kanamycin (in green). The curves are the average of 20 samples for blank and 5 for barrier and kanamycin. The gray lines are the result of fitting to Equation 3.2. b) Complementary cumulative distribution of the islands size, C_ρ(s,t), for increasing times t $\in$ [0, 50] min every 3 min (from blue to red) c) Cluster size histogram c_s(t) as a function of time, for increasing size s $\in$ [10^{-4}, 10^3] mm^2 grouped in 13 bins logarithmically distributed (from blue to red). d) Average aspect ratio (ar) of the islands at the swarming front for the three cases studied. e) Cumulative distribution of the islands aspect ratio C_ρ(ar), for increasing times t $\in$ [0, 50] min every 3 min (from blue to red). f) Cluster size histogram c_{ar}(t) as a function of time, for increasing ar $\in$ [0 10] grouped in 24 bins linearly distributed(from blue to red).

This is not our case since the number of particles increases over time and they cannot be counted within an island. In blank and barrier, we observe that just very small islands are present for times shorter than ~8 min, and then bigger islands start to emerge due to the coarsening of the small ones giving place to a scenario where new small islands keep nucleating and the old ones grow and merge. This is more pronounced for kanamycin since the nucleated islands are bigger in size and they quickly grow: after 3 min in the kanamycin case we have sizes that will not appear in the other two cases until times larger than 10 min. There is as well a difference in the predominant sizes during the timelapse. In

the kanamycin case, the smallest islands, corresponding to the nucleating islands, are not the most abundant size throughout the timelapse since the islands that nucleate quickly start growing. This contrasts the other two cases where the nucleated islands sizes are quite abundant even for late stages in the timelapse.

So far, we have just described the evolution in size of the islands with time but one of the major differences between the kanamycin and the other two cases is how they evolve in shape (Figure 3.4d). To characterize this, we have calculated the aspect ratio of the islands (subsection 6.4.1) and we observed that this magnitude remains constant around a value of 1.5 for the blank and the barrier, whereas the aspect ratio for kanamycin starts around 1.3 to then reach 2.5 in the first 20 min. The islands that emerge in presence of kanamycin become elongated along the direction going from the inoculation point to the kanamycin disk. This elongation towards the kanamycin is a contribution of two factors: the growth of the islands along the x direction and the fact that they start merging exclusively in this direction Video 10. Once the number of islands is sufficiently high, they start merging across the perpendicular direction, resulting in a decrease in aspect ratio down to 1.8 for times around 40 min. Finally, the vertical merging creates a new large rectangular second layer of bacteria separated from the rest of the swarm that results in the final increase in aspect ratio. In summary, after their emergence, islands in the kan case become elongated in the horizontal direction and once there are enough nucleated islands they start merging in the vertical direction, resulting in an oscillation in the aspect ratio. The ccdfs show that distribution of aspect ratios is roughly independent of time for both the blank and barrier cases but very large aspect ratios $\sim$8 are already present in the first 15 mins of the timelapse for kanamycin (Figure 3.4e). This can also be observed in the cluster aspect ratio distributions, where kanamycin has a high density of the highest aspect ratios for times even lower than 10 mins. In the blank case, islands do not have a well defined shape so some spurious high aspect ratios appear at early times to then disappear, as the islands are not stable.

Although useful to compare to the existing models and experiments of cluster formation, the previous characterization has some limitations. The main one is that the evolution in size and aspect ratio is an average of the islands that nucleated in a wide range of times so it does not represent the evolution of the clusters themselves but of the system as a whole. To overcome this limitation, we tracked the individual islands over time for the blank and kanamycin cases (Figure 3.5). Unfortunately, this was not possible for the barrier case due to the poor image quality. In the blank case, we tracked the islands in 5 different samples and then aligned the trajectories in time so they match at the point

of variance 0 (see subsection 6.4.2). Once aligned, the average of all trajectories for the 5 samples was calculated and their weighted average was plotted against time as shown in Figure 3.5a. The average size evolution is characterized by a continuous fluctuation in size, even more pronounced in the individual tracks since the average smooths these fluctuations. Such fluctuations are due to the lack of growth in the individual islands when nucleating since they undergo random changes in size until they merge with others (Video 11). The islands size evolution follows a power law with exponent 0.518(0.039) that then gives place to a sudden rise in islands size. As we described in Figure 3.4a, this sudden increase comes from the merging of all the islands forming a new layer. In the kanamycin case, the three samples are plotted separately so each line corresponds to the shifted average of all the trajectories in a single experiment. The size evolution starts with a short lag phase where islands grow slowly to then enter the power law phase that in average has an exponent of 1.7 for two of the curves. The outlier has two power law phases of growth with slopes 0.9 and 2.7 that in average is 1.8, similar to the slope reported for the other two experiments (for a detailed list of the fits, consult Table 7.4). In the tracks for the aspect ratios, we see that when the islands nucleate, they spend approximately 10 min with the original shape and then they become increasingly elongated towards the kanamycin disk (Figure 3.5). The main difference with the aspect ratio in Figure 3.4d is that the drop is not observed here since now we are not accounting for the merging of the islands in the vertical direction. In the blank case (not included) the shape evolution of individual islands is similar to the ensemble average in Figure 3.4d.

We have shown that swarming *B. subtilis* transits into a second layer following a dynamics that bears resemblance to MIPS. The transition is different in absence and presence of antibiotics, following a dynamics that resembles spinodal-decomposition or nucleation-and-growth respectively. The main differences between these two modes come from the distinct nuclei that form in each case. To try to elucidate more precisely the differences between these two types of islands, we will study their fast- short-term dynamics.

3.2.5 Fast time dynamics during island stabilization

We started by studying the islands for time scales of seconds just when they appeared in the field of view. To do so, we recorded timelapses of the islands in the blank case and kanamycin every 0.5 s. For the former, islands appeared and dissapeared as described above but in this fast time lapse we could observe that islands have preferred sites to appear in the field of view (Video 11). To show this, we calculated the image average of a 2 min timelapse and the standard deviation of the pixel intensity (Figure 3.6a). If the islands

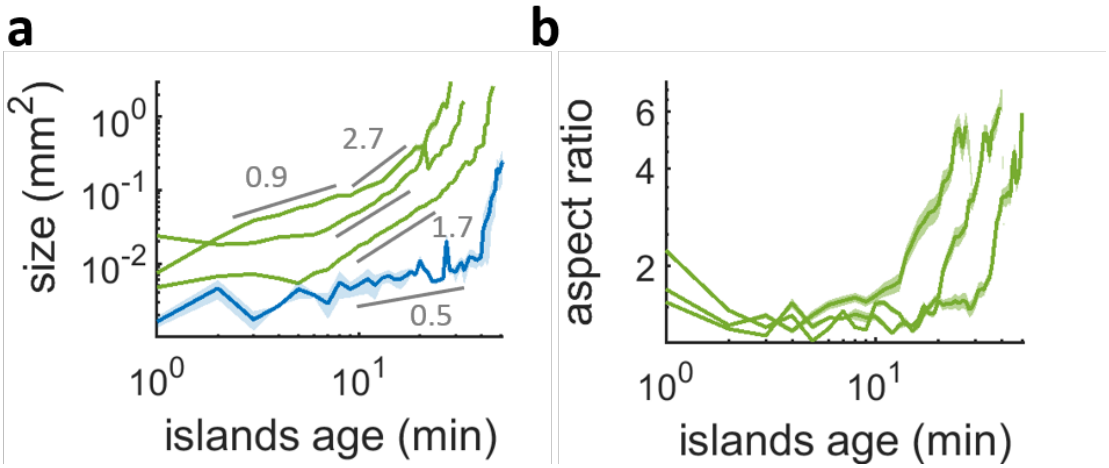

Figure 3.5: **Size and aspect ratio obtained by tracking the individual islands along time.** a) Average size evolution of the individual tracks along time for the blank (in blue) and the kanamycin (in green). The blue curve is the average of 5 different samples and the shaded region is the standard error of the mean. The green curves are the average of the individual tracks. The values in gray represent the exponent of power laws fitted to the range of data given by the gray lines. b) Average aspect ratio evolution from the individual tracks for the three samples with kanamycin.

appeared uniformily in the field of view throughout the timelapse, we would expect the average pixel intensity of the projection to be nearly homogeneous in the ROI. However, we obtained small regions where pixel intensity is low compared to the surroundings, indicating that the islands are mainly present in specific sites. This was further confirmed by the standard deviation of the pixel intensity (red shades in Figure 3.6a). The regions near the islands showed a higher standard deviation confirming that the islands appear and disappearing near those regions but less often in other parts of the ROI.

To confirm that the average projection shows the preferred sites where islands appeared and not islands that lasted for the 2 min of the timelapse, we calculated the lifetime of the islands and we observed that the maximum lifetime was 40 s and their average lifetime 3.82(0.14) s (Figure 3.6b), much shorter than the 2 min that the entire timelapse lasted. Altogether, this indicates that the dark regions in the average projection resembled islands that repeatedly appeared in the same regions instead of static islands that just remained there. Once again, this also points out the instability of the island formation in the blank case.

This is remarkably different to what happens in presence of kan. In this case, once the island nucleates, it remains there for the whole timelapse and disappearance events are very rarely observed (Video 12). The nucleated islands show instead big fluctuations in the boundaries. To try to capture the dynamics of these fluctuations and find common features to all the islands, we used Fourier series expansion as a convenient method to

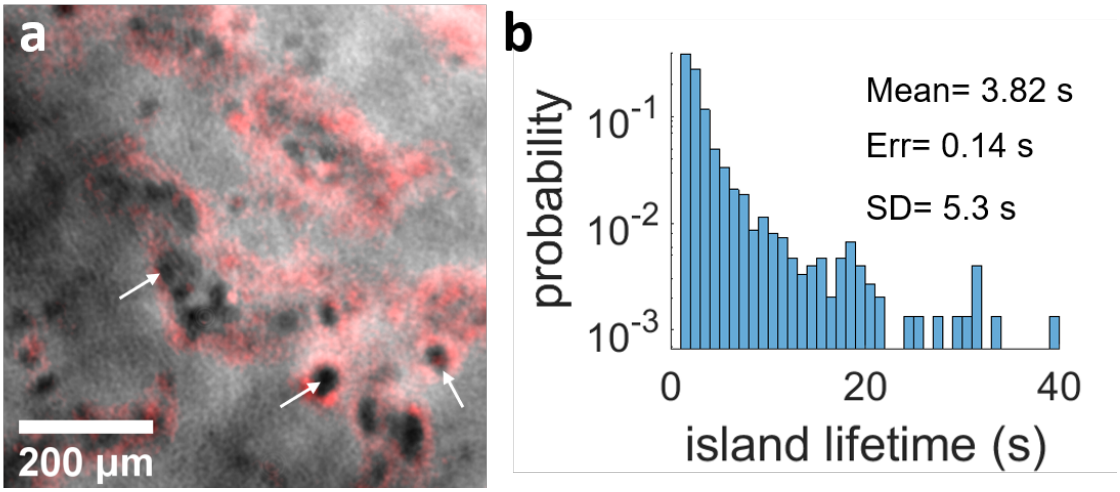

Figure 3.6: **Short time-scale characterization of islands appearance in absence of kanamycin.** a) Image average and standard deviation (in red) of a 2 min timelapse showing that islands have preferred sites to appear. The white arrows show some examples of the islands in the field of view. b) Histogram of the islands lifetime. The lifetime was measured as the time interval from island appearance until disappearance during a 2 min timelapse of images taken every 0.5 s. The bin width of the histogram in 1 s.

parametrize the boundaries (see Equation 1.9 and Figure 3.7a). The Fourier expansion works as an approximation to the real shape of the boundary of the island that can be described more accurately with an increasing number of terms (harmonics) in the Fourier series [85, 90]. To calculate how many harmonics would be convenient to describe the variation in shape of the islands boundaries over time, we calculated the root mean square error (RMSE) for an increasing number of harmonics subsection 6.4.7. The result showed that the error committed by the Fourier expansion with increasing number of harmonics decays nearly exponentially (Figure 3.7b). The standard deviation in time of the RMSE for the different harmonics showed large variation for small harmonic number n, indicating the stochasticity of how well the shape is described by this method. We also observed that after the 5^{th} harmonic, neither the RMSE nor its standard deviation are reduced significantly. These low frequencies represent the coarse structure of an object, while higher frequencies add the details [86], so with these description we are hoping to describe quantitatively the common features of the islands. With this aim, we will use just the first 5 harmonics of the Fourier series.

How important a specific Fourier term is at describing the shape of the boundary is given by the amplitudes accompanying the sin and cos in the Fourier series, noted here as: a_n, b_n, c_n and d_n, being n the harmonic number (or number of terms in the Fourier series expansion), and a_0 and c_0 the fundamental frequencies for the x and y components of the boundary, respectively. By definition, b_0 and d_0 are always 0. The temporal mean of these Fourier coefficients was calculated for each of the harmonics and plotted for 8 different

islands. As explained by the theory, the zero Fourier coefficient (n=0) contains the origin of a shape [86]. Variations in that coefficient just indicates spatial translations of the islands. The n=0,1 components are the ones that contribute the most to the Fourier description of the shape boundary. This is because the n=1 corresponds to a constant elliptical shape, and fluctuations in the boundary would not affect this very coarse description. Thus, this mode acts as a base for the higher modes to build on and create the boundary specifics needed to create the characteristic shape of the islands. A zoomed in of the higher modes can be seen in the insets of Figure 3.7c, d, e and f. Although we cannot extrapolate any direct conclusions from the Fourier coefficients, the Fourier harmonics give a quantitative description that can be used by numerical models to predict and find out the intrinsic mechanism behind the shape fluctuations.

Studying the time average of the Fourier coefficients provides a description of the predominant amplitudes needed to describe the islands boundary. However, we lose some information since there could be some periodicity in time when some of the Fourier harmonics become more or less relevant. To see whether this is the case, we calculated the power spectrum of every Fourier coefficient for every harmonic for 8 different islands and checked whether there are any frequencies that are dominant (Figure 3.8a). The mean and the standard deviation (sd) in time of the power spectrum were calculated and the frequencies at the values larger than mean+sd were selected. This process was repeated for every Fourier coefficient (a, b, c and d), for every harmonic number n and for every studied island. The selected frequencies were then plotted in histograms where the probability of each frequency for each coefficient and harmonic number were plotted (Figure 3.8b). Finally, we created a heatmap with the dominant frequencies for each Fourier coefficient and we colorcoded the probability of the dominant frequencies for each of them (Figure 3.8c). The heatmap shows that a_0, b_1, c_0 and c_1 are dominant for the shortest frequencies (0-0.1 Hz). Larger frequencies do not seem dominant for any coefficient. This indicates that changes in the islands boundaries do not have a certain periodicity at least for long or medium timescales.

The fast-timescale study of the islands highlighted some of the differences between the blank and kan cases that we already knew from the previous quantification and gave some additional information about their nature. In the blank case, the islands intermittently appear and disappear with a characteristic lifetime in preferred sites within the studied ROI. This could point to a hidden factor that promotes their appearance as for example defects on the agar or immotile cell clusters. In turn, the islands formed in presence of kan are completely stable, once they nucleate their boundaries fluctuate but they do not

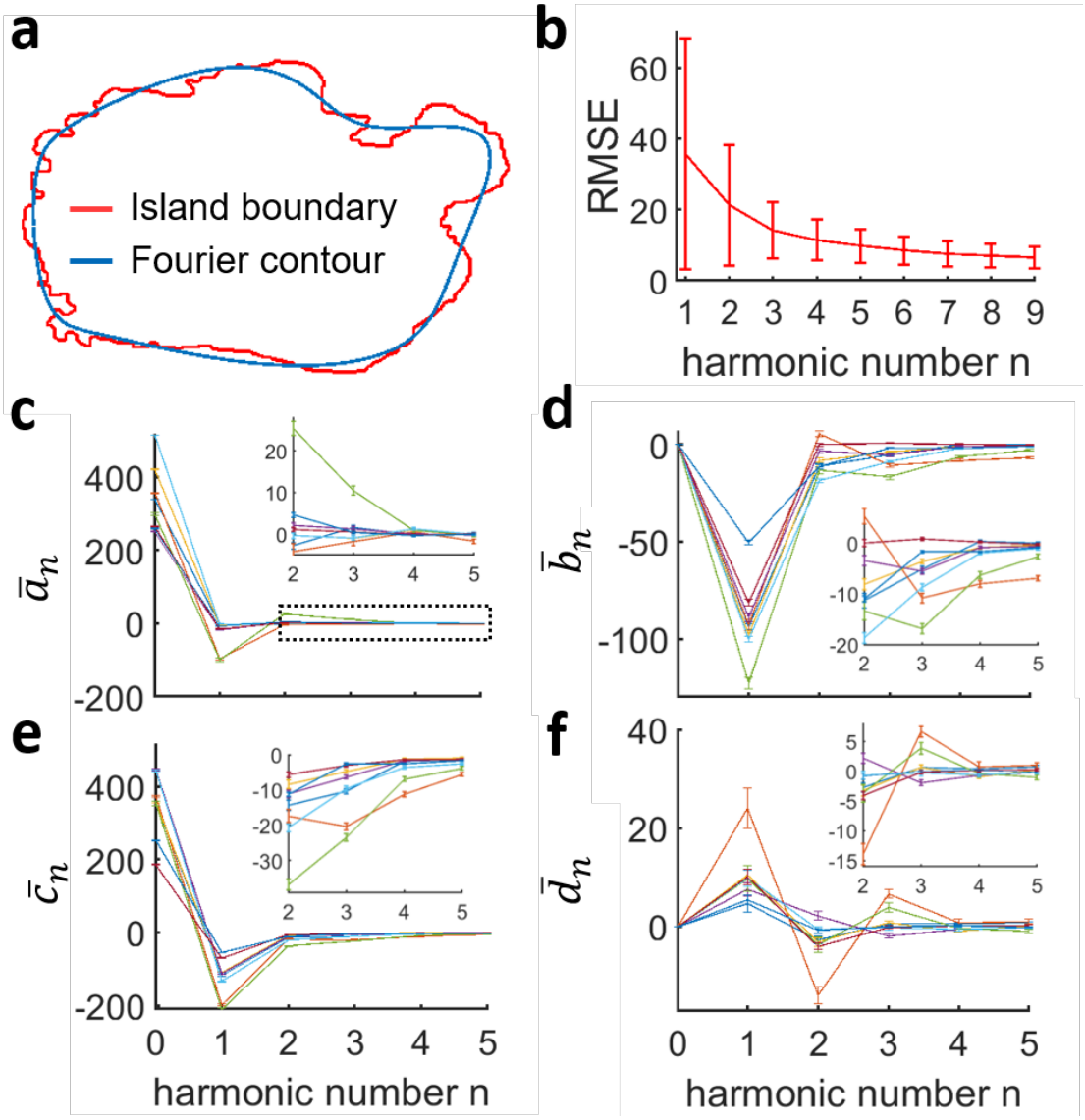

Figure 3.7: **Fourier description of islands boundaries in presence of kanamycin.** a) Detected boundary of the island (red) and Fourier contour approximation taking 5 harmonics of Fourier series. b) Root mean square error (RMSE) when comparing the actual island boundary and the approximated boundary calculated with and increasing number of Fourier series. The error bars indicate the standard deviation of the mean in the timelapse. c, d, e, f) Temporal mean of the a_n, b_n, c_n and d_n coefficients of the Fourier series for an increasing harmonic number. The insets correspond to a zoomed in region of the main graphs for harmonics ranging from 2 to 5, as indicated by the dotted rectangle. The different colours represent 8 different islands.

disappear. A characterization of this fluctuations was given by parametrizing the boundaries using Fourier series. This characterization has demonstrated to give a quantitative metric that could be used by numerical models to predict islands shape. From this metric we could not obtain a clear mechanism of what makes the specific shape of the islands or any periodicity on time. It stands to reason that the origin of the difference in island formation should be found in differences in the microscopic behaviour of the cells in the cases studied. We therefore now turn to the characterisation of critical microscopic aspects

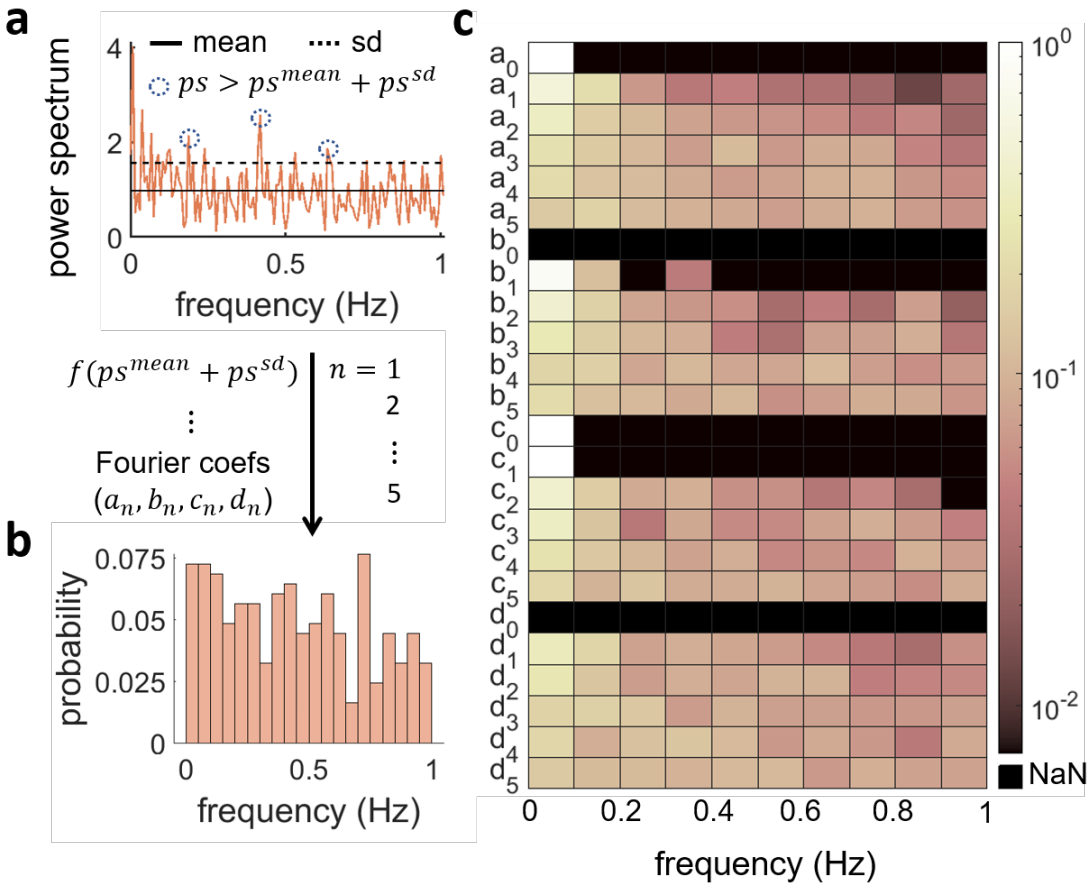

Figure 3.8: **Dominant frequencies for the Fourier coefficients at the different harmonic numbers.** a) Power spectrum of a Fourier coefficient at a specific harmonic number n. The continuous line shows the temporal mean and the dotted line the standard deviation. From this spectrum, those frequencies corresponding to values of the spectrum that are greater than the mean+sd were selected. b) A histogram of the frequencies selected from a) was calculated to identify whether there were predominant frequencies. The y axis is the probability of each bin and the bin width is 0.1 Hz. c) Heatmap of all the Fourier coefficients for all the harmonics for each of the frequencies studied. The probability of each frequency is colorcoded as indicated by the colorbar on the right.

of the cell monolayer during the different types of island formation.

3.2.6 Monolayer characterization during island formation

In the search for the origin of the differences observed between the kanamycin, blank and barrier cases, here we characterize the case-specific behaviour of the swarming monolayer, as the differences might reflect a fundamentally distinct behaviour at the microscale. To this end, we followed cell speed and surface coverage of the monolayer in a region between 0.7 cm and 2.7 cm from the kanamycin disk, for a time interval of 1 h until the emergence of the first islands, chosen as the origin of time (0 min) (Figure 3.9a). This region was selected in such a way that the points nearest to the disk correspond to the monolayer that gives place to the nucleation and growth of the front in presence of kanamycin and the

farthest point belongs to the monolayer which gives rise to the spinodal-like decomposition. At the earliest timepoint, the swarm was still expanding and was still at a distance of 1.7 cm from the disk. 30 min later, the velocity decreased in the interior of the swarm in agreement with [44], that characterized the swarming velocity in different regions of swarming *B. subtilis* and reported that the highest velocities are in a region near the advancing front. 15 min before the first island formation was observed, the front reached a position 0.7 cm away from the kanamycin disk. At this point, the speed of the front had decreased to approximately a third of the one measured between 60 min and 30 min before island formation. This reduction in speed is accompanied by an increase of the surface coverage of the monolayer from 0.583(0.001) to 0.666(0.001). It is well known that an increase in cell density usually leads to an increase in cell speed due to the formation of cell rafts well characterized in collective motion [64, 56]. The fact that here we observe a decrease in average speed despite the increase in concentration, suggests that kanamycin slows down the cells at the swarming front, in line with previous reports [47]. By the time the islands appear (0 min), the front is completely immotile and densely packed (surface coverage 0.791(0.004)). A similar effect of kanamycin exposure can be observed even at 1.7 cm from the disk, where we estimate the kanamycin concentration to be below the MIC (Figure 2.2b). Here, in the last 15 min, bacteria reduce their speed from 15.91(0.11) to 5.57(0.08) μm/s while increasing the local surface coverage from 0.697(0.001) to 0.789(0.004). In contrast, at a distance of 2.7 cm from the disk, an increase in surface coverage from 0.567(0.001) to 0.640(0.001) in the last 15 min is accompanied by a slight increase in speed from 13.92(0.10) to 18.92(0.14) μm/s. We see therefore that the regions closer and farther from the kanamycin disk enter the island-formation phase through two distinct routes: a higher-density/low motility route for the former; a lower-density/high-motility route the latter. Two different routes to buckling of a cell monolayer have been recently reported in *Pseudomonas aeruginosa*. In this system, buckling can happen either through an elastic instability (Euler-buckling) purely by an increase in cell density in absence of motility, or through rate-dependent out of plane transitions when active motion exists [105]. In the present case, however, motility in the high-density kanamycin case is still playing a fundamental role in the transition from mono- to multi-layer, as can be seen by the fact that this transition happens in a region close to but not corresponding with the immotile band closer to the kanamycin disk (Video 5).

To see if this is compatible with the MIPS picture, we characterized the swarming states through their rotational Peclet number (see Equation 6.3) and followed their dependence in time until the islands were first seen in the field of view. This was repeated for the

three cases of blank, barrier and kanamycin (Figure 3.9b). These two parameters are strongly dependent on where the data is acquired within the swarm which complicates the interpretation of the results. For example, to avoid the effect of a physical barrier that could be induced by the boundaries of the petri dish itself, we acquired the data in the blank case very close to the centre. This region is known to include clusters of immotile cells and low motility rafts [44], making the average speed in the field of view very low. This complicates the characterization of the state of the swarm when islands first appear. Despite these issues, the trajectories show that in both the blank and barrier cases what changes in the process of island creation is mostly the concentration of the monolayer, with only a minimal variation in motility with respect to the initial values. Figure 3.9c shows the phase-space parameters of the monolayer coexisting with the stable second layer. It is interesting to notice that, in the barrier case, the monolayer coexisting with the islands has a distinctly higher speed with respect to the other two cases (see also Figure 7.11a). This might be either because the barrier forces the cells to accumulate at a premature state, which potentially might be different to when they naturally accumulate, or because the meniscus formed by the barrier creates a channel that allows the cells to move faster [158]. As we mentioned in Figure 3.9a, the blank case seems to enter in the second layer with a lower surface coverage than in the kanamycin case. This indicates that the reduced speed due to kanamycin exposure, which would hinder the emergence of multilayer islands, is compensated by the increase in cell concentration due to the arrest of front propagation.

We therefore can conclude that bacteria can use two different methods to form a new layer: forming a state more dominated by interparticle extrusion due to high cell densities (kan case) resembling what happened in [105] versus a more diluted and motility-induced mechanism (blank).

The differences in the monolayer dynamics while coexisting with the second layer may not come only from the magnitude of velocities but also from higher moments of the velocity such as the skewness and the kurtosis. For example, continuum models of MIPS predict that the kurtosis of the distribution of velocities increases in a dense phase as opposed to a lower kurtosis in the diluted phase during spinodal decomposition [98]. This difference between diluted and dense phases is attributed to bacteria clustering in their numerical model. Therefore, we wondered whether we could see a similar effect in our system and we characterized the skewness and kurtosis of the x component and the modulus of the velocities for the monolayer when coexisting with the second layer (Figure 3.10 and Figure 7.11). The skewness, which is commonly used to quantify the

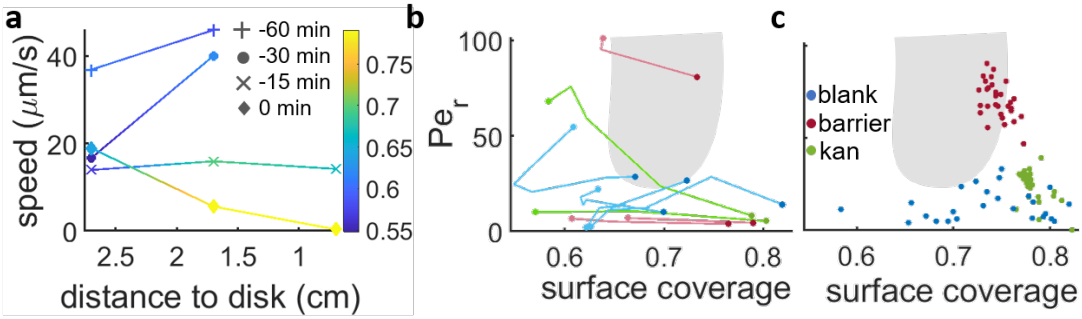

Figure 3.9: **Speed and surface coverage characterization during multilayer formation.** a) Cell speed at 0.7, 1.7 and 2.7 cm away from the kanamycin disk for a time interval of 1 h before the initial formation of the islands (0 min corresponds to island formation). For reference, in our kanamycin experiments the islands form within a band that goes from ∼1.7 cm from the disk to just before the region where cells are immotile. The colorscale shows the surface coverage. b) Phase diagram showing the Peclet number vs the surface coverage of the system. The lines show the trajectories that the swarm follows in the phase space to form the islands. c) Monolayer Peclet number and surface coverage while coexisting with the multilayer. The gray area shows the region where MIPS occur according to the numerical simulations for disks in [1]

.

asymmetry of a distribution, is <0 for the x component of the velocity v_x in the blank case Figure 3.10a. A possible reason is that the data for the blank case was taken in a petri with kanamycin but where the disk was at a distance of 5 cm away from it, so the cells in this position still tended to travel outwards (the direction of the swarming front). The kurtosis of the velocity component (Figure 3.10b) is much higher than 3, the value expected for a monolayer swarm in absence of stress [47]. Remarkably, the value of kurtosis spikes for the blank case, in agreement with the description of anomalous statistics in continuum models of MIPS for spinodal decomposition [98]. The kurtosis in the kanamycin case is also double the one expected for a monolayered swarm in absence of stress but still in agreement with the anomalous kurtosis reported for monolayered swarms of *B. subtilis* in presence of sub-lethal concentrations of kanamycin [47]. In the barrier case, the kurtosis seems quite similar to the monolayered swarm, demonstrating that the monolayer does not change significantly while coexisting with the islands. The moments for the modulus of the velocity follow a similar pattern (Figure 7.11b and c).

To further analyze the differences in the monolayer when coexisting with the second layer, we calculated the time autocorrelation function (Equation 1.3), the directional correlation (Equation 1.6) and the radial correlation (Equation 1.5). To calculate the characteristic magnitudes from the correlation functions, we fitted the functions to an exponential decay and then we calculated the autocorrelation time τ, the directional time Θ and the radial correlation length ρ as the inverse of the exponent in the exponential fit.

The blank case shows the highest autocorrelation times (0.4 s), followed by 0.2 s for the barrier and 0.05 s for kanamycin. In the barrier case, the monolayer seems to preserve

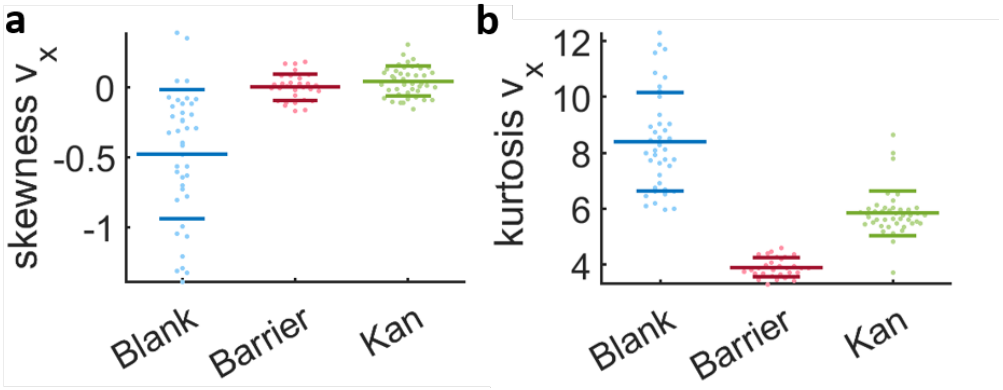

Figure 3.10: **Skewness and kurtosis of the x component of velocity for the blank, barrier and kanamycin.** a) Skewness of the x component v_x of velocities calculated for the blank, barrier and kanamycin. b) Kurtosis of the x component v_x and modulus v of velocities. The long horizontal bars represent the mean of the distribution and the upper and lower short bars represent the standard deviation.

the characteristic high speed of monolayered swarms according to the measurements of cell speed and the trajectories in the phase diagram (Figure 3.9c and Figure 7.11a). In this case, we expect the correlation to decay faster since the system is more dynamic. Surprisingly, this is not what our results suggest (Figure 3.11a), since the correlation times are lower than for the blank case. The lowest autocorrelation time is for kanamycin where cells move slower and the monoloyer is more packed. This might indicate that the rafts are less cohesive in the kanamycin case and the average time of the rafts being together is lower in the presence of kanamycin. The directional correlation indicates for how long the rafts go in certain direction, i. e. how fast they change direction. We can see that these characteristic times are ∼0.2 s for all cases, about one order of magnitude less than the autocorrelation times (except for kanamycin) (Figure 3.11b). The differences between the three cases are small, with the barrier rafts apparently having a slightly longer persistence time than in the blank and kanamycin cases (0.057(0.014)s vs 0.031(0.031)s and 0.026(0.012)s). The differences in the correlation lengths between the cases seem to mirror those of the autocorrelation time.

In conclusion, the characterization of the monolayer demonstrates that to undergo spinodal decomposition in absence of stress, the swarm dynamics do not change significantly and the monolayer seems to behave like a diluted fluid. In contrast, in presence of kanamycin, the monolayer forms a packed state where cell-to-cell forces might have a greater contribution. Since it has been previously hypothesized that multilayer formation in swarms could increase the resistance to antibiotic [121, 144], in the next section we will suggest a possible biological function for the swarm multilayer.

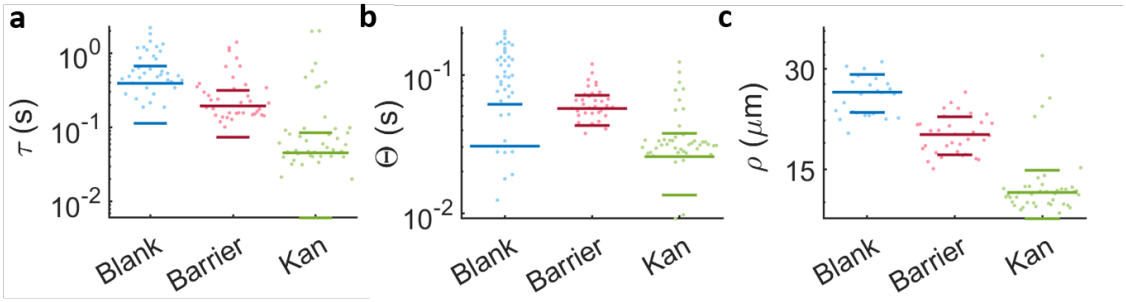

Figure 3.11: **Characteristic magnitudes obtained from exponential fits to autocorrelation and directional correlation in time and cross correlation in space.** a) Autocorrelation time, defined as the inverse of the exponent in an exponential fit to the autocorrelation function Equation 1.3. b) Directional correlation time, defined as the inverse of the exponent in an exponential fit to the directional correlation function Equation 1.6. c) The cross-correlation length, defined as the inverse of the exponent in an exponential fit to the radial correlation function Equation 1.5. The long horizontal bars represent the weighted mean of the distribution and the upper and lower short bars represent the weighted standard deviation.

.

3.2.7 Waves of bacteria resulting from island formation expand further into the kanamycin gradient

The fact that the nucleation and growth happens near the kanamycin gradient made us think that it could involve a strategy that bacteria use to fight against antibiotics. To check this possibility, we recorded what happens after the nucleation of the islands formed a confluent layer. First, we noticed that in the kan case, the formed multilayer is local, meaning that it occupies a band of approximately ∼0.5 cm width, followed by a single layer of 1 cm width towards the interior of the swarm Figure 3.12. This creates a natural gap in cell density across the swarm since the multilayer formed by nucleation and growth happens in a restricted region, isolated from the multilayer that naturally emerges in the interior of the swarm by spinodal decomposition (Video 10). This gap was maintained for at least 80 min after the islands emerged. During these 80 min, we observed the nucleation and merging of islands for up to 4 layers before we lost the ability to recognize further transitions due to a flattening of the image contrast.

After the localized multilayer formation, bacteria used this confined region of high cell density to move towards the kanamycin disk (Figure 3.13). The mechanism used by the multilayer to move forwards is not completely clear. Our hypothesis is that the second layer spreads following the same mechanism as the first, i. e. the cells keep producing surfactin which makes the colony to spread. To track this 1^{st} wave of bacteria, we measured the intensity profile of a brightfield timelapse over time during multilayer formation at 30°C (Figure 3.13a). The 1^{st} wave appears as a very dark thick line in the field of view due to its high cell density. The wave first appeared at 10.8 mm from the kanamycin disk

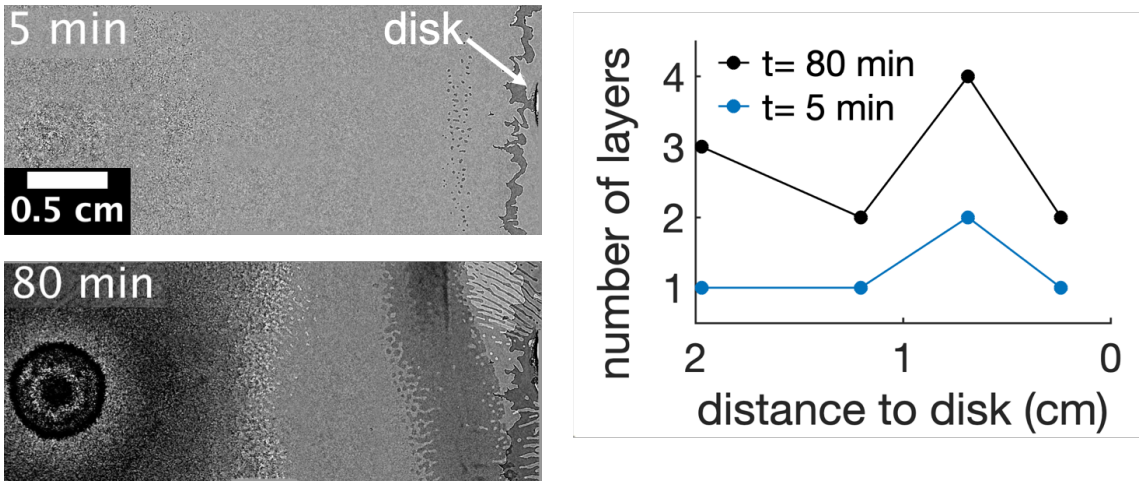

Figure 3.12: **Asymmetric multilayer formation along time in presence of kanamycin.** The multilayer starts 0.7 cm away from the kanamycin disk. The formation of these islands marks where the multilayer first develops. Here, the number of layers continuously increases but it does not spread towards the center of the swarm giving rise to a gap in cell density between the swarming front and the center. The number of layers were measured by the number of times that a darker layer could be observed in the field of view. The origin of times is when the first island is seen in the field of view. Data taken from a single replicate.

and then it travelled forward a total amount of 1 mm in 1.5 h to finally stop probably due to the presence of kanamycin. After that, the spinodal decompositon happening at the interior of the swarm created a 2^{nd} wave of bacteria, remarkably different to the first one, created by nucleation and growth. The 2^{nd} wave started at 18.9 mm from the disk and travelled 3.7 mm in 5.3 h towards the kanamycin disk. Remarkably, the expansion speeds of both waves is quite similar since the 1^{st} wave expands at ~0.67 mm/h and the 2^{nd} wave at 0.70 mm/h. This indicates a similar mechanism of spreading for both waves. The main difference is the distance travelled, larger for the 2^{nd} wave , probably due to the lower concentration of antibiotic that the 2^{nd} wave has to face (Figure 2.2b). For the blank case, the waves are not observed.

Thus, it seems that the two mechanisms that bacterial swarms use to transit to a multilayer swarm, namely spinodal decomposition and nucleation and growth, trigger waves of bacteria that travel towards higher concentration of antibiotic. To check whether there is any net transport of cells towards the antibiotic, we inoculated fluorescent beads at three different points in the trajectory of these waves (Figure 3.13b and c, Video 13). The three points were separated by 1 cm from each other and they were placed in such a way that the left inoculum was just behind where the 2^{nd} wave appears and the middle inoculum was just by the 1^{st} wave . The third inoculum on the right acts as a control to demonstrate the net transport of beads in absence of these waves. Qualitatively, we can tell that after all the waves (Figure 3.13c), the beads have been displaced towards the

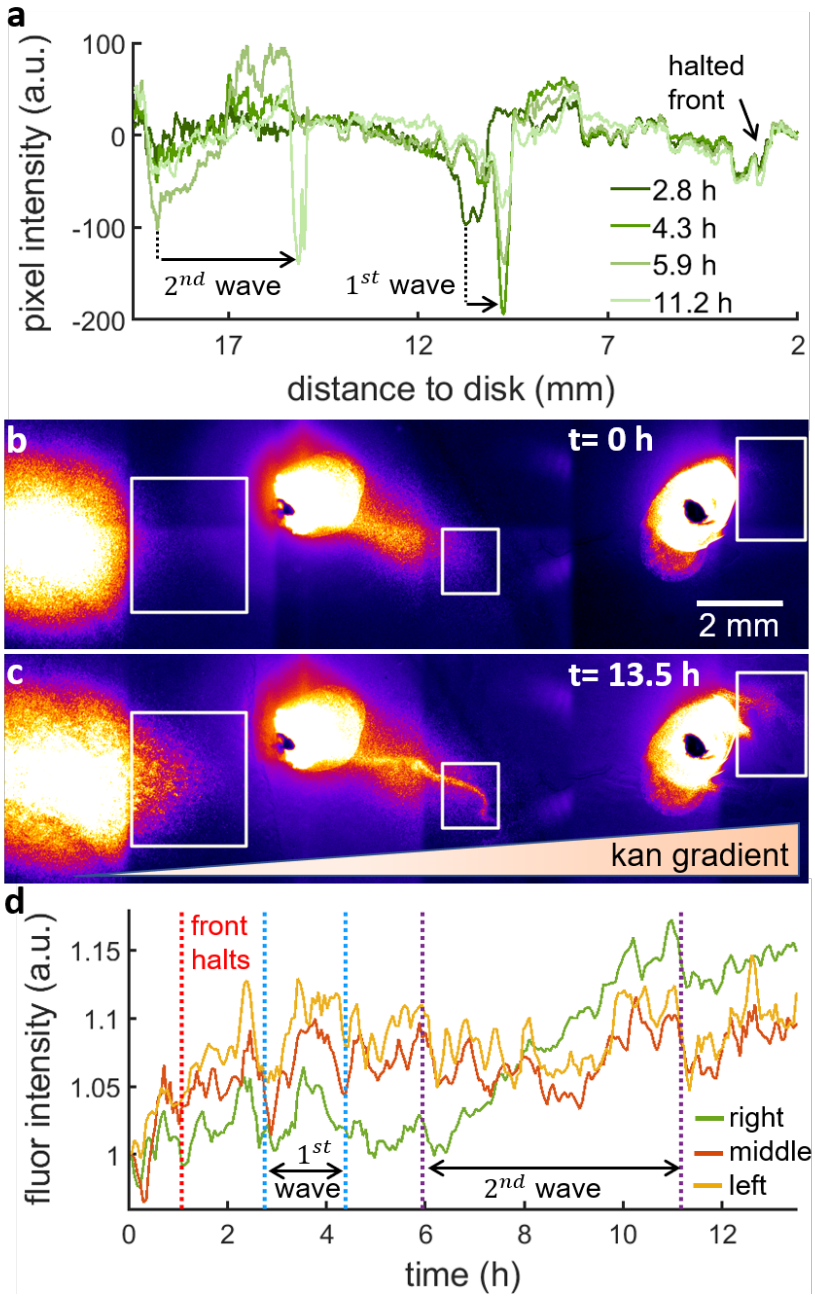

Figure 3.13: **Fluorescent beads show that the waves create a net flow of bacteria moving towards the kanamycin disk.** a) Brightfield intensity profile of the swarm for 2.8, 4.3, 5.9 and 11.2 h after island formation. The drops in the pixel intensity correspond to high density regions. From the kanamycin disk, the profile shows a small drop corresponding to the halted front, then two drops for two different timepoints corresponding to the 1 mm distance that the 1^{st} wave travels and finally the two last drops corresponding to the 3.7 mm travelled by the 2^{nd} wave . b) Fluorescent beads inoculated at three different points from the inoculation point (at the left of the image) to the kanamycin disk (at the right of the image). The fluorescent beads on the left were inoculated 15 mm away from the inoculum and the three points are equally spaced by 10 mm. The inoculum on the right is approximately 5 mm from the disk. The image corresponds to the start of island formation. c) Distribution of fluorescent beads after ∼13.5 h, when the waves had already passed through all the points. d) Normalized fluorescent intensity measured for the three rectangular regions drawn in b) and c). The vertical lines represent from left to right: when the front halts, the beginning and end of the 1^{st} wave and the beginning and end of the 2^{nd} wave . The fluorescent signal was normalized by the first frame of the timelapse.

kanamycin disk. To quantify in which extent, we have measured the fluorescent intensity in three ROIs just on the right of each inocula (white rectangles in Figure 3.13b and c). The measurements of the fluorescent intensity start when the islands appear in the field of view. From that moment until the front halts, 1 h after islands appear, there is an increase in the fluorescent signal for the three measured areas, confirming that the monolayer can drag beads towards the front. This increase can be quantified as the difference in fluorescent signal between the signal at the beginning of the timelapse and when the front halts. The measured differences in intensity for the ROIs going from left to right are: -0.008, 0.035 and 0.041, which suggests that there is no transport of beads at the left ROI. After the front stops, there is a marginal increase in the fluorescent intensity of the three ROIs: 0.026, 0.030 and 0.019, since the bacteria in the inner regions are still expanding towards the front. The fact that during this period the front does not move and the beads are still moving forwards, indicates that there is still a net flow of particles towards the disk, matching the fact that the islands become elongated towards the kanamycin disk. Furthermore, this effect is probably the origin itself of the islands created by nucleation and growth. Bacteria from the inner part of the swarm are expanding and the front is not moving which creates a net increase in cell density that gives rise to the islands. After 2.8 h from island formation, the 1^{st} wave appears but the fluorescent signal does not increase significantly when compared to the other two points. However, the 1^{st} wave does change the spatial conformation of the beads (Figure 3.13c). 1.6 h after the 1^{st} wave wave halts, the 2^{nd} wave wave appears and makes the fluorescent intensity to increase 0.13, in comparison to 0.006 and 0.009 for the right and middle ROIs respectively. This high increase demonstrates that the 2^{nd} wave has a higher ability to transport bacteria towards the front more than the 1^{st} wave or even the monolayered swarm.

Altogether the results suggest that the localized multilayer formed by spinodal decomposition and by nucleation and growth are quite different and the former drags bacteria to regions of higher concentrations of antibiotic.

The radial spread of the multilayer in form of waves, carries swarming bacteria to regions of high antibiotic, where the monolayer is immotile. However, whether the bacteria carried by the waves are alive or not is unknown. To find out, we have calculated the CFU per unit of area across the swarm as an estimation of the living cells in the system for three different times: when the islands form (0 h), 17 h after island formation, when the waves have already stopped moving and, finally, 65 h after island formation. For the first time point, the CFU/mm^2 is approximately 10^6 and quite homogeneous across the swarm, with the exception of the centre at 45 mm from the disk where the CFU/mm^2 drops to 10^5 and

at the closest position to the kanamycin disk where it drops to 10^4 (Figure 3.14), probably because of the high cell death caused by kanamycin. Approximately 4 h after the 2^{nd} wave stopped moving (t=17 h), no alive bacteria were found at 5 mm from the disk. At 15 mm from the disk, there were still some alive bacteria but 130 times less than for the previous timepoint, making evident the killing effect of kanamycin. The number of viable bacteria increase to almost 10^7 at 25 and 35 mm from the disk to finally increase up to 10^9 for the farthest point from the disk. Finally, for t=65 h, there are no viable bacteria up to 35 mm in the swarm. When viable bacteria was counted, the CFU/mm^2 was 5 to 40 times lower than in the previous timepoint across the swarm, indicating that cells die probably due to nutrient scarcity. With this we cannot conclude whether the waves contribute or not to the amount of viable bacteria near the kanamycin. In our system the amount of kanamycin increases over time, particularly where the 1^{st} wave stops (Figure 2.2b). Then, the 1^{st} wave could be transporting bacteria that are temporally alive and then die due to the increasing concentration of kanamycin. Apart from bacterial transport, we cannot discard that the waves could be acting as a diffusion barrier or have a protective function such as sending a warning signal to the rest of the swarm since, as we will see in the next chapter, resistant colonies to the kanamycin appear just behind the waves, at 35 mm from the disk.

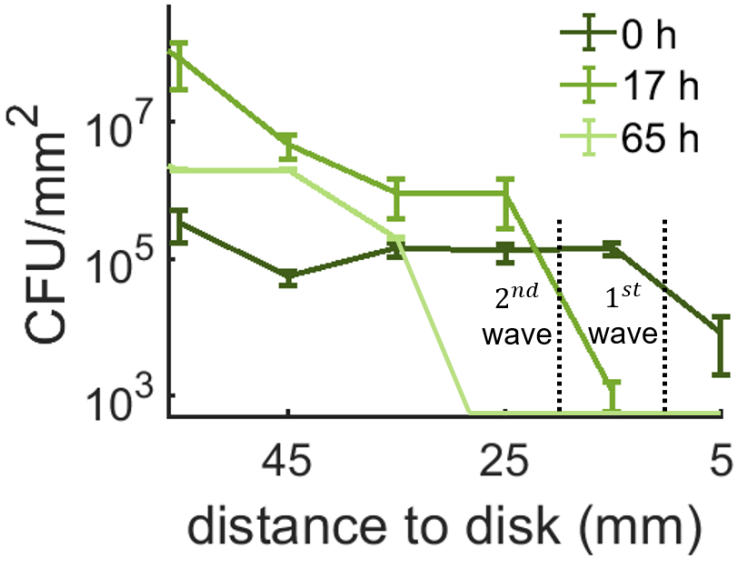

Figure 3.14: **Concentration of bacteria in the swarm for three different timepoints.** The concentration per unit of area was calculated for three different times. The origin of times corresponds to the island formation. The first time profile was measured before the waves occurred, when the islands appeared. The second timepoint is after the waves and finally a third timepoint was acquired after 65 h. The vertical dashed lines indicate where the waves appear. The errorbars are the standard error of the mean. The CFU takes a value of 0 when the lines disappear.

3.3 Discussion

In this study we have described how bacterial swarms can develop multiple layers employing principles of active matter. In absence of stress, the swarm generates small islands that emerge suddenly to form a new layer, resembling what happens in phase transitions during spinodal decomposition. In presence of stress, such as a gradient of antibiotic, the swarm creates nuclei that grow in size and become elongated towards higher concentrations of antibiotic, resembling nucleation and growth in temperature gradients. The macroscopic description of how these islands evolve with time match some of the quantitative aspects reported for motility-induced cluster formation in active colloids, gliding bacteria and even swarming monolayers. However, we observed that the traditional models of MIPS failed to describe quantitatively some aspects of our system. For example, the characteristic wavelength of a phase transition with a constant number of particles is expected to increase as a power law over time. We observed here that, despite observing a characteristic wavelength for a certain time window, the wavelengths do not increase but rather shorten probably due to the constant creation of nuclei because of the increase in cell density. Thus, our quantification could inspire novel models of phase transitions where the number of particles is not constant, a common phenomenon in nature.

In absence of stress, the study of the fast time scale during island formation revealed that the emergence is not stochastic throughout the field of view. Instead, islands appear in specific regions. This could be linked to the presence of obstacles that promote cluster formation according to recent studies of numerical simulations of self-propelled particles [159]. However, we have not studied this possibility.

In case of stress, we link this localized phase transition with the development of waves of bacteria that carry cells in the swarm towards the regions of higher concentration of antibiotic, to a greater extent than the monolayer. This could give swarmers an advantage at conquering new territories and it could inspire new technologies using bacteria to transport particles or drugs for novel therapies. Altogether this study puts together a quantification of the phase separation in bacterial swarms in presence and absence of stress and links such phase separation to novel biological functions.

Chapter 4

Swarming *B. subtilis* develops resistant colonies in antibiotic gradients

4.1 Introduction

In previous chapters we have seen that swarming bacteria can undergo a phase transition that ultimately leads to the development of biofilms in an antibiotic gradient. However, biofilm development is highly conditioned to the specific enviromental conditions that the swarm grows in. In this chapter, we will address the question of how bacterial swarms adapt to the antibiotic gradient when the transition to biofilm is prohibited by using LB media, where biofilms cannot grow. We will demonstrate that swarming bacteria can find a new strategy, alternatively to biofilm formation, and develop colonies that either become resistant to the antibiotics or that present a fitness advantage when grown in sub-lethal concentrations of antibiotic.

Previous studies demonstrated that exposure to sub-lethal concentrations of antibiotic leads to mutagenesis [160, 7]. This promotes emerging antibiotic resistant mutants through different mechanisms [6, 161, 162]. Antimicrobial resistance may not always be uniform throughout a population. Cells may display a variety of resistance levels and some of them may remain susceptible [163], a phenomenon coined heteroresistance [6]. Here, we characterize the variability of this mutagenesis in a spatial landscape. Our experimental set up allows to study each individual emerging mutant and to identify the differences among them. Moreover, our data suggest that exposure to sub lethal concentration of kanamycin make bacteria resistant not only to this antibiotic but to antibiotics which

have the same target within the cell.

Commonly, the mutations associated to antimicrobial exposure carry a metabolic disadvantage. In most cases, there are compensatory mutations which restore metabolic fitness but not to the wild type level [10]. In this study, we measured cell growth over time of some kanamycin resistant mutants that emerged in the kanamycin gradient. Although the mutant strain is 10^5 times more resistant than the WT, measurements in cell growth do not display a substantial difference in fitness when compared to the WT. Furthermore, whole genome sequencing results do not show compensatory mutations.

Finally, we found that the increase in resistance to these drugs comes with a great increase in vulnerability to antimicrobials that target similar cellular processes. This increase in vulnerability is common to all the colonies that appeared in the antibiotic gradient, independently on their level of resistance and on their genetic mutations. This opens a new way to treat infections of antibiotic resistant bacteria and could shed light onto new mechanisms that bacteria use to become resistant to antibiotics.

4.2 Results

4.2.1 Exposure to an antibiotic gradient leads to the development of resistant colonies

In the previous chapter we observed that the local accumulation of cells at the front in presence of antibiotic leads to the formation of waves that move towards the antibiotic. These waves are the border between an inhibition area (radius 1.5 cm) created by the kanamycin gradient and the bulk of the swarm. Just behind these waves, new colonies emerged 1 day later (Figure 4.1a, Video 14). According to our estimation of the kanamycin profile (Figure 2.2b) and the CFU results (Figure 3.14), these colonies appeared in a sub-lethal concentration of antibiotic, since they are just behind the inhibition zone created by kanamycin. Therefore, we believe that this sub-lethal concentration of antibiotics stresses the bacteria leading to the formation of the colonies.

The fact that the colonies could grow in presence of kanamycin made us think that they could have developed tolerance to the antibiotic. To check this, we made a serial dilution assay (subsection 6.6.5) where we estimated the CFUs of the WT and the resistant colonies for three concentrations of kanamycin: 3μg ml^{-1} , 5μg ml^{-1} , and 8μg ml^{-1} . At 3 μg ml^{-1} of kan, the emerging colonies showed to be 10^4 times more resistant than the WT (Figure 4.1 b). When exposed to 5 μg ml^{-1} of kan, the increase in resistance was 10^3, similar to the previous one. Neither the WT nor the colonies survived at 8 μg ml^{-1} of

kan. So we can conclude that these colonies are more tolerant to kanamycin than the WT for concentrations around the MIC.

Although we know that the colonies are more resistant to kanamycin, we do not know how that resistance is distributed across the plate and if all the colonies that appeared are resistant to the antibiotic. To check the spatial distribution of the resistant colonies we performed replica plating at 3 μg ml^{-1} of kanamycin (see subsection 6.6.5), and check which colonies could survive at this concentration (Figure 4.1c). What we saw is that the majority of the colonies are not resistant to 3 μg ml^{-1} of kanamycin and that the resistant ones were mainly located at the front of the plate. This suggests that the antibiotic exerts a selective pressure on the new colonies that arise. This coincides with previous studies of resistance development under sub-lethal concentrations of antibiotics. Specifically, in [6] demonstrated that 5 days treatment with 1 μg ml^{-1} ampicillin in *E. coli* led to an increased resistance to the antibiotic at population-level MIC but exhibited heterogeneity in MIC at the single level (isolation of individual colonies displayed higher resistance to ampicillin (>2.5–12.5 μg ml^{-1}), whereas some isolates were completely susceptible ($\leq$ 2.5 μg ml^{-1})).

Since this selective pressure promotes kanamycin resistance, we wondered whether it could promote resistance to other antibiotics. To test this, we repeated the serial dilution assay to quantify the resistance to streptomycin which targets the 30S subunit of the ribosome, like kanamycin [164]. In this case, the colonies showed an increase in tolerance with respect to the WT (Figure 4.1 d). For all the streptomycin concentrations tested, the WT did not survive whereas the survival rate for the colonies was 3% at 3 μg ml^{-1} and 100 times lower for 5 and 8 μg ml^{-1} . This indicates that the kanamycin gradient promotes the formation of resistant colonies to antibiotics that work in similar way, i. e. targeting protein synthesis in bacteria. We will address further this point in the following sections of the chapter.

In conclusion, exposure to a kan gradient leads to the emergence of resistant colonies. Some of these were 10^4 times more resistant than the WT whereas others did not show any resistance under 3 μg ml^{-1} of kan. The exposure to the sub-lethal concentration of kan makes them to develop resistance also to antibiotics which target the same process as for example streptomycin.

4.2.2 The resistant colonies are not exclusive to swarming motility

As it happens for the transition from swarming to biofilm that we observed in chapter 2, we wanted to check whether the development of the resistant colonies is exclusive to

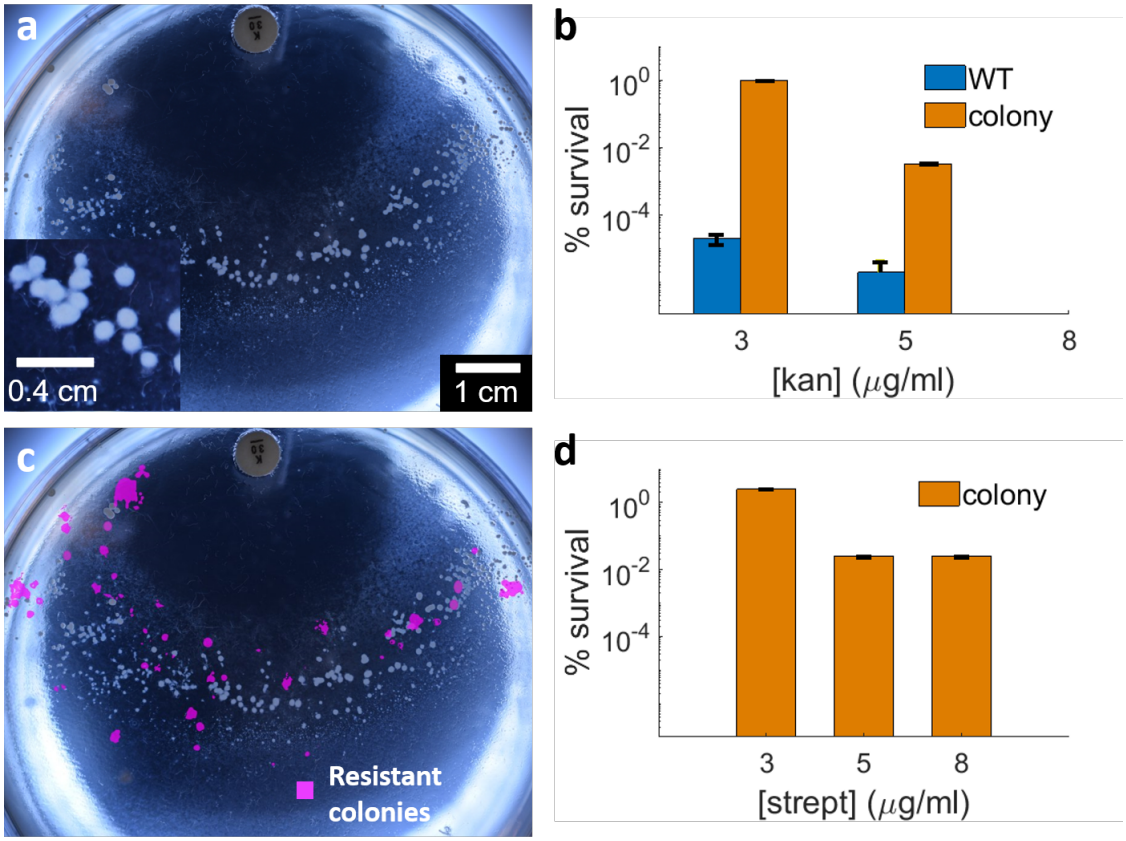

Figure 4.1: **Emerging resistant colonies at the swarming front**. a) Swarming plate 75h after inoculation. Swarming bacteria were inoculated at the centre of the Petri dish. The kanamycin disk was placed at the top of the dish and the resistant colonies emerged 3 cm away from the antibiotic. b) Quantification of resistance of WT and resistant colonies at 3, 5 and 8 μg ml^{-1} of kan. The emerging colonies seem to be 10^4 times more resistant than the WT. c) Overlapping between the original plate showed in (a) and the emerging colonies which resisted the 3μg ml^{-1} of kanamycin after replica plating. d) Quantification of survivability of WT and resistant colonies at 3, 5 and 8 μg ml^{-1} of streptomycin. Colonies could not be counted for the WT since they could not survive any concentration of streptomycin.

swarms or happens as well with swimming and immotile bacteria.

To test whether swimming bacteria can develop resistant colonies, we used *B. subtilis PY79* which cannot swarm but can swim. As agar concentrations lower than 0.4% promote swimming motility instead of swarming [43], we repeated the kanamycin diffusion assay for 0.3% agar plates and we inoculated 4 μl of the strain *PY79* at the centre of the plate. After 3 days of inoculation, the colonies appeared just behind a depletion region of 3 cm radius (Figure 4.2a), double the radius of the swarming depletion region, confirming that swarming motility can reach farther in the gradient of antibiotic. These colonies were formed inside the agar as opposed to the swarming case, where they appeared on the surface. The colonies were qualitatively similar, just slightly bigger than in the swarming case. We tested the resistance of these colonies to 3 μg ml^{-1} of kanamycin and they gave a similar result than for the swarming case (Figure 4.2a).

We repeated the experiment with the WT strain 3610 for hard 1.5% agar by placing the kanamycin disk in the centre of the plate 24 h prior to inoculation. As bacteria do not expand in hard agar, we manually spread 700 μl of bacteria culture over the plate. After 3 days, bacteria formed a depletion region of 1.4 cm around the kanamycin disk and the colonies appeared 3.3 cm away from the centre of the disk (Figure 4.2b). These colonies were smaller than for the swimming plate and they appeared on the surface of the hard agar. We repeated the serial dilution assay to determine whether they were resistant to 3 μg ml^{-1} and the survival rate was similar to the swarming case.

This indicates that the resistant colonies may appear regardless of the characteristic motility of the bacteria, just purely due to the gradient of kanamycin. We tested also whether the gradient is important or they can appear in a homogeneous concentration of kanamycin. For this, we inoculated 4 μl of swarming bacteria at the centre of a swarming plate with 3 μg ml^{-1} of kanamycin. After 3 days, bacteria developed colonies (Figure 7.12a). To further test whether the colonies were due to contamination, we simultaneously put a plate without any bacteria in the incubator and we did not observe any colonies (Figure 7.12b), concluding that the gradient is not necessary for the formation of the colonies either.

4.2.3 The resistance is hereditary but not linked to a specific genetic mutation

Independently of the motility, the swarming gradient assay allows the characterization of different phenotypes that can overcome an antibiotic gradient. We saw that these phenotypes are diverse since not all of them showed the same resistance at a certain concentration of kanamycin. The reason why just some colonies developed resistance while others managed to emerge apparently without an increased resistance to the antibiotic is surprising and it will be the subject of study in the rest of the chapter.

First, we will check whether this resistance can be passed to future generations when cultured in absence of antibiotic, i. e. we will test if once the stress is removed, the colonies are still capable of inheriting kanamycin resistance. To check whether this resistance can be transferred to future generations of bacteria, we picked one resistant colony from the swarming front and we streaked it onto a new LB agar plate without any antibiotic. This plate was incubated overnight and, after this, a new single colony was chosen from this new plate and streaked again onto a new LB agar plate. This process was repeated 11 times until we obtained 12 passages of the initial colony. We will refer to the original colony of these passages as α and we will name its 10^{th} passage as IL2. The amount

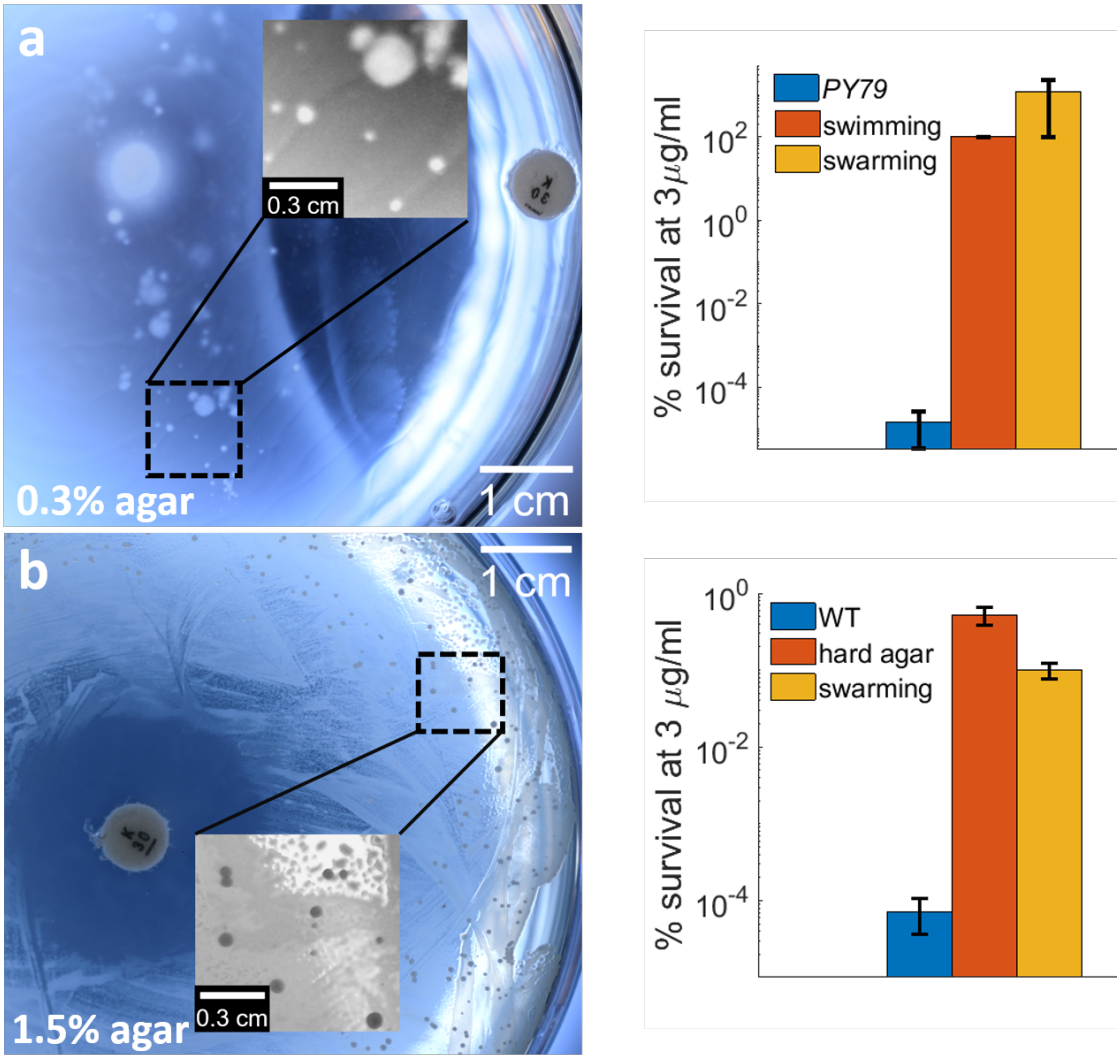

Figure 4.2: **Emerging resistant colonies in swimming and solid agar**. a) Swimming plate 75h after inoculation. Swimming *PY79* was inoculated at the centre of the Petri dish. The kanamycin disk was placed at the right of the dish 24h before inoculation and the resistant colonies emerged 3 cm away from the antibiotic. The inset shows a zoomed in region where the colonies can be distinguished in white. The graph shows that these colonies can survive to 3μg ml^{-1} of kanamycin as much as the ones taken from the swarming plate. c) Hard agar plate 75 h after inoculation. The kanamycin disk was placed at the centre of the plate and 24 h later 700 μl of WT *B. subtilis* were spread over the plate. The colonies emerged 3.3 cm away from the disk. The inset shows a zoomed in version of the colonies. The graph shows that the colonies showed approximately the same resistance as for the swarming case.

of living bacteria on each passage was calculated by serial dilution assay at 3 μg ml^{-1} of kanamycin. The resistance was higher than the WT along the 12 passages tested for colony α (Figure 4.3). Whereas the WT displayed a survivability of 10^{-5}%, at least 5% of the bacteria were resistant for all the passages of α. The resistance remained quite steady for all the passages, with slight increasing trend. This demonstrates that the resistance can be maintained along the next generations of bacteria even when they are not exposed to the kanamycin selective pressure.

We repeated the kan gradient assay, creating another map of colonies and we picked

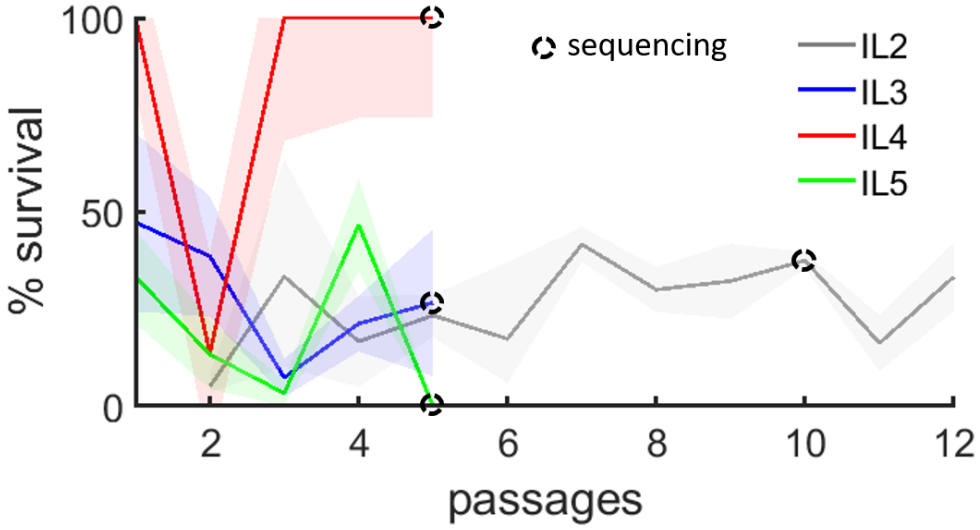

Figure 4.3: **Transmission of resistance along passages**. a) Quantification of antibiotic resistance for the four different colonies which were sent to whole genome sequencing. IL2 comes from a different swarming plate than the other colonies and its resistance was measured along 12 different passages under exposure to 3 μg ml^{-1} of kanamycin. The resistance of other three colonies (IL3, IL4 and IL5) was checked along 5 passages. The error bands show the weighted standard error of three replicates.

10 of the ones which appeared in the swarming front. We passaged these colonies 5 times and we tested the resistance in each passage. For this plate, 3 out of the 10 picked colonies showed a higher resistance when compared to the WT. We will refer to the last passage of these resistant colonies as IL3, IL4 and IL5. Not all the colonies showed the same level of resistance and it fluctuated during the different passages (Figure 4.3). Overall, IL3 and IL5 displayed a lower resistance than IL4 across all passages. Within these colonies, IL5 showed that the resistance can be lost during the passages since its first passage displayed a survival rate of 35% but it decreased down to WT level in the fifth one. Finally, IL4 seemed not to be susceptible to the antibiotic since nearly 100% of bacteria survived. The high variability in resistance of these colonies suggests that they might use a different mechanism to resist the antibiotic.

These variations in antimicrobial resistance are likely to be due to the different genotypes in our strains since it has been reported that bacteria can adapt to antibiotic gradients by genetic mutations [123]. To check whether the resistance is caused by genetic mutations, we performed whole genome sequencing in WT and the 5th passage of four different colonies: IL3, IL4 and IL5 which were tested in Figure 4.3 and IL6, a colony from the same plate which never showed any resistance to kanamycin. We hoped that sending resistant and non resistant colonies could identify the mutations that were important to survive in presence of the antibiotic and whether these mutations could be responsible for the increase in resistance to antibiotics similar to kan.

All the strains which were sent had a mutation in the NorM gene (Table 4.1), responsible for the synthesis of a multidrug resistance efflux pump of the MATE family [165]. To confirm this result from whole genome sequencing, we designed primers targeting the mutation in the Norm gene to sequence it by Sanger sequencing (Table 7.6). We confirmed the mutations in the Norm gene for IL3, IL4, IL5 and IL6. Nevertheless, according to our data, this mutation is not enough to confer antibiotic resistance since both resistant and non resistant strains showed the Norm mutation (Table 4.1). Apart from Norm, the non resistant strains IL5 and IL6 displayed a mutation which affects the phosphoenolpyruvate-dependent sugar phosphotransferase system (sugar PTS) (Table 7.5). This system is involved in maltose transport since it catalyzes the phosphorylation of incoming sugar substrates and actively participates in their translocation across the cell membrane [166]. We checked this mutation with Sanger sequencing for IL6 (IL5 could not be checked due to problems with primer design) and we could not detect it so we will assume from now on that IL6 just has the Norm genetic mutation. Finally, IL5 also has a deletion in the GTPase ObgE which plays a role in the control of stress response and ribosome biogenesis. Both processes are directly related to the target of aminoglycosides since they have been reported to induce stress by creating Reactive Oxygen Species (ROS) and they target the ribosome. However, this deletion does not increase substantially IL5 resistance to kan since the survival rate is the same as for WT.

IL3 and IL4 had several mutations affecting the plipastatin synthase subunit D and they are the only two strains from this plate which showed antibiotic resistance (Table 7.5). Plipastatin synthase is a multifunctional enzyme, which can have a ligase activity. This could lead to a mechanism to alter the chemical structure of kanamycin so that it decreases its affinity for the binding site. However, after checking these mutations with Sanger sequencing, we could not observe any of them in these two strains. Sanger sequencing targeting these mutations was repeated 4 times and no mutations were detected in any of them. Then, the only explanation for the increased resistance to kan in IL3 must come from its other mutation in the elongation factor G which participates in translocation. Mutations in the fusA gene, which encodes the elongation factor G, are the most found mutations in lineage studies of *P. aeruginosa* and *E. coli* exposed to sub-lethal concentrations of aminoglycosides so their implications in antibiotic resistance seem evident [167]. The most resistant strain is IL4, which shows an insertion in a gene related to the 50S ribosomal protein L7/L12 (Table 4.2). The ribosome is the target of aminoglycosides such as kan or strep so it seems feasible that such mutation could lead to resistance. Nonetheless, kan and strep specifically target the 30S subunit and not the 50S so the link between

the resistance and the mutation is not completely clear.

As we discussed, all the colonies have a mutation in Norm so we wondered whether this is a common phenomenon when exposing swarming bacteria to kan gradients. To check that, we made a replicate of the experiment and we selected three colonies: a colony from the swarm that was very far away from kan and that did not show any resistance (β), a colony from the swarming front (α) and its tenth passage IL2 also resistant to kan as we showed in Figure 4.3. We sent these three colonies to whole genome sequencing. β -susceptible to kan- had a mutation in the elongation factor G as IL3, just in a different position in the gene. This makes us doubt of the link between mutations in the elongation factor G and an increase in resistance. In α, an insertion in the tRNA-leu was detected. tRNA-leu is an enzyme that binds an activated aminoacid with the correspondent tRNA during translation. This seems a crucial process that is targeted by kanamycin. However, exactly the same insertion was also detected in β, which is not resistant to kanamycin, so again the link between this mutation and the increase in resistance is not clear. Strikingly, IL2, the 10^{th} passage of α, has InDels in the glutamine-fructose-6-phosphate aminotransferase (gfat), which were not found in α. This is quite surprising because one would expect IL2 to have a genotype identical to α since during passaging it was never exposed to antibiotics. Ggfat is the rate-limiting enzyme which catalyzes the conversion of fructose-6-phosphate to glucosamine-6-phosphate [168] but its link to aminoglycoside resistance has not been reported, to the best of our knowledge. The fact that these InDels were detected in IL2 but not in α means that maybe they were missed by the whole genome sequencing in the latter and that α's increased resistance comes from these mutations.

As Norm mutation was common to all the colonies in the first plate that we sent, we targeted the Norm mutation in IL2 -coming from a second assay- with Sanger sequencing to see whether it was missed by the whole genome sequencing. After repeating the Sanger sequencing 4 times, we confirmed that this mutation was not present in IL2.

In summary, the higher resistance in IL3 could only come from the mutation in the elongation factor G. The higher resistance in IL4 can only be due to the deletion in the 50S ribosomal subunit, although kan targets the 30S one. IL5 and IL6 do not show a higher resistance to kanamycin and the latter does not show any mutations apart from the one in Norm. The elevated resistance of α is unlikely to be due to the insertion in tRNA-leu since this is shared with β which is not resistant. The results of the sequencing seem puzzling since there are a lot of mutations found by the whole genome sequencing that are involved in the translation process targeted by kanamycin and still they do not seem related to an increase in resistance. A possible explanation could be that the resistance was always

WT	IL3	IL4	IL5	IL6	α	β	IL2	Gene ID	Gene product
G	G	G	G	G	G	T	G	B4U62_RS05915	ATP-dependent helicase/deoxyribonuclease subunit B
C	C	C	C	C	C	T	C	B4U62_RS00710	elongation factor G
G	A	G	G	G	G	G	G	B4U62_RS00710	elongation factor G
C	**A**	**A**	**A**	**A**	C	C	**C**	**B4U62_RS10595**	**multidrug resistance protein NorM**
G	G	A	G	G	G	G	G	B4U62_RS20260	prespore-specific transcriptional regulator RsfA
G	G	G	A	G	G	G	G	B4U62_RS04590	PTS maltose EIICB component

Sequenced by BGI sequencing Sequenced by microbesNG

Table 4.1: SNPs of colonies from two different plates analysed by BGI sequencing. The rows in bold correspond to the mutations that we confirmed with Sanger sequencing.

TYPE	IL3	IL4	IL5	IL6	α	β	IL2	gene ID	gene product
INSERTION	-	-	-	-	A	A	-	B4U62_RS00515	tRNA-leu
INSERTION	-	-	-	-	-	A	-	B4U62_RS02875	tetratricopeptide repeat protein
INSERTION	-	-	-	-	-	-	A	B4U62_RS01150	glutamine--fructose-6-phosphate aminotransferase
DELETION	-	-	-	-	-	-	AT	B4U62_RS01150	glutamine--fructose-6-phosphate aminotransferase
DELETION	-	CTC	-	-	-	-	-	B4U62_RS00675	50S ribosomal protein L7/L12
DELETION	-	-	AAATTC	-	-	-	-	B4U62_RS15065	GTPase ObgE

Sequenced by BGI sequencing Sequenced by microbesNG

Table 4.2: InDels for the same colonies as before. Something remarkable here is that more insertions were detected in IL2 than in α even though the former comes from the latter and it was never exposed to antibiotics after the passage experiment.

tested at 3 μg ml^{-1} of kan but these mutations, including Norm, could increase the survival rate with respect to the WT at lower concentrations of kan. In the next sections, we will explore the differences between these resistant and non resistant phenotypes in sub-lethal concentration of kan.

4.2.4 The fitness of the resistant colonies is similar to the WT

The sequencing analysis demonstrates that the ability of the colonies to emerge in presence of antibiotic is not necessarily linked to a specific mutation. This made us think that there might be a more general mechanism that confers an advantage to the colonies over the other bacteria in the plate. We also know that this mechanism can trigger either kanamycin tolerant or susceptible colonies capable of growing in the antibiotic gradient. Then, it is natural to think, that the susceptible colonies must have an alternative mechanism that confers and advantage to grow in the kanamycin gradient. To try to elucidate the key factor that makes them different, first we will study the growth and sensitivity to other antibiotics of the resistant mutant IL2.

The higher resistance of IL2 might come from gfat. If that was the case, we hypothesize that its fitness would decrease in absence of kan with respect to the WT since it has been reported that resistant mutants decrease their fitness unless they have compensatory mutations [10, 169, 170]. As gfat is the only mutation in IL2, compensatory mutations cannot exist so the resistance should carry a fitness cost. To check this, first we characterized the dispersion in cell growth due to variability in samples. With this aim, we prepared 3 WT cultures whose turbidity was monitored along 20 h (Figure 4.4a) using the microbemetre [171]. After an initial lag phase of 3 to 4 h, cells started to replicate exponentially. Around 2 h later, bacteria entered into the diauxic shift leading to a pause in this exponential phase. Afterwards, they continued growing until they finally entered in the stationary phase, 15 h after the measurements started. The highest variability among the samples was in the lag phase since differences among the cultures were up to 1h. The growth profile after the lag phase was similar for all the curves.

In a separated experiment, we compared the growth of the WT with respect to IL2 to see if there were any differences (Figure 4.4a). Qualitatively, it seems that IL2 grows in a similar way than the WT in absence of antibiotics since the curves are within the range of variability of WT. Then, we performed another experiment to compare the growth curves in presence of 3 μg ml^{-1} of kan (Figure 4.4 b). Here, the striking difference is that the WT undergoes a 13 h lag phase in presence of 3 μg ml^{-1} of kan whereas IL2 delays its lag phase a maximum of 2 h when in presence of antibiotic. After this long lag phase, IL2 seemed to grow resembling the normal WT behaviour.

To give a more quantitative comparison, we measured the lag phase, defined as the period of time when turbidity remains flat; the growth rate, defined as the slope of the curve before the diauxic shift; and the normalized integral, defined as the area under the curves normalized by the time acquisition of each turbidity curve. The growth rate is given by the slope in Equation 1.1 which was obtained fitting the logarithm of turbidity to a straight line. The results showed that the WT had a similar growth rate to the mutants under 3 μg ml^{-1} of kan (Figure 4.4d). This indicates that there is no difference between the WT population after the lag period and the mutants. However, kanamycin did have an effect in the overall growth rate of both strains: both growth rates dropped 1.3 times in presence of antibiotic. Another interesting feature of IL2 is that, in absence of antibiotic, it grows roughly at the same rate as wild type which is uncommon in genetically resistant strains [10, 169, 170]. The normalized integral showed no difference between WT and IL2 without antibiotic but we could see that the antibiotic made the integral decrease for both strains. This is probably due to the slightly slower growth rate induced by kanamycin. We

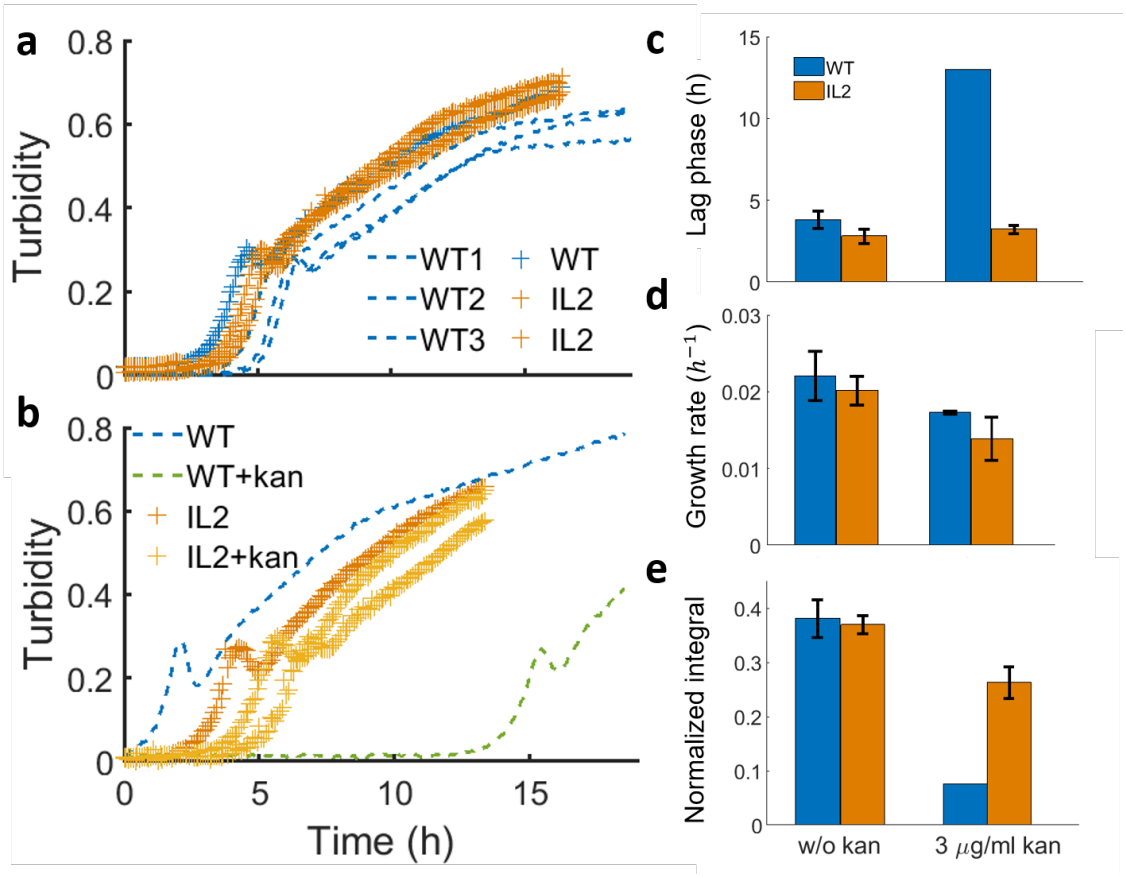

Figure 4.4: **Growth profiles for WT and IL2 in presence and absence of kan**. a) Growth curves for two independent experiments where we measured the turbidity over time. In the first experiment, the turbidity for 3 different samples of WT (–) was checked. For the second experiment, turbidity for WT (+) and IL2 (+) was measured. b) Growth curves for two independent experiments by measuring the turbidity over time in presence of kan. In the first experiment, the turbidity of the WT was measured in absence (–) and presence of 3 μg ml^{-1} of kan (–). For the second experiment, the turbidity was measured for IL2 in absence (+) and presence of 3 μg ml^{-1} of kan (+). c) Differences in lag phase between WT and IL2 when they are exposed to kan. d) Growth rates calculated from the linear region after the lag phase and before the diauxic shift of the growth curves. e) The integral or area under the curve for the WT and IL2 without kanamycin and in presence of 3 μg ml^{-1} of kan normalized by the total time interval of each curve. The error bars show the weighted standard error of the mean.

could also observe that the integral of IL2+kan is 3 times larger than for WT+kan. This could be explained by the difference in lag phase, since the lag phase is 3 times shorter for IL2 than for WT.

Then, the main difference between the resistant strain IL2 and the WT is that the WT undergoes a longer lag phase in presence of antibiotic. The antibiotic stress decreases the growth rate of both WT and IL2 so it seems that IL2 is affected by the antibiotic but still can survive better. The fact that its growth rate with respect to WT in absence of kanamycin was the same, questions the importance of the mutation in gfat, since antibiotic resistance associated mutations usually come with a metabolic cost [172], and IL2 did not seem to have compensatory mutations which restores the metabolic state at WT level.

4.2.5 IL2 is more resistant to aminoglycosides than the WT but more vulnerable to spectinomycin

Different antibiotics target different processes within the cells. Even within aminoglycosides, the different antibiotics bind to different parts of the ribosome and disrupt slightly different processes. We expected that testing the resistance of IL2 to different antibiotics helped to better understand the mechanism behind the resistance and whether the genetic mutations are related to it.

First, we compared the MIC of WT and IL2 for the antibiotics: kanamycin, neomycin (neo), gentamicin (gent), chloramphenicol (cm) and spectinomycin (spt). The MIC assay consisted of a linear gradient of antibiotic on an agar plate (see subsection 6.6.5). The antibiotics apramycin (apra) and tetramycin (tetra) were also tested but the MIC could not be checked with this method since bacteria formed an incompatible pattern with the symmetry expected for the linear gradient. Instead of creating a bacteria lawn that follows the linear gradient, the border where the bacteria stopped growing due to the antibiotic was not well defined, since regions of growth and inhibition appeared for regions of agar with the same concentration of antibiotic. For the former antibiotics, the distance from the extreme of the petri dish to the region where cells started to grow was measured and then translated into the corresponding antibiotic concentration.

The MIC assay suggested that the MIC for the WT is slightly lower than for IL2 when testing the aminoglycosides kan, neo and gent (Figure 4.5 a). In case of chloramphenicol which targets the 50S subunit of the ribosome, there is no difference for both strains. In case of spt the relationship reverts, since the MIC for IL2 is 16 μg ml^{-1} and for WT is 23 μg ml^{-1} . We point out that the calculated MIC in liquid culture for kan 5 μg ml^{-1} and this assay gave 1.6 μg ml^{-1} so it seems to underestimate the MICs for the different antibiotics. However, we were using this assay just to estimate roughly the concentrations needed to test both strain in the serial dilution assay so this level of discrepancy is not a problem.

The linear gradient of antibiotics permitted to test a wide range of concentrations in a very simple way. Nonetheless, the results were just an estimation of the real MIC since the zone of inhibition highly depended of the cell density. To overcome this, we used the Kirby-Bauer (KB) assay and measure the radius of the inhibition zone around a diffusive disk for both strains (Figure 4.5 b). The radius of the inhibition zone will be larger the more susceptible the tested strain is. The difference of the radius of the inhibition zone between WT and the mutants determined which one was more susceptible to the drug. A positive difference would indicate that the WT was more susceptible and a negative

difference would indicate that IL2 was more susceptible. In general, the susceptibility test confirmed an increase in resistance to aminoglycosides which bind to the A site of the ribosome: kan, gent and apra (Figure 4.5b). Again, spectinomycin is slightly more effective against the mutants than against the WT. In this assay we tested also ampicillin which targets the cell wall instead of ribosome. The KB showed no difference between both strains. Likewise, chloramphenicol showed the same depletion region for both strains.

Finally, we made a serial dilution assay for the concentrations around the MICs calculated in Figure 4.5a. The results showed that IL2 was more resistant than the WT to the antibiotics targeting the 30S subunit of the ribosome. Specifically, IL2 was 10^6 times more resistant than the WT to kan and gent and 10^4 more resistant to apra. In the case of neomycin the difference shortens showing roughly the same survival rate, contradicting Figure 4.5a. We suspect this was a problem of the assay with this antibiotic since neo has an identical way of action than kan and gent. The only difference is that neo has two binding sites in the bacterial ribosome instead of one [173, 174], but IL2 does not have any specific mutations in the encoding ribosome genes so we do not think that the difference in resistance is caused by this. Tetra is only 100 times more effective against WT than to IL2, a shorter difference than in kan, gent and apra cases. This could be because tetracyclines have a slightly different mode of action since they bind to the A site of the ribosome, blocking the attachment of aminoacyl t-RNA whereas the aminoglycosides prevent tRNA translocation [11]. Whether this could be the source of the difference or not is not clear. This is consistent with previous studies which showed a lack of cross-resistance to tetracycline or chloramphenicol after aminoglycosides exposure [6, 175]. Again, spectinomycin, which has a similar mechanism of action than aminoglycosides but differs slightly in their chemical structure, gives 10^4 times more survival for WT than IL2. Almost 100% of the WT survives under 30μg ml^{-1} of spt whereas just 10^{-4}% of the resistant mutants can survive.

These last three data sets displayed that kan, neo, gent and apra are less effective against IL2 in comparison to the WT. The difference in effect of tetra is not fully determined since the KB assay shows that IL2 is slightly more sensitive but the dilution assay suggests the opposite. This could be explained by the fact that KB assay might depend on the initial cell density which was not completely the same for both strains tested. For cm, no differences have been shown for any of the three assays. This suggests that they key mechanism of resistance might be related to the 30S subunit of the ribosome since cm targets the 50S. A surprising result is that, IL2 is more susceptible to spt than the WT even though spt targets the 30S subunit too.

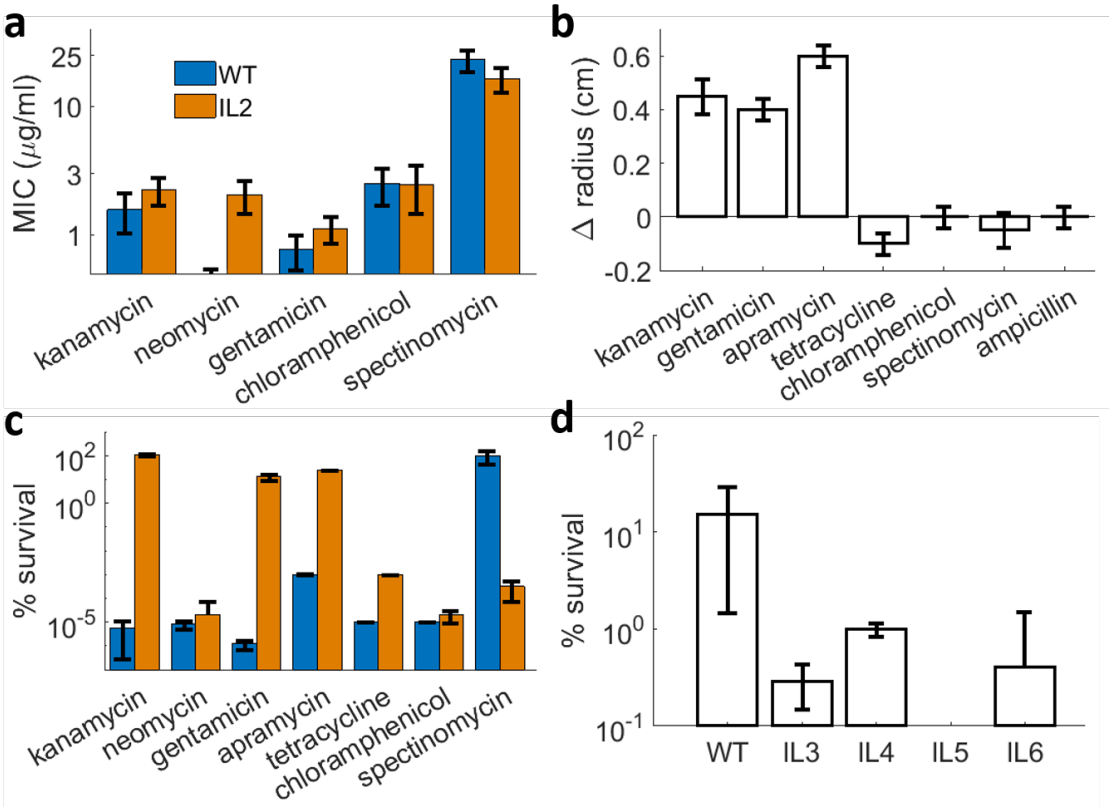

Figure 4.5: **Susceptibility tests for the different resistant strains tested under ribosome-targeting antibiotics**. a) Semilog plot of the MIC for different concentrations of antibiotics by creating a linear sloped petri dish (see subsection 6.6.5). IL2 was used together with the WT. b) Differences in radius of the clearance regions created in the KB method. Positive difference means that the size of the clearance region was bigger in the WT and negative values mean that the clearance was bigger for IL2. c) Semilog plot of the differences in susceptibility for 7 different antibiotics for WT and IL2 calculated by CFU. The concentrations used for each antibiotic are: 3μg ml^{-1} of kan, neo, tetra and cm, 1μg ml^{-1} of gent and apra and 30μg ml^{-1} spt d) Semilog plot of susceptibility for IL3, IL4, IL5 and IL6 under exposure to 30μg ml^{-1} of spec calculated by the CFU assay. The error bars represent the weighted standard error of the mean of at least three replicates.

The fact that IL2 is more susceptible to spt could come from its mutation in *gfat*. To check if the increased susceptibility was either due to this mutation or to a common mechanism affecting all the colonies that appeared in the swarm, we run a serial dilution assay with IL3, IL4, IL5 and IL6 at 30μg ml^{-1} of spt (Figure 4.5 d). The susceptibility to all of them, independently on their resistance to kanamycin and their genetic mutations, was larger than for the WT. Among the resistant mutants, IL4 was the most resistant to spt but still at least 10 times less resistant than the WT. IL3 and IL6 displayed a similar behaviour and, IL5 showed the highest susceptibility since no colonies survived at this concentration of spt. The most striking result was that, IL6 despite not having any mutations apart from Norm and IL2 despite not having other mutations than gfat, were both more vulnerable to spt. Therefore, the increased susceptibility to spt was not associated to any genetic mutation but to the fact that the colonies were previously

exposed to kan.

4.2.6 Kanamycin resistance cannot be reverted after exposure to spectinomycin

The fact that the colonies were more sensitive to spt just by growing in presence of kan, made us think that this resistance could be reverted when exposing the colonies to spt. To test this, we repeated the swarming assay with IL2 using a spectinomycin diffusive disk instead of a kanamycin disk. For that, we prepared 3 plates with spectinomycin diffusive disks containing: 150 μg , 300 μg and 600 μg of spt. After 3 days, the colonies emerged on the spt plates. The resistance of these colonies to 3 μg ml^{-1} of kan was tested by using the serial dilution assay (Figure 4.6a). As in previous experiments, just 10^{-5}% resisted for the WT and 100% resisted for IL2. The colonies that grew in the 3 spt plates developed resistance to kan to a similar level than IL2 for the gradients with 150 μg and 300 μg and to a lower extent with the 600 μg spt disk (0.6% survived in this case).

These results show that the resistance to kan cannot be reverted by exposing the colonies to spt. Now we wondered whether these colonies that emerged in the spt gradient are still more vulnerable to spt than the WT. To test so, we repeated the serial dilution assay and calculated the % survival at 50 μg ml^{-1} of spt (Figure 4.6b). The result showed that IL2 was still more sensitive than the WT, as expected, but the colonies taken from the spt gradient became also resistant to spt.

In summary, repeating the swarming assay with IL2 in a spt gradient did not revert the resistance to kan and allowed the emergence of colonies that were resistant to both spt and kan.

4.2.7 The non resistant mutant IL6 shows a different phenotype in presence of kanamycin

So far, we have characterized the fitness and resistance of the resistant mutant IL2 to kan. It is natural that a resistant colony can emerge in a gradient of the antibiotic since it has a clear advantage with respect to the surrounding non resistant bacteria. Nevertheless, the replica plating in Figure 4.1b shows that not all the colonies that emerge are resistant to kan, at least for the tested concentration. To understand better the advantage of these colonies with respect to the WT, we characterized the fitness of the mutant IL6 for different concentrations of kan.

The OD over time for WT and IL6 were measured with a plate reader for 6 different concentrations of kan (Figure 4.7 a). In absence of kan, the WT and IL6 were quite similar

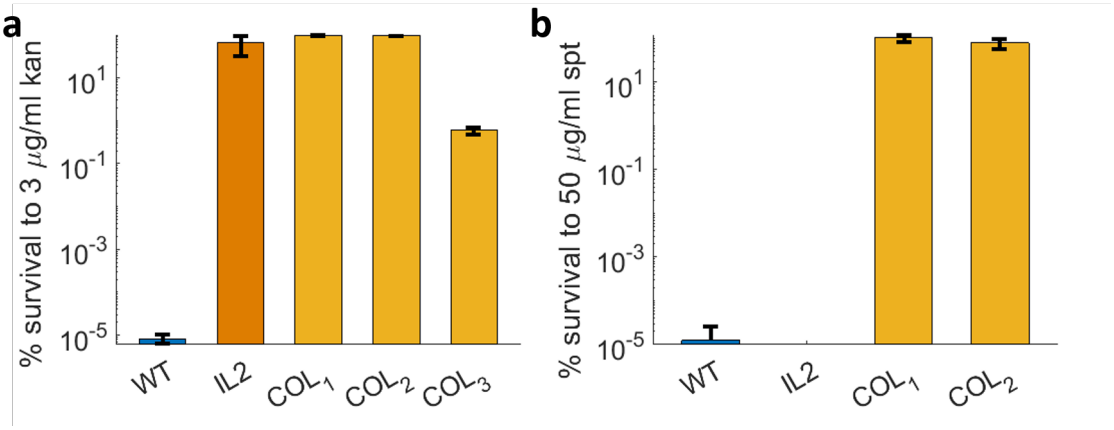

Figure 4.6: **Survival rate for colonies emerging in a spectinomycin gradient**. a) Semilog plot of the rate of survival at 3 μg ml^{-1} of kan for the WT, IL2 and three colonies that emerged in 3 different spt gradients. b) Semilog plot of the rate of survival at 50 μg ml^{-1} of kan for the WT, IL2 and two colonies that emerged in 2 different spt gradients. The error bars represent the weighted standard error of the mean of at least three replicates.

but when we cultured them in presence of low concentrations of kan, both behaviors diverged. For 1 and 2 μg ml^{-1} of kan, the WT increased its OD up to a maximum point. This maximum OD went down with increasing kan concentration. After this maximum OD, the OD decreased over time and after 40 h started increasing again. Roughly at the same time than maximum OD in the WT, IL6 underwent a plateau where the cell growth nearly paused for 2h to then continue growing. For higher concentrations of kan, there was a large variability in both strains (Figure 7.14), but attending to the overall growth we saw that the main difference was that IL6 could have a sustained growth over time at a higher OD than the WT.

To quantitatively describe the differences in cell growth, we quantified the lag phase, the growth rate and the integral for each of the growth curves (Figure 4.7 b,c and d). Overall, the three magnitudes were affected by the increasing concentration of kan. The lag phase in absence of kan was approximately 2h and it increased with the concentration of kan until it reached a plateau for concentrations higher than 2 μg ml^{-1} (Figure 4.7b). For 3, 4 and 5 μg ml^{-1} , the differences between lag phases were small: the average lag phase for the WT was 11 h and for IL6 was 13 h.

The growth rate decayed nearly exponentially with increasing concentrations of kan (Figure 4.7c). In absence of antibiotic, IL6 grew 1.3 times slower than the WT, which could be caused by the Norm mutation. This suggests that in absence of antibiotic, IL6 has a fitness disadvantage when compared to the WT. For 1 μg ml^{-1} of kan the growth rate dropped 1.4 times for the WT and only 1.1 times for IL2, which indicates that IL2 is adapted to grow in sub-inhibitory concentrations of antibiotic whereas the WT can notice the effect of kan already at this concentration. For 2 μg ml^{-1} , the WT decreased its

growth rate 2.3 times and IL2 did it 1.8 times. Here we see that increasing concentrations of kan affected more the WT than the mutant IL2. For higher concentrations of kan, the variability among the experiments was quite large (Figure 7.14). Taking this into account, we could argue that the rate remains nearly constant at 0.045 h^{-1} for these concentrations.

The only magnitude that gave a substantial difference between both strains was the area under the curves or integral (Figure 4.4 d) which can be understood as the total growth of the sample during the experiment. In absence of kan, both strains reached approximately the same value but in presence of kan there was a large difference between strains. For 1 μg ml^{-1} of kan, the integral value for IL6 doubled the WT and this difference became even larger for 2 μg ml^{-1} . For larger concentrations of kan, the growth inhibition was quite high so both integral values got very low (but still higher for IL6).

4.2.8 Growing WT at sub-lethal concentrations of antibiotics results in a phenotype more similar to IL6

From the fitness parameters characterized so far, the main difference between the WT and IL6 was that IL6 could sustain a higher growth over time. These parameters changed in a step-wise fashion: after a threshold concentration of kan, the values remained nearly constant. This could indicate that bacteria have a first mechanism of adaptation which allow them to tolerate low concentrations of kan and, if they needed to resist higher concentrations they would adapt through a different mechanism. According to this hypothesis, when the WT is exposed to a low concentration of kan, it would adapt to it, behaving as IL6 did. Therefore, if we took the WT which grew in liquid culture at 1 μg ml^{-1} of kan after 44 h, it should behave as IL6 when it was exposed to that same concentration of kan. To check this, we run a 96 well plate assay and then we took the WT exposed to 1 μg ml^{-1} of kan after 44 h. This sample was streaked on a plate and a single colony was selected to run a new 96 well plate assay at 0, 1, 2 and 3 μg ml^{-1} of kan to check whether this new strain, which we will call m, grew as IL6 in presence of antibiotic. The growth of m was similar in absence of antibiotic and in 1 μg ml^{-1} of kan, the concentration of kan that it grew in (Figure 4.8a). At 2 μg ml^{-1} the curve became very similar to IL6 growing at 2 μg ml^{-1} of kan (see Figure 4.7a). For 3 μg ml^{-1} the variability in growth is very large and it became difficult to compare the growth profiles.

To quantitatively compare whether m behaved similarly to IL6 or the WT, we have calculated the differences in lag phase, growth rate and the integral between m and the WT and between m and IL6 (Figure 4.8b, c and d). The differences in lag phase were negligible in absence of kan and at 1 μg ml^{-1} (Figure 4.8b). At 2μg ml^{-1} , the difference

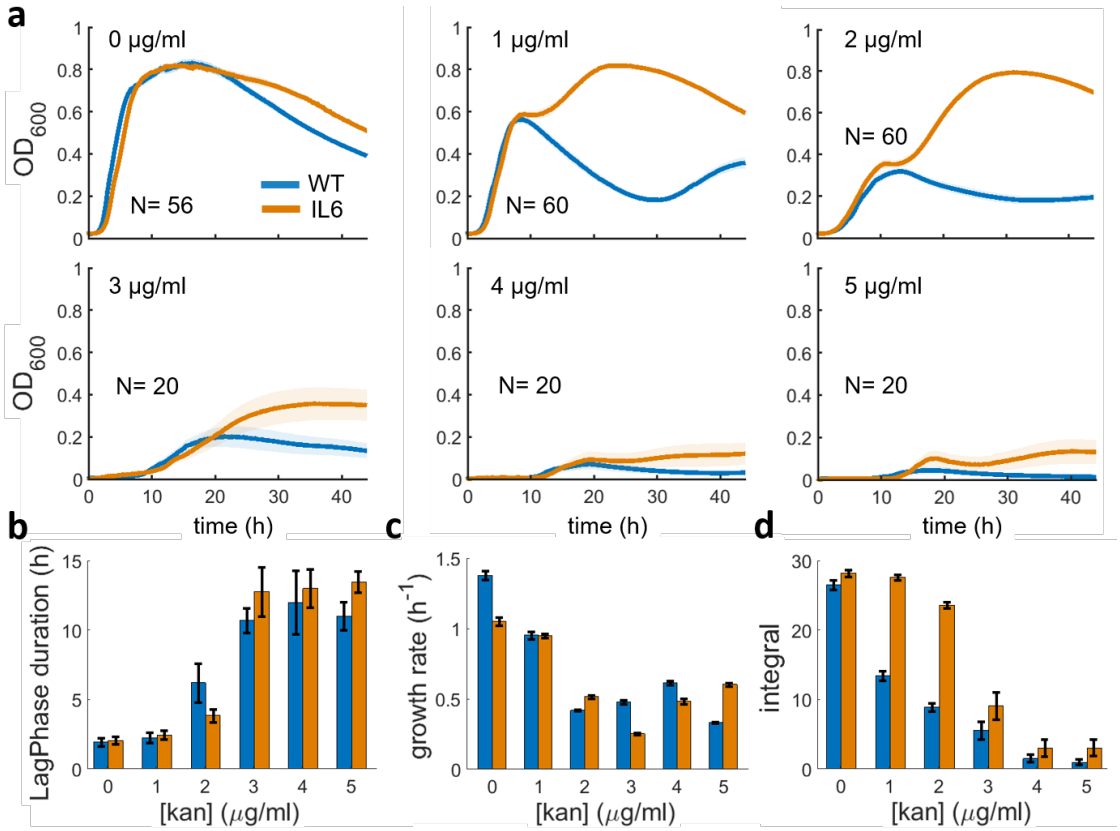

Figure 4.7: **Growth curves and quantification of lag phase, growth rate and integral for WT and IL6**. a) The OD of WT and IL6 was measured for 44 h in a 96 well plate for different concentrations of kan, from 0 to 5 μg ml^{-1} . The curves show the average and standard errors of the correspondent number of samples indicated as N in the figures. We see a clear difference between the general behaviour of IL6 with respect to the WT, specially at 1 and 2 μg ml^{-1} . b) The lag phase of each of the curves was calculated by eye. There is no significant difference between the samples but we see how the lag phase increases with higher concentrations of kan and saturates for 3 μg ml^{-1} . c) Growth rate of the curves calculated as the slope of the straight line fitted to the logarithm of the OD. The growth rate was calculated for the mean of the curves and the error given is the error coming fromt the fit. d) The area under the curve (integral) shows a clear difference between WT and IL6 in presence of kan, especially at 1 and 2 μg ml^{-1} of kan. The integrals were calculated for 5 representative curves and the errorbars showed the standard error of the mean.

became larger between m and WT but there was no difference between m and IL6. At 3 μg ml^{-1} , the lag phase for m became larger than for WT and IL6 but the difference was not quantifiable due to the great variability among the samples.

For the growth rate, the differences between m and the other two strains were larger. In absence of kan, m behaved similar to the WT and it grew faster than IL6 (Figure 4.8c). In 1 μg ml^{-1} of kan, the difference in growth rate was equal for IL6 and WT, and m grew faster than both of them, probably because it was originated at that concentration. Increasing kan concentration at 2 μg ml^{-1} made the growth rate more similar to IL6 than to WT but still the last two strains grew slower. Again, at 3 μg ml^{-1} the differences were not quantifiable due to the large variability in the growth curves.

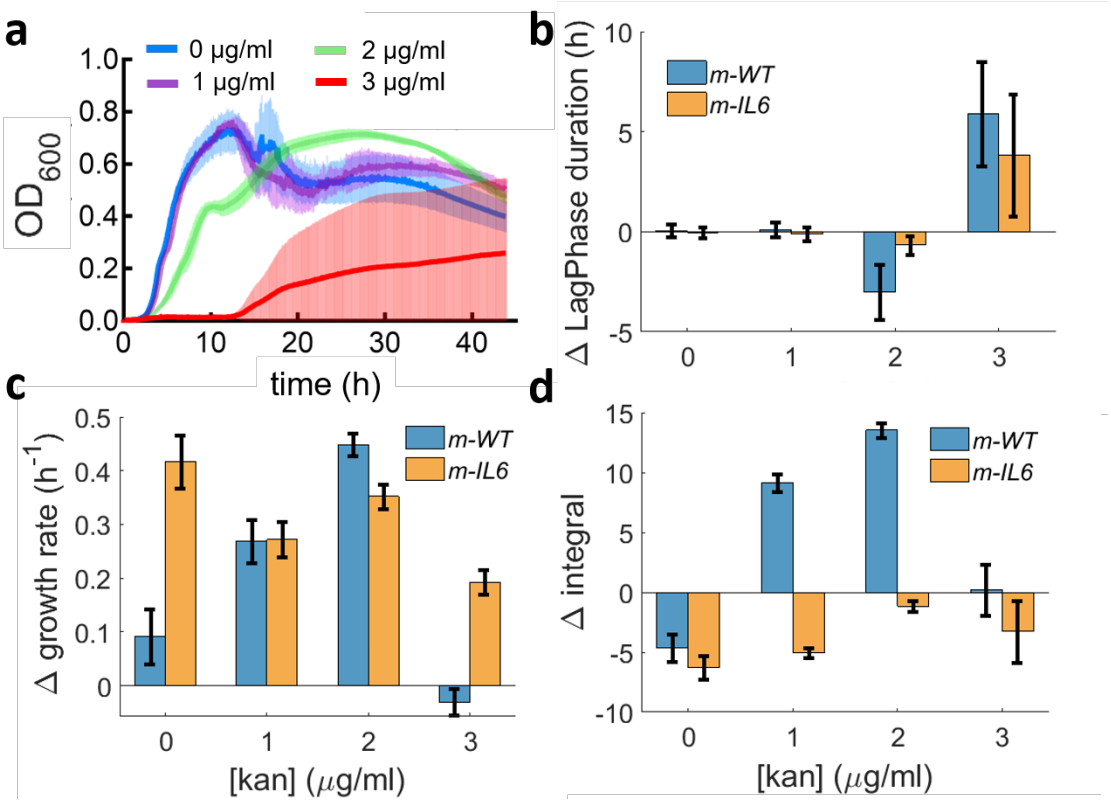

Figure 4.8: **Growth features of the WT exposed for 42h to 1μg ml^{-1} of kanamycin.** a) Growth curves of the WT exposed for 42h to 1μg ml^{-1} of kanamycin (m). The curves represent the mean and the standard error for 10 samples in absence of kan and 15 samples at 1, 2 and 3 μg ml^{-1} . b) Difference in the lag phases between the new strain m and WT and m and IL6 at 0, 1, 2 and 3μg ml^{-1} of kan. The errorbars represent the result of the propagation of uncertainties of the standard error of the mean. c) Growth rate differences between m-WT and {emphm-IL6 at 0, 1, 2 and 3μg ml^{-1} of kan. The error bars are calculated by propagating the uncertainties of the errors associated to the fit to calculate the slope. d) Growth rate differences between m-WT and {emphm-IL6 at 0, 1, 2 and 3μg ml^{-1} of kan. The errorbars represent the result of the propagation of uncertainties of the standard error of the mean.

Finally, the differences in the integral, which was the magnitude that showed the largest difference between the WT and IL6, were the same for both strains in absence of kan. At 1 μg ml^{-1} of kan, the difference was 2 times shorter between m and IL6 than for m and the WT. Here we can already see that also in this strain m, the main adaptation is a higher sustained growth in comparison to the WT. At 2 μg ml^{-1} , there is no difference between m and IL6 whereas the difference with respect to the WT was the largest of all the concentrations tested. For higher concentrations of kan, the high variability made difficult to judge the similarities between the strains.

In conclusion, the colonies which appeared in the kan gradient had a different phenotype than the WT. This was mostly reflected in how much they could sustain their growth along time in presence of low concentration of kan. When a new strain was created just by exposing it to sub-lethal concentrations of antibiotics for 44 h, its integral in presence of kan was closer to the colony picked from the kan gradient than to the WT. Therefore,

the advantage of these strains with respect to the WT seemed related to the total growth over time and not to how quickly they grew in presence of kan.

4.3 Discussion

Our method to study mutagenesis in antibiotic gradients has proven to be useful at identifying the different mechanisms of antibiotic resistance. Once the colonies emerged in the swarming front, we could map their resistance and study the genotypes and phenotypes associated to it. Previous research which focuses on mutagenesis has the main limitation of working with liquid culture, where the concentrations of antibiotic tested are limited. In liquid culture, some relevant antibiotic concentrations that promote different mutations could be missed, This would not happen in a solid gradient. Potentially, our experimental set up makes possible to study individual mutations in a continuous band of antibiotic concentrations. Taking into account that each emergent colony comes from a single bacterium with a specific adaptation to the antibiotic, this method allows the characterization of the geno and phenotypes of tolerant bacteria at single cell level. Potentially, this could complement more complex techniques of single cell characterization tools such as microfluidics [176, 177].

Thanks to this set up we also identified colonies that can emerge and survive gradients of antibiotics without developing resistance, understanding resistance as growing with the same curve profile in presence of antibiotics, but just sustaining their growth over time. This points out to a different mechanism, widely neglected, that the cells can use to grow in antibiotic gradients. We discovered that this mechanism is not necessarily correlated to genetic mutations that the bacteria developed, although further research needs to be done to prove this point. Thus, a possible explanation could be persistence, a mechanism where a subpopulation of bacteria with low metabolic rate can survive to antibiotic exposure [178]. This could explain why the resistant microcolonies were only partially resistant to the antibiotic since the microcolony itself could be formed by two subpopulations of bacteria, the sensitive population and the persisters [178]. However, it is well known that persistence is not heritant but the microcolonies seemed to pass the resistance to further generations [179]. Moreover, persistence is not antibiotic specific since it is just based on the metabolic rate of the bacteria but the selected microcolonies were only resistant to antibiotics related to previous exposures [178]. Finally, persisters normally start regrowth after antibiotic removal [180]. Nonetheless, our characterization of cell growth indicates that the microcolonies were able to grow in presence of antibiotic, just after a longer lag

phase. This indicates that further studies need to be done to discover the mechanism behind the resistance we observed.

It is also interesting that all the colonies that appeared in presence of kan presented a higher susceptibility to spectinomycin, independently on whether they were resistant to the kanamycin or not. A possible explanation for this is that sub-lethal concentrations of kanamycin leads to the 70S unit of the ribosome to split in the 50S and 30S subunits even without killing the bacteria [181]. This could increase the effect that spt has when it binds to the 16 rRNA in the 30S subunit and stops the translocation. Another possible hypothesis is that spt uptake is increased after kan exposure. Aminoglycosides are known for changing the cell's membrane potential so the changes produced by kan could increase the uptake of spt [181, 182]. However, how bacteria would pass this mechanism throughout generations remains unknown.

This discovery is crucial as a first step to identify weak points in multridrug resistant bacteria. One of the common results in antibiotic exposure history is that bacteria become weaker when exposed to sequences of antibiotics that target a completely different process within the cells [167]. Nevertheless, this chapter presents a new way of fighting multidrug resistant strains with antibiotics that target the same process as the ones that become resistant to. Potentially, this combination of antibiotics would be less harmful for the patients in a real treatment since the concentration of spt which is necessary to inhibit the resistant bacteria is 10^6 times lower than to kill the WT.

Chapter 5

Conclusions and future work

Our full understanding of bacterial collectives and the mechanisms that they use to increase their tolerance to antibiotics is essential to battle the fight against antimicrobial resistance. The potential rise in tolerance of bacterial collectives has been shown to come from a variety of emergent properties: diffusive barriers [50], reduced uptake of antibiotics through necrosignalling [119], cooperative behaviour [65, 67], etc. and many emergent properties remain still unexplored. In this thesis, we yet have unravelled new emergent properties which bacterial swarms can use to increase their resilience against antibiotics.

We have shown that swarming bacteria can become more resistant to antibiotics by an unexpected transition to biofilms. Here, we demonstrated that such transition can be induced either by antibiotic gradients or by physical barriers that promote local accumulation of cells. This local accumulation starts with a localized phase separation compatible with MIPS, a novel phenomenon predicted by the theory of active matter.

A further characterization of the phase transition demonstrated that swarming bacteria can phase separate through two different mechanisms, depending whether they were in presence or absence of antibiotics. These two possible phase separations resembled nucleation and growth in presence of antibiotics and spinodal decomposition in absence of stress. The quantification demonstrated that the evolution in time of the emergent nuclei matched the dynamic scaling exponents of previous studies using bacteria and active particles to characterize cluster aggregation [84, 83, 64]. Now that the experimental evidence has been given, it would be interesting to see if numerical models could explain exactly how these two different phase separations happen in the swarm. For that, approaches going beyond the current mean-field models describing phase transitions in active particles for a fixed cell density are needed. We demonstrated that our system is influenced by the increasing number of particles coming either from cell replication or from other regions of the swarm. Numerical models implementing birth and death are emerging to study

self-organization among motile bacteria [183, 184]. Further development of these models can provide a better characterization of the described phase separation and presumably reveal novel phenomena that could potentially have biomedical or industrial implications for other active matter systems with increasing number of particles. One of the possible applications, that we also characterized in this study, could be linked to the active transport by bacterial multilayers.

Alternatively to the transition from swarm to biofilm, we saw that swarming bacteria could also develop resistant colonies when biofilm formation was not possible. We suggest that the origin of the resistant colonies might not be linked to genetic mutations even though it can be heritable. After detailed analysis of the resistant colonies, we observed that the increase in resistance comes with a price, and that the emergent colonies become more susceptible to other antibiotics. Inspired by the gained knowledge, we proposed a way to tackle the rise in resistance consisting on a dual-antibiotic treatment, where the first antibiotic, in this case kanamycin, triggers the resistant colonies, and the second antibiotic, spectinomycin, can kill them by using concentrations much lower than for the WT, minimizing the dose of antibiotic required. When the transition from swarms to biofilms is possible, we have also proposed a new treatment to reduce this transition. Instead of increasing the total amount of antibiotics, ineffective at preventing wrinkly biofilms, we demonstrated that splitting the dose in two steps, giving a first low dose and then a higher second dose during multilayer formation, substantially reduced the emergence of the biofilm. These two methods suggest novel strategies of combining and administering antibiotics to tackle the antimicrobial resistance problem which could be clinically relevant.

Every discovery opens new questions. Although we showed a possible transition from swarming to biofilm and we gave a possible mechanism behind this transition, our study is only correlational and further work needs to be done to understand exactly how the multilayer formation results in a wrinkly biofilm. We suspect that after the islands and the first layer formation, swarming bacteria keep generating new islands in further layers and the interspaces between these islands result in wrinkle development. The more multilayers, the higher the biomass of the islands and therefore the greater the stress between adjacent islands. Previous studies have shown that this stress is essential to produce buckling and lead to wrinkle formation [185].

Intriguingly, the mechanism behind the islands elongation is not well understood. We suspect that the islands become elongated because bacteria keep producing surfactin which decreases the surface tension and helps the spread of the swarm. A way to test this could

be using a surfactin knock out strain and add the surfactin externally. In this way, the expansion of the colony can be controlled since the final size of the swarm, i.e. how far it can spread, will depend on the concentration of surfactin added. Once the swarm reaches the maximum size, islands would appear since cells would continue to replicate. In this way, the formation of islands could be observed decoupling the effect of the colony expansion. If the elongation of the islands did not happen in this scenario, it would indicate that the elongation in our assays happen because of the swarm expansion.

An important direction not only to understand island elongation but also how they form could come from the modelling side. In the kan case, our experiments suggest that island formation happens where bacteria are still motile (and therefore not completely killed by the kan) and where cell accumulation due to healthy cells coming from unexposed regions of the swarm meet the immotile lawn killed by kan. In this regard, models of MIPS with an increasing number of particles would be crucial to understand exactly how island formation happens. To study the island elongation, those models could include a global translation of the monolayer, simulating the effect of the colony expansion due to surfactin.

Alternative theoretical frameworks exist that could be relevant to characterize island formation. A remarkable example is buckling instabilities due to nematic alignment, such as the ones characterized in expanding colonies of P. aeruginosa in [105]. Nevertheless, according to [105], these buckling instabilities are only relevant for particles moving at low speed. Indeed, *P. aeruginosa* in [105] is moving at 10 μm/min whereas our swarming *B. subtilis* Moves at $\sim$ 50 μm/s. This is also the case for the buckling instabilities driving fruiting body formation in *M. xanthus* since the velocity in this system is 1 μm/min. Therefore, we expect that nematic alignment is less relevant in our system. This is supported by the fact that our data matches the MIPS region for a system of active rods, pointing towards a motility-induced mechanism to induce the multilayers. To finally confirm whether nematic alignment could play a role in island formation, more studies at single cell level of swarming *B. subtilis* and a numerical model would be necessary.

Although our study used swarming *B. subtilis* as a model organism, the phenomenology discovered here can span through different length scales and organisms. Particularly interesting is the case of sperm. In sperm, the physical magnitudes such as swimming speed are linked to the fertility and sperm group dynamics can facilitate egg fecundation [186]. During fecundation, sperm also faces different stresses and move on top of a surface which resembles the situation studied here. Another example where emergent phenomena in collective migration might become relevant is during cancer invasion or embryo development where cohesive cell groups form complex tissues and organs. Here, different

multicellular dynamics result in different tissues with different resulting shapes and functions [187]. One common model organism to study mammalian cell locomotion is amoeba that sometimes forms group of organisms called a "slug". In this group motility, amoeba shows a polar ordered phase which can undergo phase separation [188]. Therefore, the study of emergent behaviours observed in this thesis and applied to other groups of living organisms moving on surfaces could be an interesting research direction.

Moreover, in our studies we observed that there could be a hidden variable that helps the transition. In this thesis we have already explored some environmental cues such as temperature and humidity which did not seem to affect the outcome. Changing the agar concentration of the media and, hence, its stiffness, did not seem to affect the result either. Swarming *B. subtilis* is quite sensitive to the stiffness of the surface and, lowering the agar concentration below 0.4% or increasing it beyond 0.8% inhibits swarming. We tried a range of concentrations within this window but we did not observe a clear effect on the wrinkle development. Other parameters that could play a role are the concentration of Manganese and Glycerol in the media since these have been reported to affect biofilm formation [189]. We tuned mainly the concentration of glycerol in the plate which affected the formation of the biofilm as a whole, i. e. it induced more biofilm formation even in absence of any stressor. This resulted in a poor distinction between the biofilm formed due to a stressor (kanamycin or barrier) and the biofilm formed in the background (regions of the plate away from the stressors), just due to the high concentration of glycerol. An unchecked environmental variable is the pH of the media which might change depending on the metabolic processes that the bacteria undergo and that could be key in biofilm formation. In our assays, we often observed a change of color in the agar, indicating that bacteria do not always follow the same metabolic route [190]. It is unclear whether this change in color is related to the actual pH but we believe that it could be related to the ion abundance. Specifically, iron content is highly linked to the color of the agar and, when it drops below a certain threshold, it can hinder biofilm formation [190]. Varying the concentration of iron in the media could shed light onto the transition from swarm to biofilm. Another promising direction would be to monitor oxygen levels, since enclosing the swarm with a hollow or a standard lid highly affected wrinkle formation as shown in Figure 7.5 and Figure 2.10a. The main difference between the two enclosures is the air flow that bacteria might feel so this could be correlated with oxygen levels within the swarm. To test this, the same assay could be repeated in an environmental chamber where the exact air composition is known and the oxygen levels could be tuned to see how that would affect biofilm formation. Finally, we explored whether this hidden variable

could be linked to cell death which was demonstrated to facilitate buckling and hence wrinkle formation [126]. Here, our studies could not find an increase in sytox signal prior to wrinkle development (Video sytox). However, this could mean that cell death is not as essential in wrinkle formation for swarming *B. subtilis* as for planktonic *B. subtilis* . The mechanical properties of the swarm and of a confluent layer of planktonic bacteria are very different due to the fluid-like behaviour of swarming and due to the properties of the substrate, softer for the swarming case. All this suggests that the conditions to trigger wrinkle formation in swarming bacteria and planktonic cells might be different. This could be an interesting area of future research and we encourage studies of how wrinkle formation can happen beyond the traditional solid-air biofilm.

Curiously, another open question of our study is why we have never observed the transition to a biofilm and the development of resistant microcolonies simultaneously. Even in the experiments with biofilm promoting media where biofilm formation was not observed, emerging colonies appeared near the antibiotic when biofilm failed to emerge, discarding the fact that the media affects the decision between these two phenomena. Thus, it seems that the swarm 'chooses' one of the paths to become tolerant to the antibiotic, either through the development of resistant colonies or through biofilm formation. Studying the key factor that triggers this decision could shed light onto unknown environmental cues that swarms can use to increase their resilience against stress.

In addition, the mechanism behind the increased tolerance of the microcolonies is unclear. We have shown that the bacteria mutate upon exposure to sub-lethal concentrations of antibiotics but these mutations are not directly linked to antimicrobial resistance. This opens the question of the preferred mechanism that swarmers use to tolerate antibiotic gradients. One of these mechanisms could be persistence, where a bacterial population is split in two subpopulations of actively growing cells and dormant cells [178]. As antibiotics target important processes in the life cycle of bacteria, dormant cells are not generally affected by those since they are metabolically inactive [191]. These bacteria can become active once the antibiotic is removed and generate a new population of sensitive cells. This also means that persistence cannot be heritant which is in contradiction with the assays carried out in this study [179]. A more likely explanation would be heteroresistance, which happens when some cells within a population remain sensitive to the antibiotic while others present different levels of resistance [6]. The origin of these subpopulations of resistant cells are stress-induced mutations upon exposure to sub-lethal concentrations of antibiotics. This could explain why the microcolonies were able to pass the resistance to future generations and why the resistant is antibiotic specific, i. e. to drugs that target

similar processes within the cells.

It would also be interesting to understand if the transition from swarm to biofilm could occur in physiological conditions. We now know that swarming bacteria can be found in mice instestinal tissues [42]. The intestine is host of the most abundant bacteria reservoir in our body: the gut microbiome. During infection, antibiotic treatment affects the gut microbiome and several studies suggest that these treatments make a long-term or even irreversible disruption in the gut [192, 193]. Since swarming bacteria can exist there, it is possible that some of the irreversible effects in the gut could be due to a permanent change in the bacteria lifestyle upon antibiotic exposure such as the transition from swarm to biofilm. Testing whether this transition is possible in the gut under exposure to sub-lethal concentrations of antibiotics and how could potentially affect the host, is an exciting and unexplored research line.

More widely, the gut is host of a diverse microbial community where multiple microorganisms such as bacteria, virus and fungi coexist together [194]. Thus, the phenomenon of MIPS could be relevant in microbial ecology since it could be triggered by the stress caused by other microorganisms. For example, fungi hyphae could act as physical barriers which promote local accumulation of bacteria that ultimately give place to biofilm formation. Thus, it would be interesting to test this scenario just using a simple agar plate and observing whether the hyphae can trigger MIPS in swarmers. Apart from this physical accumulation, fungi and bacteria are in constant competition for space and nutrients [195]. Thus, inter kingdom interactions give place to the release of toxins that could resemble the kanamycin gradient in our assays.

Chapter 6

Methods

6.1 Creating and characterizing the kanamycin gradient

6.1.1 Kanamycin gradient assay

-80°C glycerol stock of *B. subtilis* NCIB3610 wild-type strain (WT) was streaked on a lysogeny-broth (LB) 1.5% agar plate and grown overnight at 37°C . When specified in figure caption, a genetically modified strain (listed in Table 7.9) was used instead of WT. A single colony was picked from this plate and incubated in 1 ml of liquid LB for 3 h at 37°C . A 4 μl inoculum from this culture was placed in the center of a 0.5% LB agar plate supplemented with glycerol ranging from 1-3% and 0.1 mM MnSO4 (LBGM [189]) to promote biofilm formation. Notice that the change in glycerol concentration could have changed the properties of the media. An increase in glycerol from 1 to 3% could lead to a change in viscosity of a 5.8% (calculated in http://www.met.reading.ac.uk/ sws04cdw/viscosity$_c$*alc.html*). A kanamycin diffusive disk (Oxoid^{TM} 30 μg) was placed on a side of the plate 24 h before inoculation to allow the antibiotic to diffuse at room temperature. The distance between the inoculum and the kanamycin disk was approximately 3.2 cm, and plates were incubated for additional 40 h after inoculation at 30°C .

6.1.2 Estimation of the kanamycin profile on the swarming plate

The concentration profile of the kanamycin in the plate (Figure 2.2b) was characterized by using a variation of the Kirby-Bauer assay [196]. 800 μl of a 18 h bacteria culture at 30°C was inoculated in 3 plates containing LB with 1.5% agar. Immediately after, disks containing 0.1, 0.2, 0.4, 0.78, 1.56, 3.13, 6.3, 12.5, 25, 50, 100, 150 and 200 μg of kanamycin were placed on the surface of separate confluent LB agar plates. After an incubation of

24 h at 37°C , we measured the diameter of the clearance region around the disks. Each measurement was done in triplicates. The logarithm of the mass of kanamycin added was plotted against the difference between the diameter of the clearance region and the diameter of the disk. This calibration curve was then used to characterize the kanamycin profile in both the swarming and the biofilm-inhibition assays. For each replica agar plate, a 3 mm diameter biopsy puncher was used to extract 5 small samples in a range of 0 to 2 cm every 0.5 cm distance from the kanamycin diffusive disk. The agar punches were then placed on top of a confluent plate of WT *B. subtilis* and incubated overnight at 37°C . We then measured the clearance around the pads and used the local linear fits to the calibration curve to estimate the (logarithm of) total amount of kanamycin within the punch. This was then divided by the volume of the punch to estimate the concentration.

6.1.3 Quantification of the speed at the swarming front

To calculate the speed at the swarming edge (Figure 2.2c), the position of the front closest to the diffusive disk was recorded over time with a DSLR camera (Nikon D5300; lens AF-S Micro NIKKON 40 MM 1.28) at 37°C . Consecutive frames were subtracted to highlight the position of the front. This was then used to estimate the front's speed on both the kanamycin side and the opposite side of the agar pad using the inter-frame time of 5 min. From these time lapses we also extracted the distance at which the swarming front halts from the kanamycin disk.

6.1.4 Calculation of the Minimum Inhibitory Concentration (MIC)

A single colony of *B. subtilis* was incubated in 1 ml of LB overnight in a shaking incubator at 37°C . The OD was measured 18 h later and the culture was diluted down to an OD of 0.0085 and incubated for 18 h in 5 concentrations of kanamycin from 1 to 5 μg/ml. The MIC was determined as the minimum concentration at which growth was not observed in the liquid culture. Each well plate had 5 replicates and the experiment was repeated at least 3 times for each concentration.

6.2 Biofilm formation and wrinkle quantification

6.2.1 Images of swarming plates

Low magnification images of the plates were acquired with a DSLR D5000 Nikon camera (lens AF-S Micro NIKKON 40 MM 1.28) in a 30°C incubator. The incubator was covered by black tape to avoid reflections and the illumination was provided by a white LED

placed on a side of the plate or just a simple lamp. Higher magnification images (e.g. of wrinkly biofilms) were taken by an Olympus SZ61 microscope by placing the plates in a dark background with illumination coming from a LED ring attached to the microscope.

6.2.2 Distance from wrinkles to kanamycin disks of different concentration

To characterize how the distance between the kanamycin disk and the wrinkles depends on the initial antibiotic concentration within the disk Figure 7.1, diffusive disks containing 30, 100 and 200 μg of kanamycin were placed on 2-3% glycerol LBGM agar plates. To create the disks, Whatman filter paper was punched with a hole puncher (diameter 7 mm) and imbibed with 0.6, 2 or 4 μl of a 50 μg/μl kanamycin solution in water. The minimum distance between the kanamycin disk and the nearest wrinkles was measured in 6 different experiments for 30 μg and 200 μg of antibiotic and one experiment with three replicates for 100 μg .

6.2.3 Biofilm formation in solid agar near the kanamycin

To check whether wrinkle formation was promoted also in absence of motility near the kanamycin diffusive disk, the kanamycin diffusive assay was repeated in 1.5% agar. To do so, a kanamycin diffusive disk was placed on a side of the solid agar LBGM (2% glycerol) plate, like in the swarming assay. After 24 h a single colony of *B. subtilis* was incubated in 5 ml of LB for 3 h. 700 μl of this culture was spread on each solid agar plate and then incubated for 40 h at 30°C . We also checked the wrinkle formation in 1.5% agar by spotting 4 μl of the bacteria culture without spreading them to see if wrinkles were promoted in the wrinkly biofilms that appear when bacteria are spotted in hard agar. In total, 4 different colonies were spotted on the plate: the closest one was spotted 2 cm away from the kanamycin disk, other two spots were placed 2 cm to the right and the left of this central spot and finally, a last colony was spotted 6 cm away from the kanamycin disk (Figure 2.5b).

6.2.4 Measuring the width of the band where wrinkles appear

The width of the band where wrinkles appeared around the kanamycin disk was measured for three independent experiments using 30 and 200 μg of kanamycin. The width was determined by drawing a line across the band where the wrinkles appeared.

6.2.5 Quantification of the *PtapA-yfp* reporter

Biofilm extracellular matrix production was characterized by using a modified strain carrying *PtapA-yfp*, a fluorescence reporter for the expression of *tapA-sipW-tasA* operon. The kanamycin gradient assay and the barrier experiments were repeated by inoculating this strain in LBGM (1% to 2% glycerol) swarming agar plates. Images of the plates were acquired every 30 min over a total approximate period of 40 h. The images were taken in brightfield channel first and then in the fluorescent channel, using an approximate excitation wavelength of 480 nm and an emission filter of 535 nm. The BF images were used as a template to stitch them together using the "Grid/Collection stitching" plugin [197] in Fiji [198]. The experiment was replicated three times for the kanamycin case with three different lenses and microscopes: 2x (Nikon Apo Lambda 2x UW, NA 0.1), 2x (Nikon Plan 2x UW, NA 0.06), 2.5x (Leica 2.5x N PLAN, NA 0.07); microscopes: two Nikon Eclipse Ti2 and a Leica DMi8. For the barrier case the experiment was repeated 4 times and it was performed in the Nikon Eclipse Ti2 using 2x (Nikon Plan 2x UW, NA 0.06). Images were taken in a region of 3x9 cm^2 going from the disk to the inoculum. The experiment was repeated three times in absence of kanamycin with the first two microscopes and lenses. To calculate the fluorescent signal, a region of interest was drawn in Fiji around the area where the wrinkles appeared, normally found just at the edge of the depletion region created by the kanamycin disk or just right next to the physical barrier. For the kanamycin assay, the signal was normalized by subtracting the minimum value of pixel intensity recorded in the time-lapse and dividing by the maximum of the signal for each of the microscopes to account for the difference in signal of each microscope. In the barrier case, all the experiments were performed with the same microscope and lens, so the normalization is not needed and the raw signal is shown.

6.2.6 Quorum sensing experiments

The same protocol explained in the section 'kanamycin gradient assay' was also used to investigate the swarming behavior, the formation of islands and the biofilm development of the two quorum-sensing knockout strains: Δopp and $\Delta hprc$. Formation of islands and biofilm images were acquired as explained in previous sections.

6.2.7 Physical barrier

A 3% agarose solution in water was autoclaved and then poured in a Petri dish. Once it solidified, a rectangular region (6 cm x 1 cm) was cut out and placed vertically on a molten swarming liquid LBGM (0.5% agar). After the system solidified, swarming bacteria were

inoculated in the centre of the plate. Different barriers and barrier geometries were tried. For example, another common barrier was the stick of an inoculation loop placed as the agarose barrier. We also tried putting two of these sticks forming a triangular shape. Finally, a small petri dish with a whole in it was used for a circular confinement. All the confinements gave similar results. Videos of the formation of islands were recorded under 2x (Nikon Plan 2x UW, NA 0.06) in a Nikon Eclipse Ti2 microscope.

6.2.8 Biofilm inhibition assay

4 μl of the antibiotic kanamycin coming from four different stocks at concentrations of 50, 37.5, 25 and 12.5 μg/μl were added to four different diffusive disks. The diffusive disks were then placed on a side of four different LBGM 0.5% agar plates for 24 h. After inoculation, the plates were incubated at 30°C for roughly 6 h until the swarming front halted due to the kanamycin gradient. Then, additional 4 μl of the second stock concentrations of kanamycin were added to the initial ones. For the four concentrations above, these were respectively 0, 12.5, 25 and 37.5 μg/μl. As a result, the total amount of kanamycin administered was kept constant and equal to 200 μg .

6.2.9 Wrinkle wavelength quantification

To measure the wavelength of the wrinkles we calculated the interdistance of nearest parallel wrinkles. When this was not possible, the wavelength was estimated by calculating the autocorrelation function of image intensity in space using a Fiji macro made by Michael Schmid (https://imagej.nih.gov/ij/macros/RadiallyAveragedAutocorrelation.txt) (2008) and then fitting the decay of that function to a double exponential of the form:

$$f(x) = ae^{bx} + ce^{dx}. \tag{6.1}$$

Here, the two characteristic wavelengths (1/b and 1/d) correspond to the image noise and the actual wrinkle wavelength respectively.

6.2.10 Roughness measurements for wrinkles

A 50 pixels wide strip was drawn over the wrinkles and then the intensity profile was extracted using 'Plot profile' in FIJI. The roughness of the profile was defined as:

$$roughness = \frac{\sum_i^N (I_i - \bar{I})}{N} \tag{6.2}$$

where I_i is the intensity of i-th pixel in the profile, $\bar{I}$ is the mean of the profile obtained using the 'smooth' function in Matlab and N, the total number of points in the profile.

6.3 Motility of the swarming monolayer and the phase diagram

6.3.1 Raft size

The size of the rafts within the swarm were obtained from three different experiments. A freehand line was drawn with Fiji/imageJ [198] enclosing the raft to measure the area. Previous studies have reported that the raft sizes change depending on the region of the swarming colony and also on the time since inoculation [44]. Therefore, measurements across different positions and time points were used to account for the variability in the size.

6.3.2 Motility and cell density of the monolayer

Timelapses of the monolayer were recorded with a 40x objective (Nikon 40x LWD, NA 0.55) at 37°C . Cell motility was measured by adapting a Particle Image Velocimetry (PIV) code written in Matlab [199]. The surface coverage was measured by thresholding the images and dividing the area covered by bacteria by the total area of our field of view. The threshold was set by using the command 'imbinarize' in Matlab and adapting the sensitivity of its threshold to account for the best estimate of cells in the field of view.

6.3.3 Phase diagram

To calculate the phase diagram plotting the rotational Péclet number (Pe_r) with respect to surface coverage, time-lapses of swarming bacteria coming from 6 different experiments were analyzed. The 'jammed bacteria' data plotted in the diagram (Figure 2.8a) were calculated by analyzing the 4 s of the time lapse prior to jam formation. Videos were acquired at 29-33 fps. The average speed within the swarm was calculated as described earlier and used to then calculate the Pe_r, defined as:

$$Pe_r = \frac{u}{LD_r} \tag{6.3}$$

Where u is the average cell speed within the swarm for a given time point, L=0.823±0.016 μm the average width of the swarming cells, as used in [1], and D_r is the rotational diffusivity of the bacteria. For swarming cells, the rotational diffusivity cannot be measured

directly. Therefore we decided to use, as estimate for D_r, a value such that the Péclet number of our system and that in [1] coincide at surface coverage 0.65. This is the surface coverage at which the MIPS start in the numerical simulations of 2D disks. This returns $D_r = 0.81(0.19)s^{-1}$, from an average of 13 different values from 3 independent experiments. To check whether this result was sensible, we then resuspended in water a sample of swarmer cells from a plate and extracted the rotational diffusivity of motile cells from a 10 s movie, with a Python-based tracking code which measures position and orientation of elongated objects [200]. The gradient of the angular mean-square displacement of the tracks returned a value of $D_r = 0.35s^{-1}$. Although this is slightly lower than the previous result, it should be kept in mind that the former estimate is for cells that are moving on an agar surface.

Notice that, Pe_r in [1] is obtained from instantaneous velocities of individual particles, which were challenging to follow within a swarm. Therefore, we used an effective Pe_r derived from the local average velocity within the swarm. This is likely to overestimate the value of Pe_r of the experimental points.

For the phase diagram of the monoloyer during islands formation, 4-5 s videos of bacteria monolayer were analyzed at different points of the swarm depending on the three conditions studied: blank, barrier and kanamycin. To make the trajectories, the speed and surface coverage were measured at the same ROI over time.

6.3.4 Near UV experiments

Bacteria were irradiated by near UV-Violet light for 30 s using the inverted microscope DMi8 (Leica Microsystems) and the LED light source, SOLA SM II Light Engine (Lumencor), with an excitation filter 400/16 using a 40x objective (Leica 40x PH2 HC PL FLUO, NA 0.6) for approximately 3.5 minutes at an intensity of 1.2 to 5.3 mW/mm^2. The light intensities were measured by placing a photodiode power sensor (Thorlabs S120C) on the microscope stage. To irradiate a larger area than the one with the epi-fluorescence set up, a Thorlabs 405 nm light LED was coupled to a cage cube (see Table 7.10 for details about the components of the set up). The light coming from the LED was concentrated by an aspheric condenser lens and reflected by a 45^o dichroic mirror towards the sample. The area illuminated is roughly a circle of 2.5 mm radius at an intensity of 1.5 mW/mm^2. The surface coverage was calculated by binarizing the time lapses applying a locally adaptive threshold in Matlab. The sensitivity of such threshold was changed during the time lapse since the same value of the threshold could not account for the total number of particles due to the rapid increase in cell density.

The trajectories of the swarming bacteria plotted in the phase diagram were extracted by calculating the Pe_r and the surface coverage as detailed in the previous section. In the case of UV exposure, trajectories are the result of continuous irradiation with either of the setups previously described. When illuminated by the epifluorescence the trajectories were plotted until a jamming event was observed in the field of view. When irradiating UV from the condenser, the trajectories were plotted until bacteria were completely immotile, as jamming events never happened. Data for speed and surface coverage of bacteria has been smoothed over 8 and 100 points respectively by the 'smooth' function in Matlab.

6.4 Multilayer characterization in the swarm

6.4.1 Islands geometry

To characterise the islands size and shape, time-lapses of islands formation in presence and absence of kanamycin and with a physical barrier were recorded. The period of acquisition was nearly 2 h with an interframe time of 1 min. The first frame (just before the islands appeared) was subtracted to the time-lapse and then a gaussian filter was applied to remove noise. To create a wide region to track the evolution of the islands, we stitched several field of views with the "Grid/Collection stitching" plugin [197] in Fiji [198]. Depending on the microscope and image quality, the resulting stitched image showed differences in background pixel intensity across the different stitched images. To homogenize the background in the field of view, a bandpass filter was used. Even after this pre-processing the islands were difficult to threshold specially in the barrier and blank cases. To overcome this problem, we used ilastik [201], a machine-learning based software. Here, the features relevant to distinguish the islands from the background are chosen and then lines are drawn manually to help the software distinguish between the islands and the background. The output is a layer of probabilities that can be thresholded to create a binary image. This binary timelapse is read by Matlab and here the islands below a threshold size are discarded away, to remove spurious noise from the videos. Finally, the islands sizes were measured by using the command 'regionprops' in Matlab. To determine the aspect ratio, we used the same command to obtain the 'MajorAxisLength' and 'MinorAxisLength' properties which are the two axis of an elipse fitted to the islands. The ratio between the major and minor axis lengths was defined as the aspect ratio of the islands.

The size of the stitched field of view for the blank, barrier and kanamycin were respectively: 5.31x5.31, 7x14.47 and 8.8x14.97 mm^2. The experiments in the blank and barrier cases were acquired using using 2x (Nikon Plan 2x UW, NA 0.06), 2x (Nikon Apo

Lambda 2x UW, NA 0.1) and 2.5x (Leica 2.5x N PLAN, NA 0.07) lenses in two different microscopes: Nikon Eclipse Ti2 and Leica DMi8. The experiments were repeated a total of 7 times for the blank case, 5 times for the barrier case and 3 times in presence of the kanamycin gradient. More replicates were made in all cases where the common features could be observed but there were not used for the analysis due to the lack of time resolution. As the size of the acquisition region for the blank case was around 5 times larger than the ROI used for the analysis, from each of the experiments we used more than a single region for the analysis giving a total of 20 samples. These 20 samples were averaged and their standard error was calculated, as for the barrier and kanamycin cases. To average the samples, we align them by calculating the second derivative of the size evolution and matching the maxima of this magnitude for the different experiments. The first 13 points and 11 points of the barrier and kanamycin respectively, were fitted to an exponential as $< s >= Ae^{t/t_0}$, where $< s >$ is the average value of the sizes, A is a constant, t is the time and t_0 is the characteristic time of the system. The blank case could not be fitted to these function. The linear regime in the log-log plot was fitted to a power law of the form $< s >= at^b$, where a and b are the parameters of the fit. Here, a total of 10 points starting from the 3^{rd} were fitted for the barrier and 19 points starting from the 10^{th} were fitted for kanamycin. Again, the blank case did not have a power law regime to be fitted.

6.4.2 Calculation of size and aspect ratios from the individual tracks

The tracking workflow in Ilastik was used to track the individual islands in the thresholded timelapses (see previous section). As input, Ilastik uses the raw timelapse and the probability maps generated in the pixel classification workflow. From here, a rough threshold is selected and then the next settings (with minor changes depending on the timelapse) were used: Maximum Object per Merger=1, Division Weight=100, Transition Weight=15, Appearance Cost=1, Disappearance Cost=500, Border Width=10, Transition Neighbourhood=2, Frames per Split=0 and solver=ILP. For details about the meaning of these parameters we invite the reader to check the ilastik tutorials online. This workflow tracks the trajectories of the islands in the timelapses and from there the properties of the objects such as the size and radii of fitted elipses to the islands can be extracted. These tracks were then aligned in Matlab. To align them, we select the longest track in the system and we look for the earliest common size to that trajectory in the other tracks. The position of the trajectory is then shifted as many time points needed to be aligned to the longest trajectory. Finally, the trajectories are averaged and the standard error is calculated. For the aspect ratio, the same alignment as calculated for the sizes is used.

6.4.3 Calculation of the complementary cumulative distribution functions (ccdf), the size histograms and the cluster size distributions

From the thresholded timelapses, the ccdfs were calculated using the 'cdfcalc' in Matlab. This function gives the cumulative distribution function so to obtain the complementary it is subtracted from 1. To obtain the histrogram of the sizes and the cluster size distribution, the sizes were grouped in 24 and 12 bins respectively, distributed logarithmically using the function 'logspace' going from 10^{-4} to 10^{3}, roughly the minimum and maximum sizes achievable by the islands in mm^2. The number of counts in each bin were normalized by the total amount of counts. For the aspect ratios, a similar protocol was followed with the only difference that the bins were distributed linearly, from 0 to 10.

The first 5 points of the ccdf (considered in general the linear region in a log-log scale) were fitted to a power law of the form cs^{α}. To calculate the distributions of the exponent α, the values outside an interval of 4 standard deviations from the mean were discarded. We also discarded the fits with $R^2 < 0.9$. For the histograms of sizes, the fit used is $Cs^a e^{s/s_0}$. Only the data belonging to the decay range in the size distribution functions were fitted, i. e. from the maximum of the histogram to the end. An alternative range of data going from the maximum to the minimum of the function was tried but it did not improve the quality of the fit so the original one was kept. To calculate the distribution of the exponent a, the values lower than 0.01 and higher than the mean plus 4 standard deviations were discarded. For the parameter s_0, the upper boundary was the same and the lower boundary was 0.0001 mm^2. For these both parameters, we also discarded values where $R^2 < 0.8$. Finally, we aimed to fit the cluster size distributions to:

$$c_s = A\frac{(x/t)^{v(s-1)}}{(1+x/t)^{w(s+1)}} \tag{6.4}$$

as derived in [157] and used in [83], which in our case did not fit our distributions.

6.4.4 Estimation of the nucleation rate

The number of islands that nucleate was calculated as the total number of islands whose size was below the median of the size distribution in a given timepoint. The number of islands resulting from this output was divided by the available area that they have to appear in the field of view, i. e. the entire area minus the area occupied by the islands in the previous frame. Alternative approaches to this method were tried. One of them was the strict definition of nucleation, meaning the new islands that appear in the field of view obtained by subtracting the number of islands between consecutive frames. The problem

that we encountered with this is that the islands start merging quite soon and hence the total amount of islands decreased not because the islands disappeared but instead because they merged. This resulted in a clear underestimation of the nucleation so we discarded it. Another approach was to use the individual tracks obtained from ilastik (see subsection 6.4.2). Thus, the nucleation would be given by the number of new tracks for a given time point divided by the available area. This gave a similar functional shape than the approach used here but it was not possible to use it for some of the timelapses in the blank case and for none of the timelapses in the barrier due to the impossibility of tracking the islands there. A further inconvenience was that once the islands merge, sometimes the software would count that as a new track. Moreover, the blank case has many untrackable islands -we refer here to islands that just nucleate and then disappear- which would not be counted by this method. The resulting curves for nucleation are the result of the average of 20 curves for the blank, 5 for the barrier and kan. The curves were aligned so the peaks of the nucleation matched across experiments.

To fit the functions we used an exponential fit for the blank and barrier cases. For kanamycin, the increase in nucleation was fitted to two linear increases with different slope and the decrease to another linear fit.

6.4.5 Structure factors

To characterize the wavelengths in the system, we calculated the Fourier transforms in the x and y directions. To do so, first the axis in the frequency domain were calculated and centered in 0. Then, the 2D Fourier transform of the image is calculated using 'fft2' in Matlab and then centered using 'fftshift'. From here, the sum of the real and imaginary components to the square is calculated resulting in a 2D matrix. This is necessary to compute the structure factors which are a mathematical description of a pattern. The structure factor contains information about the symmetries and periodic structures within the system [202]. To calculate the static structure factor for each component, we add all the values of this 2D matrix in the y direction to calculate the component x of the structure factor and we add the values in the x direction to obtain the y component. This process was repeated for each image in the timelapse so then the evolution of the structure factor over time can be calculated. The structure factor was then fitted to a sum of two gaussian functions, from one of which the characteristic wavelength was obtained as the inverse of the wave vector at the peak of the gaussian. A more simple fit to a single gaussian was also tried but since the structure factor's maximum is at wavenumber 0, the gaussian would fit around this peak instead of the characteristic wavelength. To calculate the distribution of

the wavelengths, the values greater than 3 mm were discarded, since they corresponded to wrong fits that did not fit any data set. The width σ of the structure factor was obtained from the gaussian fit.

To rescale the structure factors, the calculated frequency axis was divided by the wavenumber at the peak of the gaussian fit. Equally, each component of the structure factor was divided by the value at the peak of the gaussian fit.

6.4.6 Fast time-scale dynamics of islands in the blank case

A 2 min timelapse of the islands was recorded with an interframe time of 0.5 s. A time average of this video was calculated using FIJI by using 'z project→average'. In the same way, the standard deviation of the timelapse was also calculated and both projections were combined by using 'Color → Merge Channels', setting the standard deviation as the red channel.

After that, the video was filtered and thresholded using ilastik. Then, the islands were tracked over time as explained in subsection 6.4.2 with slight changes in the parameters to obtain the best possible tracks. Since these islands are quickly changing, the tracking software detected a high amount of islands lasting just a single or two frames. This was not observed when looking at Video 11 by eye so we decided to consider lifetimes longer than two frames (1 s). After the tracks were filtered, a histogram was calculated by normalizing by the probability of each lifetime setting the binwidth as 1 s.

6.4.7 Fourier series to describe the islands boundaries

From a 2 min timelapse, 8 different isolated islands were cropped and filtered using the bandpass filter in FIJI with a lower bound of 10 and an upper bound of 300. Then, the timelapse was thresholded using ilastik. In the binary image, the boundaries of the islands over time were calculated by using the function 'bwboundaries' in Matlab. From this boundary we obtained the Fourier coefficients defined in Equation 1.9 by using a Matlab function (David Thomas (2021). Elliptical Fourier shape descriptors Retrieved March 28, 2021.) based on the theory explained in [85]. This function was used to calculate the approximate boundary according to the Fourier description up to 9 harmonics n. To estimate the error made by such approximation, we calculated the RMSE between the actual boundary and the estimation given by the function. From here, we estimated that n=5 would be enough to represent substantially the main features of the boundaries and compare the different islands. With this description, we calculated the average in time of each Fourier coefficient to see how dominant they were when describing the shape.

To characterize the dynamics in time, the power spectrum of the Fourier coefficients for the different harmonics n were obtained by calculating the Fourier transform using the function 'fft' in Matlab. This would determine if there is any periodicity in the amplitudes of the Fourier series. As we were interested only in the frequency at which the amplitudes of the coefficients is dominant, we calculated the time average and standard deviation and we selected only those frequencies whose amplitude was larger than the average+sd, as explained in Figure 3.7a. We repeated this process for the 4 Fourier coefficients, for the 5 harmonics and the 8 islands. Then, we calculated the histograms of the frequencies for all the islands to obtain the likelihood of each frequency for all a_n, b_n, c_n and d_n. The frequencies in the histogram were grouped in 10 bins ranging from 0 to the maximum frequency ($\sim$1). Finally, we used the function 'heatmap' in Matlab to represent the likelihood of each frequency for each of the coefficients.

6.5 Characterization of bacterial waves in a kanamycin gradient

6.5.1 Tracking of bacterial waves with timelapse microscopy and fluorescent beads

To track the movement of the waves across the swarm, we drew a line of thickness 15 with FIJI and measure the intensity profile in the brightfield channel for a region going from the kanamycin disk to 17 mm into the swarm. A measurement of this profile was taken for the following events: when the 1^{st} wave appears at t=2.8 h, when the 1^{st} wave halts at t=4.3 h, when the 2^{nd} wave starts at t=5.9 h and finally when the 2^{nd} wave halts at t=11.2 h.

To quantify the transport of the waves, FluoSpheres^{TM} (Carboxylate-Modified Microspheres, F8823) were inoculated in three different points 1, 2 and 3 cm away from the inoculum. In this case, the images were acquired along time for different positions within the colony with the 2x (Nikon Plan 2x UW, NA 0.06) magnification objective. The motion of beads was tracked in these three positions over time for a total period of approximately 13.5 h, acquiring frames every 3.6 min. To quantify the displacement of the beads, the fluorescent intensity was measured in a ROI adjacent to the the inoculation points.

6.5.2 Estimation of viable bacteria carried by the waves

The amount of cells carried by the waves of bacteria in the kanamycin assay were estimated by performing a serial dilution assay over time. To do so, a biopsy puncher of 0.5

mm diameter was used to take samples in 6 different points inter-spaced 1 cm along the swarming plate, starting by a point at 5 mm from the disk. Each of those samples were diluted in 200 μl of LB and then 10x serial dilutions were performed 7 times by taking 20 μl of sample and mixing it with 180 μl of LB. This was done for 3 different time points: the first point was taken when the front halted, the second 17 h after this and finally a third point 65 h later. From the serial dilutions, 5 μl of solution was plated in a LBA plate and incubated overnight at 37°C . After incubation, the colony forming units (CFU) was calculated as 10^{d-1}, with d the maximum dilution at which bacteria grew in the LBA plate. For this dilution, the number of colonies were counted, if the number was greater than 10 then we would count the CFU as 10^{d}. To work out the CFU per unit of surface in the swarm, we divided this number by 5, the μls inoculated in the LBA plate, and we multiply by 200 μl , the volume where the agar pad taken with the biopsy puncher was diluted. Finally, this value was divided by the surface taken with the biopsy puncher neglecting the thickness of the agar since there bacteria are all at the surface

6.5.3 Counting the number of layers in the swarm

From the thresholded timelapses, calculated as in subsection 6.4.1, the different layers appearing in the swarm were counted for four different positions and they were identified by a local increase in grey value in a wide area of the swarm (Figure 3.12). After the 4th layer, the increase in grey value could not be further distinguished. Time is measured from the onset of the first islands within the field of view.

6.6 Characterization of the emergent colonies in a kanamycin gradient

6.6.1 Replica plating

To test the resistance of the colonies in the swarming assay, we used replica plating [203]. The method consists in pressing the plate containing the colonies to be tested against a sterile velvet lying on a block. Once the colonies were imprinted on the velvet, two new plates were pressed against the same velvet: one containing just LB agar and the other one in media containing 3 μg ml^{-1} of kan. Both plates were incubated overnight at 37°C and the colonies that appeared in the kan plate were mapped to the ones in the original plate.

6.6.2 CFU to test antimicrobial resistance

To calculate the % of survival when the colonies were exposed to kan, 200 μl of a dense culture (optical density around 1.3) of wild type (WT) and another with the resistant colonies, were diluted 8 times in 10 fold dilutions. To do so, 20 μl of the initial culture is inoculated in 180 μl of LB as explained in subsection 6.5.2. 5 μl are taken from the dilutions and plated in a LBA without antibiotics and in 3 μg ml^{-1} kan LBA plate. The plates were incubated overnight and then compared. To calculate the colony forming units (CFUs) the last number of dilutions where bacteria have grown was taken, and its power of 10 was estimated to be the concentration of living cells. Finally, the ratio of CFUs between the kan plate and the LB agar plate was calculated to work out the percentage of resistant bacteria.

6.6.3 Cell growth

Curves of cell growth for the WT and IL2 were calculated with the microbemeter [171]. Here, cell growth is calculated by measuring the turbidity of the sample over time. The greater the number of bacteria, the larger the degree of light scattered by them. Cell growth was tested in antibiotic free media and in 3 μg ml^{-1} of kan.

To calculate the growth rates, the natural logarithm of the data between the end of the lag phase and the diauxic shift was taken. This was fitted to a straight line according to Equation 1.1, where the slopes give the growth rate. The weighted mean of the slopes with their respective standard errors were calculated for the different samples and conditions.

The differences in lag phase were calculated by subtracting the time when the exponential phase started for the bacteria without and with antibiotic. The error bars of the final value are the result of applying the uncertainty propagation formula for the subtraction.

The area under the curve or integral of the cell growth was calculated with the function 'trapz' in Matlab.

6.6.4 Characterization of emergent colonies in 96 well plate in presence of antibiotics

To calculate the cell growth over time, an overnight culture of each strain was diluted to an OD of 0.0085 and then kanamycin was added to this culture according to the desired final concentration at which the cell growth wanted to be tested. The concentrations tested were: 0, 1, 2, 3, 4 and 5 μg ml^{-1} of kan. From this, 200 μl were inoculated in a 96 well plate and incubated for approximately two days at 37°C . Two of the wells were left as a blank to subtract their OD to the sample wells. The outer wells of the plate were filled

with LB to assure optimal humidity conditions and to minimise evaporation in the sample wells. Before the plate was used for first time, we checked the cell growth of WT in all the wells to see whether there were any differences in the OD reads among wells but all of them were similar (Figure 7.13).

6.6.5 Antibiotic resistance assays

The emerging colonies were tested under different methods: Kirby-Bauer (KB) diffusive method [196], serial dilutions assay and creating gradients of antibiotic by slanted plate assay.

In KB method, the antibiotics tested were nalidixic acid, tetracylcine, neomycin, streptomycin, gentamicin, apramycin, spectinomycin, chloramphenicol and ampicillin. The disks were made by punching Whatman filter paper with a hole puncher to assure same sizes. The antimicrobials where inoculated in the disks in such a way that there were two disks of 30 μg and 15 μg per antibiotic. After inoculation of the drug, the disks were let to dry for 4 h. Before the disks were placed on the plates, 150 μl of a 5 h culture of bacteria were spread over the plates. Finally, the disks were placed on top and the plates and then incubated overnight at 37°C . The resistance was determined by the size of the clearance left by bacteria around the diffusive disk. This clearance was measured for both the WT and IL2, and the larger depletion zone determined the strain that was more susceptible to each antibiotic.

The ratio of resistant bacteria within the colonies was quantified by using serial dilution assays as explained in subsection 6.6.2. The drawback of the serial dilutions method is that the suitable concentration of antibiotic to determine survivability is unknown. Too high concentration could result in not seeing any bacteria and too low in underestimating the resistance of the colonies. To avoid this, we made liquid medium which contained the following concentrations of antibiotic: 8 μg ml^{-1} of kan, neo, and cm; 3 μg ml^{-1} of gent and 50 μg ml^{-1} of spt. 15 ml of this medium was poured and left to solidify in a tilted petri dish creating a sloped LB agar plate. Once it became solid, 10 ml of liquid LB agar was poured on top and again it was left to solidify. In this way, a linear gradient of antibiotic was created along the plate. Finally, 150 μl of a 3 h culture of bacteria were spread over the plate. The resistance was determined by comparing the plates with WT and resistant colonies and measuring the size of the depletion region. Due to the linear gradient, we can calibrate the distances in the plates with the different concentration of antibiotics and estimate the MIC for each antibiotic and each strain.

6.6.6 Passage assay

To determine whether the increase in kan resistance was hereditary, we passaged a single colony from the swarming plate to a LB agar plate without any antibiotic. The latter was incubated overnight to let new colonies grow. This passage experiment was repeated up to 12 times and the resistance of our bacteria was checked in each of the passages through the serial dilutions method subsection 6.6.2.

6.6.7 Whole genome sequencing

The genome of *B. subtilis* and the colonies IL3, IL4, IL5 and IL6 was sequenced using an Illumina HiSeq 4000 system (Illumina, San Diego, CA, USA) at the Beijing Genomics Institute (Shenzhen, China) with a minimum coverage of 100x. Genomic DNA was sheared randomly to construct three read libraries with lengths by a Bioruptor ultrasonicator (Diagenode, Denville, NJ, USA) and physico-chemical methods. The paired-end fragment libraries were sequenced according to the Illumina HiSeq 4000 system's protocol. Raw reads with consecutive bases covered by fewer than five reads were discarded. The sequenced reads were assembled using SOAPdenovo v1.05 software.

With alignment software MUMmer (http://mummer.sourceforge.net/), each query sequence is aligned with reference sequence. The variation sites between the query sequence and reference sequence are found out and filtered preliminarily to detect potential SNP sites. The sequences with the length of 100 bp at both sides of SNP in the reference sequence are extracted and aligned with assembly results to verify SNP sites by using BLAST. If the length of aligned sequence is shorter than 101 bp, this SNP would be considered as incredible and it would be removed; if the extracted sequence could be aligned with the assembly results several times, this SNP was considered located in repeat region and it would also be removed.

Alternatively, colonies from a different experiment (α, β and IL2) were sent to MicrobesNG also for whole genome sequencing. Again, illumina next-generation sequencing was used at a minimum coverage of 30x. The results were analyzed by the bioinformatics team at BGI as explained before.

Chapter 7

Appendix

7.1 Tables

MIPS parameter	Theory	Experiment
Particle description	Single 2D rods	Quasi-2D Raft (10-100 cells)
Aspect ratio	2	~7
Surface coverage	0.55-0.65	0.6-0.75±0.1
Pe_r	25-100	35-100

Table 7.1: Main differences between the numerical simulations for MIPS model in [1] and swarming *B. subtilis* .

Experiment	Blank	Barrier	Kanamycin
α_{mean}	**-0.264**	**-0.076**	**-0.0389**
$u(\alpha_{mean})$	0.083	0.040	0.0042
α_{min}	-0.92	-0.47	-0.318
$u(\alpha_{min})$	0.73	0.22	0.096
α_{max}	-0.054	-0.052	-0.0189
$u(\alpha_{max})$	0.048	0.035	0.0035

Table 7.2: Parameters for the function fitted to the complementary cluster size in Figure 3.4. The first 5 points of the distributions were fitted to a power law with exponent α in the table. The mean values for these exponents are highlighted in bold in the table. The standard deviation are named u. The minimum and maximum values of the same magnitudes and their standard deviation are calculated as the mean of minimum values registered in each timelapse.

Experiment	Blank	Barrier	Kanamycin
$\boldsymbol{a_{mean}}$	**0.30**	**0.236**	**0.85**
$u(a_{mean})$	0.12	0.072	0.24
a_{min}	0.117	0.059	0.49
$u(a_{min})$	0.063	0.077	0.14
a_{max}	0.66	0.64	1.53
$u(a_{max})$	0.33	0.10	0.17
$\boldsymbol{s_0^{mean}}$	**0.037**	**0.0215**	**0.145**
$u(s_0^{mean})$	0.020	0.0021	0.069
s_0^{min}	0.001	0.001	0.0488
$u(s_0^{min})$	0.078	0.012	0.0079
s_0^{max}	0.1	0.9	0.9
$u(s_0^{max})$	1.7	1.0	2.2

Table 7.3: Parameters for the function fitted to the cluster size distributions in Figure 7.10. The distributions were fitted to a product of an exponential by a power law. The average values for the power law exponent and the inverse of the exponential's exponent are highlighted in bold in the table. The standard deviation are named u. The minimum and maximum values of the same magnitudes and their standard deviation area are calculated as the mean of minimum values registered in each timelapse.

Experiment	Exponent	Error exponent	R^2
Blank	0.518	0.039	0.90
Kanamycin top 1	0.905	0.062	0.991
Kanamycin top 2	2.72	0.10	0.999
Kanamycin middle	1.722	0.048	0.996
Kanamycin bottom	1.64	0.12	0.994

Table 7.4: Parameters for the size evolution from the islands tracks plotted in Figure 3.5. Kanamycin top 1 corresponds to the top curve, which has two slopes. The first slope in time is named 'kanamycin top 1' and the second slope in time is 'kanamycin top 2'. The curve mainly in the middle is 'kanamycin middle' and the curve closer to the blank case is 'kanamycin bottom'.

WT	IL3	IL4	IL5	IL6	α	β	IL2	Gene ID	Gene product
G	G	G	G	G	G	T	G	B4U62_RS05915	ATP-dependent helicase/deoxyribonuclease subunit B
C	C	C	C	C	C	T	C	B4U62_RS00710	elongation factor G
G	A	G	G	G	G	G	G	B4U62_RS00710	elongation factor G
C	T	C	C	C	C	C	**C**	B4U62_RS09960	plipastatin synthase subunit D
G	G	T	G	G	G	G	**G**	B4U62_RS09960	plipastatin synthase subunit D
T	T	G	T	T	T	T	**T**	B4U62_RS09960	plipastatin synthase subunit D
T	T	C	T	T	T	T	**T**	B4U62_RS09960	plipastatin synthase subunit D
G	G	T	G	G	G	G	**G**	B4U62_RS09960	plipastatin synthase subunit D
G	G	C	G	G	G	G	**G**	B4U62_RS09960	plipastatin synthase subunit D
C	**A**	**A**	**A**	**A**	C	C	**C**	**B4U62_RS10595**	**multidrug resistance protein NorM**
G	G	A	G	G	G	G	G	B4U62_RS20260	prespore-specific transcriptional regulator RsfA
G	**G**	**G**	**A**	**G**	**G**	**G**	**G**	**B4U62_RS04590**	**PTS maltose EIICB component**
C	**C**	**C**	**C**	T	**C**	**C**	**C**	**B4U62_RS04590**	**PTS maltose EIICB component**

Sequenced by BGI sequencing Sequenced by microbesNG

Table 7.5: SNPs of colonies from two different plates analysed by BGI sequencing. The rows in bold correspond to the mutations that we checked with sanger sequencing. The letters in red were the mutations discarded after checking with Sanger sequencing.

Gene targeted	Forward primer sequence	Reverse primer sequence	Position	Mutation
NORM	GCTGATTTAGCTG GTGTCGCC	GGTCAGAAGTGTAC ATGCCCGC	2119991	C->A
Plipastatin Subunit D	CGCCTCCTGCATTT TGTACG	CCTACACAGCGCCG AGAAAC	1968288 1968374 1968443 1968463 1968495 1968505	C->T G->T T->G T->C G->T G->C
PTS maltose EIICB component	TCGCCCTGGCTTTT TATGTGACAG	GTCATGATCGGGCT GACCGTG	893298	C->T

Table 7.6: Primers designed to target some of the SNPs detected by whole genome sequencing

REFERENCE	WT	gene ID	gene product	detected by
G	A	B4U62_RS08840	GTP-sensing pleiotropic transcriptional regulator CodY	both
C	A	intergenic	--	bgi sequencing

Table 7.7: Differences in the SNPs between the WT and the reference genome used to compare the sequences of our strains.

TYPE	WT	gene ID	gene product
INSERTION	G	B4U62_00615	serine O-acetyltransferase
INSERTION	**C**	**B4U62_RS03805**	**methyltransferase**
INSERTION	**G**	**B4U62_RS06855**	**tagaturonate reductase**
INSERTION	**G**	**B4U62_RS06855**	**tagaturonate reductase**
INSERTION	**C**	**B4U62_RS13085**	**acetyl-CoA C-acetyltransferase**
INSERTION	**C**	**B4U62_RS10860**	**hypothetical protein**

Table 7.8: Differences in the InDels between the WT and the reference genome. The InDels in bold were further checked with PCR and Sanger sequencing. In both, SNPs and InDels, all the strains coincide with WT.

Strain	**Genotype**	**Source**	**Strain ID**
Wild Type	*B. subtilis* NCIB3610	Gift from Wade Winkler laboratory (University of Maryland, College Park, MD) (Irnov and Winkler, 2010)	MA-002
Δeps	epsH::tet^R	Gift from Roberto Kolter laboratory (Harvard Medical School, Cambridge, MA) (Branda et al., 2001)	MA-013
Δphrc	phrC::neo^R	(Asally et al., 2012)	MA-109
Δopp	oppD::cm^R	(Asally et al., 2012)	MA-130
ΔtasA	sacA::P$_{yqxM}$-trsA216-YFP, cm^R	Gift from Gurol Suel laboratory (UC San Diego, La Jolla, CA)	MA-463

Table 7.9: List of strains used in this study

Item	Model	Specifications
Mounted LED	M405L4	405 nm, 1000 mW
Aspheric Condenser Lenses	ACL25416U-B	Ø1", f = 16.0 mm
25mm SPUTTERED EDGEPASS FILTER	FELH0450	Longpass 450 nm
Retaining Ring	CMRR	C-Mount (1.00"-32)
Cage cube	Cm1-dch	Dichroic Filter Mount
Adapter	Sm1a9	External C-Mount Threads and Internal SM1 Threads
Leica DMI Microscope Camera Port Adapter	Sm1a50	Internal SM1 Threads, External SM2 Threads
Coupler, External Threads	Sm1t2	0.5" Long
Adapter	Sm1a10	External SM1 Threads and Internal C-Mount Threads

Table 7.10: Items used to build the set-up which was used to irradiate a wide area of bacteria with UV. All the components were bought from Thorlabs.

7.2 Figures

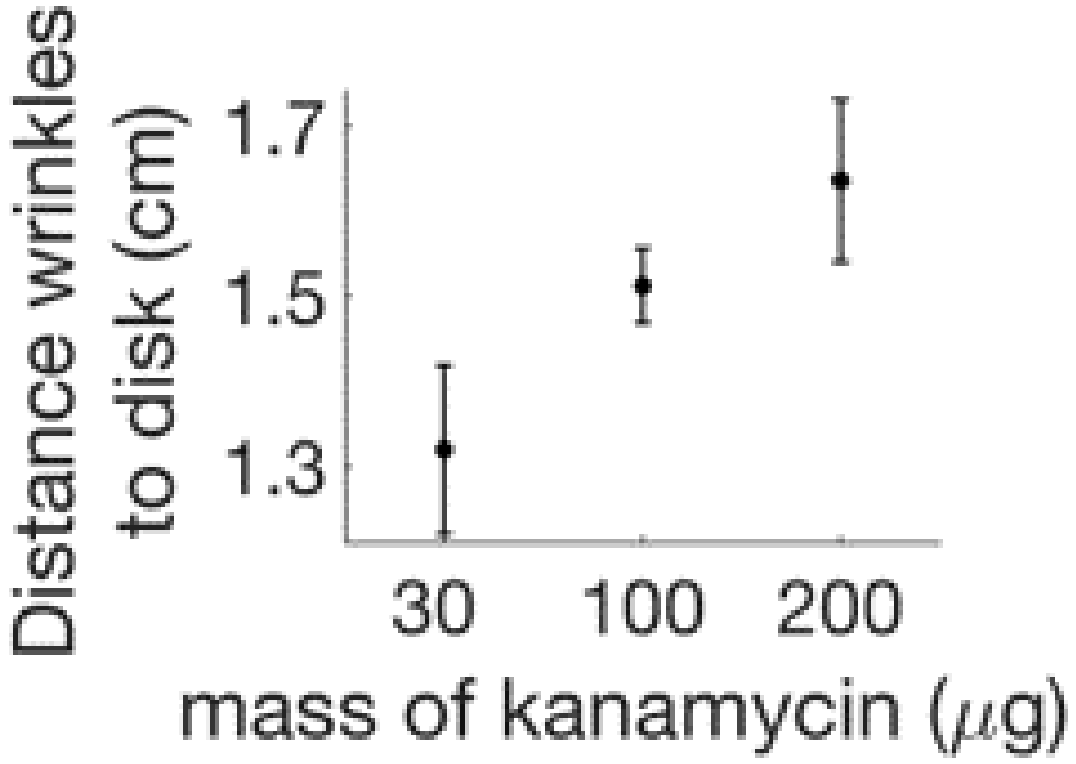

Figure 7.1: **Distance where the wrinkles appear depending on the amount of kanamycin in the diffusive disk.**. The wrinkles appear further from the kanamycin disk with increasing concentration of the antibiotic. The data for 100 μg comes from 3 replicates in a single experiment. Data for 30 and 200 μg come at least from three different replicates.

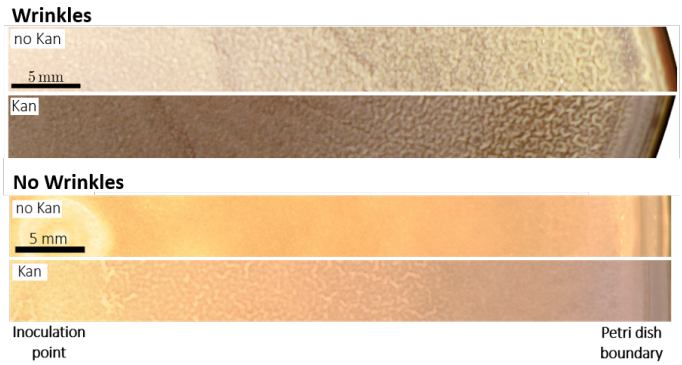

Figure 7.2: **Radial transects of a 9 cm-diameter petri dish with a swarming *B. subtilis* culture in conditions corresponding to "no kanamycin" and "kanamycin".**. There were times that wrinkles appeared near the boundary but it was not only the case.

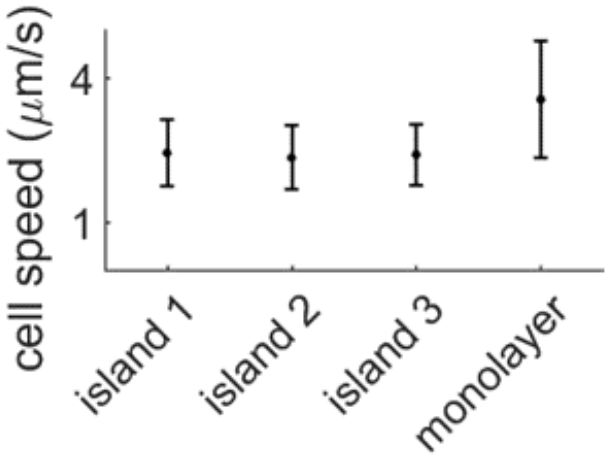

Figure 7.3: **Average speed in the monolayer vs speed within the island.**. The average cell speed of the swarm was measured with PIV for 3 different multi-layered regions and for the monolayer surrounding them. The speed in the monolayer is almost double the multilayer case. Data comes from a single replicate.

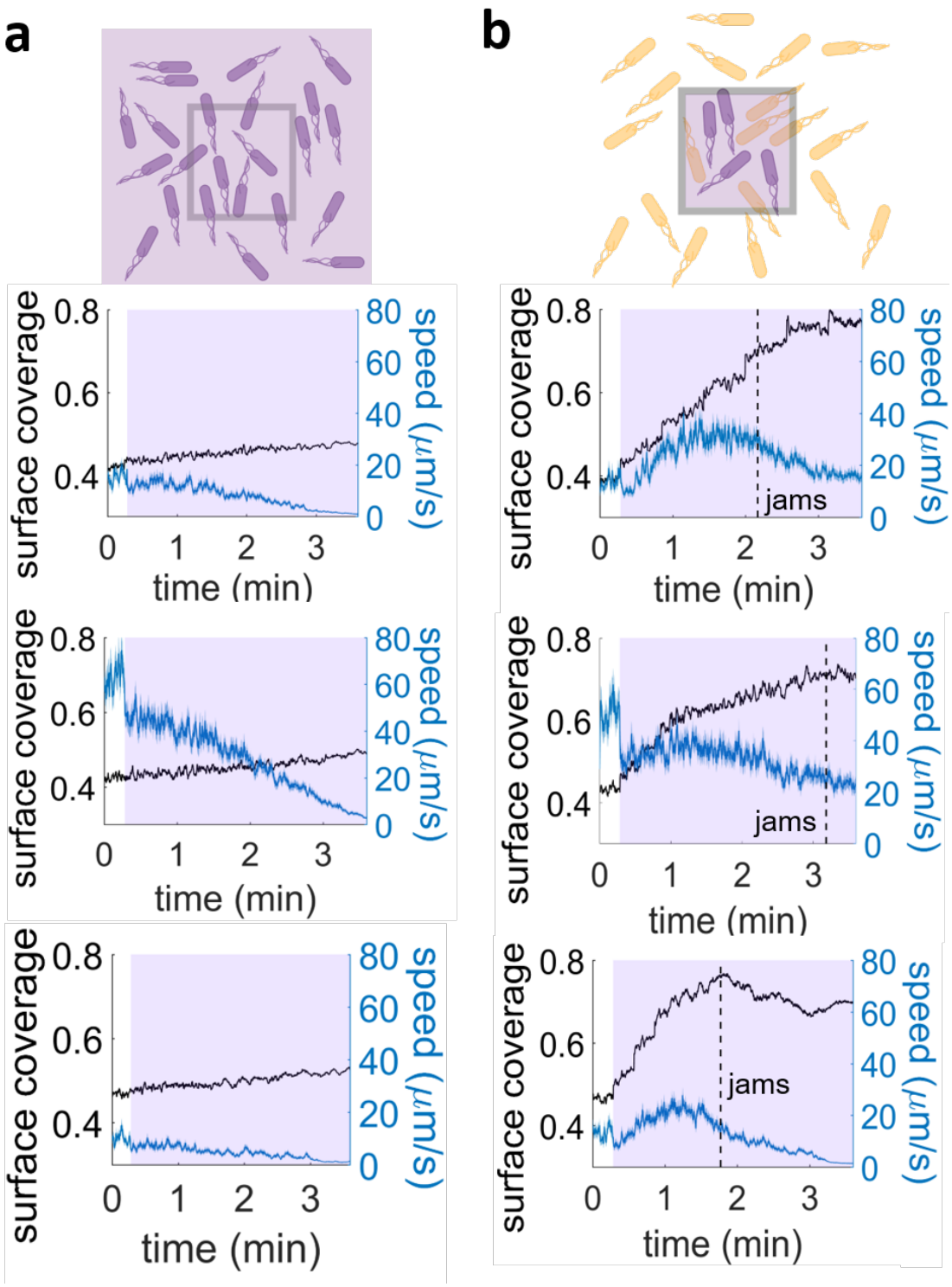

Figure 7.4: **Effect of UV light in cell speed and surface coverage for thor labs set up and epi set up.** a) Diffferent examples of speed and surface coverage manipulation using the thorlabs set up. b) Same as a) with epi-fluorescence set up.

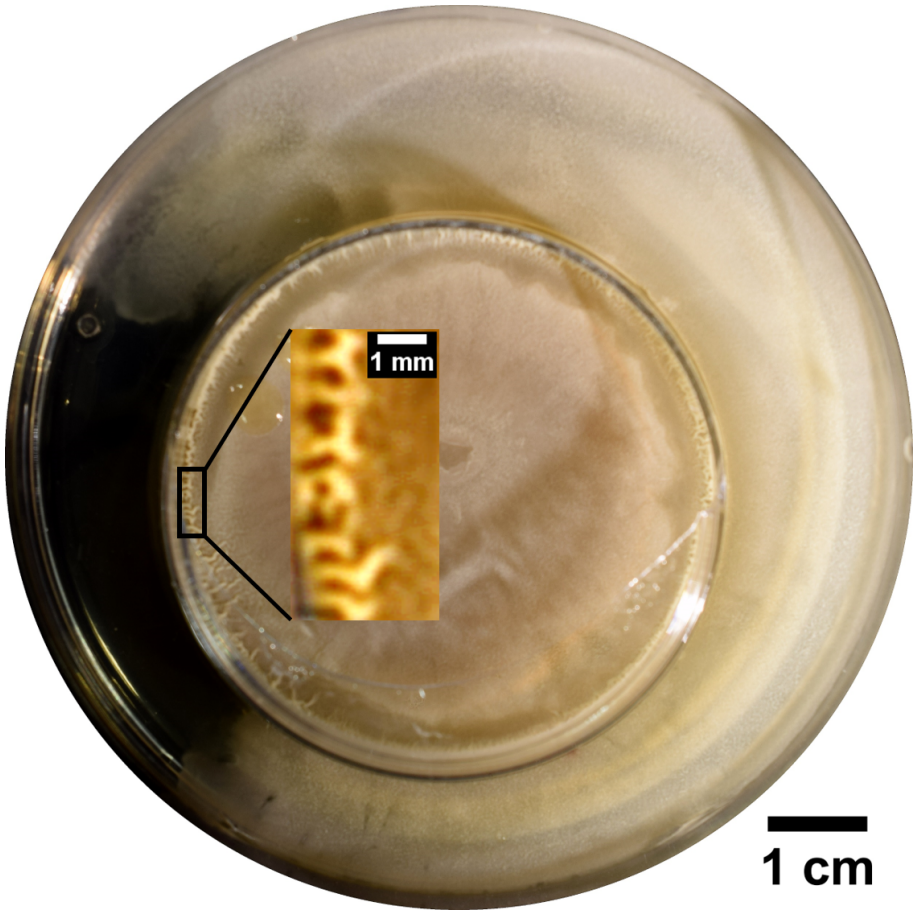

Figure 7.5: **Swarming assay with a concentric hollow petri dish enclosing the swarm.** The wrinkles were formed in the inner side of the small concentric petri dish.

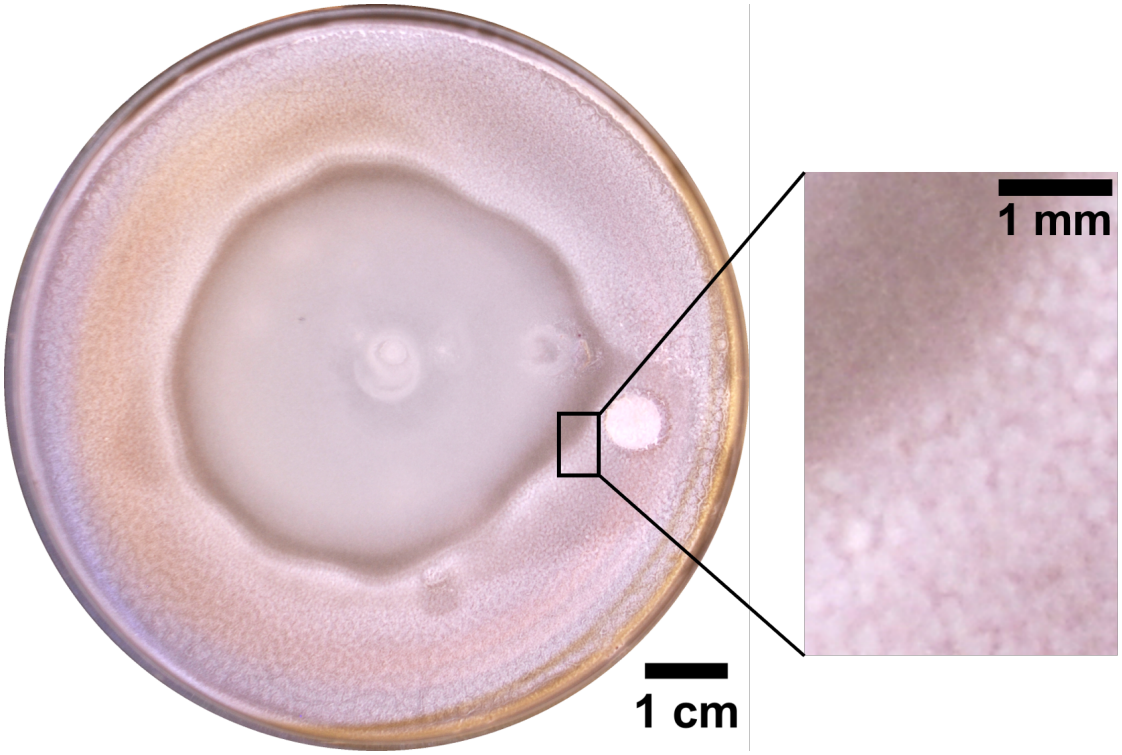

Figure 7.6: **Swarming assay with a blank disk displaying a transparent and opaque regions.**

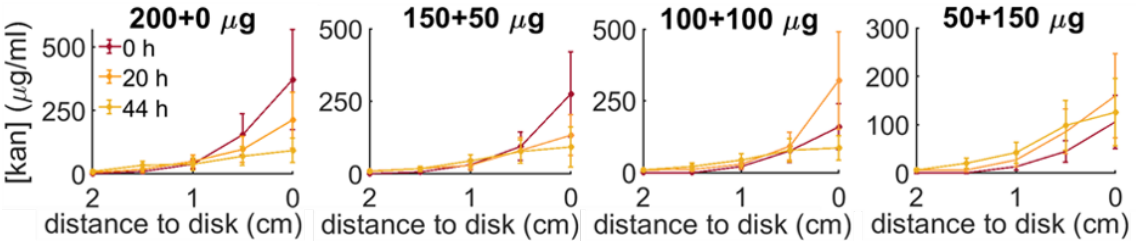

Figure 7.7: **Kanamycin concentration profiles for the four administration protocols.** Kanamycin concentration profiles for the four administration protocols (200 μg -0 μg ; 150-50; 100-100; 50-150) at increasing distances from the kanamycin disk along the radius connecting the inoculation point to the antibiotic disk. The profiles are measured at 0 h, 20 h, 44 h, starting when the front propagation towards the kanamycin disk stopped.

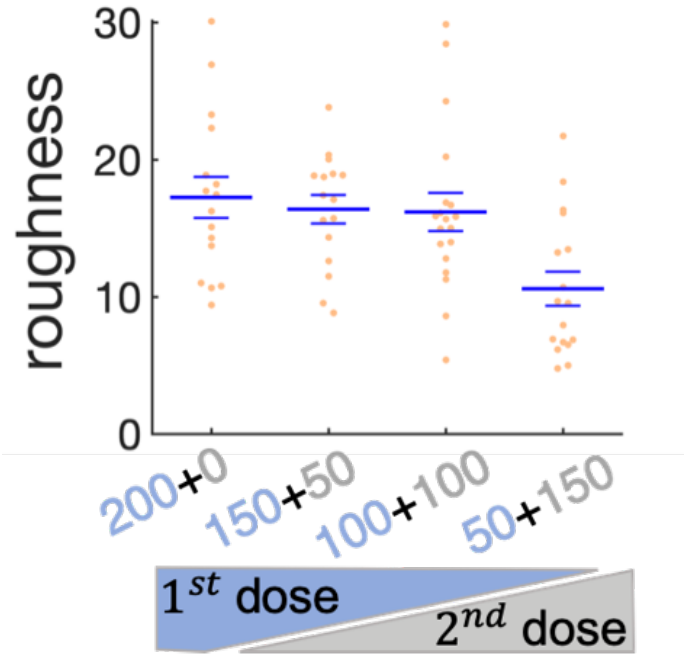

Figure 7.8: **Effect of sequential administration of kanamycin in wrinkles' roughness.** Scatter plot for the roughness of the wrinkles when the kanamycin dose is split in two times. The first dose of kanamycin is in blue and the second dose in gray. The large bars are the mean of the roughness and the small bars are the s.e.m.

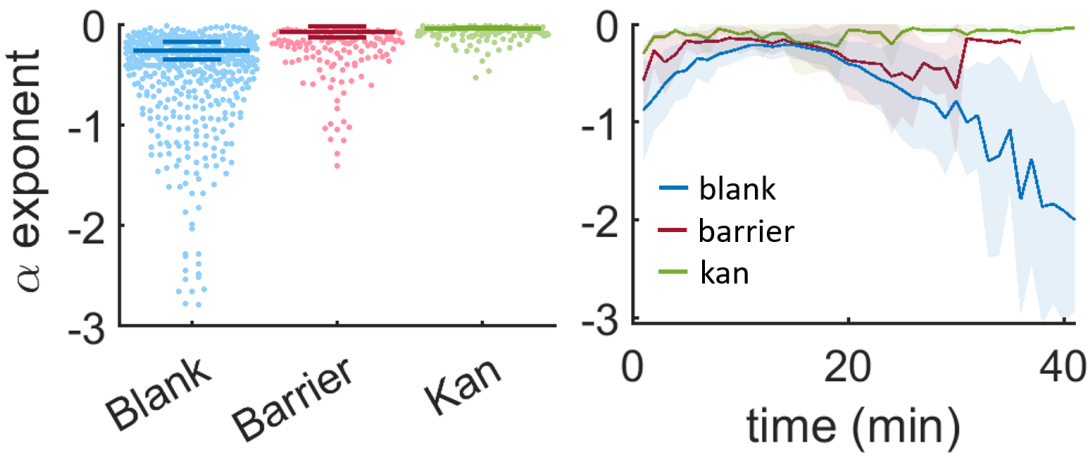

Figure 7.9: **Power law exponent** *alpha* **distributions and evolution with time for the complementary cumulative distributions in Figure 3.4**. The first points of the ccdfs were fitted to a power law of the form cs^{α}. The main lines indicate the mean of the distribution and the small ones -or the shades- indicate the standard deviation of the mean.

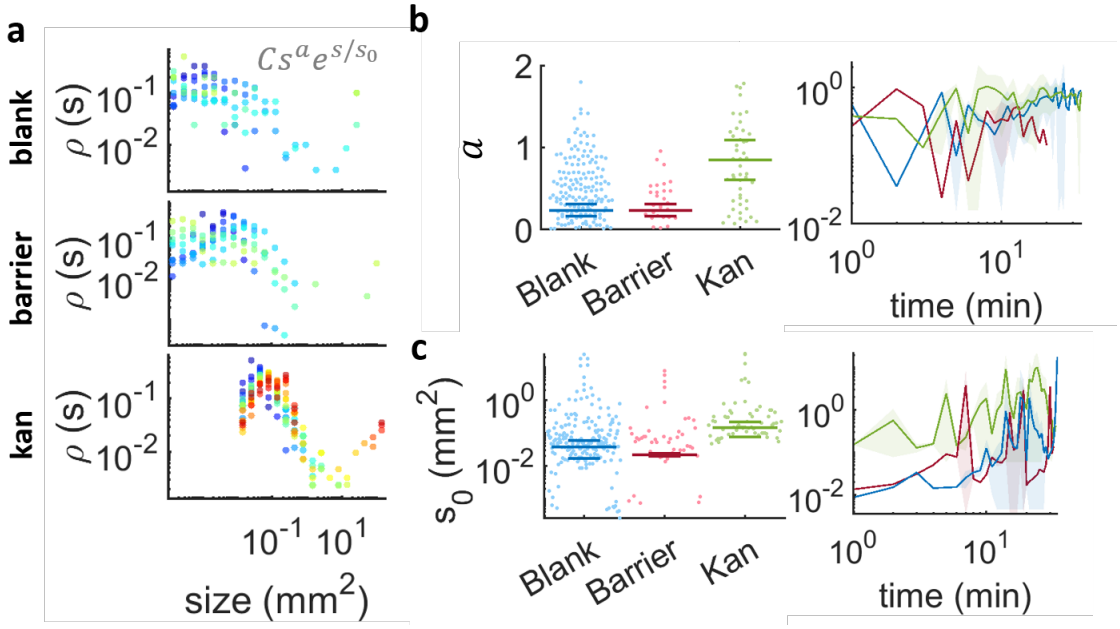

Figure 7.10: **Islands size distributions and fit exponents for the blank, barrier and kanamycin cases**. a) Islands size distribution for the three studied cases. The distributions were fitted to a power law by an exponential indicated in gray in the figure. The sizes were grouped in 13 bins logarithmically distributed for s ∈ [$10^{-}6$ 10^{3}]. b) Distribution of the exponents of the power law exponent and their evolution along time. c) Distributions of the exponent in the fitted exponential and their evolution along time. The long horizontal lines indicate the mean of the distributions and the short horizontal lines their standard deviation.

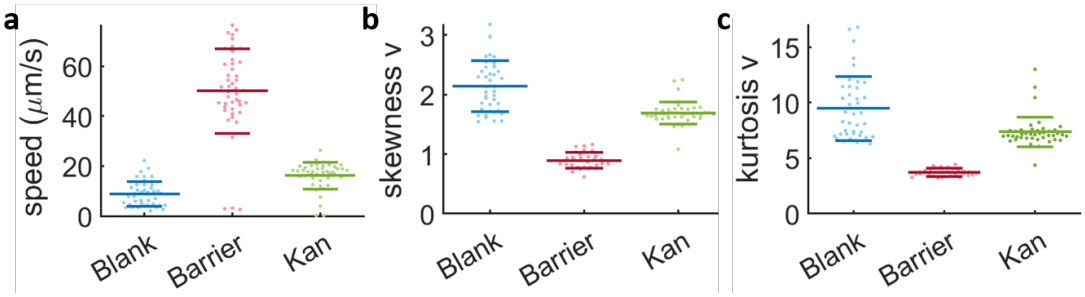

Figure 7.11: **Modulus of velocities in the monolayer while coexisting with the second layer**. For the blank case, the speed was calculated in a plate with kanamycin but at least 5 cm away from the disk and 4 cm away from any boundary. For the barrier case the speed was measured just after the meniscus formed by the barrier to avoid image artifacts. Finally, in the kanamycin case the timelapses were acquired for points comprehend within 1.5 cm from the disk. Skewness of the x component v_x and modulus v of velocities. c), d) Kurtosis of the x component v_x and modulus v of velocities. The long horizontal bars represent the mean of the distribution and the upper and lower short bars represent the standard deviation.

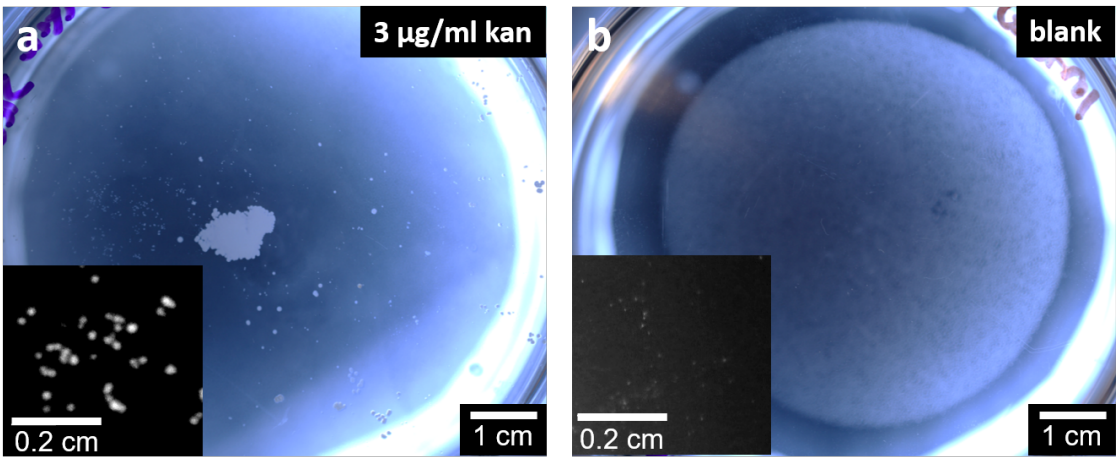

Figure 7.12: **Colonies in homogeneous concentration of kanamycin**. a) Colonies appeared after 3 days of inoculating swarming bacteria in a homogeneous concentration of 3 μg ml^{-1} of kanamycin. b) A plate from the same batch without any bacteria or antibiotic to test whether the colonies are due to contamination.

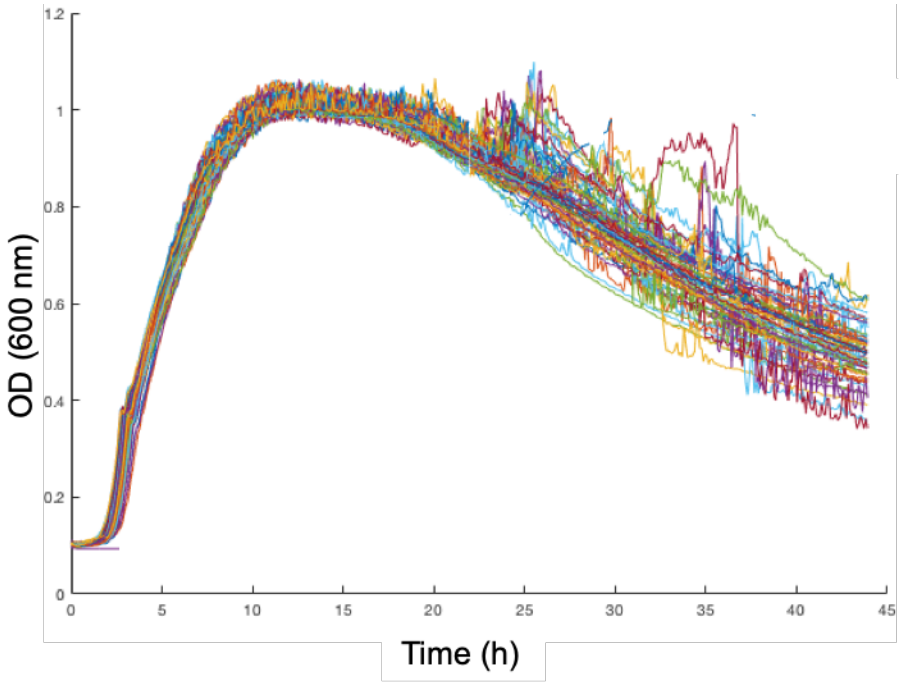

Figure 7.13: WT run in all the wells of a 96 well plate. The graph does not show a deviation within the wells.

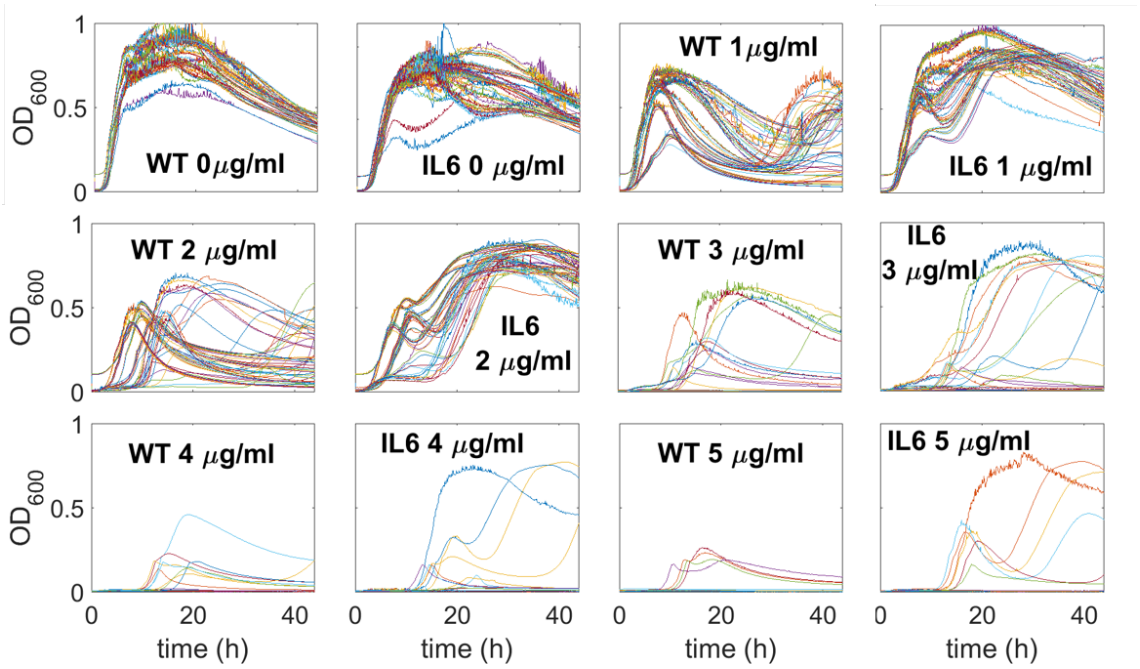

Figure 7.14: All the growth curves for WT and IL6 for the concentrations of antibiotic tested in Figure 4.7.

7.3 Videos

Video 1

https://youtu.be/UDH8InpXEgI

Expansion of swarming bacteria in presence of a gradient of kanamycin. Wild type *B. subtilis* was inoculated at the center of the plate. Eventually, bacteria at the swarming front halt due to the presence of the kanamycin diffusive disk placed on a side of a 9 cm Petri Dish 24 h prior inoculation. After the front stops, the swarm is still dynamic since multiple waves of swarming bacteria come from the centre of the plate.

Video 2

https://youtu.be/Dd-2sxQ71G4

Swarming *B. subtilis* Δeps deletion strain was inoculated at the center of the plate. Eventually, bacteria at the swarming front halt due to the presence of the kanamycin diffusive disk placed on a side of a 9 cm Petri dish 24 h before inoculation.

Video 3

https://youtu.be/rgNlZOcENow

Swarming bacteria during the jamming process visualized as darker cells in the field of view observed at 60x magnification. The speed plot shows the average speed in the field of view and the blue shade represents s.e.m. The vertical line in the graph indicates the frame of the time-lapse in which the average speed was calculated. It can be observed that the jam makes the overall speed to drop by half of the initial magnitude.

Video 4

https://youtu.be/k1wh699vssY

Process of jams and islands formation under 10x magnification. The left panel shows swarming bacteria continuously jamming. The jams look like dark localized small regions in the field of view which continuously appear and disappear. The right panel shows the same scenario 10 min later, when the islands become more stable. Islands look like extended dark regions in the field of view which are highly dynamic and with highly fluctuating boundaries.

Video 5

https://youtu.be/YYusbarTtWw

Coexistence between a second layer of swarming bacteria (darker region in the field of view) and a surrounding monolayer of swarming cells under 40x magnification. The boundaries of the island continuously exchange cells with the monolayer surrounding it. Within the island, cell seem to meander across the layers.

Video 6

https://youtu.be/y9wdRmXKaqU

Formation of multilayers in a swarming plate with a kanamycin diffusive disk. The multilayer starts forming in the region near the disk where multiple islands appear. The islands become very elongated at the front and they grow in size until they merge. The nucleation and merging of islands were observed up to 4 layers before we lost the ability to recognize further transitions due to a flattening of the image contrast. In the opposite side of the plate, away from kanamycin, the islands appear and merge homogeneously in the whole region.

Video 7

https://youtu.be/UN4MprDdzhI

Time-lapse of accumulation of bacteria over time when they are being continuously irradiated by UV light in a region that is as large as the field of view. Eventually, bacteria accumulation gives rise to the formation of localized islands, which appear as dark regions in the field of view, finally leading to a confluent second layer.

Video 8

https://youtu.be/Oxp0e6qw0xQ

Process of island formation when the swarming front hits a physical barrier which is placed just on the right of the field of view. Islands start forming in the region closer to the barrier and then propagate towards the opposite direction. After the initial island formation, we can see that the swarm is still dynamic and keep forming multiple layers through island formation and merging.

Video 9

https://youtu.be/EfBD-$\jmath usMU$

Formation of islands in absence of a kanamycin gradient. The islands come mainly from the centre of the swarm (on the right) but they also originate near the boundary of the petri dish (on the left). Both islands merge and form a second layer. In the video it can be seen that the process continues for future layers.

Video 10

https://youtu.be/MdoFGGXFV9Y

Islands formation in presence of a gradient of kanamycin crated by a diffusive disk placed on the right and with bacteria inoculated on the left (dark circle). The islands near the disk resemble a nucleation and growth process and the islands near the inoculum a spinodal decomposition. The local accummulation at the front leads to a 1^{st} wave of bacteria at t=80 min that halts at t=130 min. Further into the swarm, we can see the emergence of a 2^{nd} wave of bacteria at t=120 min coming from the inoculum.

Video 11

https://youtu.be/HkZsWD8owCM

Timelapse of island formation in the blank case recorded every 0.5 s. The islands appear as dark regions in the field of view that intermittently appear and disappear. An increasing number of islands appear with time resulting in an increasing surface coverage of the second layer. The video has been sped up 20x.

Video 12

https://youtu.be/grM2z-nBIkQ

Timelapse of island formation in presence of a gradient of kanamycin recorded every 0.5 s. The islands nucleate and they fluctuate in shape and grow but they rarely disappear as opposed to the blank case. The video has been sped up 20x.

Video 13

https://youtu.be/j12Kuymn-gM

Transport of beads by the swarming monolayer (bead cluster on the right), by the first wave (bead cluster on the centre) and by the second wave (bead cluster on the left). The video was recorded at 30 °C .

Video 14

https://youtu.be/81b$_t$$McjU7E$

Video showing the emergence of microcolonies 24 h after the expansion of the swarm begins. The microcolonies appear as bright spots at the swarming front that then spread towards the back of the plate. The video was recorded at 37 °C .

Video sytox

https://youtu.be/g6-6bQJ06w8

The timelapse shows the sytox signal of the swarm when facing a kanamycin gradient. The kanamycin disk was placed at the top of the video. The video shows a clearance region around the kanamycin disk. Brighter regions show higher sytox signal either coming from an increased cell death or due to a higher cell density.

Bibliography

[1] Robin van Damme, Jeroen Rodenburg, René van Roij, and Marjolein Dijkstra. Interparticle torques suppress motility-induced phase separation for rodlike particles. *The Journal of Chemical Physics*, 150(16):164501, 4 2019.

[2] Porooshat Dadgostar. Antimicrobial Resistance: Implications and Costs. *Infection and Drug Resistance*, Volume 12:3903–3910, 12 2019.

[3] Ayari Fuentes-Hernández, Anastasia Hernández-Koutoucheva, Alán F. Muñoz, Raúl Domínguez Palestino, and Rafael Peña-Miller. Diffusion-driven enhancement of the antibiotic resistance selection window. *Journal of the Royal Society Interface*, 16(158), 2019.

[4] Matthew I Hutchings, Andrew W Truman, and Barrie Wilkinson. Antibiotics: past, present and future. *Current Opinion in Microbiology*, 51:72–80, 10 2019.

[5] Jose M Munita, Cesar A Arias, Antimicrobial Resistance Unit, and Alemana De Santiago. HHS Public Access. *Mechanisms of Antibiotic Resistance*, 4(2):1–37, 2016.

[6] M Kohanski, MA DePristo, and JJ Collins. Sub-lethal antibiotic treatment leads to multidrug resistance via radical induced mutagenesis. *Molecular cell*, 37(3):19, 2010.

[7] R. Hermsen, J. B. Deris, and T. Hwa. On the rapidity of antibiotic resistance evolution facilitated by a concentration gradient. *Proceedings of the National Academy of Sciences*, 109(27):10775–10780, 7 2012.

[8] Stan Deresinski. Vancomycin in Combination with Other Antibiotics for the Treatment of Serious Methicillin-Resistant Staphylococcus aureus Infections. *Clinical Infectious Diseases*, 49(7):1072–1079, 10 2009.

[9] Matthew E. Levison and Julie H Levison. Pharmacokinetics and Pharmacodynamics of Antibacterial Agents. *Infectious Disease Clinics of North America*, 23(4):791–815, 12 2009.

[10] Daniel N. Wilson. Ribosome-targeting antibiotics and mechanisms of bacterial resistance. *Nature Reviews Microbiology*, 12(1):35–48, 2014.

[11] Daniel N. Wilson. The A-Z of bacterial translation inhibitors. *Critical Reviews in Biochemistry and Molecular Biology*, 44(6):393–433, 2009.

[12] Claudio O. Gualerzi and Cynthia L. Pon. Initiation of mRNA translation in prokaryotes. *Biochemistry*, 29(25):5881–5889, 6 1990.

[13] Nimo M. Abdi and Kurt Fredrick. Contribution of 16S rRNA nucleotides forming the 30S subunit A and P sites to translation in Escherichia coli. *Rna*, 11(11):1624–1632, 2005.

[14] William H. McClain. Rules that Govern tRNA Identity in Protein Synthesis. *Journal of Molecular Biology*, 234(2):257–280, 11 1993.

[15] Xinying Shi, Katie Chiu, Srikanta Ghosh, and Simpson Joseph. Bases in 16S rRNA important for subunit association, tRNA binding, and translocation. *Biochemistry*, 48(29):6772–6782, 2009.

[16] Christopher Walsh. Where will new antibiotics come from? *Nature Reviews Microbiology*, 1(1):65–70, 2003.

[17] Jacob Poehlsgaard and Stephen Douthwaite. The bacterial ribosome as a target for antibiotics. *Nature Reviews Microbiology*, 3(11):870–881, 11 2005.

[18] Frank Schluenzen, Ante Tocilj, Raz Zarivach, Joerg Harms, Marco Gluehmann, Daniela Janell, Anat Bashan, Heike Bartels, Ilana Agmon, François Franceschi, and Ada Yonath. Structure of functionally activated small ribosomal subunit at 3.3 Å resolution. *Cell*, 102(5):615–623, 2000.

[19] Marie Paule Mingeot-Leclercq, Youri Glupczynski, and Paul M. Tulkens. Aminoglycosides: Activity and resistance. *Antimicrobial Agents and Chemotherapy*, 43(4):727–737, 1999.

[20] Julia Romanowska, Nathalie Reuter, and Joanna Trylska. Comparing aminoglycoside binding sites in bacterial ribosomal RNA and aminoglycoside modifying enzymes. *Proteins: Structure, Function and Bioinformatics*, 81(1):63–80, 2013.

[21] B D Davis. Mechanism of bactericidal action of aminoglycosides. *Microbiological reviews*, 51(3):341–350, 1987.

[22] John P. Overington, Bissan Al-Lazikani, and Andrew L. Hopkins. How many drug targets are there? *Nature Reviews Drug Discovery*, 5(12):993–996, 2006.

[23] Peter Imming, Christian Sinning, and Achim Meyer. Drugs, their targets and the nature and number of drug targets. *Nature Reviews Drug Discovery*, 5(10):821–834, 2006.

[24] Sumantha Salian, Tanja Matt, Rashid Akbergenov, Shinde Harish, Martin Meyer, Stefan Duscha, Dmitri Shcherbakov, Bruno B. Bernet, Andrea Vasella, Eric Westhof, and Erik C. Böttger. Structure-activity relationships among the kanamycin aminoglycosides: Role of ring I hydroxyl and amino groups. *Antimicrobial Agents and Chemotherapy*, 56(12):6104–6108, 2012.

[25] Joo Hee Chung, Young Seoub Park, Jim Kim, Gi Won Shin, Myung Hee Nam, Min Kyu On, Chan Wha Kim, Gyoo Yeol Jung, and Jin Hyun Park. Parallel analysis of antimicrobial activities in microbial community by SSCP based on CE. *Electrophoresis*, 28(14):2416–2423, 2007.

[26] Anthony R. Cukras, Daniel R. Southworth, Julie L. Brunelle, Gloria M. Culver, and Rachel Green. Ribosomal proteins S12 and S13 function as control elements for translocation of the mRNA:tRNA complex. *Molecular Cell*, 12(2):321–328, 2003.

[27] N Bilgin, A A Richter, M Ehrenberg, A E Dahlberg, and C G Kurland. Ribosomal RNA and protein mutants resistant to spectinomycin. *The EMBO journal*, 9(3):735–9, 1990.

[28] E P Bakker. Aminoglycoside and aminocyclitol antibiotics: hygromycin B is an atypical bactericidal compound that exerts effects on cells of Escherichia coli characteristics for bacteriostatic aminocyclitols. *Journal of general microbiology*, 138(3):563–9, 1992.

[29] L. McMurry, R. E. Petrucci, and S. B. Levy. Active efflux of tetracycline encoded by four genetically different tetracycline resistance determinants in Escherichia coli. *Proceedings of the National Academy of Sciences*, 77(7):3974–3977, 1980.

[30] Laura J V Piddock. Clinically Relevant Chromosomally Encoded Multidrug Resistance Efflux Pumps in Bacteria Clinically Relevant Chromosomally Encoded Multidrug Resistance Efflux Pumps in Bacteria. *Clinical infectious diseases : an official publication of the Infectious Diseases Society of America*, 19(2):382–402, 2006.

[31] G Thom and C D Prescott. The selection in vivo and characterization of an RNA recognition motif for spectinomycin. *Bioorg Med Chem*, 5(6):1081–1086, 1997.

[32] Beatriz Llano-Sotelo, Eduardo F. Azucena, Lakshmi P. Kotra, Shahriar Mobashery, and Christine S. Chow. Aminoglycosides Modified by Resistance Enzymes Display Diminished Binding to the Bacterial Ribosomal Aminoacyl-tRNA Site. *Chemistry & Biology*, 9(4):455–463, 4 2002.

[33] Maria S. Ramirez and Marcelo E. Tolmasky. Aminoglycoside modifying enzymes. *Drug Resistance Updates*, 13(6):151–171, 12 2010.

[34] Peleg Micha and Maria G. Corradini. Microbial growth curves: What the models tell us and what they cannot. *Critical Reviews in Food Science and Nutrition*, 51(10):917–945, 2011.

[35] Luc Vinet and Alexei Zhedanov. A 'missing' family of classical orthogonal polynomials. *Journal of Physics A: Mathematical and Theoretical*, 44(8):085201, 2 2011.

[36] William F. Loomis and Boris Magasanik. Glucose-Lactose Diauxie in Escherichia coli. *Journal of Bacteriology*, 93(4):1397–1401, 4 1967.

[37] Hans-Curt Flemming, Jost Wingender, Ulrich Szewzyk, Peter Steinberg, Scott A. Rice, and Staffan Kjelleberg. Biofilms: an emergent form of bacterial life. *Nature Reviews Microbiology*, 14(9):563–575, 9 2016.

[38] Natalie Verstraeten, Kristien Braeken, Bachaspatimayum Debkumari, Maarten Fauvart, Jan Fransaer, Jan Vermant, and Jan Michiels. Living on a surface: swarming and biofilm formation. *Trends in Microbiology*, 16(10):496–506, 2008.

[39] Bettina Rosche, Xuan Zhong Li, Bernhard Hauer, Andreas Schmid, and Katja Buehler. Microbial biofilms: a concept for industrial catalysis? *Trends in Biotechnology*, 27(11):636–643, 11 2009.

[40] Jingjing Feng, Zexin Zhang, Xiaodong Wen, Jianfeng Xue, and Yan He. Single Nanoparticle Tracking Reveals Efficient Long-Distance Undercurrent Transport in Upper Fluid of Bacterial Swarms. *iScience*, 22:123–132, 12 2019.

[41] V.T. Nayar, J.D. Weiland, C.S. Nelson, and A.M. Hodge. Elastic and viscoelastic characterization of agar. *Journal of the Mechanical Behavior of Biomedical Materials*, 7:60–68, 3 2012.

[42] Weijie Chen, Neha Mani, Hamid Karani, Hao Li, Sridhar Mani, and Jay X Tang. Confinement Discerns Swarmers from Planktonic Bacteria. *bioRxiv*, page 2020.08.30.274316, 1 2020.

[43] Daniel B Kearns. A field guide to bacterial swarming motility. *Nature Reviews Microbiology*, 8(9):634–644, 9 2010.

[44] Hannah Jeckel, Eric Jelli, Raimo Hartmann, Praveen K. Singh, Rachel Mok, Jan Frederik Totz, Lucia Vidakovic, Bruno Eckhardt, Jörn Dunkel, and Knut Drescher. Learning the space-time phase diagram of bacterial swarm expansion. *Proceedings of the National Academy of Sciences*, 116(5):1489–1494, 1 2019.

[45] Daniel B. Kearns and Richard Losick. Swarming motility in undomesticated Bacillus subtilis. *Molecular Microbiology*, 49(3):581–590, 2003.

[46] Tohey Matsuyama, Taichiro Tanikawa, and Yoji Nakagawa. Serrawettins and Other Surfactants Produced by Serratia. pages 93–120. Springer Berlin Heidelberg, Berlin, Heidelberg, 2011.

[47] Sivan Benisty, Eshel Ben-Jacob, Gil Ariel, and Avraham Be'er. Antibiotic-induced anomalous statistics of collective bacterial swarming. *Physical Review Letters*, 114(1):1–5, 2015.

[48] Seonghee Yoon, Kyunghoon Kim, and Jung Kyung Kim. Live-cell imaging of swarming bacteria in a fluidic biofilm formed on a soft agar gel substrate. *Journal of Visualization*, 16(2):123–131, 5 2013.

[49] L Karygianni, Z Ren, H Koo, and T Thurnheer. Biofilm Matrixome: Extracellular Components in Structured Microbial Communities. *Trends in Microbiology*, 28(8):668–681, 8 2020.

[50] J W Costerton. Bacterial Biofilms: A Common Cause of Persistent Infections. *Science*, 284(5418):1318–1322, 5 1999.

[51] Thien-Fah Mah. Biofilm-specific antibiotic resistance. *Future Microbiology*, 7(9):1061–1072, 9 2012.

[52] Divakar Sharma, Lama Misba, and Asad U Khan. Antibiotics versus biofilm: an emerging battleground in microbial communities. *Antimicrobial Resistance & Infection Control*, 8(1):76, 12 2019.

[53] Lucas R. Hoffman, David A. D'Argenio, Michael J. MacCoss, Zhaoying Zhang, Roger A. Jones, and Samuel I. Miller. Aminoglycoside antibiotics induce bacterial biofilm formation. *Nature*, 436(7054):1171–1175, 2005.

[54] Yun Wang, Jessica C. Wilks, Thomas Danhorn, Itzel Ramos, Laura Croal, and Dianne K. Newman. Phenazine-1-carboxylic acid promotes bacterial biofilm development via ferrous iron acquisition. *Journal of Bacteriology*, 193(14):3606–3617, 2011.

[55] Wenbo Zhang, Agnese Seminara, Melanie Suaris, Michael P Brenner, David A Weitz, and Thomas E Angelini. Nutrient depletion in Bacillus subtilis biofilms triggers matrix production. *New Journal of Physics*, 16(1):015028, 1 2014.

[56] Avraham Be'er and Gil Ariel. A statistical physics view of swarming bacteria. *Movement Ecology*, 7(1):9, 12 2019.

[57] Joyce E Patrick and Daniel B Kearns. Swarming motility and the control of master regulators of flagellar biosynthesis. *Molecular Microbiology*, 83(1):14–23, 1 2012.

[58] Susana Mariconda, Qingfeng Wang, and Rasika M Harshey. A mechanical role for the chemotaxis system in swarming motility. *Molecular Microbiology*, 60(6):1590–1602, 6 2006.

[59] Mark Burkart, Adam Toguchi, and Rasika M. Harshey. The chemotaxis system, but not chemotaxis, is essential for swarming motility in Escherichia coli. *Proceedings of the National Academy of Sciences of the United States of America*, 95(5):2568–2573, 1998.

[60] Andrey Sokolov, Raymond E. Goldstein, Felix I. Feldchtein, and Igor S. Aranson. Enhanced mixing and spatial instability in concentrated bacterial suspensions. *Physical Review E*, 80(3):031903, 9 2009.

[61] Andrey Sokolov and Igor S. Aranson. Physical Properties of Collective Motion in Suspensions of Bacteria. *Physical Review Letters*, 109(24):248109, 12 2012.

[62] Gil Ariel, Amit Rabani, Sivan Benisty, Jonathan D. Partridge, Rasika M. Harshey, and Avraham Be'er. Swarming bacteria migrate by Lévy Walk. *Nature Communications*, 6(1):8396, 12 2015.

[63] Avraham Be'er, Bella Ilkanaiv, Renan Gross, Daniel B. Kearns, Sebastian Heidenreich, Markus Bär, and Gil Ariel. A phase diagram for bacterial swarming. *Communications Physics*, 3(1):66, 12 2020.

[64] H. P. Zhang, Avraham Be'er, E. L. Florin, and Harry L. Swinney. Collective motion and density fluctuations in bacterial colonies. *Proceedings of the National Academy of Sciences of the United States of America*, 2010.

[65] Wenlong Zuo and Yilin Wu. Dynamic motility selection drives population segregation in a bacterial swarm. *Proceedings of the National Academy of Sciences of the United States of America*, 117(9):4693–4700, 2020.

[66] Xiaorong Wang, Yu Kang, Chunxiong Luo, Tong Zhao, Lin Liu, Xiangdan Jiang, Rongrong Fu, Shuchang An, Jichao Chen, Ning Jiang, Lufeng Ren, Qi Wang, J Kenneth Baillie, Zhancheng Gao, and Jun Yu. Heteroresistance at the Single-Cell Level: Adapting to Antibiotic Stress through a Population-Based Strategy and Growth-Controlled Interphenotypic Coordination. *mBio*, 5(1):e00942, 2 2014.

[67] Alin Finkelshtein, Dalit Roth, Eshel Ben Jacob, and Colin J. Ingham. Bacterial Swarms Recruit Cargo Bacteria To Pave the Way in Toxic Environments. *mBio*, 6(3):1–10, 5 2015.

[68] Daniel Needleman and Zvonimir Dogic. Active matter at the interface between materials science and cell biology. *Nature Reviews Materials*, 2(9):17048, 9 2017.

[69] S A Gudipaty, J Lindblom, P D Loftus, M J Redd, K Edes, C F Davey, V Krishnegowda, and J Rosenblatt. Mechanical stretch triggers rapid epithelial cell division through Piezo1. *Nature*, 543(7643):118–121, 3 2017.

[70] Ying Tan and Zhong-yang Zheng. Research Advance in Swarm Robotics. *Defence Technology*, 9(1):18–39, 2013.

[71] Tamás Vicsek, András Czirók, Eshel Ben-Jacob, Inon Cohen, and Ofer Shochet. Novel Type of Phase Transition in a System of Self-Driven Particles. *Physical Review Letters*, 75(6):1226–1229, 8 1995.

[72] Sriram Ramaswamy. The Mechanics and Statistics of Active Matter. *Annual Review of Condensed Matter Physics*, 1(1):323–345, 8 2010.

[73] Jeremie Palacci, Stefano Sacanna, Asher Preska Steinberg, David J Pine, and Paul M Chaikin. Living crystals of light-activated colloidal surfers. *Science (New York, N.Y.)*, 339(6122):936–40, 2 2013.

[74] Vijay Narayan, Sriram Ramaswamy, and Narayanan Menon. Long-Lived Giant Number Fluctuations in a Swarming Granular Nematic. *Science*, 317(5834):105–108, 7 2007.

[75] Giuseppe Gonnella, Davide Marenduzzo, Antonio Suma, and Adriano Tiribocchi. Motility-induced phase separation and coarsening in active matter. *Elsevier Masson SAS*, 16(3):316–331, 2015.

[76] Pasquale Digregorio, Demian Levis, Antonio Suma, Leticia F Cugliandolo, Giuseppe Gonnella, and Ignacio Pagonabarraga. Full Phase Diagram of Active Brownian Disks: From Melting to Motility-Induced Phase Separation. *Physical Review Letters*, 121(9):98003, 8 2018.

[77] Michael E Cates and Julien Tailleur. Motility-Induced Phase Separation. *Annual Review of Condensed Matter Physics*, 6(1):219–244, 3 2015.

[78] S. Ramaswamy, R. Aditi Simha, and J. Toner. Active nematics on a substrate: Giant number fluctuations and long-time tails. *Europhysics Letters*, 62(2):196–202, 2003.

[79] Peter H. Westfall. Kurtosis as Peakedness, 1905–2014. R.I.P. *The American Statistician*, 68(3):191–195, 7 2014.

[80] Joel Berry, Clifford P Brangwynne, and Mikko Haataja. Physical principles of intracellular organization via active and passive phase transitions. *Reports on Progress in Physics*, 81(4):046601, 4 2018.

[81] A R Kolahchi. Polyethylene Terephthalate (PET) Films Surface Modification Through Blending. 2014.

[82] Guannan Liu, Adam Patch, Fatmagül Bahar, David Yllanes, Roy D. Welch, M. Cristina Marchetti, Shashi Thutupalli, and Joshua. W. Shaevitz. Self-Driven Phase Transitions Drive Myxococcus xanthus Fruiting Body Formation. *Physical Review Letters*, 122(24):248102, 6 2019.

[83] Marjolein N. van der Linden, Lachlan C Alexander, Dirk G. A. L. Aarts, and Olivier Dauchot. Interrupted Motility Induced Phase Separation in Aligning Active Colloids. *Physical Review Letters*, 123(9):098001, 8 2019.

[84] Fernando Peruani, Jörn Starruß, Vladimir Jakovljevic, Lotte Søgaard-Andersen, Andreas Deutsch, and Markus Bär. Collective motion and nonequilibrium cluster formation in colonies of gliding bacteria. *Physical Review Letters*, 108(9):1–5, 2012.

[85] Frank P. Kuhl and Charles R Giardina. Elliptic Fourier features of a closed contour. *Computer Graphics and Image Processing*, 18(3):236–258, 3 1982.

[86] Karl Skoglund. Fourier Series , the DFT and Shape Modelling. *October*, pages 1–16, 2004.

[87] Charles T. Zahn and Ralph Z. Roskies. Fourier descriptors for plane closed curves. *IEEE Transactions on Computers*, C-21(3):269–281, 1972.

[88] P.E. Lestrel, R.M. Cesar, O. Takahashi, and E. Kanazawa. Sexual dimorphism in the Japanese cranial base: A Fourier-wavelet representation. *American Journal of Physical Anthropology*, 128(3):608–622, 11 2005.

[89] Mélissa Niel, Kathia Chaumoître, Julien Corny, Loïc Lalys, and Pascal Adalian. Maturation of the human foetal basioccipital: quantifying shape changes in second and third trimesters using elliptic Fourier analysis. *Journal of Anatomy*, 235(1):joa.12997, 4 2019.

[90] Zhanwei Yuan, Fuguo Li, Peng Zhang, and Bo Chen. Description of shape characteristics through Fourier and wavelet analysis. *Chinese Journal of Aeronautics*, 27(1):160–168, 2014.

[91] Rodrigo Soto and Ramin Golestanian. Self-assembly of active colloidal molecules with dynamic function. *Physical Review E*, 91(5):052304, 5 2015.

[92] M. Reza Shaebani, Adam Wysocki, Roland G. Winkler, Gerhard Gompper, and Heiko Rieger. Computational models for active matter. *Nature Reviews Physics*, 2(4):181–199, 4 2020.

[93] Nobuhiko Watari and Ronald G Larson. The Hydrodynamics of a Run-and-Tumble Bacterium Propelled by Polymorphic Helical Flagella. *Biophysical Journal*, 98(1):12–17, 1 2010.

[94] Franziska Matthäus, Mario S Mommer, Tine Curk, and Jure Dobnikar. On the Origin and Characteristics of Noise-Induced Lévy Walks of E. Coli. *PLoS ONE*, 6(4):e18623, 4 2011.

[95] Alka A Potdar, Jenny Lu, Junhwan Jeon, Alissa M Weaver, and Peter T Cummings. Bimodal Analysis of Mammary Epithelial Cell Migration in Two Dimensions. *Annals of Biomedical Engineering*, 37(1):230–245, 1 2009.

[96] Maryam Khatami, Katrin Wolff, Oliver Pohl, Mohammad Reza Ejtehadi, and Holger Stark. Active Brownian particles and run-and-tumble particles separate inside a maze. *Scientific Reports*, 6(1):37670, 12 2016.

[97] I.M. Lifshitz and V.V. Slyozov. The kinetics of precipitation from supersaturated solid solutions. *Journal of Physics and Chemistry of Solids*, 19(1-2):35–50, 4 1961.

[98] Vasco M. Worlitzer, Gil Ariel, Avraham Be'er, Holger Stark, Markus Bär, and Sebastian Heidenreich. Motility-induced clustering and meso-scale turbulence in active polar fluids. *New Journal of Physics*, 23(3):033012, 3 2021.

[99] Luis H Cisneros, Ricardo Cortez, Christopher Dombrowski, Raymond E Goldstein, and John O Kessler. Fluid dynamics of self-propelled microorganisms, from individuals to concentrated populations. *Experiments in Fluids*, 43(5):737–753, 11 2007.

[100] Christopher Dombrowski, Luis Cisneros, Sunita Chatkaew, Raymond E Goldstein, and John O Kessler. Self-Concentration and Large-Scale Coherence in Bacterial Dynamics. *Physical Review Letters*, 93(9):098103, 8 2004.

[101] T Ishikawa, N Yoshida, H Ueno, M Wiedeman, Y Imai, and T Yamaguchi. Energy Transport in a Concentrated Suspension of Bacteria. *Physical Review Letters*, 107(2):028102, 7 2011.

[102] Kuo-An Liu and Lin I. Multifractal dynamics of turbulent flows in swimming bacterial suspensions. *Physical Review E*, 86(1):011924, 7 2012.

[103] Edward B. Steager, Chang-Beom Kim, and Min Jun Kim. Dynamics of pattern formation in bacterial swarms. *Physics of Fluids*, 20(7):073601, 7 2008.

[104] Guannan Liu, Adam Patch, Fatmagül Bahar, David Yllanes, Roy D Welch, M Cristina Marchetti, Shashi Thutupalli, and Joshua W Shaevitz. Self-Driven Phase Transitions Drive Myxococcus xanthus Fruiting Body Formation. *Physical Review Letters*, 122(24):248102, 6 2019.

[105] Sho C Takatori and Kranthi K Mandadapu. Motility-induced buckling and glassy dynamics regulate three-dimensional transitions of bacterial monolayers. 3 2020.

[106] Olga E. Petrova and Karin Sauer. Sticky Situations: Key Components That Control Bacterial Surface Attachment. *Journal of Bacteriology*, 194(10):2413–2425, 5 2012.

[107] Judith H Merritt, Daniel E Kadouri, and George A O'Toole. Growing and Analyzing Static Biofilms. In *Current Protocols in Microbiology*, volume Chapter 1, pages Unit–1B.1. John Wiley & Sons, Inc., Hoboken, NJ, USA, 7 2005.

[108] Clara Bleuven and Christian R Landry. Molecular and cellular bases of adaptation to a changing environment in microorganisms. *Proceedings of the Royal Society B: Biological Sciences*, 283(1841):20161458, 10 2016.

[109] Aurélie Crabbé, Peter Østrup Jensen, Thomas Bjarnsholt, and Tom Coenye. Antimicrobial Tolerance and Metabolic Adaptations in Microbial Biofilms. *Trends in Microbiology*, 27(10):850–863, 10 2019.

[110] Eshel Ben-Jacob, Inon Cohen, and Herbert Levine. Cooperative self-organization of microorganisms. *Advances in Physics*, 49(4):395–554, 6 2000.

[111] Marc Kirschner, John Gerhart, and Tim Mitchison. Molecular 'vitalism'. *Cell*, 100(1):79–88, 2000.

[112] François Schweisguth and Francis Corson. Self-Organization in Pattern Formation. *Developmental Cell*, 49(5):659–677, 2019.

[113] Mark L. Hanke and Tammy Kielian. Deciphering mechanisms of staphylococcal biofilm evasion of host immunity. *Frontiers in cellular and infection microbiology*, 2(May):62, 2012.

[114] A. Bridier, R. Briandet, V. Thomas, and F. Dubois-Brissonnet. Resistance of bacterial biofilms to disinfectants: a review. *Biofouling*, 27(9):1017–1032, 10 2011.

[115] Hannah R Meredith, Jaydeep K Srimani, Anna J Lee, Allison J Lopatkin, and Lingchong You. Collective antibiotic tolerance: mechanisms, dynamics and intervention. *Nature Chemical Biology*, 11(3):182–188, 3 2015.

[116] Tianshu Liu, Ali Merat, M. H M Makhmalbaf, Claudia Fajardo, and Parviz Merati. Comparison between optical flow and cross-correlation methods for extraction of velocity fields from particle images. *Experiments in Fluids*, 56(8), 2015.

[117] Alexander K. Epstein, Boaz Pokroy, Agnese Seminara, and Joanna Aizenberg. Bacterial biofilm shows persistent resistance to liquid wetting and gas penetration. *Proceedings of the National Academy of Sciences of the United States of America*, 108(3):995–1000, 2011.

[118] Eric K. Chu, Onur Kilic, Hojung Cho, Alex Groisman, and Andre Levchenko. Self-induced mechanical stress can trigger biofilm formation in uropathogenic Escherichia coli. *Nature Communications*, 9(1), 2018.

[119] Souvik Bhattacharyya, David M. Walker, and Rasika M. Harshey. Dead cells release a 'necrosignal' that activates antibiotic survival pathways in bacterial swarms. *Nature Communications*, 11(1):4157, 12 2020.

[120] Sandra Lai, Julien Tremblay, and Eric Déziel. Swarming motility: a multicellular behaviour conferring antimicrobial resistance. *Environmental Microbiology*, 11(1):126–136, 1 2009.

[121] Mitchell T Butler, Qingfeng Wang, and Rasika M Harshey. Cell density and mobility protect swarming bacteria against antibiotics. *Proceedings of the National Academy of Sciences*, 107(8):3776–3781, 2 2010.

[122] Sherry L. Kuchma, Kimberly M. Brothers, Judith H. Merritt, Nicole T. Liberati, Frederick M. Ausubel, and George A. O'Toole. BifA, a cyclic-Di-GMP phosphodiesterase, inversely regulates biofilm formation and swarming motility by Pseudomonas aeruginosa PA14. *Journal of bacteriology*, 189(22):8165–78, 11 2007.

[123] Felix J H Hol, Bert Hubert, Cees Dekker, and Juan E Keymer. Density-dependent adaptive resistance allows swimming bacteria to colonize an antibiotic gradient. *The ISME Journal*, 10(1):30–38, 1 2016.

[124] Julien Barré, Raphaël Chétrite, Massimiliano Muratori, and Fernando Peruani. Motility-Induced Phase Separation of Active Particles in the Presence of Velocity Alignment. *Journal of Statistical Physics*, 158(3):589–600, 2 2015.

[125] M E Cates, D Marenduzzo, I Pagonabarraga, and J Tailleur. Arrested phase separation in reproducing bacteria creates a generic route to pattern formation. *Proceedings of the National Academy of Sciences*, 107(26):11715 LP – 11720, 6 2010.

[126] Munehiro Asally, Mark Kittisopikul, Pau Rué, Yingjie Du, Zhenxing Hu, Tolga Çağatay, Andra B. Robinson, Hongbing Lu, Jordi Garcia-Ojalvo, and Gürol M. Süel. Localized cell death focuses mechanical forces during 3D patterning in a biofilm. *Proceedings of the National Academy of Sciences of the United States of America*, 109(46):18891–18896, 2012.

[127] Pushpita Ghosh, Eshel Ben-Jacob, and Herbert Levine. Modeling cell-death patterning during biofilm formation. *Physical Biology*, 10(6):066006, 11 2013.

[128] Lynne S. Cairns, Laura Hobley, and Nicola R. Stanley-Wall. Biofilm formation by Bacillus subtilis: New insights into regulatory strategies and assembly mechanisms. *Molecular Microbiology*, 93(4):587–598, 2014.

[129] D. Lopez, Hera Vlamakis, and Roberto Kolter. Biofilms. *Cold Spring Harbor Perspectives in Biology*, 2(7):a000398–a000398, 7 2010.

[130] Steven S. Branda, J. E. Gonzalez-Pastor, Sigal Ben-Yehuda, Richard Losick, and Roberto Kolter. Fruiting body formation by Bacillus subtilis. *Proceedings of the National Academy of Sciences*, 98(20):11621–11626, 9 2001.

[131] Sara Kesel, Stefan Grumbein, Ina Gümperlein, Marwa Tallawi, Anna-kristina Marel, Oliver Lieleg, and Madeleine Opitz. Direct Comparison of Physical Properties of Bacillus subtilis NCIB 3610 and B-1 Biofilms. *Applied and Environmental Microbiology*, 82(8):2424–2432, 4 2016.

[132] Diego Romero, Claudio Aguilar, Richard Losick, and Roberto Kolter. Amyloid fibers provide structural integrity to Bacillus subtilis biofilms. *Proc. Natl. Acad. Sci. USA*, 107(5):2230–4, 2 2010.

[133] Hera Vlamakis, Claudio Aguilar, Richard Losick, and Roberto Kolter. Control of cell fate by the formation of an architecturally complex bacterial community. *Genes & Development*, 22(7):945–953, 4 2008.

[134] F. Peruani, L. Schimansky-Geier, and M. Bär. Cluster dynamics and cluster size distributions in systems of self-propelled particles. *The European Physical Journal Special Topics*, 191(1):173–185, 12 2010.

[135] Sebastian Weitz, Andreas Deutsch, and Fernando Peruani. Self-propelled rods exhibit a phase-separated state characterized by the presence of active stresses and the ejection of polar clusters. *Physical Review E*, 92(1):012322, 7 2015.

[136] Margarita Kalamara, Mihael Spacapan, Ines Mandic-Mulec, and Nicola R. Stanley-Wall. Social behaviours by Bacillus subtilis : quorum sensing, kin discrimination and beyond. *Molecular Microbiology*, 110(6):863–878, 12 2018.

[137] Ekaterina Krasnopeeva, Chien Jung Lo, and Teuta Pilizota. Single-Cell Bacterial Electrophysiology Reveals Mechanisms of Stress-Induced Damage. *Biophysical Journal*, 116(12):2390–2399, 2019.

[138] Junyi Yang, Paulo E. Arratia, Alison E. Patteson, and Arvind Gopinath. Quenching active swarms: effects of light exposure on collective motility in swarming Serratia marcescens. *Journal of The Royal Society Interface*, 16(156):20180960, 7 2019.

[139] Tina Netzker, Evan M.F. Shepherdson, Matthew P Zambri, and Marie A Elliot. Bacterial Volatile Compounds: Functions in Communication, Cooperation, and Competition. *Annual Review of Microbiology*, 74(1):409–430, 9 2020.

[140] Tamás Vicsek and Anna Zafeiris. Collective motion. *Physics Reports*, 517(3):71–140, 2012.

[141] G. De Magistris and D. Marenduzzo. An introduction to the physics of active matter. *Physica A: Statistical Mechanics and its Applications*, 418:65–77, 2015.

[142] Iago Grobas, Dario G. Bazzoli, and Munehiro Asally. Biofilm and swarming emergent behaviours controlled through the aid of biophysical understanding and tools. *Biochemical Society Transactions*, 48(6):2903–2913, 2020.

[143] Katherine Copenhagen, Ricard Alert, Ned S. Wingreen, and Joshua W. Shaevitz. Topological defects induce layer formation in Myxococcus xanthus colonies. *arXiv*, 2020.

[144] Jonathan D. Partridge, Gil Ariel, Orly Schvartz, Rasika M. Harshey, and Avraham Be'er. The 3D architecture of a bacterial swarm has implications for antibiotic tolerance. *Scientific Reports*, 8(1):15823, 12 2018.

[145] Feng Qiu, Gongwen Peng, Valeriy V Ginzburg, Anna C Balazs, Hsuan-Yi Chen, and David Jasnow. Spinodal decomposition of a binary fluid with fixed impurities. *The Journal of Chemical Physics*, 115(8):3779–3784, 8 2001.

[146] Hua Jiang, Nannan Dou, Guoqiang Fan, Zhaohui Yang, and Xiaohua Zhang. Effect of temperature gradient on liquid-liquid phase separation in a polyolefin blend. *Journal of Chemical Physics*, 139(12), 2013.

[147] Arianna Bartolini, P. Tempesti, Ahmad F. Ghobadi, Debora Berti, J. Smets, Yousef G. Aouad, and P. Baglioni. Liquid-liquid phase separation of polymeric microdomains with tunable inner morphology: Mechanistic insights and applications. *Journal of Colloid and Interface Science*, 556:74–82, 2019.

[148] Pierre Papon, Jacques Leblond, and Paul H.E. Meijer. *The Physics of Phase Transitions*. Springer Berlin Heidelberg, Berlin, Heidelberg, 2006.

[149] A. J. Bray. Theory of phase-ordering kinetics. *Advances in Physics*, 51(2):481–587, 3 2002.

[150] P. M. Chaikin and T. C. Lubensky. *Principles of Condensed Matter Physics*. Cambridge University Press, 6 1995.

[151] Yue Sun, W. Beck Andrews, Katsuyo Thornton, and Peter W. Voorhees. Self-Similarity and the Dynamics of Coarsening in Materials. *Scientific Reports*, 8(1):17940, 12 2018.

[152] Thein Kyu and Jae-Hyung Lee. Nucleation Initiated Spinodal Decomposition in a Polymerizing System. *Physical Review Letters*, 76(20):3746–3749, 5 1996.

[153] Demian Levis and Ludovic Berthier. Clustering and heterogeneous dynamics in a kinetic Monte Carlo model of self-propelled hard disks. *Physical Review E*, 89(6):062301, 6 2014.

[154] F. Ginot, I. Theurkauff, F. Detcheverry, C. Ybert, and C. Cottin-Bizonne. Aggregation-fragmentation and individual dynamics of active clusters. *Nature Communications*, 9(1), 2018.

[155] Gabriel S. Redner, Caleb G. Wagner, Aparna Baskaran, and Michael F. Hagan. Classical Nucleation Theory Description of Active Colloid Assembly. *Physical Review Letters*, 117(14):148002, 9 2016.

[156] Fernando Peruani, Andreas Deutsch, and Markus Bär. Nonequilibrium clustering of self-propelled rods. *Physical Review E*, 74(3):030904, 9 2006.

[157] Pavel L. Krapivsky, Sidney Redner, and Eli Ben-Naim. *A Kinetic View of Statistical Physics*. Cambridge University Press, Cambridge, 2010.

[158] Vasily Kantsler, Elena Ontañón-McDonald, Cansu Kuey, Manjari J Ghanshyam, Maria Chiara Roffin, and Munehiro Asally. Pattern Engineering of Living Bacterial Colonies Using Meniscus-Driven Fluidic Channels. *ACS Synthetic Biology*, 9(6):1277–1283, 6 2020.

[159] P. Aceves-Sanchez, P. Degond, E. E. Keaveny, A. Manhart, S. Merino-Aceituno, and D. Peurichard. Large-Scale Dynamics of Self-propelled Particles Moving Through Obstacles: Model Derivation and Pattern Formation. *Bulletin of Mathematical Biology*, 82(10):129, 10 2020.

[160] Nour Ghaddar, Mona Hashemidahaj, and Brandon L. Findlay. Access to high-impact mutations constrains the evolution of antibiotic resistance in soft agar. *Scientific Reports*, 8(1):1–10, 2018.

[161] Lucía Fernández, Elena B.M. Breidenstein, and Robert E.W. Hancock. Creeping baselines and adaptive resistance to antibiotics. *Drug Resistance Updates*, 14(1):1–21, 2 2011.

[162] Erdal Toprak, Adrian Veres, Sadik Yildiz, Juan M. Pedraza, Remy Chait, Johan Paulsson, and Roy Kishony. Building a morbidostat: An automated continuous-culture device for studying bacterial drug resistance under dynamically sustained drug inhibition. *Nature Protocols*, 8(3):555–567, 2013.

[163] H. Lencastre, A. M. S. Figueiredo, and A Tomasz. Genetic control of population structure in heterogeneous strains of methicillin resistantStaphylococcus aureus. *European Journal of Clinical Microbiology & Infectious Diseases*, 12(S1):S13–S18, 1 1993.

[164] L Luzzatto, D Apirion, and D Schlessinger. Mechanism of action of streptomycin in E. coli: interruption of the ribosome cycle at the initiation of protein synthesis. *Proceedings of the National Academy of Sciences of the United States of America*, 60(3):873–80, 1968.

[165] Teruo Kuroda and Tomofusa Tsuchiya. Multidrug efflux transporters in the MATE family. *Biochimica et Biophysica Acta - Proteins and Proteomics*, 1794(5):763–768, 2009.

[166] J. Reidl and W. Boos. The malX malY operon of Escherichia coli encodes a novel enzyme II of the phosphotransferase system recognizing glucose and maltose and an enzyme abolishing the endogenous induction of the maltose system. *Journal of Bacteriology*, 173(15):4862–4876, 8 1991.

[167] Phillip Yen and Jason A. Papin. History of antibiotic adaptation influences microbial evolutionary dynamics during subsequent treatment. *PLOS Biology*, 15(8):e2001586, 8 2017.

[168] G L McKnight, S L Mudri, S L Mathewes, R R Traxinger, S Marshall, P O Sheppard, and P J O'Hara. Molecular cloning, cDNA sequence, and bacterial expression of human glutamine:fructose-6-phosphate amidotransferase. *The Journal of biological chemistry*, 267(35):25208–12, 12 1992.

[169] Mattia Zampieri, Tim Enke, Victor Chubukov, Vito Ricci, Laura Piddock, and Uwe Sauer. Metabolic constraints on the evolution of antibiotic resistance. *Molecular Systems Biology*, 13(3):917, 2017.

[170] Linda L Marcusson, Niels Frimodt-Møller, and Diarmaid Hughes. Interplay in the Selection of Fluoroquinolone Resistance and Bacterial Fitness. *PLoS Pathogens*, 5(8):e1000541, 8 2009.

[171] Kalesh Sasidharan, Andrea S Martinez-Vernon, Jing Chen, Tiantian Fu, and Orkun Soyer. A low-cost DIY device for high resolution, continuous measurement of microbial growth dynamics. *bioRxiv*, page 407742, 2018.

[172] Jorge Olivares Pacheco, Carolina Alvarez-Ortega, Manuel Alcalde Rico, and José Luis Martínez. Metabolic Compensation of Fitness Costs Is a General Outcome for Antibiotic-Resistant Pseudomonas aeruginosa Mutants Overexpressing Efflux Pumps. *mBio*, 8(4):1–13, 9 2017.

[173] Maria A. Borovinskaya, Raj D. Pai, Wen Zhang, Barbara S. Schuwirth, James M. Holton, Go Hirokawa, Hideko Kaji, Akira Kaji, and Jamie H.Doudna Cate. Structural basis for aminoglycoside inhibition of bacterial ribosome recycling. *Nature Structural and Molecular Biology*, 2007.

[174] Leyi Wang, Arto Pulk, Michael R. Wasserman, Michael B. Feldman, Roger B. Altman, Jamie H. Doudna Cate, and Scott C. Blanchard. Allosteric control of the ribosome by small-molecule antibiotics. *Nature Structural and Molecular Biology*, 2012.

[175] G Gialdroni Grassi. Drug-Inactivating Enzymes of Bacteria Grown in Subminimal Inhibitory Concentrations of Antibiotics. *Clinical Infectious Diseases*, 1(5):852–857, 9 1979.

[176] Rosemary A. Bamford, Ashley Smith, Jeremy Metz, Georgina Glover, Richard W. Titball, and Stefano Pagliara. Investigating the physiology of viable but non-culturable bacteria by microfluidics and time-lapse microscopy. *BMC Biology*, 15(1):121, 12 2017.

[177] Ping Wang, Lydia Robert, James Pelletier, Wei Lien Dang, Francois Taddei, Andrew Wright, and Suckjoon Jun. Robust Growth of Escherichia coli. *Current Biology*, 20(12):1099–1103, 6 2010.

[178] Sung-Hee Jung, Choong-Min Ryu, and Jun-Seob Kim. Bacterial persistence: Fundamentals and clinical importance. *Journal of Microbiology*, 57(10):829–835, 10 2019.

[179] Nathalie Q Balaban. Bacterial Persistence as a Phenotypic Switch. *Science*, 305(5690):1622–1625, 9 2004.

[180] Kim Lewis. Persister Cells. *Annual Review of Microbiology*, 64(1):357–372, 10 2010.

[181] Giancarlo Noe Bruni and Joel M. Kralj. Membrane voltage dysregulation driven by metabolic dysfunction underlies bactericidal activity of aminoglycosides. *eLife*, 9:1–25, 8 2020.

[182] P D Damper and W Epstein. Role of the membrane potential in bacterial resistance to aminoglycoside antibiotics. *Antimicrobial agents and chemotherapy*, 20(6):803–8, 12 1981.

[183] Tobias Grafke, Michael E. Cates, and Eric Vanden-Eijnden. Spatiotemporal Self-Organization of Fluctuating Bacterial Colonies. *Physical Review Letters*, 119(18):1–5, 2017.

[184] Yuting I Li and Michael E Cates. Non-equilibrium phase separation with reactions: a canonical model and its behaviour. *Journal of Statistical Mechanics: Theory and Experiment*, 2020(5):053206, 5 2020.

[185] Munehiro Asally, Mark Kittisopikul, P. Rue, Yingjie Du, Zhenxing Hu, T. Cagatay, A. B. Robinson, Hongbing Lu, Jordi Garcia-Ojalvo, and G. M. Suel. Localized cell death focuses mechanical forces during 3D patterning in a biofilm. *Proceedings of the National Academy of Sciences*, 109(46):18891–18896, 11 2012.

[186] Simon F. Schoeller, William V. Holt, and Eric E. Keaveny. Collective dynamics of sperm cells. *Philosophical Transactions of the Royal Society B: Biological Sciences*, 375(1807):20190384, 9 2020.

[187] Andreas Deutsch, Guy Theraulaz, and Tamas Vicsek. Collective motion in biological systems. *Interface Focus*, 2(6):689–692, 12 2012.

[188] Masayuki Hayakawa, Tetsuya Hiraiwa, Yuko Wada, Hidekazu Kuwayama, and Tatsuo Shibata. Polar pattern formation induced by contact following locomotion in a multicellular system. *eLife*, 9:1–18, 4 2020.

[189] Moshe Shemesh and Yunrong Chai. A Combination of Glycerol and Manganese Promotes Biofilm Formation in Bacillus subtilis via Histidine Kinase KinD Signaling. *Journal of Bacteriology*, 195(12):2747–2754, 6 2013.

[190] Sofia Arnaouteli, D. A. Matoz-Fernandez, Michael Porter, Margarita Kalamara, James Abbott, Cait E. MacPhee, Fordyce A. Davidson, and Nicola R. Stanley-Wall. Pulcherrimin formation controls growth arrest of the Bacillus subtilis biofilm. *Proceedings of the National Academy of Sciences*, 116(27):13553–13562, 7 2019.

[191] Stephanie M. Amato, Christopher H. Fazen, Theresa C. Henry, Wendy W. K. Mok, Mehmet A. Orman, Elizabeth L. Sandvik, Katherine G. Volzing, and Mark P. Brynildsen. The role of metabolism in bacterial persistence. *Frontiers in Microbiology*, 5(MAR):1–9, 2014.

[192] Les Dethlefsen and David A Relman. Incomplete recovery and individualized responses of the human distal gut microbiota to repeated antibiotic perturbation. *Proceedings of the National Academy of Sciences*, 108(Supplement_1):4554–4561, 3 2011.

[193] Elizabeth Thursby and Nathalie Juge. Introduction to the human gut microbiota. *Biochemical Journal*, 474(11):1823–1836, 2017.

[194] Carolina Tropini, Kristen A. Earle, Kerwyn Casey Huang, and Justin L. Sonnenburg. The Gut Microbiome: Connecting Spatial Organization to Function. *Cell Host & Microbe*, 21(4):433–442, 4 2017.

[195] B. Anne Neville, Christophe D'Enfert, and Marie-Elisabeth Bougnoux. Candida albicans commensalism in the gastrointestinal tract. *FEMS Yeast Research*, 15(7):fov081, 11 2015.

[196] A. W. Bauer, W. M. M. Kirby, J. C. Sherris, and M. Turck. Antibiotic Susceptibility Testing by a Standardized Single Disk Method. *American Journal of Clinical Pathology*, 45(4_ts):493–496, 4 1966.

[197] Stephan Preibisch, Stephan Saalfeld, and Pavel Tomancak. Globally optimal stitching of tiled 3D microscopic image acquisitions. *Bioinformatics*, 25(11):1463–1465, 6 2009.

[198] Johannes Schindelin, Ignacio Arganda-Carreras, Erwin Frise, Verena Kaynig, Mark Longair, Tobias Pietzsch, Stephan Preibisch, Curtis Rueden, Stephan Saalfeld, Benjamin Schmid, Jean Yves Tinevez, Daniel James White, Volker Hartenstein, Kevin Eliceiri, Pavel Tomancak, and Albert Cardona. Fiji: An open-source platform for biological-image analysis. *Nature Methods*, 9(7):676–682, 2012.

[199] J Kristian Sveen. An introduction to MatPIV v. 1.6.1. 2004.

[200] Lewis S. Mosby, Marco Polin, and Darius Vasco Köster. A Python based automated tracking routine for myosin II filaments. *Journal of Physics D: Applied Physics*, 4 2020.

[201] Stuart Berg, Dominik Kutra, Thorben Kroeger, Christoph N. Straehle, Bernhard X. Kausler, Carsten Haubold, Martin Schiegg, Janez Ales, Thorsten Beier, Markus Rudy, Kemal Eren, Jaime I. Cervantes, Buote Xu, Fynn Beuttenmueller, Adrian Wolny, Chong Zhang, Ullrich Koethe, Fred A. Hamprecht, and Anna Kreshuk. ilastik: interactive machine learning for (bio)image analysis. *Nature Methods*, 16(12):1226–1232, 12 2019.

[202] B E Warren. *X-ray diffraction*. Addison-Wesley Pub. Co., Reading, Mass., 1969.

[203] Adam S Wilkins and Robin Holliday. The Evolution of Meiosis From Mitosis. *Genetics*, 181(1):3–12, 1 2009.